Analysis and Synthesis of Shell Flexures

van de Sande, W.W.P.J.

DOI
10.4233/uuid:03dae8b4-4b3e-49af-8783-807882c62338

Publication date
2024

Document Version
Final published version

Citation (APA)
van de Sande, W. W. P. J. (2024). *Analysis and Synthesis of Shell Flexures*. [Dissertation (TU Delft), Delft University of Technology]. https://doi.org/10.4233/uuid:03dae8b4-4b3e-49af-8783-807882c62338

Important note
To cite this publication, please use the final published version (if applicable).
Please check the document version above.

Analysis and Synthesis of Shell Flexures

Analysis and Synthesis of Shell Flexures

Proefschrift

ter verkrijging van de graad van doctor
aan de Technische Universiteit Delft,
op gezag van de Rector Magnificus prof. dr. ir. T.H.J.J. van der Hagen,
voorzitter van het College voor Promoties,
in het openbaar te verdedigen op
maandag 11 maart 2024 om 15.00 uur

door

Werner Wilhelmus Petrus Johannes VAN DE SANDE

Master of Science in Mechanical Engineering,
Universiteit Twente, Enschede, Nederland
geboren te 's-Hertogenbosch, Nederland.

Dit proefschrift is goedgekeurd door de promotor.

Samenstelling promotiecommissie:

Rector Magnificus,	voorzitter
Prof. dr. ir. J.L. Herder	Technische Universiteit Delft, *promotor*
Onafhankelijke leden:	
Prof. dr. ir. P. Breedveld	Technische Universiteit Delft
Prof. Dr. Dipl.Ing. C.A. Dransfeld	Technische Universiteit Delft
Prof. Dr. CMath MIMA K.A. Seffen	University of Cambridge
Prof. dr. ir. EngD. D.M. Brouwer	Universiteit Twente
Overig lid:	
Prof. Dr. C.J. Kim	Bucknell University

This work was part of the research programme HTSM-2012 with project number 12814, which is (partly) financed by the Netherlands Organisation for Scientific Research (NWO).

Printed by: Gildeprint

Cover: Color scheme, graphics and typography inspired by the tape springs that are heavily featured in this dissertation.

ISBN 978-94-6366-837-8

An electronic copy of this dissertation is available at
https://repository.tudelft.nl/.

I seldom end up where I wanted to go, but almost always end up where I need to be.

Douglas Adams

Contents

Summary

Compliant shell mechanisms are defined as spatially curved thin-walled structures able to transfer or transform motion, force or energy through elastic deflection. They are a sub-category of compliant mechanisms which also gain there motion from elastic deformation. As such they store energy during motion, in addition to providing desired kinematics. One major benefit of this attribute is that several functions of a mechanism or a machine can be integrated into a single monolithic part; this is often called function integration.

Certain force-deflection behaviour can be purposefully designed by tailoring the energy storage over the range of motion. This is useful for passive exoskeletons where shell mechanisms are used to compensate the user's body weight and thereby decrease the fatigue accumulated during work. Other applications can be medical devices which often need specific kinetics while operating in a small environment. Shell mechanisms or shell flexures provide different kinetic behaviour than their flat counterparts: the wire flexure and leaf spring flexure. These properties of shell flexures can be leveraged to create more compact force generators.

Shell mechanism research is a relatively new field, with articles introducing novel designs with a specific behaviour in mind, such as constant force or moment generators. The state of the art presents what shell mechanisms are capable of. However, the state of the art provides little guidance in how to analyse and design shell mechanisms in general. The objective of this thesis is to propose tools for the analysis and design of compliant shell mechanisms or flexures and to develop understanding of this class of mechanisms. This thesis is divided into three parts. Part I presents the eigenscrew decomposition as a tool to understand and design the kinetics of all compliant (shell) mechanisms. Part II discusses the properties of a buckled tape spring and a method to synthesise a wide array of force-deflection behaviour. In part III, a novel category of shell mechanisms is introduced. A curved surface is patterned with a lattice, which is able to deform in the membrane of the shell. This is opposed to other shell mechanism that work primarily through the bending of the membrane.

Part I consists of chapters 2 to 4. Chapter 2 uses the eigenscrew decomposition to show the kinetics of several shells. It also introduces the unified stiffness metric, which allows the comparison of the rotational and translational stiffness. This metric is based on intrinsic properties of the eigenscrews and enables the user to determine the degrees of freedom of any compliant mechanism. Chapter 3 introduces a scoliosis brace that was designed with the help of the eigenscrew decomposition. It uses the decomposition in two ways: an eigenscrew is used as an objective function in an optimisation scheme and aligned eigenscrews are also used to design a parallel shell mechanism. Chapter 4 demonstrates the use of the eigenscrew decomposition in the analysis of compliant mechanisms in general. It can be used to show the parasitic motions present in

a variety of compliant mechanisms. Chapter 4 ends with an analysis of a buckled tape spring, which validates the behaviour seen in literature and shows it can also be used for zero stiffness flexures.

Chapter 5 is the first chapter of part II and continues with an analysis of a buckled tape spring. Specifically it presents the influence of the geometry on the energy content and deformation of the tape spring. A tape loop is a straight-line mechanism created by two buckled tape springs in parallel. Chapter 6 introduces a constant-force tape loop based on the knowledge gained in chapter 5. It achieves this by varying the cross-section of the tape spring along its length.Chapter 7 is the final chapter of part II and builds on the work in chapter 5 and chapter 6. A synthesis method is proposed that can generate a wide array of force-displacement behaviour. It does this through obtaining a mathematical model of tape loop behaviour and using this model in a system identification scheme.

Chapter 8 is the only chapter of part III and introduces the use of lattices on curved surfaces. The resulting structures are capable of uniform scaling or dilation. The proposed method first converts a surface into a polyhedron consisting of only triangles. These triangles are then replaced by pantographs that are capable of uniform scaling. The triangles are connected to each other in such a manner that the entire structure is able to dilate with a single degree of freedom. This method is proven to work on any surface.

Samenvatting

Elastische schaalmechanismen worden gedefinieerd als ruimtelijk gekromde dunwandige structuren die in staat zijn om beweging, kracht of energie over te dragen of te transformeren door middel van elastische vervorming. Ze zijn een subcategorie van elastische mechanismen die hun beweging ook verkrijgen door elastische vervorming. Naast het leveren van gewenste kinematica, slaan ze ook energie op tijdens hun beweging. Een groot voordeel van deze eigenschap is dat verschillende functies van een mechanisme of een machine kunnen worden geïntegreerd in een enkel monolithisch onderdeel; dit wordt vaak functie-integratie genoemd.

Bepaald kracht-weggedrag kan doelbewust worden ontworpen door deze energieopslag over het bewegingsbereik aan te passen. Dit is handig voor passieve exo-skeletten waarbij schaalmechanismen worden gebruikt om het lichaamsgewicht van de gebruiker te compenseren en zo de tijdens het werk opgebouwde vermoeidheid te verminderen. Andere toepassingen kunnen medische apparaten zijn die vaak specifiek kracht-weggedrag nodig hebben terwijl ze in een kleine ruimte moeten werken. Schaalmechanismen of gekromde elastische elementen hebben ander gedrag dan hun vlakke tegenhangers: de spriet en bladveer. Deze eigenschappen kunnen vervolgens worden gebruikt om compactere krachtgeneratoren te creëren.

Onderzoek naar schaalmechanismen is relatief nieuw, dit onderzoek introduceert vaak nieuwe ontwerpen met een specifiek gedrag in gedachten, zoals constante kracht- of momentgeneratoren. De huidige stand van het onderzoek laat goed zien waartoe schaalmechanismen in staat zijn. De huidige stand van het onderzoek biedt echter weinig richtlijnen voor het analyseren en ontwerpen van shell-mechanismen in het algemeen. Het doel van dit proefschrift is om hulpmiddelen voor de analyse en het ontwerp van elastische schaalmechanismen te introduceren en om begrip van deze klasse van mechanismen te ontwikkelen. Dit proefschrift is verdeeld in drie delen. Deel I presenteert de eigenscrew-decompositie als hulpmiddel om de kinematica en kinetica van alle elastische (schaal) mechanismen te begrijpen en te ontwerpen. Deel II bespreekt de eigenschappen van een geknikte rolmaat en introduceert een methode om een breed scala aan kracht-weggedrag te synthetiseren met dit element. In deel III wordt een nieuwe categorie van schaalmechanismen geïntroduceerd. Een gebogen oppervlak met een rasterwerk, dat kan vervormen in het membraan van de schaal. Dit is in tegenstelling tot andere schaalmechanismen die voornamelijk werken door het buigen van het membraan.

Deel I bestaat uit hoofdstuk 2, 3 en 4. Hoofdstuk 2 gebruikt de eigenschroefdecompositie om de kinetica van verschillende schalen te tonen. Het introduceert ook de gecombineerde stijfheidsmaat (unified stiffness metric), die de vergelijking van een rotatiestijfheid met een translatiestijfheid mogelijk maakt. Deze maat is gebaseerd op intrinsieke eigenschappen van de eigenschroeven en stelt de gebruiker in staat om de vrijheidsgraden van een elastisch mechanisme te bepalen. Hoofdstuk 3 introduceert een scoliose-

corset dat is ontworpen met behulp van de eigenschroef-decompositie. Het gebruikt de decompositie op twee manieren: een eigenschroef wordt gebruikt als een doelfunctie in een optimalisatieschema en uitgelijnde eigenschroeven worden ook gebruikt om een parallel schaalmechanisme te ontwerpen. Hoofdstuk 4 demonstreert het gebruik van de eigenschroefdecompositie bij de analyse van elastische mechanismen in het algemeen. Het kan worden gebruikt om de parasitaire bewegingen aan te tonen die aanwezig zijn in veel elastische mechanismen. Hoofdstuk 4 eindigt met een analyse van een geknikte rolmaat, die het gedrag uit de literatuur valideert en aantoont dat het ook kan worden gebruikt voor elastische elementen zonder stijfheid.

Hoofdstuk 5 is het eerste hoofdstuk van Deel II en gaat verder met een analyse van een geknikte rolmaat. Hoofdstuk 5 presenteert het de invloed van de geometrie op de energie-inhoud en vervorming van de rolmaat. Een bandlus is een rechtgeleidingsmechanisme dat wordt gecreëerd door twee parallelle geknikte rolmaten. Hoofdstuk 6 introduceert een bandlus met constante kracht op basis van de kennis die is opgedaan in hoofdstuk 5. Dit wordt bereikt door de dwarsdoorsnede van de rolmaat over de lengte te variëren. Hoofdstuk 7 is het laatste hoofdstuk van deel II en bouwt voort op hoofdstukken 5 en 6. Er wordt een synthesemethode voorgesteld die een breed scala aan krachtweggedrag van bandlussen kan genereren. Dit wordt gedaan door een wiskundig model van bandlusgedrag te verkrijgen en dit model te gebruiken in een systeemidentificatieschema.

Hoofdstuk 8 is het enige hoofdstuk van deel III en introduceert het gebruik van rasters op gebogen oppervlakken. De resulterende structuren zijn in staat tot uniforme schaalvergroting of dilatatie. De voorgestelde methode zet eerst een oppervlak om in een veelvlak dat alleen uit driehoeken bestaat. Deze driehoeken worden vervolgens vervangen door pantografen die uniform kunnen schalen. De driehoeken zijn zodanig met elkaar verbonden dat de hele structuur kan schalen met een enkele vrijheidsgraad. Daarnaast is het bewezen dat deze methode op elk oppervlak werkt.

1

Introduction

Shells often evoke images of eggs, shells of crustaceans and tortoises or the exoskeletons of insects. In the domain of human-made structures, shells can be seen in domes, vaulted ceilings, pressure vessels and wings, among others. The common denominator is that these shells are designed for minimum compliance; thin shells are very resistant to loads and deformation due to their geometry.

Calladine [1] distils the two main attributes of shells : *continuity* and *curvature*. Curvature is relatively self-explanatory. A shell needs to be curved in order be considered a shell; e.g. a flat plate is at best a degenerate shell. Continuity can have more than one meaning. Calladine makes the distinction that shells need to be *structurally continuous* in order to be able to transmit forces. This allows structures consisting of multiple parts, such as masonry domes or riveted pressure vessels, to classify as shells. Incidentally, this distinction also allows a shell with holes to be classified as a shell structure; as a shell containing holes is able to transmit forces. These two attributes, *continuity* and *curvature*, also will be of use in categorising compliant shell mechanisms. A compliant shell mechanism is a shell, and thus curved and structurally continuous, and a compliant mechanism.

Compliant Mechanisms

Compliant mechanisms make use of high compliance to achieve specific kinematics. They make use of elastic deformation to achieve motion or load transmission, which requires the same structural continuity as shells [2]. Compliant mechanisms can be completely monolithic, i.e. consisting out of one single uninterrupted piece of material. In some cases, most of the mechanism deforms when loaded, which is called distributed compliance. In other cases, only parts of the mechanism deform whereas other parts stay rigid; this is called lumped compliance. The rigid parts carry the same functionality as links in rigid mechanisms; the deforming parts are similar to joints and are called flexures. The rigid parts and flexures exist in different configurations or topologies to achieve the desired kinematics.

Despite the many possible topologies of compliant mechanisms, there are two main flexures that make up most of the flexure elements: the wire flexure and the leaf spring flexure. In precision engineering, both can be considered as straight beam

elements and vary only in the type of cross section. Their cross-sectional lengths are comparatively small to the length of the flexure, allowing the use of beam theory.

A wire flexure usually has a circular or square cross section, whereas a leaf spring flexure has a rectangular cross section with a high aspect ratio. These flat and prismatic flexures meet part of the requirements for shells as they are (structurally) continuous. They lack curvature, however. A simple way to create a compliant shell mechanism is then to add a curvature to an existing flexure or mechanism. This is precisely what has been done in literature. In some mechanisms, compliant shells are used as flexures which are connected to rigid parts [3–5]; which can be considered as lumped compliance . In other mechanisms the entire shells deform to achieve the desired behaviour [6, 7], which can be considered as distributed compliance.

Kinetics of Mechanisms

Compliant shell mechanisms have more complex shapes that their flat and straight counterparts; however all mechanisms in the real world are inherently spatial. The kinematics of most existing compliant mechanisms, including compliant shell mechanisms, is mostly planar [2, 6–11]. Usually the analysis is then also only planar, with some analyses looking at attributes such as support stiffness separately [12, 13]. For compliant mechanisms with straight flexures, this is logical due to the small size, small deformations and lumped compliance. In compliant shell mechanisms this cannot be so easily overlooked as they have spatial geometries, large non-linear deformations, and distributed compliance. As such a comprehensive strategy of analysing these mechanisms in three dimensions is needed.

Rigid link spatial mechanisms are often analysed in a complete three dimensional fashion. A fully spatial analysis is needed to fully understand the kinematics or dynamics of delta robots, steward platforms, among others. Synthesis is also done in a spatial manner [14].

A method that is often used for this purpose is screw theory. Screw theory builds on the fact that any rigid body motion can be defined by the combination of a rotation about a line and a translation along that same line. This is known as Chasles' theorem. A similar concept can be derived for loads using Poinsot's theorem [15]. The mathematical framework provided by screw theory allows to express the kinetics of rigid bodies as geometry. This makes it a visual method; it allows the user to see rotational axes, translations and loads on mechanisms. This type of analysis is very insightful for compliant mechanisms to see the kinetics of a mechanism. It is especially useful for shell mechanisms where the kinetics are not immediately obvious.

Eigenscrew decomposition is a method that links screw theory with compliant mechanisms. It is a specific eigenvalue decomposition of the stiffness and compliance matrix and was introduced by Lipkin et al. [16, 17]. The eigenvalues are eigenstiffnesses and the accompanying eigenvectors are screws. These screws and eigenstiffnesses give insight into the kinetic behaviour of a compliant mechanism. As long as the stiffness matrix of a compliant mechanism at a certain pose is

known, insight can be gained from performing the eigenscrew decomposition. In this thesis eigenscrew decomposition is used to analyse and design compliant (shell) mechanisms.

Categorization of Shells

Compliant shell mechanisms have already been discussed in literature. Seffen [18] defined them as "open, thin-walled, discretely corrugated structures, with flat facets or curved regions of shell interconnected by folds or hinge lines", or "discretely corrugated structures, capable of undergoing large, reversible displacements". In turn Radaelli [19] combined Farshad's and Howell definitions of shells and complaint mechanisms respectively to arrive at the following definition:"compliant shell mechanisms are spatially curved thin-walled structures able to transfer or transform motion, force or energy through elastic deflection". Both definitions focus on the elastically deformable geometries that are thin-walled and curved. Nijssen [20] used these definitions and the attributes described by Calladine and categorised compliant shell mechanisms by their geometrical continuity and curvature. This is useful as it is then possible to classify completely different mechanisms as shell mechanisms, but in fundamentally different categories. Categories such origami shell mechanisms as devised by Schenk et al. [21] or smooth shell mechanisms as devised by Radaelli et al. [7, 9, 22].

This notion of geometric and structural continuity and Gaussian curvature can be used to extend the framework so that any shell mechanism can be placed into a distinct sub-category of shell mechanisms.

A subdivision of shells based on continuity can be made; there are several categories of geometric continuity [23].

- In a G^2 surface adjacent points will have common centres of curvature, this is often seen as perfectly smooth. This class contains all classical shell shapes, such as the cylinder, double parabolic, sphere and a saddle shape.
- A G^1 surface does not have sharp edges, but adjacent points on the geometry can have different centres of curvature, examples are rounded polyhedra, such as a rounded cube. This type of surfaces appear smooth but are in fact not.
- A G^0 surface is completely continuous, but will contain sharp edges, such as the hinge lines of origami.

These are the classical categories of geometric continuity, however to also cover structural continuity, another category is needed. This type of geometry is not completely geometrically continuous, but can be structurally continuous as it can transmit and transform deformations and loads. Shells with holes or non-monolithic shell fall in this category, which is dubbed a G^{-1} surface, see chapter 1 for examples of all the categories of continuity.

Geometric continuity is also present in computer aided design (CAD) programs, where structures are constructed with mathematically defined surfaces. For instance, a shell can be modelled by a NURBS surface, which consists of several interconnected

1

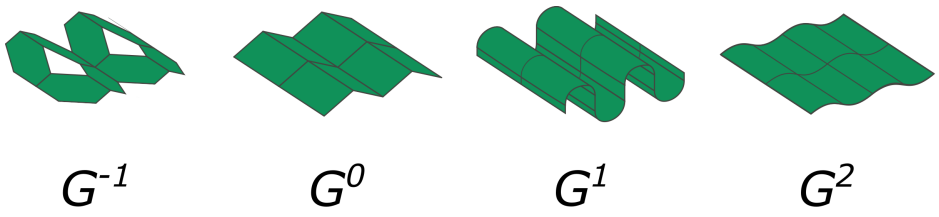

Figure 1.1.: The different categories of structural continuous shapes: a shell with holes, G^{-1}, a shell with sharp edges, such as origami G^0, a shell with rounded edges, $G^1$and a completely corrugated shell, G^2.

NURBS patches. The continuity of each patch can be controlled by the knot vector of the NURBS patch. A single NURBS patch can be G^0,G^1 or G^2 continuous and therefore cannot have holes [24]. Several patches can create a surface with holes, with adjacent patches connecting with positional continuity.

Surfaces that are G^2 continuous are called regular surfaces [25]. They are completely smooth over their domain. Apart from the edges, locally any shell will be G_2 continuous. In these areas several distinctions can be made. On every point on a regular surface, the Gaussian curvature can be determined; the Gaussian curvature is the product of the principal curvatures, see fig. 1.2. Several types of points can be denoted:

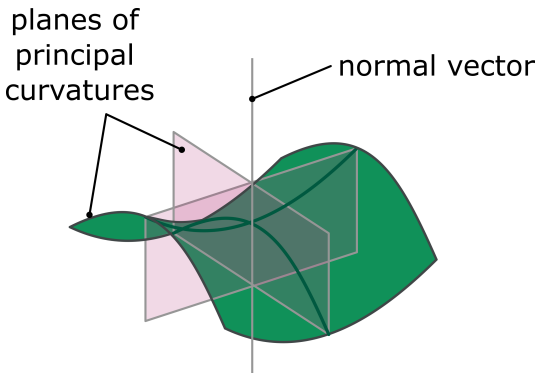

Figure 1.2.: A shell of which at any point the two principal curvatures (dark green) can be determined. The two planes (magenta) of principal curvature are perpendicular to each other.

- elliptical point - a point where both curvatures have the same sign, also positive Gaussian curvature.
- hyperbolic point - a point where the curvatures have opposite signs, also negative Gaussian curvature.

- parabolic point - a point where one of the curvatures is zero, also zero Gaussian curvature.
- umbilical point - a point where the curvatures are equal.

The arrangement of points on a surface determines what type of surface it is. There are surfaces that have only a single type of Gaussian curvature; these can be either all negative, positive or zero Gaussian curvature. A regular surface with only elliptical points is a *synclastic* surface; whereas a surface with only hyperbolic points is a *anticlastic* surface. A *monoclastic* surface is a surface with only parabolic points[25]. Several types of surfaces are not covered by this definition and will be defined presently. An *aclastic* surface is a surface with there is no curvature at all. Any other surface has multiple types of points is coined *amphiclastic*. The last category is when there is a repeating series of sign curvature changes in one or more directions. This repeating pattern is defined as polyclastic. This type of curvature is also known as a *corrugation*. An overview of all type of surfaces is given in fig. 1.3.

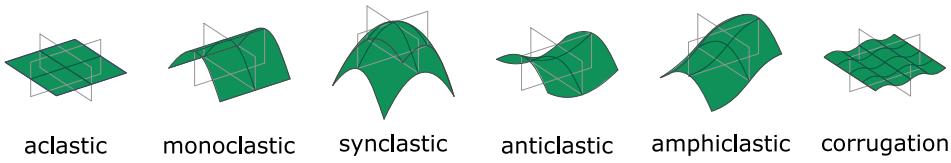

Figure 1.3.: The types of surfaces determined by the arrangement of Gaussian curvature on their membrane

In these categories there exist special geometries where the (Gaussian) curvature is equal everywhere on the surface. This type of surface is not possible in the *amphiclastic* and *corrugation* categories as curvature change is the defining property of those categories. For the other categories the geometries with constant curvature are as follows:

- aclastic - plate, which is the only surface in the aclastic category
- monoclastic - open cylinder
- synclastic - open (half) sphere
- anticlastic - open pseudosphere

An overview of these surfaces is given in fig. 1.4.

This classification of continuity and curvature allows assigning any shell mechanism to one of the described categories. In terms of continuity, a regular surface, G^2, is the most rudimentary surface since all other surface are at least a collection of smooth surfaces. Of the regular surfaces, the *aclastic* is the simplest geometry as it contains no curvature al all. A flat plate is not a shell, however. The next simplest geometry is the open cylinder, which only has a constant curvature in one direction. In this thesis the open cylinder or tape spring geometry is studied further to better understand its capabilities as a shell flexure or mechanism.

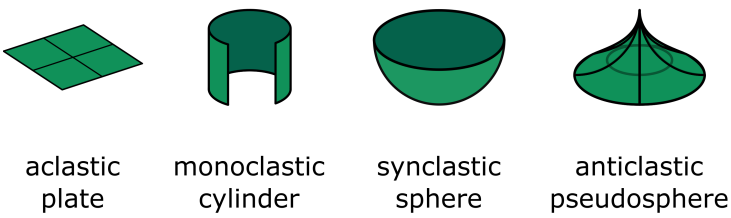

Figure 1.4.: Geometries that have a constant curvature across their surface

Applications of Compliant Shell Mechanisms

Compliant shell mechanisms or shell flexures are an extension of their non-curved counterparts and so they can be used in similar applications. Compliant mechanisms store energy during motion along with providing the desired kinematics. Containing several functions in one monolithic part is one major benefit of compliant mechanisms in general; this is often called function integration.

Shells distinguish themselves from flat elastic elements by displaying more complex behaviour. For instance, a tape spring will buckle when deformed sufficiently; the fold that was created during buckling will act as a constant moment hinge [26]. This is a degree of freedom that was not there before buckling. This behaviour is leveraged in, for example, the deployment of solar panels in space. The solar panels are connected by tape springs. When the solar panels are folded together during launch, the tape spring are buckled, enabling rotation of the panels. In orbit the solar array is unfolded and the tape springs return to their straight configuration. The straight tape springs prohibit rotation and as a result the solar array forms a relatively rigid surface [3–5].

Tape springs or slit tubes are also found in extensible booms; so called STEMs are used as rigid booms for e.g. antennas [27]. When extended the tape spring is rigid; however, it can be rolled up to a relatively small package when the tape spring is buckled. This is of course very similar to a carpenter tape: an everyday use shell mechanism.

Their distinct degrees of freedom and force-deflection behaviour could make shell mechanisms useful in an array of other applications: applications such as gravity balancers [7]. Gravity balancers are useful for e.g. passive exoskeletons where shell mechanisms are used to compensate the user's body weight and thereby decreasing the fatigue accumulated during work [20]. Other applications could be medical devices which often need specific kinetics while operating in a small environment. The properties of shell flexures can be leveraged to created smaller and more compact force generators.

Objectives and Contributions of this Thesis

This thesis aims to further the understanding and capabilities of shell mechanisms. It does this in two ways. First, it illustrates the capabilities of eigenscrew decomposition

in both the analysis and design of compliant (shell) mechanisms. This thesis presents a framework for the analysis of shell mechanisms using eigenscrew decomposition and presents an application where eigenscrew decomposition was used as an integral part of the design process.

Furthermore, it elaborates on the tape spring as a shell flexure element. The tape spring is a cylindrical flexure and a *monoclastic* geometry with a constant Gaussian curvature. It is the simplest shell flexure in the categorisation of shells in this thesis and its behaviour makes it useful as a flexure in mechanisms. However, the analysis was never done in a spatial manner which limits its implementation as a flexure. This thesis provides an in-depth analysis of the capabilities of this curved flexure element. This thesis also presents an application of a tape spring mechanism, where its unique behaviour is used to achieve a desired force-deflection behaviour. Lastly, this thesis also present an synthesis method which captures the unique behaviour of tape spring mechanisms and provides an accessible and quick approach to design an array op tape spring mechanisms.

Thesis Outline

This thesis is split into three parts.

Part I contains chapters 2 to 4 and pertains to the use of eigenscrew decomposition in compliant (shell) mechanisms. Chapter 2 discusses a method to ascertain the kinematics of complex shell geometries and ways to discern between degrees of freedoms and constraints of several shell flexures. Chapter 3 discusses the use of eigenscrew decomposition in the design of a scoliosis brace, showcasing the decomposition as a design and optimisation tool. Chapter 4 discusses ways to analyse parasitic motion and other well-known effects in compliant mechanism using eigenscrew decomposition.

Part II contains chapters 5 to 7 and discusses tape springs as a flexure element. Chapter 5 discusses the effect of the geometry of the tape spring on its mechanical behaviour. Chapter 6 elaborates on a mechanism consisting of tape springs and how the geometry can be tailored to get a constant force behaviour. Chapter 7 elaborates on this design and proposes a method to synthesize tape spring geometries given a desired force-displacement behaviour.

Part III contains chapter 8 and discusses a class of shell mechanism that is curved and structurally continuous, but is not based on any of the regular shapes. The deformation can also happen in the membrane of shell and not only due to bending of the shell. This is different from the archetypal shell mechanism and is added to this thesis to illustrate the spectrum of behaviours shell mechanisms are capable of.

Bibliography

[1] C. R. Calladine. *Theory of Shell Structures*. Cambridge University Press, 1983.

[2] L.L. Howell. *Compliant Mechanisms*. New York: Wiley, 2001.

[3] Ö. Soykasap. "Analysis of tape spring hinges". In: *International Journal of Mechanical Sciences* 49 (2007), pp. 853–860.

[4] J. Costantine, Y. Tawk, C. G. Christodoulou, J. Banik, and S. Lane. "CubeSat Deployable Antenna Using Bistable Composite Tape-Springs". In: *IEEE Antennas and Wireless Propagation Letters* 11 (2012), pp. 285–288.

[5] H. Mallikarachchi and S. Pellegrino. "Quasi-Static Folding and Deployment of Ultrathin Composite Tape-Spring Hinges". In: *Journal of Spacecraft and Rockets* 48.1 (Jan. 2011), pp. 187–198.

[6] S. Kok, A. Amoozandeh, and G. Radaelli. "Neutrally stable double-curved shells by inflection point propagation". In: *Journal of the Mechanics and Physics of Solids* 171 (Nov. 2022), p. 105133.

[7] G. Radaelli and J. L. Herder. "Shape optimization and sensitivity of compliant beams for prescribed load-displacement response". In: *Mechanical Sciences* 7 (2016), pp. 219–232.

[8] L. L. Howell, S. P. Magleby, and B. M. Olsen, eds. *Handbook of Compliant Mechanisms*. New Delhi, India: John Wiley & Sons Ltd., 2013, p. 342.

[9] G. Radaelli and J. Herder. "Gravity balanced compliant shell mechanisms". In: *International Journal of Solids and Structures* 118-119 (2017), pp. 78–88.

[10] K. Seffen and S. Pellegrino. "Deployment dynamics of tape springs". In: *Proceedings of The Royal Society A: Mathematical, Physical and Engineering Sciences* 455 (Mar. 1999), pp. 1003–1048.

[11] K. Seffen, Z. You, and S. Pellegrino. "Folding and deployment of curved tape springs". In: *International Journal of Mechanical Sciences* 42.10 (2000), pp. 2055–2073.

[12] M. Naves, R. Aarts, and D. Brouwer. "Large stroke high off-axis stiffness three degree of freedom spherical flexure joint". In: *Precision Engineering* 56 (2019), pp. 422–431.

[13] D. Brouwer, J. Meijaard, and J. Jonker. "Large deflection stiffness analysis of parallel prismatic leaf-spring flexures". In: *Precision Engineering* 37.3 (2013), pp. 505–521.

[14] R. Hartenberg and J. Denavit. *Kinematic Synthesis of Linkages*. McGraw-Hill series in mechanical engineering. McGraw-Hill, 1964.

[15] J. M. Selig. *Geometric Fundamentals of Robotics (Monographs in Computer Science)*. SpringerVerlag, 2004.

[16] H. Lipkin and T. Patterson. “Geometrical properties of modelled robot elasticity: part I - Decomposition”. In: *ASME Design Tech. Conf. and Computers in Engineering Conf.* Vol. 45. 1992, pp. 179–185.

[17] H. Lipkin and T. Patterson. “Geometrical Properties of Modelled Robot Elasticity: part II - Center of Elasticity”. In: *ASME Design Tech. Conf. and Computers in Engineering Conf.* Vol. 45. 1992, pp. 187–193.

[18] K. A. Seffen. “Compliant shell mechanisms”. In: *Philosophical Transactions of the Royal Society A: Mathematical, Physical and Engineering Sciences* 370.1965 (2012). 2010, pp. 2010–2026.

[19] G. Radaelli. “Synthesis of Mechanisms with Prescribed Elastic Load-Displacement Characteristics”. PhD Thesis. Delft University of Technology, 2017, p. 255.

[20] J. Nijssen. “A Type Synthesis Approach to Compliant Shell Mechanisms”. English. MA thesis. 2017.

[21] M. Schenk and S. D. Guest. “Geometry of Miura-folded metamaterials”. In: *Proceedings of the National Academy of Sciences* 110.9 (2013), pp. 3276–3281.

[22] G. Radaelli. “Reverse-twisting of helicoidal shells to obtain neutrally stable linkage mechanisms”. In: *International Journal of Mechanical Sciences* 202-203 (May 2021), p. 106532.

[23] B. Barsky and T. DeRose. “Geometric continuity of parametric curves: three equivalent characterizations”. In: *IEEE Computer Graphics and Applications* 9.6 (1989), pp. 60–69.

[24] J. A. Cottrell, T. J. R. Hughes, and Y. Bazilevs. *Isogeometric analysis : toward integration of CAD and FEA*. Wiley, New York, USA, 2009, p. 335.

[25] E. Kreyszig. *Differential Geometry*. Differential Geometry. Dover Publications, 1991.

[26] K. A. Seffen. “On the Behavior of Folded Tape-Springs”. In: *Journal of Applied Mechanics* 68 (2001), pp. 369–375.

[27] F. P. J. Rimrott. “Storable tubular extendible members”. In: *Engineering Digest* (1966).

I

Eigenscrew decomposition and its uses in compliant mechanism design

2

Unified Stiffness Characterization of Nonlinear Compliant Shell Mechanisms

Joost R. Leemans, Charles J. Kim, Werner W.P.J. van de Sande, Just L.Herder

Compliant shell mechanisms utilize spatially curved thin-walled structures to transfer or transmit force, motion, or energy through elastic deformation. To design spatial mechanisms, designers need comprehensive nonlinear characterization methods, while the existing methods fall short of meaningful comparisons between rotational and translational degrees-of-freedom. This paper presents two approaches, both of which are based on the principle of virtual loads and potential energy, utilizing properties of screw theory, Plücker coordinates, and an eigen-decomposition. This leads to two unification lengths that can be used to compare and visualize all six degrees-of-freedom directions and magnitudes in a nonarbitrary, physically meaningful manner for mechanisms exhibiting geometrically nonlinear behaviour.

This chapter originally appeared as J. R. Leemans, C. J. Kim, W. W. P. J. van de Sande, and J. L. Herder. “Unified Stiffness Characterization of Nonlinear Compliant Shell Mechanisms”. In: *Journal of Mechanisms and Robotics* 11.1 (2019)[1]

2.1. Introduction

The geometry of compliant shell elements makes them useful as building blocks for spatial mechanism design. The behavior of compliant shell mechanisms has been researched analytically by Seffen [2] and Pellegrino [3] and computationally by Radaelli and Herder [4]. Similar to other compliant mechanisms, characterizing compliant shell mechanisms is challenging due to intertwined kinematics and kinetics. Furthermore, stiffness, compliance, and thus, freedom and constraint directions change in a nonlinear fashion under large deformations.

A fundamental characteristic of a rigid body mechanism is its degrees-of-freedom describing the constraint and free motion directions. Compliant shell mechanisms, however, do not have clear distinctive constraint and free motion directions, since motion tendencies are determined by the relative compliance of the mechanisms.

To characterize compliant shell mechanisms, we consider the relative compliances of the kinematic degrees-of-freedom for spatial compliant mechanisms defined by Nijssen [5] as

> The motion tendency of a mechanism in 3D space, defined by the relationship between the three rotational and three translational compliances

The phrase relative compliances refers to the ratio of compliances between the relative kinematic degrees-of-freedom, which are from here on referred to as the degrees-of-freedom. Determining and utilizing these degrees-of-freedom has proven useful in the characterization and synthesis of spatial mechanisms [5–7].

In related work, different methods have been used to characterize the degrees-of-freedom of compliant mechanisms.

The existing methods do not address the coupling between translations and rotations, and thus, discuss the rotations and translation separately, for example, by using compliance ellipsoids [6]. Methods to characterize principal compliance axes while including coupling were first introduced by Lipkin and Patterson [8], utilizing Plücker coordinates. Lin et al. [9] introduced an independent derivation of principal compliance axes using hybrid coordinates. Two incomparable principal rotational and translational compliance directions and corresponding magnitude multiplier groups, containing all six degrees-of-freedom result from Lin and Lipkin's derivation. A full comparison and order of the six degrees-of-freedom would give deeper insight into kinematic characteristics, such as the determination of whether a mechanism is predominantly rotational or translational compliant. Methods to convert these multiplier groups into compatible units introduce arbitrarily defined characteristic lengths [10–12] lacking a physical consistent meaning. Because the lengths are arbitrary, unified compliances are not systematically comparable between mechanisms.

A method with comparable results to a section of this paper is introduced by Lin et al. [9]. Lin's derivation is based on a geometrical interpretation of hybrid coordinates to derive principal stiffness axes. The corresponding stiffnesses are converted to similar units based on the principle of potential energy. By introducing the principle of potential energy, all directional information is lost, since energy is a

scalar quantity. Lin introduces a method to show that the results of their paper are frame-invariant. The same method can be applied to show that the results of this paper are frame-invariant.

This paper presents two approaches that utilize properties of screw theory, Plücker coordinates, and Lipkin's eigen-decomposition which lead to the unified compliances. The unified compliances, consisting of two multiplier groups with identical units, facilitate a comparison between all six degrees-of-freedom compliance magnitudes in a consistent, insightful manner while including coupling. The unification is utilized in a spatial characterization of nonlinear behaving compliant mechanisms.

Section 2.2 presents background theory on Pücker coordinates, stiffness matrices, and Lipkin's eigen-decomposition. Section 2.3 presents Lipkin's eigen-decomposition graphically. The background theory and visualization are used to determine two approaches that lead to the unification of the compliances in section 2.4. The unification is used to present a visual characterization of the kinematic behavior of two well-known compliant flexure mechanisms as illustrated in section 2.5. In section 2.6, the characterization is used to analyze the nonlinear behavior of compliant shell mechanisms. Section 2.7 introduces a physical prototype that demonstrates the efficacy of the presented characterization method. Section 2.8 discusses the contributions of the presented work, while a brief summary is given and a general conclusion is drawn in section 2.9.

2.2. Background

According to Chasles' theorem [13], a displacement in three-dimensional space can be expressed in Plücker axis coordinates vector form as a twist $\mathbf{T}$ containing linear $\boldsymbol{\delta}$ and angular $\boldsymbol{\gamma}$ displacements defined as

$$\mathbf{T} = \begin{bmatrix} \boldsymbol{\delta}_i \\ \boldsymbol{\gamma}_i \end{bmatrix} = \begin{bmatrix} (\mathbf{r}_i \times \boldsymbol{\gamma}_i) + h_i \boldsymbol{\gamma}_i \\ \boldsymbol{\gamma}_i \end{bmatrix}, \qquad i = 1,2,3 \tag{2.1}$$

This form expresses the translation in terms of a combination of angular displacement $\boldsymbol{\gamma}$ and the 3×1 location vector $\mathbf{r_i}$ and h the pitch scalar. The Plücker axis coordinates in vector form are visualized in fig. 2.1.

The magnitude of the twist is defined as

$$|\mathbf{T}| = \begin{cases} \sqrt{\boldsymbol{\delta} \cdot \boldsymbol{\delta}} & \text{if } \gamma = 0 \\ \sqrt{\boldsymbol{\gamma} \cdot \boldsymbol{\gamma}} & \text{otherwise} \end{cases} \tag{2.2}$$

and the direction of the twist is defined as the direction of the angular deformation. The dual of Chasles' theorem is Poinsot's theorem. It states that any wrench can be constructed by a force and torque along the same axis [14]. In Plüker ray, coordinate vector from the wrench $\mathbf{w}$ contains the linear forces $\mathbf{f}$ and the moment couples $\boldsymbol{\tau}$ defined as

$$\mathbf{w} = \begin{bmatrix} \boldsymbol{f}_i \\ \boldsymbol{\tau}_i \end{bmatrix} = \begin{bmatrix} \boldsymbol{f}_i \\ (\mathbf{b}_i \times \boldsymbol{f}_i) + d_i \boldsymbol{f}_i \end{bmatrix}, \qquad i = 1,2,3 \tag{2.3}$$

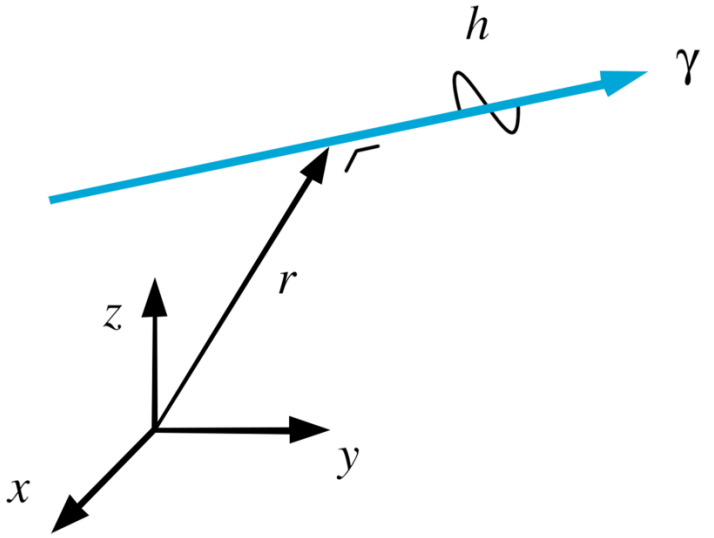

Figure 2.1.: Visual representation of the Plücker axis coordinates in vector form

where $\mathbf{b}_i$ is the 3×1 location vector pitch and d_i is the ratio of angular torque to linear force. The magnitude of the wrench is defined as

$$|\mathbf{w}| = \begin{cases} \sqrt{\boldsymbol{\tau} \cdot \boldsymbol{\tau}} & \text{if } f = 0 \\ \sqrt{\boldsymbol{f} \cdot \boldsymbol{f}} & \text{otherwise} \end{cases} \tag{2.4}$$

and the direction of the wrench is seen as the direction of the force. The relationship between the displacement and the load of a specific point of interest can be described by the secant stiffness matrix $\mathbf{K}_s$ or its inverse, the secant compliance matrix $\mathbf{C}_s$, respectively, expressed as

$$\boldsymbol{w} = \boldsymbol{K}_s \boldsymbol{\Delta T}, \qquad \boldsymbol{\Delta T} = \boldsymbol{C}_s \boldsymbol{w} \tag{2.5}$$

where $\mathbf{K}_s$ and $\mathbf{C}_s$ are the 6×6 secant stiffness and secant compliance matrix, respectively, and $\Delta\mathbf{T}$ is an incremental displacement step [15]. A secant matrix describing an infinitesimal incremental step is known as the tangent matrix, and it is defined as

$$\mathbf{K}_t = \lim_{\boldsymbol{\Delta T} \to 0} \mathbf{K}_s, \qquad \mathbf{C}_t = \lim_{\boldsymbol{\Delta T} \to 0} \mathbf{C}_s \tag{2.6}$$

The tangent matrices describe a linearized configuration-dependent relation between the displacement and the load. The tangent stiffness and compliance matrices are composed of a physical and geometrical stiffness and compliance matrix. Nonlinear behavior can be analyzed by using either the secant stiffness matrix or by making an incremental linearized analysis of each quasi-static equilibrium based on the tangent stiffness matrix. As noted by Simo, analyzing geometric

nonlinearities while assuming linear material behavior results in symmetric tangent stiffness matrices [16].

Any symmetric positive definite nonsingular tangent stiffness $\mathbf{K}_t$ and tangent compliance matrix $\mathbf{C}_t$ can be decomposed into an eigen-system as described by Lipkin and Patterson [8]. The eigen-decomposition describes three translational and three rotational principal axes, with corresponding stationary multiplier values of the translational and rotational stiffness. Lipkin's eigen-decomposition of the tangent stiffness matrix $\mathbf{K}_t$ is defined as

$$\mathbf{K}_t = \begin{bmatrix} \hat{\boldsymbol{w}}_f & \hat{\boldsymbol{w}}_\gamma \end{bmatrix} \begin{bmatrix} k_f & 0 \\ 0 & k_\gamma \end{bmatrix} \begin{bmatrix} \hat{\boldsymbol{w}}_f^T \\ \hat{\boldsymbol{w}}_\gamma^T \end{bmatrix} \tag{2.7}$$

and the resulting tangent compliance matrix eigen-decomposition is defined as

$$\mathbf{C}_t = \begin{bmatrix} \hat{\boldsymbol{T}}_f & \hat{\boldsymbol{T}}_\gamma \end{bmatrix} \begin{bmatrix} a_f & 0 \\ 0 & a_\gamma \end{bmatrix} \begin{bmatrix} \hat{\boldsymbol{T}}_f^T \\ \hat{\boldsymbol{T}}_\gamma^T \end{bmatrix} \tag{2.8}$$

where for $i = 1,2,3$, multipliers $k_{\gamma i} > 0$ are the angular stiffnesses in the directions of the γ_i, multipliers and $k_{fi} > 0$ are the translational stiffnesses in the directions of f_i. The inverse of a translational stiffness gives the translational compliance

$$a_{f_i} = \frac{1}{k_{f_i}} \tag{2.9}$$

and the inverse of a rotational stiffness gives the rotational compliance

$$a_{\gamma_i} = \frac{1}{k_{\gamma_i}} \tag{2.10}$$

$\mathbf{w}_f$ are the eigen-wrenches, these directions are also known as the wrench axes, defined as

$$\mathbf{w}_{f_i} = \begin{bmatrix} \boldsymbol{f}_i \\ \boldsymbol{\tau}_i \end{bmatrix}, \qquad i = 1,2,3 \tag{2.11}$$

Applying an eigen-wrench $\mathbf{w}_{fi}$ leads to an induced twist $\mathbf{T}_{fi}$ a pure translational displacement parallel to the force direction f_i, the induced twists $\mathbf{T}_f$ are defined as

$$\mathbf{T}_{f_i} = \begin{bmatrix} a_{f_i} \boldsymbol{f}_i \\ 0 \end{bmatrix}, \qquad i = 1,2,3 \tag{2.12}$$

$\mathbf{T}_\gamma$ are the eigen-twists, these directions are also known as the twist axes, defined as

$$\mathbf{T}_{\gamma_i} = \begin{bmatrix} \boldsymbol{\delta}_i \\ \boldsymbol{\gamma}_i \end{bmatrix}, \qquad i = 1,2,3 \tag{2.13}$$

Applying an eigen-twist $\mathbf{T}_{\gamma i}$ leads to an induced wrench $\mathbf{w}_{\gamma i}$ a pure moment parallel to the rotational direction γ_i, the induced wrenches $\mathbf{w}_\gamma$ are defined as

$$\mathbf{w}_{\gamma_i} = \begin{bmatrix} 0 \\ k_{\gamma_i} \boldsymbol{\gamma}_i \end{bmatrix}, \qquad i = 1,2,3 \tag{2.14}$$

The above wrenches and twists are normalized with respect to the defined magnitudes to be used in the eigen-decompositions of eq. (2.7) and eq. (2.8)

$$\hat{\mathbf{T}} = \frac{\mathbf{T}}{|\mathbf{T}|} \tag{2.15}$$

and

$$\hat{\mathbf{w}} = \frac{\mathbf{w}}{|\mathbf{w}|} \tag{2.16}$$

Upon the normalization of the twist and wrench eigen-decomposition described in eq. (2.2) and eq. (2.4), the direct magnitude relation is lost. In terms of magnitude, the induced twists and wrenches are no longer a direct result of the eigen-wrenches and eigen-twists. After normalization, only the directional relations remain valid.

2.3. Visualization of the Eigen-Decomposition

In this section, we provide visual interpretation of the eigen-wrench directions for a specific shell mechanism to increase the understanding of the wrench and twist axes. Consider the compliant shell mechanism that is fully constrained along the bottom edge and the point of interest at which $\boldsymbol{C}_t$ is determined is indicated by a black dot fig. 2.2.

The acrylic (E=3.2GPa, ν=0.35) shell mechanism is analyzed as an isogeometric analysis (IGA) shell [17] . The 2mm thick geometry is defined by NURBS [18], wherein a third polynomial follows a 3×5 grid. Five coordinates are placed on three planes in $y = -0.05$, $y = 0$, and $y = 0.05$. The x and z coordinates are defined in table 2.1. The three principal eigen-twist directions are shown in fig. 2.2a. A rotation of the point of interest around a twist axis plus a translation along this axis leads to pure parallel moments around this twist axis.

Table 2.1.: NURB coordinates corrugated shell

point	1	2	3	4	5
x	0.00	0.00	0.04	0.00	0.00
y	0.00	0.04	0.08	0.11	0.15

The three principal eigen-wrench directions can be seen in fig. 2.2b. A force along a wrench axis plus a moment around this axis leads to a pure translation along the wrench axis.

Figure 2.2a and fig. 2.2b both provide information on the twist and wrench spatial directions, while excluding the compliance and stiffness multipliers. Thus, these figures do not show the magnitude of compliance corresponding to these directions.

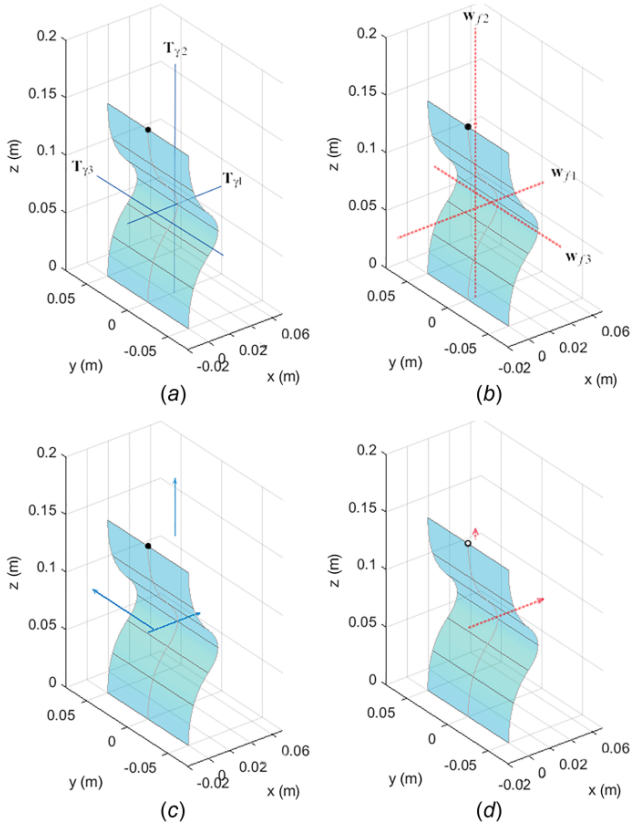

Figure 2.2.: Visual representation eigen-decomposition: (a) twist axes, (b) wrench axes, (c) twist compliance vectors, and (d) wrench compliance vectors

By plotting vectors along the directions of the wrench and twist axes with the length of their corresponding stationary compliance multipliers, both the direction and the magnitude of compliance are visualized in an intuitive manner.

Figure 2.2c shows the vectors along the twist axes with the magnitude of the corresponding rotational compliance multipliers a_γ. The longer the vector, the larger the rotational compliance around the twist axis that the vector represents.

Figure 2.2d shows the vectors along the wrench axes with the magnitude of the corresponding translational compliance multipliers a_f. The longer the vector, the larger the translational compliance along the wrench axis that the vector represents.

Figure 2.2d and fig. 2.2c both provide the directional information of the twist and wrench axes and the corresponding compliance magnitude.

2.4. Unification Methods

The eigen-decomposition presented in section 2.2 is insightful, however, the magnitudes of the rotational and translational vectors cannot be compared because they are composed of different units. Consider the decomposition in eq. (2.8). The upper three stationary multipliers a_f are translational compliances given as length per force. The lower three stationary multipliers a_γ are rotational compliances given as angle divided by force multiplied by length. The rotational and translational multipliers are not directly comparable due to their different units. To enable this comparison, we utilize unification variables, which will be defined based on equivalent compliance by virtual load or potential energy. In this section, we discuss two unification approaches by converting the units of a_{f_i} into a_{γ_i} and the units of a_{γ_i} into a_{f_i}. The conversion of the units of a_{γ_i} into a_{f_i} can be done by expressing rotational compliance as an equivalent translational compliance at the point of interest using a unification length χ_i. The conversion of the units of a_{f_i} into a_{γ_i} can be done by expressing translational compliance at the point of interest as an equivalent rotational compliance using a unification length ψ_i. In equation form, the unification approaches are given as

$$\tilde{a}_{f_i} = \chi_i^2 a_{\gamma_i} \tag{2.17}$$

and

$$\tilde{a}_{\gamma_i} = \frac{a_{f_i}}{\psi_i^2} \tag{2.18}$$

We introduce two methods to obtain the unification lengths. The first method utilizes virtual load and displacements, and the second method is based on the principle of potential energy. The strengths and weaknesses of both methods are discussed in section 2.4.3.

2.4.1. RasT: Rotational as Equivalent Translational Compliance

The first approach expresses rotational compliance as an equivalent translational compliance at the point of interest. We call this the RasT approach. Both the virtual loads and the potential energy are used separately to determine unification length χ_i.

Virtual Load Method

Converting the rotational compliance into an equivalent translational compliance at the point of interest using the virtual load method can be done in three consecutive steps:

1. Express δ_{eq_i}, an equivalent translation at the point of interest in terms of rotation around the twist axis.
2. Express F_{eq_i}, an equivalent virtual force at the point of interest in terms of the induced counteracting pure parallel moment couple that corresponds to a rotation around the twist axis.

3. Calculate an equivalent translational compliance $\tilde{a}_{f_i}$ by dividing the expressions above such that

$$\tilde{a}_{f_i} = \frac{\delta_{eq_i}}{F_{eq_i}} \tag{2.19}$$

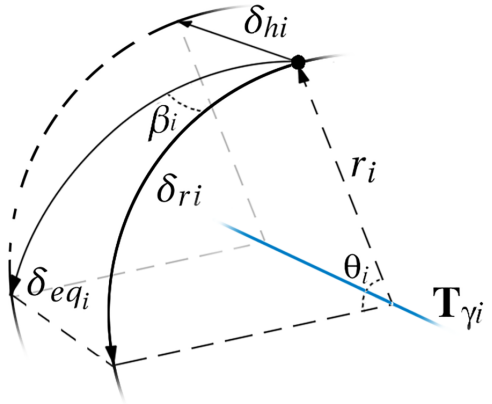

Figure 2.3.: Equivalent translation geometry

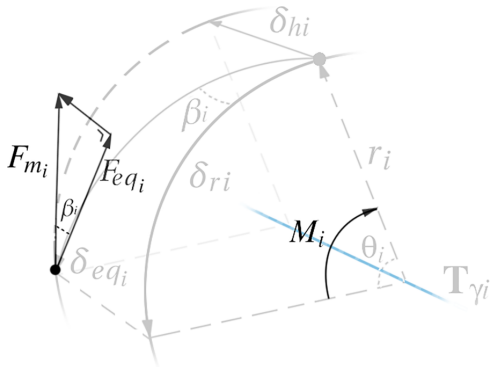

Figure 2.4.: Equivalent virtual force geometry

Figure 2.3 and fig. 2.4 both show the point of interest of a spatial compliant mechanism as indicated by the dot and one of the three principal twist axes $\boldsymbol{T}_{\gamma_i}$, used to explain the three steps:

Step I. Express δ_{eq_i}, equivalent translation.

The equivalent translation at the point of interest is expressed in terms of a screw around the twist axis. The total translation corresponding to a rotation θ_i is a combination of translation, δ_{r_i}, along the arc length around the twist axis and a

translation, δ_{h_i}, along the twist axis. The resulting equivalent translation δ_{eq_i} follows a path along a cylinder, is illustrated in fig. 2.3.

The displacement along the arc can be expressed as the product of the angle of rotation and the radius (the arc-length). The radius that defines the displacement along the arc is the shortest distance between the point of interest and the twist axis. This length is defined in Plücker axis coordinates as the location vector r_i as shown in fig. 2.1. The displacement along the arc-length is thus given as

$$\delta_{r_i} = |r_i|\theta_i \tag{2.20}$$

The point of interest translates along the twist axis, due to the pitch h_i, given by the pitch times the rotation

$$\delta_{h_i} = h_i\theta_i \tag{2.21}$$

The resulting displacement due to the two perpendicular displacements on a cylinder is calculated using the Pythagorean theorem. The equivalent translation expressed in terms of the corresponding rotation is thus given as

$$\delta_{eq_i} = \sqrt{h_i^2 + |r_i|^2}\theta_i \tag{2.22}$$

Step II. Express F_{eq_i},equivalent virtual force.

The equivalent virtual force at the point of interest in the opposite direction of the equivalent displacement is expressed in terms of the induced moment corresponding to a rotation around the twist axis.

Consider a virtual force F_{m_i} applied at a distance r_i. The magnitude and direction of F_{m_i} results in the same moment magnitude, M_i, parallel to the corresponding rotation θ_i. By decomposing this virtual moment force vector, with one of the components in the direction of the equivalent translation determined in Step I, the equivalent virtual force F_{eq_i} can be defined. The introduced virtual moment force vector F_{m_i} is given as

$$F_{m_i} = \frac{M_i}{|r_i|} \tag{2.23}$$

The geometry required to decompose the virtual moment force F_{M_i} to the equivalent virtual force F_{eq_i} is shown in fig. 2.4, where β_i is the angle between δ_{eq_i} and δ_{r_i}. By geometry, β_i is also the angle between F_{m_i} and F_{eq_i}, which is defined as

$$\beta_i = \frac{F_{m_i}}{F_{eq_i}} = \frac{\delta_{eq_i}}{\delta_{r_i}} = \frac{\sqrt{(h_i^2 + |r_i|^2)}\theta_i}{|r_i|\theta_i} \tag{2.24}$$

Combining eq. (2.23) and eq. (2.24), the equivalent virtual force is

$$F_{eq_i} = \frac{M_i}{\sqrt{h_i^2 + |r_i|^2}} \tag{2.25}$$

Step III: Express $\tilde{a}_{f_i}$, The equivalent translational compliance.

The third step is to substitute eq. (2.22) and eq. (2.25) with eq. (2.19)

$$\tilde{a}_{f_i} = \frac{\delta_{eq_i}}{F_{eq_i}} = (h_i^2 + |r_i|^2)\frac{\theta_i}{M_i} \tag{2.26}$$

The unification length χ_i follows from eq. (2.17) and eq. (2.26)

$$\chi_i = \sqrt{h_i^2 + |r_i|^2} \tag{2.27}$$

Potential Energy Method

To unify the rotational compliance multipliers a_{γ_i} into equivalent translational compliance multipliers, $\tilde{a}_{f_i}$, the principle of potential energy can be used as well. In this section, the rotational energy is compared with the corresponding virtual equivalent translational energy due to the rotation. The eigentwist induces a pure moment around the twist axis, and therefore, the corresponding potential energy is solely dependent on the rotational stiffness and rotation. The potential energy of the eigentwist is defined as

$$U_{\gamma_i} = \frac{1}{2} k_{\gamma_i} \theta_i^2 \tag{2.28}$$

By introducing an equivalent translational stiffness $\tilde{k}_{f_i}$ and the equivalent translation δ_{eq_i} corresponding to the rotation given in eq. (2.22), we can express the stored energy as

$$\frac{1}{2} k_{\gamma_i} \theta_i^2 = \frac{1}{2} \tilde{k}_{f_i} \delta_{eq_i}^2 \tag{2.29}$$

By substituting eq. (2.22) with eq. (2.29), the equivalent translational stiffness can be defined as

$$\tilde{k}_{f_i} = \frac{k_{\gamma_i}}{h_i^2 + |r_i|^2} \tag{2.30}$$

The inverse of the translational and rotational stiffness results in the translational and rotational compliance, as stated in eq. (2.9) and eq. (2.10). The equivalent translational compliance of the rotational compliance is thus given as

$$\tilde{a}_{f_i} = (h_i^2 + |r_i|^2) a_{\gamma_i} \tag{2.31}$$

The unification length follows from eq. (2.17) and eq. (2.31)

$$\chi_i = \sqrt{h_i^2 + |r_i|^2} \tag{2.32}$$

which exactly matches eq. (2.27).

2.4.2. TasR: Translational as Equivalent Rotational Compliance

The TasR approach expresses the translational compliance as an equivalent rotational compliance. Converting the translational compliance into an equivalent rotational compliance at the point of interest can be done using both the TasR equivalent of the virtual load and the potential energy RasT approach. The analogous steps in the virtual load method for TasR are the following:

1. Express an equivalent rotation at the point of interest, θ_{eq_i}, in terms of a translation parallel to the wrench axis.

2. Express an equivalent virtual moment at the point of interest, M_{eq_i}, in terms of the counteracting force corresponding to a translation parallel to the wrench axis.

3. Calculate an equivalent rotational compliance, $\tilde{a}_{\gamma_i}$, by dividing the expressions above to obtain the equivalent translational compliance.

The potential energy method TasR equivalent is accomplished by introducing an equivalent rotational stiffness. This stiffness is defined in terms of the translational stiffness corresponding to the wrenches. Both the virtual load and the potential energy TasR approaches result into the unification length

$$\psi_i = \sqrt{|d_i^2| + b_i^2} \tag{2.33}$$

which has the same form as the unification length expressed in eq. (2.32) from the RasT approach.

2.4.3. Approach and Method Comparison

Both the virtual load method and the potential energy method result into the same unification lengths. The potential energy method is more straightforward, however, it gives less insight into the actual kinematics compared to the virtual load method. While the end results of both methods yield similar conclusions, the virtual load method includes interesting substeps with physical relevance. The substep results in themselves can form the basis for specific designs. Knowledge of the composition of the substeps provides the opportunity to vary parameters in an intelligent manner to achieve specific objectives. In addition, energy in any form is a scalar quantity. Using the introduced potential energy method, all directional information is excluded.

The RasT unification approach characterizes a mechanism as if a point of interest will be displaced using solely forces. The RasT approach is physically comparable as if the point of interest is displaced, along the wrench and around the twist axis, using a ball-and-socket-joint while evaluating the traveled path and the reaction force. Consequently, using the RasT approach pure decoupled rotations around the point of interest is impossible to excite, therefore the RasT approach cannot evaluate the corresponding compliance multipliers. The TasR approach characterizes a mechanism as if the less intuitive opposite is the case, when a point of interest will be displaced solely using couple moments. Consequently, using the TasR approach,

the unified compliance values corresponding to eigen-wrenches that are pure forces in line with the point of interest cannot be evaluated.

To circumvent degrees of freedoms that cannot be evaluated, one could use either the TasR or the RasT approach. If both approaches result in degrees-of-freedom magnitudes that cannot be evaluated, the combination of the two will give the best characterization. The RasT approach is more intuitive and accounts for the coupling of the rotations and translations by including twist pitch, hence section 2.5 and section 2.6 will focus on this approach. However, both approaches in their context, separately or combined, are a powerful characterization for comparing all six degrees-of-freedom.

2.5. Characterization

This section shows the effectiveness of the characterization to compare all six degrees-of-freedom using the unification lengths.

All subsequent introduced mechanisms are analyzed in SPACAR and IGA shells of which the accuracy and validation are evaluated in the work of references [17] and [19]. The accuracy of the introduced methods depends on the accuracy of the determined tangent stiffness matrices, which are calculated from the computational analysis. A number of well-known compliant elements are presented along with an example of a compliant shell. A brief physical prototype demonstrates the efficacy of the presented characterization in **??**.

2.5.1. Unified Compliance Matrix

The unification lengths χ_i and ψ_i result in unified stationary compliance multipliers, which can be represented in matrix form. In the RasT approach, the unification length of eq. (2.27) is substituted with eq. (2.8). The rotational compliance multipliers are multiplied by the unification length squared $h_i^2 + |r_i|^2$, which yields the equivalent translational compliance. In matrix form, this produces the diagonal unified stationary translational compliance multiplier matrix $\tilde{\boldsymbol{a}}_f$ given as

$$\tilde{\boldsymbol{a}}_f = \begin{bmatrix} a_{f_i} & 0 \\ 0 & (h_i^2 + |r_i|^2) a_{\gamma_i} \end{bmatrix} \tag{2.34}$$

In the case of the TasR approach, the unified rotational compliance multiplier matrix $\tilde{\boldsymbol{a}}_\gamma$ is found by substituting the unification length in eq. (2.33) with eq. (2.8)

$$\tilde{\boldsymbol{a}}_\gamma = \begin{bmatrix} \frac{a_{f_i}}{(b_i^2 + |d_i|^2)} & 0 \\ 0 & a_{\gamma_i} \end{bmatrix} \tag{2.35}$$

The complete eigen-decomposition of the tangent compliance matrix can be expressed as

$$\boldsymbol{C}_t = \begin{bmatrix} \hat{\boldsymbol{T}}_f & \hat{\boldsymbol{T}}_\gamma \end{bmatrix} \begin{bmatrix} I & 0 \\ 0 & \frac{1}{\sqrt{(h_i^2 + |r_i|^2)}} \end{bmatrix} \tilde{\boldsymbol{a}}_f \begin{bmatrix} I & 0 \\ 0 & \frac{1}{\sqrt{(h_i^2 + |r_i|^2)}} \end{bmatrix} \begin{bmatrix} \hat{\boldsymbol{T}}_f \\ \hat{\boldsymbol{T}}_\gamma \end{bmatrix} \tag{2.36}$$

The TasR approach yields the complete decomposition as

$$\boldsymbol{C}_t = \begin{bmatrix} \hat{\boldsymbol{T}}_f & \hat{\boldsymbol{T}}_\gamma \end{bmatrix} \begin{bmatrix} b_i^2 + |d_i|^2 & 0 \\ 0 & I \end{bmatrix} \tilde{\boldsymbol{a}}_\gamma \begin{bmatrix} b_i^2 + |d_i|^2 & 0 \\ 0 & I \end{bmatrix} \begin{bmatrix} \hat{\boldsymbol{T}}_f \\ \hat{\boldsymbol{T}}_\gamma \end{bmatrix} \tag{2.37}$$

2.5.2. Direction and Unified Compliance Magnitude Visualized

The eigen-twists $\hat{\boldsymbol{T}}_{\boldsymbol{\gamma_i}}$ and the eigen-wrenches $\hat{\boldsymbol{w}}_{\boldsymbol{f_i}}$ can be visualized as unified compliance vectors, with lengths corresponding to values in the unified compliance matrix $\tilde{a}_{f_i}$ or $\tilde{a}_{\gamma_i}$. The introduced unified compliance vectors are indicated with $\tilde{\boldsymbol{T}}_{\gamma_i}$ and $\tilde{\boldsymbol{w}}_{f_i}$, where $|\tilde{\boldsymbol{T}}_{\gamma_i}| = \tilde{a}_{\gamma_i}$ and $|\tilde{\boldsymbol{w}}_{f_i}| = \tilde{a}_{f_i}$. Using this visualization, the dominant compliance directions become evident.

The utility of this method is first shown through two well-known compliant flexure mechanisms, the cross-pivot flexure and the double-parallelogram flexure. These examples have been chosen because they have distinct kinematic characteristics. The visualization using the unified compliance matrix confirms the expected behavior of these well-described mechanisms.

Both mechanisms are analyzed in SPACAR. The mechanisms are composed of blue spring steel (E=205GPa, ν=0.3) flexures with the following geometry: l = 75mm, w = 15mm, and h = 0.5mm.

Cross Pivot Flexure Mechanism

The cross pivot flexure mechanism consists of two perpendicular flexures and two parallel rigid bodies. The lower rigid body is fully constrained and the center of the upper rigid body is considered to be the point of interest. Using SPACAR, the 6×6 tangent compliance matrix $\boldsymbol{C}_t$ is determined. Figure 2.5 shows the twist and wrench compliant axes of the mechanism.

The stationary translational compliance multipliers corresponding to the wrench axes are given in table 2.2. The largest translational compliance multiplier is underlined and corresponds to wrench $\boldsymbol{w}_{f_1}$. The stationary rotational compliance multipliers and the pitches corresponding to the twist axes are given in table 2.3. The largest rotational compliance multiplier is underlined and corresponds to twist axis $\boldsymbol{T}_{\gamma_3}$. The compliance multipliers in table 2.2 and table 2.3 cannot be compared directly, therefore the unified compliance matrices are introduced. Figure 2.6 shows all six unified compliance vectors along the twist and wrench axes with unified compliance magnitudes $\tilde{\boldsymbol{a}}_{\boldsymbol{f}}$ using the RasT approach. As expected, the largest unified compliance vector is in the direction of twist axis $\boldsymbol{T}_{\gamma_3}$ at the intersection of the flexures. The other unified compliance vectors are too small to visualize using linear magnitude representation, because they are orders of magnitude smaller than the vector along $\boldsymbol{T}_{\gamma_3}$. The corresponding comparable unified compliance magnitudes are given in table 2.4.

As can be seen in table 2.4, the multipliers are at least three orders smaller than the underlined multiplier corresponding to the most dominant rotational degree-of-freedom. The cross flexure mechanism is dominantly rotational compliant, which is consistent with what is known about the cross-pivot flexure. The total relative degree-of-freedom order based on the unified compliance multipliers

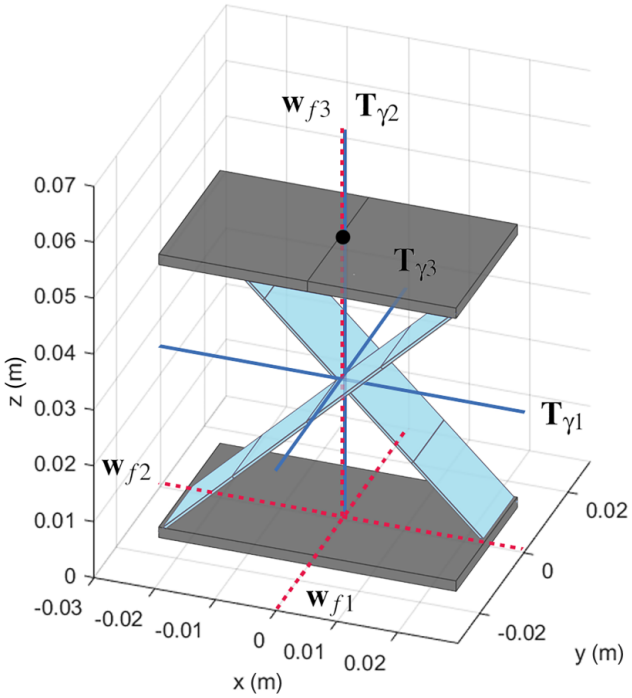

Figure 2.5.: Principal compliance directions of the cross pivot flexure mechanism

Table 2.2.: Compliance magnitudes and corresponding wrench axes of the cross pivot flexure

correspondence wrench	translational compliance (a_{f_i})
$\boldsymbol{w}_{f_1}$	$2.50 \times 10^{-7}\,\mathrm{m\,N^{-1}}$
$\boldsymbol{w}_{f_2}$	$2.00 \times 10^{-8}\,\mathrm{m\,N^{-1}}$
$\boldsymbol{w}_{f_3}$	$2.00 \times 10^{-8}\,\mathrm{m\,N^{-1}}$

Table 2.3.: Compliance magnitudes and corresponding twist axes of the cross pivot flexure

correspondence twist	rotational compliance (a_{γ_i})	pithch (h_i)
$\boldsymbol{T}_{\gamma_1}$	$1.06 \times 10^{-3}\,\mathrm{rad\,N^{-1}\,m^{-1}}$	$7.50 \times 10^{-3}\,\mathrm{m}$
$\boldsymbol{T}_{\gamma_2}$	$1.06 \times 10^{-3}\,\mathrm{rad\,N^{-1}\,m^{-1}}$	$7.50 \times 10^{-3}\,\mathrm{m}$
$\boldsymbol{T}_{\gamma_3}$	$4.8 \times 10^{-1}\,\mathrm{rad\,N^{-1}\,m^{-1}}$	$0.00 \times 10^{1}\,\mathrm{m}$

following from the RasT approach indicated by the unified compliance vector magnitudes is given as

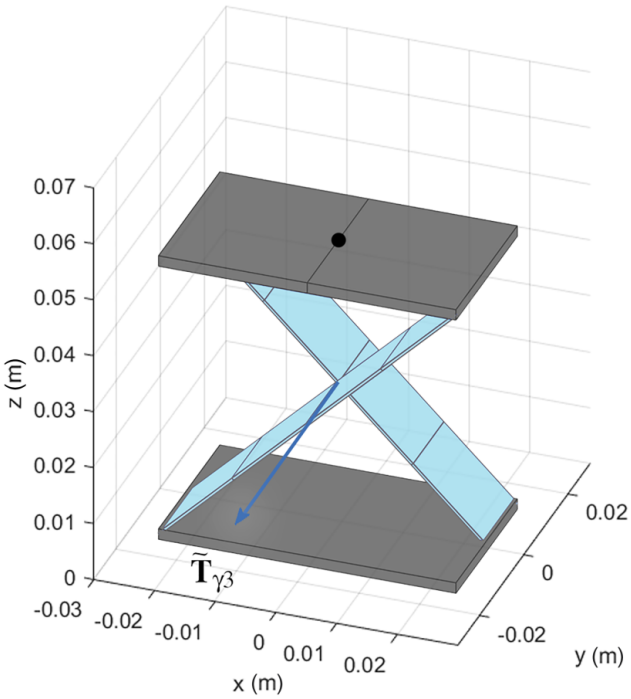

Figure 2.6.: Unified compliance vectors of the cross pivot flexure mechanism

Table 2.4.: Twist and wrench axes with corresponding unified compliance magnitudes of the cross pivot flexure mechanism

correspondence axes	unified compliance ($\tilde{a}_{f_i}$)
$\boldsymbol{w}_{f_1}$	$2.50 \times 10^{-7}\mathrm{m\,N^{-1}}$
$\boldsymbol{w}_{f_2}$	$2.00 \times 10^{-8}\mathrm{m\,N^{-1}}$
$\boldsymbol{w}_{f_3}$	$2.00 \times 10^{-8}\mathrm{m\,N^{-1}}$
$\boldsymbol{T}_{\gamma_1}$	$8.08 \times 10^{-7}\mathrm{m\,N^{-1}}$
$\boldsymbol{T}_{\gamma_2}$	$5.99 \times 10^{-8}\mathrm{m\,N^{-1}}$
$\boldsymbol{T}_{\gamma_3}$	$3.38 \times 10^{-4}\mathrm{m\,N^{-1}}$

$$|\tilde{\boldsymbol{T}}_{\gamma_3}| \gg |\tilde{\boldsymbol{T}}_{\gamma_1}| > |\tilde{\boldsymbol{w}}_{f_1}| > |\tilde{\boldsymbol{T}}_{\gamma_2}| > |\tilde{\boldsymbol{w}}_{f_3}| / |\tilde{\boldsymbol{w}}_{f_2}| \tag{2.38}$$

Double Parallelogram Flexure Mechanism

The double parallelogram flexure is designed to have one dominant translational degree-of-freedom. Figure 2.7 shows the twist and wrench compliant axes of the mechanism.

The translational compliance multipliers corresponding to the wrench axes are

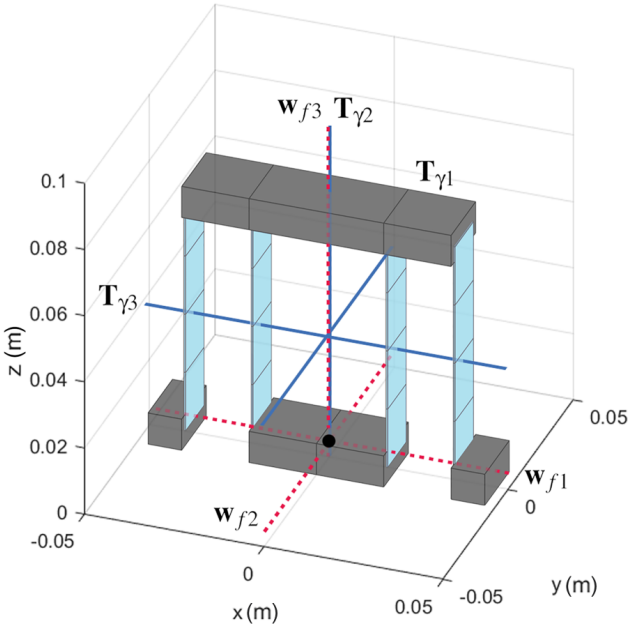

Figure 2.7.: Principal compliance directions of the double parallel flexure mechanism

given in table 2.5, and the rotational compliance multipliers and the pitches corresponding to the twist axes are given in table 2.6. The largest translational and rotational compliance multipliers are underlined and correspond to wrench $\boldsymbol{w}_{f_1}$ and twist $\boldsymbol{T}_{\gamma_3}$. The compliance multipliers in table 2.5 and table 2.6 can only be compared directly using the unified compliances $\tilde{\boldsymbol{a}}_\gamma$ and $\tilde{\boldsymbol{a}}_f$. Figure 2.8 shows the unified compliance vectors along the twist and wrench axes with the corresponding unified compliances as magnitudes.

Table 2.5.: Compliance magnitudes and corresponding wrench axes of the double parallel flexure mechanism

correspondence wrench	translational compliance (a_{f_i})
$\boldsymbol{w}_{f_1}$	$\underline{4.50 \times 10^{-4}\,\mathrm{m\,N^{-1}}}$
$\boldsymbol{w}_{f_2}$	$5.00 \times 10^{-7}\,\mathrm{m\,N^{-1}}$
$\boldsymbol{w}_{f_3}$	$2.00 \times 10^{-8}\,\mathrm{m\,N^{-1}}$

As can be seen in fig. 2.8, the largest unified compliance vector is in the direction of wrench axis $\boldsymbol{w}_{f_1}$ as is expected. It originates from the point of interest in the x-direction perpendicular to the face of the flexures. The other unified compliance vectors are too small to visualize using linear magnitude representation. The corresponding unified compliance magnitudes resulting from both approaches are given in table 2.7. As can be seen in table 2.4, resulting from both approaches,

Table 2.6.: Compliance magnitudes and corresponding twist axes of the double parallel flexure mechanism

correspondence twist	rotational compliance (a_{γ_i})	pithch (h_i)
$\boldsymbol{T}_{\gamma_1}$	$3.12 \times 10^{-3}\,\mathrm{rad\,N^{-1}\,m^{-1}}$	0.00m
$\boldsymbol{T}_{\gamma_2}$	$7.80 \times 10^{-3}\,\mathrm{rad\,N^{-1}\,m^{-1}}$	0.00m
$\boldsymbol{T}_{\gamma_3}$	$1.07 \times 10^{-1}\,\mathrm{rad\,N^{-1}\,m^{-1}}$	0.00m

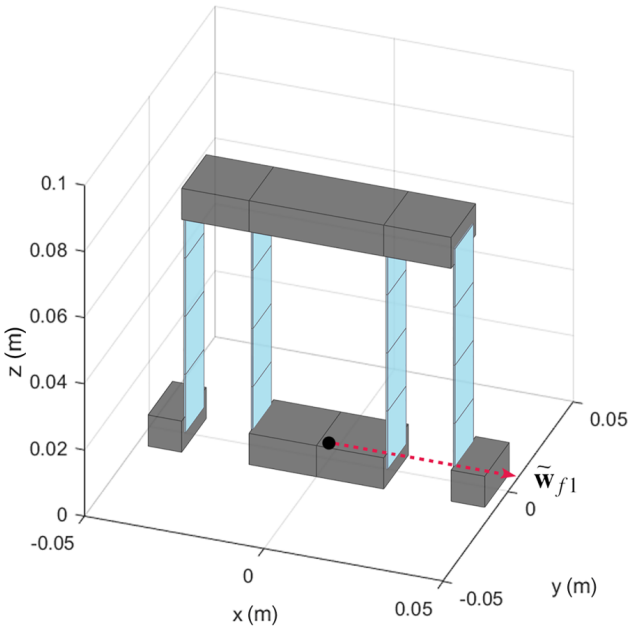

Figure 2.8.: Unified compliance vectors of the double parallel flexure mechanism

the largest unified compliance magnitude, corresponding to the most dominant degree-of-freedom, is at least two orders larger than the other magnitudes. The double flexure mechanism is thus dominantly translational compliant consistent with the objective of the design. The total degree-of-freedom order based on the unified compliance multipliers $\tilde{a}_{f_i}$ following from the RasT approach indicated by the unified compliance vector magnitudes is given as

$$|\tilde{\boldsymbol{w}}_{f_1}| \gg |\tilde{\boldsymbol{T}}_{\gamma_3}| > |\tilde{\boldsymbol{w}}_{f_2}| > |\tilde{\boldsymbol{T}}_{\gamma_1}| > |\tilde{\boldsymbol{w}}_{f_3}| \tag{2.39}$$

As discussed in section 2.4.3, the fully decoupled rotational degree-of-freedom $\boldsymbol{T}_{\gamma_2}$ cannot be calculated using the RasT approach. More insight is accumulated using the TasR approach. The total degree-of-freedom order based on the unified compliance multipliers $\tilde{a}_{\gamma_i}$ following from the TasR approach indicated by the unified compliance vector magnitudes is given as

Table 2.7.: Twist and wrench axes with corresponding unified compliance magnitudes of the cross pivot flexure mechanism

correspondence axes	unified compliance ($\tilde{a}_{f_i}$)	unified compliance ($\tilde{a}_{\gamma_i}$)
$\boldsymbol{w}_{f_1}$	$4.50\times10^{-4}\,\mathrm{m\,N^{-1}}$	$3.20\times10^{1}\,\mathrm{rad\,N^{-1}\,m^{-1}}$
$\boldsymbol{w}_{f_2}$	$5.00\times10^{-7}\,\mathrm{m\,N^{-1}}$	$3.56\times10^{-4}\,\mathrm{rad\,N^{-1}\,m^{-1}}$
$\boldsymbol{w}_{f_3}$	$2.00\times10^{-8}\,\mathrm{m\,N^{-1}}$	-
$\boldsymbol{T}_{\gamma_1}$	$4.40\times10^{-8}\,\mathrm{m\,N^{-1}}$	$3.12\times10^{-5}\,\mathrm{rad\,N^{-1}\,m^{-1}}$
$\boldsymbol{T}_{\gamma_2}$	-	$7.80\times10^{-4}\,\mathrm{rad\,N^{-1}\,m^{-1}}$
$\boldsymbol{T}_{\gamma_3}$	$1.50\times10^{-6}\,\mathrm{m\,N^{-1}}$	$1.07\times10^{-3}\,\mathrm{rad\,N^{-1}\,m^{-1}}$

$$|\tilde{\boldsymbol{w}}_{f_1}| \gg |\tilde{\boldsymbol{T}}_{\gamma_3}| > |\tilde{\boldsymbol{T}}_{\gamma_2}| > |\tilde{\boldsymbol{w}}_{f_2}| > |\tilde{\boldsymbol{T}}_{\gamma_1}| \tag{2.40}$$

where the multiplier corresponding to wrench $\boldsymbol{w}_{f_3}$ cannot be evaluated. Apart from the unevaluated degrees-of-freedom, both approaches show the same order of compliance. The order based on both the RasT and the TasR approach can be interpreted as

$$|\tilde{\boldsymbol{w}}_{f_1}| \gg |\tilde{\boldsymbol{T}}_{\gamma_3}| > |\tilde{\boldsymbol{T}}_{\gamma_2}| > |\tilde{\boldsymbol{w}}_{f_2}| > |\tilde{\boldsymbol{T}}_{\gamma_1}| > |\tilde{\boldsymbol{w}}_{f_3}| \tag{2.41}$$

2.6. Nonlinear Characterization

The visualization using the unified compliance mulitpliers $\tilde{a}_f$ and $\tilde{a}_\gamma$, introduced in section 2.5 can be used to characterize the nonlinear behavior of compliant mechanisms. A displacement of the point of interest can be analyzed incrementally. For each quasi-static-equilibrium, the wrench and twist axes with the corresponding unified compliance multiplier matrices can be determined. This section shows the nonlinear analysis of the introduced cross pivot flexure mechanism and two shell mechanisms using the unified compliances $\tilde{a}_f$ following from the RasT approach.

2.6.1. Cross Pivot Flexure Mechanism Nonlinear Characterization

The point of interest of the cross pivot flexure mechanism introduced in section 2.5.2 is subjected to a counter-clockwise rotation around the y-direction of magnitude $\frac{\pi}{3}$. Figure 2.9 shows the unified stiffness visualization applied to the cross pivot flexure mechanism. The initial mechanism and unified compliance vectors are more transparent.

Only the unified compliance vector corresponding to twist $\boldsymbol{T}_{\gamma_3}$ appears in fig. 2.9, since the other compliance magnitudes corresponding to the degrees-of-freedom are too small to visualize using linear magnitude representation. The vector magnitude corresponding to twist $\boldsymbol{T}_{\gamma_3}$ is constant at $3.38\times10^{4}\,\mathrm{m\,N^{-1}}$ during the rotation, but shows axis drift, another known quality of the cross-pivot flexure.

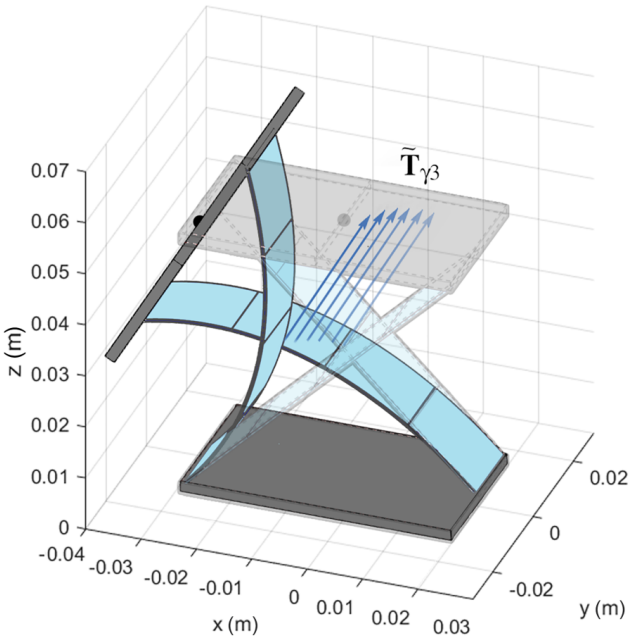

Figure 2.9.: Unified compliance vectors along a rotation of the point of interest around the y-axis range of motion

2.6.2. Single Corrugated Compliant Shell

The examples of the cross-pivot flexure and the double-parallelogram flexure demonstrate the utility of the characterization and how the results may be interpreted with respect to a compliant mechanisms primary kinematic behavior. The power of the characterization becomes more apparent in compliant shell mechanisms, as they have even less predictable and distinguishable degrees-of-freedom. The single corrugated shell mechanism was introduced in section 2.3. The mechanism is fully constrained along the bottom edge and the point of interest is in the center of the opposing edge, indicated by a black dot. Figure 2.10 shows the unified compliance visualization applied to the single corrugated compliant shell mechanism.

It shows the largest unified compliance vector corresponding to direction of twist $\boldsymbol{T}_{\gamma_3}$, which means that the largest compliance direction is a screw around the direction of twist $\boldsymbol{T}_{\gamma_3}$. The second largest unified compliance vector corresponds to direction of wrench $\boldsymbol{w}_{f_1}$ which is a pure translation parallel to the direction of wrench $\boldsymbol{w}_{f_1}$. The other unified compliance magnitudes are relatively small, intuitively explainable by the larger moment of inertia of the corresponding cross section. The total initial relative degree order based on the unified compliance multipliers $\tilde{a}_f$ following from the RasT approach indicated by the unified compliance vector magnitudes is given as

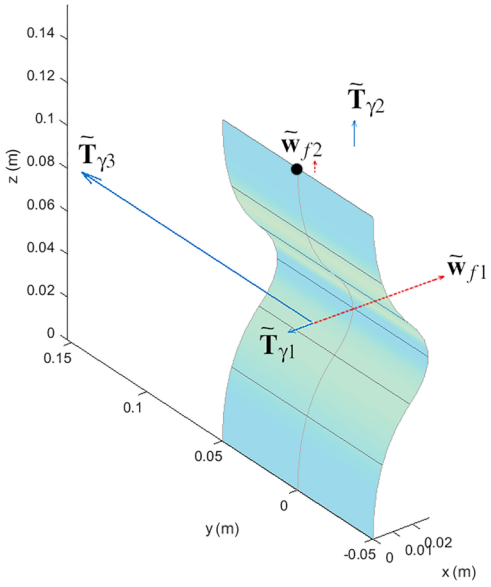

Figure 2.10.: Unified compliance vectors single corrugated shell

$$|\tilde{\boldsymbol{T}}_{\gamma_3}| > |\tilde{\boldsymbol{w}}_{f_1}| > |\tilde{\boldsymbol{T}}_{\gamma_2}| > |\tilde{\boldsymbol{T}}_{\gamma_1}| > |\tilde{\boldsymbol{w}}_{f_2}| > |\tilde{\boldsymbol{w}}_{f_3}| \tag{2.42}$$

What is of specific interest is how these unified compliance vectors change over a large range of motion. Figure 2.11shows the unified compliance vectors through a large deformation along the transverse bending direction. The point of interest is subjected to a displacement along the positive x-axis direction. All other degrees-of-freedom are unconstrained. The unified compliance vectors are shown per quasi-static-equilibrium state during the displacement of the point of interest, as shown in fig. 2.11. The path of the point of interest is indicated with a black line. The initial configuration and unified compliance vectors are represented more transparently. Additionally, for visibility, only the four largest vectors are shown.

The magnitudes of the unified compliance,$\tilde{a}_f$, are plotted against the absolute displacement of the point of interest in fig. 2.12.

The initial values on the left of the graph represent the compliances for the undeformed mechanism. As shown, the mechanism is predominantly rotational compliant. Figure 2.12 shows that this order remains along the displacement of the point of interest. As discussed in section 2.2, the unified compliances are derived from the tangent stiffness matrix. The tangent stiffness matrix is composed of a physical stiffness and a geometrical stiffness matrix.

The change of vector directions and magnitude ratios is relatively constant. The directions of both wrench $\boldsymbol{w}_{f_1}$ and twist $\boldsymbol{T}_{\gamma_3}$ relative to the point of interest remain similar along the deformation. $\boldsymbol{w}_{f_1}$ stays perpendicular to the flexure mechanism and $\boldsymbol{T}_{\gamma_3}$ stays parallel to the face of the shell. The compliance magnitudes related

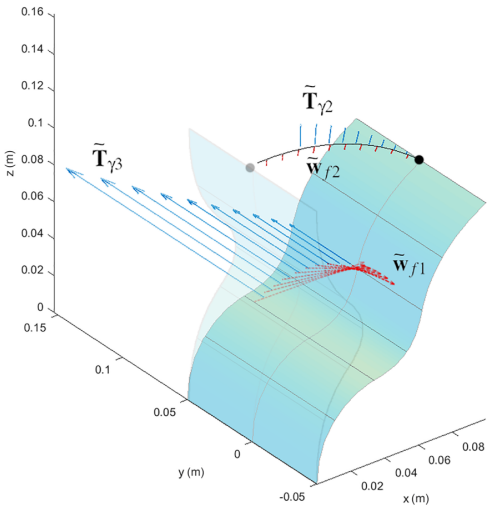

Figure 2.11.: Unified compliance vectors single corrugated shell along displacement

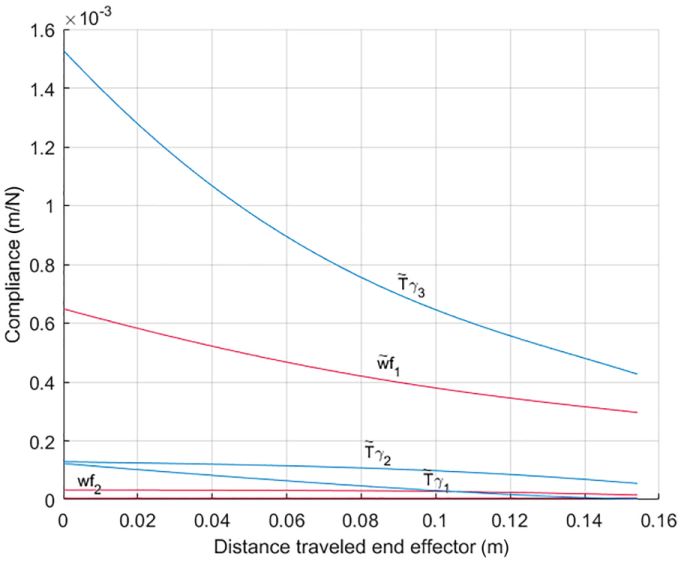

Figure 2.12.: Magnitude plot unified compliance over range of motion of the single corrugated shell

to the twist and wrench axes in the direction of displacement decrease along the motion, which are explained by, build up, internal stress. Despite the assumed linear material behavior, described by Hookes Law in the physical stiffness matrix, the mechanism exhibits nonlinear behavior. This behavior is induced by the nonlinear geometry stiffness matrix. However, the physical stiffness matrix is dominant since

the overall shape of the mechanism does not undergo significant changes.

Extruded Spiral Compliant Shell

Another interesting compliant shell mechanisms is the extruded spiral compliant shell mechanism (fig. 2.13). The material properties are identical to the single corrugated shell mechanism. The 2mm thick geometry is defined by NURBS [18], a third polynomial follows a 3×5 grid. Five coordinates are placed on three planes in y = -0.05, y = 0, and y = 0.05. The x and z coordinates are defined in table 2.8. The mechanism is fully constrained along the bottom edge and the point of interest is in the center of the opposing edge, indicated by a black dot. The initial configuration is shown in fig. 2.13.

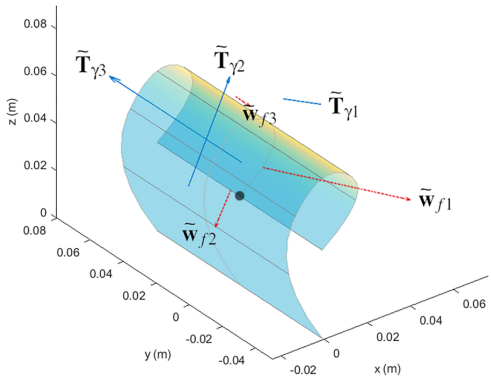

Figure 2.13.: Unified compliance vectors of the spiral shell mechanism

Table 2.8.: NURB coordinates extruded spiral shell

point	1	2	3	4	5
x	0.00	-0.03	0.00	0.03	0.00
y	0.00	0.04	0.08	0.06	0.04

The total initial degree-of-freedom order based on the unified compliance multipliers $\tilde{a}_f$ following from the RasT approach indicated by the unified compliance vector magnitudes is given as

$$|\tilde{\boldsymbol{T}}_{\gamma_3}| > |\tilde{\boldsymbol{w}}_{f_1}| > |\tilde{\boldsymbol{T}}_{\gamma_2}| > |\tilde{\boldsymbol{T}}_{\gamma_1}| > |\tilde{\boldsymbol{w}}_{f_2}| > |\tilde{\boldsymbol{w}}_{f_3}| \tag{2.43}$$

Although the mechanism is still a developable surface, predicting the locations and magnitudes of the compliance vectors is already more challenging compared to the previous shell mechanism. The two largest unified compliance vectors are twist $\boldsymbol{T}_{\gamma_3}$ and wrench $\boldsymbol{w}_{f_1}$. As in the previous example, these vectors are visualized during a displacement of the point of interest. The initial configuration of the mechanism

is depicted in fig. 2.13. The point of interest is translated along the x-axis, while motion in the other directions is unconstrained, as can be seen in fig. 2.14.

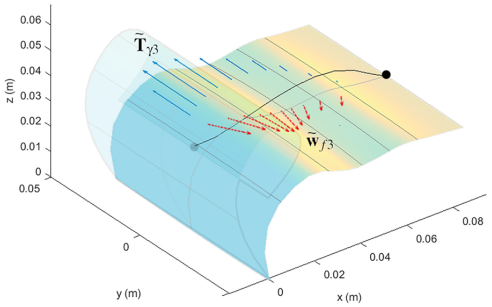

Figure 2.14.: Unified compliance vectors of the spiral shell mechanism during motion

The most significant difference with the previous shell mechanism is the nonlinear behavior of the compliance magnitudes, which results in a changing compliance magnitude order under large deformation. This behavior is represented in fig. 2.15 which shows the unified compliance against absolute displacement of the point of interest.

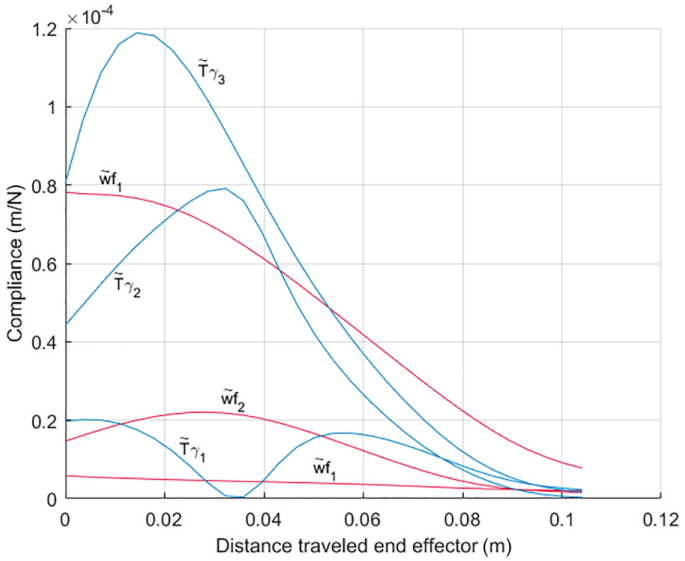

Figure 2.15.: Magnitude graph unified compliance over range of motion of the spiral shell mechanism

The magnitude of the compliance directions behaves highly nonlinearly along the translational trajectory of the point of interest. The direction of twist $\boldsymbol{T}_{\gamma_3}$ stays the same along the deformation, while the direction of wrench $\boldsymbol{w}_{f_1}$ changes substantially

relative to the face of the mechanism. As discussed in the previous shell example, the nonlinearity cannot be due to the stress building up, since this is defined by Hookes linear law. The nonlinearity is due to the geometric stiffness matrix. The change in magnitudes is significant, resulting in a changing order of the unified compliances along the motion. In this example, half of the compliance magnitudes increase initially, as the mechanism unfolds and undergoes significant geometrical changes. The decreasing geometry stiffness matrix change is more significant than the linearly increasing physical stiffness matrix halfway through the motion, when the mechanism is unfolded. From then on, the geometry stays relatively similar, thus less nonlinearity is induced by the geometry change. The increased physical stiffness becomes the most predominant factor and the unified compliance start to decrease at the end of the motion.

2.7. Validation

To demonstrate the efficacy and validate critical components of the unification method presented in section 2.4, an experiment was conducted on a physical model of a single corrugated shell. The geometry of the physical model is the same as the shell introduction in three, except for the smaller corrugation amplitude of 14mm. The experiment compared a physical compliant shell mechanism, fabricated from polyethylene terephthalate (E=2.1GPa, ν=0.35) using vacuum thermoforming, with a computational model based on the isogeometric analysis framework of [17]. The measurement setup of the experiment is shown in fig. 2.16.

The eigen-twist and eigen-wrench of the physical model were analyzed in a Zwick Z005 universal tester with two separate experiments. One eigen-twist and one eigen-wrench were identified by applying various twists on the top edge of a clamped-free physical model similar to the mechanism in fig. 2.10, while evaluating the induced loads using an ATI Mini40-2 6 DoF load cell. Based on the analysis and assumed preserved symmetry during fabrication of the physical model, the applied twists were varied by varying the location vector along a predefined path.

The location vector is varied by brackets with a variable offset, which can be seen with different offsets in fig. 2.17. The offsets vary the location vector magnitude $|r_i|$ of the applied twists. The offset in the brackets is varied by varying the amount and thickness of the used steel plates.

The applied twist and the induced load were compared until they matched the definitions of the eigen-twist and eigen-wrench presented in section 2.2, to find the location and corresponding stationary stiffness multipliers.

The resulting RasT and TasR unified stiffnesses based on the determined components of Lipkin's eigen-decomposition of the experiment and computational model were compared per eigen-twist and eigen-wrench. The unified stiffness results of the model and experiment are shown in table 2.9 and table 2.10.

The RasT and TasR unified stiffnesses of the corresponding eigen-twist, respectively, differ by +9.21% and -0.93%. The RasT and TasR unified stiffnesses of the corresponding eigen-wrench, respectively, differ by +3.90% and -13.90%.

The experimental results are well within a reasonable margin of error and

Figure 2.16.: Measurement setup

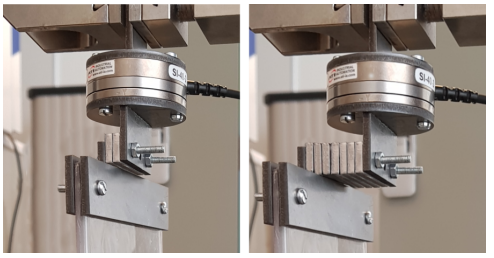

Figure 2.17.: Location vector offset bracket

Table 2.9.: Eigen-twist T_{γ_3} components

	Model	Experiment
RasT unified stiffness	$3.91 \times 10^4 \mathrm{N\,m^{-1}}$	$4.3 \times 10^4 \mathrm{N\,m^{-1}}$
TasR unified stiffness	$4.33 \mathrm{N\,m\,rad^{-1}}$	$4.3 \mathrm{N\,m\,rad^{-1}}$

corroborate the accuracy of the model proposed in this paper. The discrepancies can be partially attributed the production process of the physical model, friction in

Table 2.10.: Eigen-wrench w_{f_3} components

	Model	Experiment
RasT unified stiffness	$8.26 \times 10^4 \mathrm{N\,m^{-1}}$	$7.95 \times 10^4 \mathrm{N\,m^{-1}}$
TasR unified stiffness	$1.47 \mathrm{N\,m\,rad^{-1}}$	$1.23 \mathrm{N\,m\,rad^{-1}}$

the test setup, and the variability in material properties.

2.8. Discussion

The characterization presented in this paper has benefits compared to the existing methods. Most characterizations do not address the coupling between rotations and translations [6] and are only able to separately compare rotational degrees-of-freedom and translational degrees-of-freedom, within one mechanism [7]. To compare rotational and translational compliances with each other, it is necessary to introduce a unification variable. Where the existing methods introduce arbitrarily chosen unification variables [10], this paper introduces two consistently derived unification lengths with physical significance. The unification lengths account for coupling, thus allowing the fair comparison of rotational and translational compliances within and between mechanisms.

Two unification lengths were developed based on two approaches. The unification length resulting from the RasT approach, based on Plücker coordinates, is derived independently and yielded similar results as Lin's et al. [9] work, based on hybrid coordinates, used to optimize graspers. Lin does not recognize the limitations of the results that became apparent when used to characterize the behavior of nonlinear compliant shell elements. We eliminate these limitations by introducing both the RasT and the TasR approach. Both Lin's derivation and the introduced potential energy method are more straightforward than the introduced virtual load method; however, they give less insight into the actual kinematics. The virtual load method includes substeps with physical relevance, these substeps themselves can form the basis for designs. Thorough knowledge of the composition of these substeps provides the opportunity to vary parameters in an intelligent manner to reach specific objectives. Additionally, energy, in any form, is a scalar quantity. By introducing the principle of potential energy, all valuable directional information is lost.

2.9. Conclusion

This paper introduces a method for the characterization of nonlinear behavior for large deflections in complex compliant mechanisms that considers coupling and allows the comparison of stiffness between all six degrees-of-freedom. The characterization is based on consistently derived nonarbitrary unification variables based on equivalent compliance by virtual load and potential energy, therefore allows the comparison of compliance between degrees-of-freedom of different mechanisms. With this comprehensive comparison, the opportunity rises to order all

degrees-of-freedom, within and between mechanisms in terms of the corresponding compliance. The most predominant degrees-of-freedom can be identified along the trajectory of large deflections of compliant mechanisms. The characterization, presented in this paper, applied to any mechanism with a symmetric positive definite nonsingular compliance matrix. This includes both compliant flexure and shell mechanisms.

2.10. Author Contributions

J.R.L. and C.J.K. proposed the research. J.R.L. designed the research and did the analyses and experiments and wrote the paper. W.W.P.J.S. modeled and performed the simulation on the cross pivot flexure and double parallel flexure mechanism. J.R.L. and W.W.P.J.S. designed the experiment. C.J.K. and W.W.P.J.S double checked all the analyses and equations. C.J.K., W.W.P.J.S. and J.L.H. supervised the project and reviewed the paper.

Bibliography

[1] J. R. Leemans, C. J. Kim, W. W. P. J. van de Sande, and J. L. Herder. "Unified Stiffness Characterization of Nonlinear Compliant Shell Mechanisms". In: *Journal of Mechanisms and Robotics* 11.1 (2019).

[2] K. A. Seffen. "Compliant shell mechanisms". In: *Philosophical Transactions of the Royal Society A: Mathematical, Physical and Engineering Sciences* 370.1965 (2012). 2010, pp. 2010–2026.

[3] S. Pellegrino. "Bistable Shell Structures". In: *46th AIAA/ASME/ASCE/AHS/ASC Structures, Structural Dynamics and Materials Conference*. 2005. eprint: https://arc.aiaa.org/doi/pdf/10.2514/6.2005-1934.

[4] G. Radaelli and J. Herder. "Isogeometric Shape Optimization for Compliant Mechanisms With Prescribed Load Paths". In: Aug. 2014, V05AT08A046.

[5] J. Nijssen. "Design and Analysis of a Shell Mechanism Based Two-Fold Force Controlled Scoliosis Brace". English. MA thesis. 2017.

[6] C. Kim. *A Conceptual Approach to the Computational Synthesis of Compliant Mechanisms*. University of Michigan., 2005.

[7] J. Nijssen. "Overview and Kinematic Characterization of Compliant Shells". English. MA thesis. 2016.

[8] H. Lipkin and T. Patterson. "Geometrical properties of modelled robot elasticity: part I - Decomposition". In: *ASME Design Tech. Conf. and Computers in Engineering Conf.* Vol. 45. 1992, pp. 179–185.

[9] Q. Lin, J. W. Burdick, and E. Rimon. "A stiffness-based quality measure for compliant grasps and fixtures". In: *IEEE Transactions on Robotics and Automation* 16.6 (2000), pp. 675–688.

[10] M. Teichmann. "A grasp metric invariant under rigid motions". In: *Proceedings of the 1996 IEEE International Conference on Robotics and Automation, Minneapolis, Minnesota, USA, April 22-28, 1996*. IEEE, 1996, pp. 2143–2148.

[11] G. Hao and X. Kong. "A normalization-based approach to the mobility analysis of spatial compliant multi-beam modules". In: *Mechanism and Machine Theory* 59 (2013), pp. 1–19.

[12] Y. Zhang, H.-J. Su, and Q. Liao. "Mobility criteria of compliant mechanisms based on decomposition of compliance matrices". In: *Mechanism and Machine Theory* 79 (2014), pp. 80–93.

[13] M. Chasles. “Note sur les propriétés génerales du système de deux corps semblables entr’eux et placés d’une manière quelconque dans l’espace; et sur le déplacement fini ou infiniment petit d’un corps solide libre [A note on the general properties of a system of two similar bodies arbitrarily positioned in space; and on the finite or infinitely small displacement of an unconstrained solid body]”. In: *Bulletin des Sciences Mathématiques, Férussac* 14 (1830), pp. 321–26.

[14] R. M. Murray, Z. Li, and S. S. Sastry. *A Mathematical Introduction to Robotic Manipulation*. CRC Press, Dec. 1994.

[15] E. Oñate. “On the derivation and possibilities of the secant stiffness matrix for non linear finite element analysis”. In: *Computational mechanics* 15.6 (1995), pp. 572–593.

[16] J. Simo. “The (symmetric) Hessian for geometrically nonlinear models in solid mechanics: intrinsic definition and geometric interpretation”. In: *Computer Methods in Applied Mechanics and Engineering* 96.2 (1992), pp. 189–200.

[17] J. A. Cottrell, T. J. R. Hughes, and Y. Bazilevs. *Isogeometric analysis : toward integration of CAD and FEA*. Wiley, New York, USA, 2009, p. 335.

[18] L. Piegl and W. Tiller. *The NURBS Book*. Monographs in Visual Communication. Springer Berlin Heidelberg, 1996.

[19] J. B. Jonker and J. P. Meijaard. “SPACAR — Computer Program for Dynamic Analysis of Flexible Spatial Mechanisms and Manipulators”. In: *Multibody Systems Handbook*. Ed. by W. Schiehlen. Berlin, Heidelberg: Springer Berlin Heidelberg, 1990, pp. 123–143.

3

Shape optimization framework for the path of the primary compliance vector in compliant mechanisms

Hylke Kooistra, Charles J. Kim, Werner W.P.J. van de Sande, Just L.Herder

The primary compliance vector (PCV) captures the dominant kinematic behaviour of a com pliant mechanism. Its trajectory describes large deformation mechanism behaviour and can be integrated in an optimization objective in detailed compliant mechanism design. This paper presents a general framework for the optimization of the PCV path, the mechanism trajectory of lowest energy, using a unified stiffness characterization and piecewise curve representation. We present a meaningful objective formulation for the PCV path that evaluates path shape, location, orientation, and length independently and apply the framework to two design examples. The framework is useful for design of planar and shell compliant mechanisms that traverse a specified mechanism trajectory and that are insensitive to load perturbations.

This chapter originally appeared as H. Kooistra, C. J. Kim, W. W. P. J. van de Sande, and J. L. Herder. "Shape optimization framework for the path of the primary compliance vector in compliant mechanisms". In: *Journal of Mechanisms and Robotics* 12.6 (2020)[1]

3.1. Introduction

Compliant mechanisms have been designed for a variety of purposes [2]. One fundamental quality that has received less attention is the nature of large displacements in compliant mechanisms. Often mechanisms are designed by intuition to achieve a single degree of freedom [3]. Most flexure designs are of this type. Yet, these same designs sometimes suffer from parasitic error even without the application of off-axis loads. In other work that pertains to path generating compliant mechanisms, output displacement is largely unconstrained [4]. As a consequence, output displacement is often very sensitive to external load.

One of the limitations of previous work in large deflection compliant mechanisms is that the designs are sometimes created in an ad-hoc way that relies heavily on tacit knowledge. This is the case with many flexure-based designs. As noted by Zhu, et. al [5], while there has been much progress in topology optimization, there is limited research in topology optimization for path generating compliant mechanisms [4, 6, 7]. The research has yielded non-obvious designs that meet path requirements, but it does not consider the fundamental three-dimensional stiffness characteristics of the mechanisms. Thus, the optimization often yields designs which traverse desired paths only under the specified boundary or loading conditions.

We consider the trajectory of the primary compliance vector (PCV) to capture the dominant kinematic behavior of a mechanism [8, 9]. The PCV is a generalized 6-vector representing a twist that captures the direction and location of a degree of freedom (DOF) axis and is intrinsic to the geometry of a mechanism and invariant under coordinate transformations. Both the location and direction of the PCV change as the mechanism deforms. All PCV locations combined form a path that characterizes large deformation behavior. The PCV of a cross-pivot flexure is in the direction of flexure width and initially located at half the height. Under large deformation, it moves in the direction of the actuation; that movement is defined as axis drift [10].

In this paper, we give particular attention to compliant shell mechanisms, which are a sub-category of compliant mechanisms. They are defined as spatially curved thin-walled structures able to transfer or transmit force, motion or energy through elastic deformation [11–13]. They have similar benefits over rigid-body mechanisms as compliant mechanisms. They reduce wear and backlash making them useful in high precision environments, or eliminating the need for lubrication making them useful in many different types of environments [14]. Added to these benefits compliant shell mechanisms have topological advantages over typical compliant mechanisms [12]. They are useful in applications where compliant mechanisms need to be shaped around objects, such as the human body for the use of support system against gravity [13].

While previous research has focused on large deflection characterization of flexure-based designs or topology optimization for path generation, there is a need to develop a systematic means by which compliant mechanism designs can achieve large deflection motion by drawing from intrinsic characteristics of a mechanism. We present an optimization framework that refines mechanism shape to satisfy large deformation kinematic requirements. It meets these requirements by tracking the

PCV path. Furthermore, we explore relevant design variables. The optimization framework can equally be applied to topologies consisting of flexures, beams, or other compliant elements. Compliant shell mechanisms, however, have distinct parameterizations that can be more versatile than simpler linear or curvilinear elements.

The paper is organized as follows. In section 3.2 we present background concepts that are incorporated into the shape optimization framework. In section 3.3, we present the framework in terms of objective function, design variables, and solution method. Next, we demonstrate the framework with two design examples. Finally, we discuss the contributions of this paper and draw conclusions in section 3.5.

3.2. Background

In this section we review the literature pertaining to background concepts utilized in the shape optimization framework and describe specific aspects of the research that is distinct from the literature. First, the PCV is described using a unified stiffness characterization. The full description of this characterization is found in [9], and the text gives a summary of the results. Second, we present a simplified polygonal curve representation drawing from the research on Fourier Descriptors [15] that will be used to describe both the desired and actual PCV trajectory. Lastly, surrogate-based optimization is described as an optimization algorithm suited to the task of shell mechanism optimization undergoing large deformations.

3.2.1. Primary Compliance Vector (PCV)

Lipkin developed the eigentwist and eigenwrench decompositions to describe the primary characteristics of the stiffness of a robot [8]. The primary stiffness and compliance characteristics of a mechanism can be ascertained by two eigenvalue problems that yield the eigenwrenches and eigentwists. A wrench or a load is expressed in Plücker coordinates as follows [16].

$$W = \{f \quad | \quad m\}^T = \{f \quad | \quad r_W \times f + h_W f\}^T \tag{3.1}$$

A wrench is a screw that is expressed as six by one column vector. The force f makes up the upper half and the moment m the lower half. The moment is split into two parts. One is perpendicular to the direction of the force f and is the cross product of the force and the location vector r_W. The second is parallel to the force and influenced by the scalar pitch h_W.

A twist is also a screw in which the translation δ makes up the upper half and the rotation ρ the lower half.

$$T = \{\delta \quad | \quad \rho\}^T = \{r_T \times \rho + h_T \rho \quad | \quad \rho\}^T \tag{3.2}$$

The translation δ is split. One part is perpendicular to the direction of the rotation ρ and is the product of the force and the location vector r_T. The second part is parallel to the rotation and influenced by the scalar pitch h_T.

For a given 6×6 stiffness matrix, K_t, and its inverse, $C_t = K_t^{-1}$, the eigenwrenches and eigentwists are found by solving the eigenvalue problems [8].

$$k_f \hat{\mathbf{w}}_\mathbf{f} = K_t \Gamma \hat{\mathbf{w}}_\mathbf{f} \tag{3.3}$$

$$a_\gamma \hat{\mathbf{T}}_\gamma = C_t \Delta \hat{\mathbf{T}}_\gamma \tag{3.4}$$

where

$$\Gamma = \begin{bmatrix} I & 0 \\ 0 & 0 \end{bmatrix}, \Delta = \begin{bmatrix} 0 & 0 \\ 0 & I \end{bmatrix} \tag{3.5}$$

and $\hat{\mathbf{w}}_\mathbf{f}$ are eigenwrenches, k_f are eigenwrench stiffness multipliers, $\hat{\mathbf{T}}_\gamma$ are eigentwist and a_γ are eigentwist compliance multipliers. The force parts of the eigenwrenches are orthonormal, while the rotational parts of the eigentwists are orthonormal. The eigenwrenches and eigentwists are normalised so that the force and rotation parts are unit vectors.

Solving the eigenvalue problem yields eigenwrenches that induce pure and parallel translations and eigentwists that induce pure and parallel moments.

The eigencompliances, a_γ and $a_f = k_f^{-1}$, cannot be directly compared because they describe distinct phenomena and have different units. To reconcile this, Leemans developed a unified stiffness characterization that enables systematic and meaningful ordering of the rotational and translational compliances [9]. The unification variable χ_i expresses rotational compliance as equivalent translational compliance.

$$\tilde{\alpha}_f = \begin{bmatrix} a_{f1} & a_{f2} & a_{f3} & \chi_1^2 a_{\gamma 1} & \chi_2^2 a_{\gamma 2} & \chi_3^2 a_{\gamma 3} \end{bmatrix} \tag{3.6}$$

$$\chi_i = \sqrt{h_i^2 + \left|\boldsymbol{r}_i\right|^2} \tag{3.7}$$

Where: h_i is the pitch of the eigen-twist, and $\boldsymbol{r}_i$ is the shortest vector from the point of interest (POI) on a mechanism to the line of an eigen-twist.

The reconciliation of units in eq. (3.6) and eq. (3.7) is significant in that the relative compliance of the eigentwists and eigenwrenches can be directly compared. Lipkin showed that the eigentwists and eigenwrenches are invariant under coordinate transformation, and Leemans showed that the unified characterization is also invariant. Finally, the PCV is the eigen-twist or eigen-wrench with the largest unified compliance multiplier value.

The unified characterization can be applied to a mechanism that undergoes large deformation by incremental calculation of the tangent stiffness (or compliance) matrix. The incremental evaluation of the eigen-decomposition results in a PCV at a specific deformation, because the tangent stiffness matrix changes as the deformation increases. The path of the PCV can be traced for a mechanism through large deformations; this path is obtained by incrementally applying a moment that is parallel to the PCV. Thus, the PCV path represents the direction of lowest stored strain energy.

3.2.2. Curve shape representation

In this paper we are interested in comparing the shape of target curves with the trajectory of a compliant mechanism. Consider the red and blue curves in fig. 3.1. The shapes of the blue curves in fig. 3.1b-d are similar to the red curve but are of different location, scale, and orientation, respectively. The shape of the red curve in fig. 3.1a, however, is very different from the blue curve. If shape similarity were calculated using structural (point to point) error, the blue curve in fig. 3.1a would yield the best results. It is clear that structural error does not directly capture shape similarity. Further, the example in fig. 3.1e illustrates a case in which structural error cannot be utilized, because the number of comparison points is not the same between the red and blue curves.

In related research, Fourier descriptors have been developed to capture the *shape* of a curve and address the challenges presented in fig. 3.1. Zahn developed Fourier descriptors and used them successfully for pattern recognition [15]. Ullah developed a synthesis method for rigid link mechanism path generation using Fourier descriptors [17]. These descriptors characterize a path shape independent of length, orientation, and location. Rai and Mankame adapted this method for end-effector path generation of hybrid planar path generators and compliant non-smooth path generators, respectively [4, 18].

In this paper, we utilize a simplified curve representation that is independent of curve location, scale, orientation, and number of control points, while still capturing the shape of the curve. In this representation, curves are normalized with respect to arc-length, which renders the representation independent of scale. Further, only change in curve orientation is captured, which eliminates dependence on both location and orientation.

Consider a piece-wise linear curve with m vertices $v_i \in (x_i, z_i)$ for $i = 1..m$. The curve segment length may be found as the distance between vertices

$$\ell_i = |v_{i+1} - v_i| = \sqrt{(x_{i+1} - x_i)^2 + (z_{i+1} - z_i)^2}. \tag{3.8}$$

where ℓ_i is the length of ith the curve segment.

The total length of the curve is $L = \sum_1^{m-1} \ell_i$ and the normalized segment length, $\tilde{\ell}_i$, is found by dividing each curve segment length by L such that

$$\tilde{\ell}_i = \frac{l_i}{L}. \tag{3.9}$$

We define the *bend*, ϕ_i, as the angle change between successive curve segments. In terms of vertex locations, the bend at each vertex is found as

$$\phi_i = \angle(v_{i+2} - v_{i+1}) - \angle(v_{i+1} - v_i). \tag{3.10}$$

for $i = 2..m-2$.

We assume that the first and last vertices are connected by a line segment , so $\phi_{m-1} = \angle(v_1 - v_m) - \angle(v_m - v_{m-1})$ and $\phi_m = \angle(v_2 - v_1) - \angle(v_1 - v_m)$.

Finally, the bend function can be represented as a function parameterized with respect to normalized arc-length such that

$$y(t) = \phi_1 + \sum_{i=2}^{m-1} \phi_i H(t - \tilde{l}_{i-1}) \tag{3.11}$$

where t = (0,1) is the normalized arc-length parameter and H is the Heaviside step function.

This formulation is consistent with the parameterization of polygonal curves in Zahn [15], except that Zahn takes further steps to make $y(t)$ periodic and describe it using a Fourier Series. The advantages of those two steps is that such a representation is insensitive to starting points, meaning that two curves under comparison could be assessed for similarity even if they were described at different relative starting points. In this paper, we are not concerned about the ability to assess curves in this manner because we consider the starting point as a known.

There are certain advantages of not representing $y(t)$ as a Fourier Series (fig. 3.1c). Representing $y(t)$ as a Fourier Series raises several questions such as: (i) how many terms of amplitudes and phases should be compared? and (ii) what is the relationship between the shape of the curve and the amplitudes and phases? These questions are particularly problematic in a optimization context because they introduce additional complexity and abstraction from a physical phenomenon.

As will be presented in section 3.3.2, we directly utilize $y(t)$ to compare candidate and target curves. The representation still addresses the goals of insensitivity to location, scale, orientation, and number of control points.

3.2.3. Surrogate-Based Optimization

In this paper we utilize surrogate-based optimization due to the computationally expensive non-linear finite element analysis necessary to determine the path of the PCV. In surrogate-based optimization, a fast and analytically tractable surrogate model replaces a computationally expensive model [19, 20]. The optimization process comprises construction, optimization, checking, and updating of the surrogate model as illustrated by fig. 3.3.

The main advantage of surrogate-based optimization is the decrease in calls to the objective function [20]. Which causes a large reduction of computation time for complicated objective functions based on finite element modeling. Furthermore, it overcomes discontinuities, local minima, noise in the objective function, and it is easier to differentiate. Finally, a surrogate-based optimization converges for a given search-space due to the manner in which the model is represented [21].

3.3. Optimization Framework

In this section we present a shape optimization framework for the lowest energy path of a compliant shell mechanism. To that end the following subsections describe the objective formulation, error formulation, and design variables.

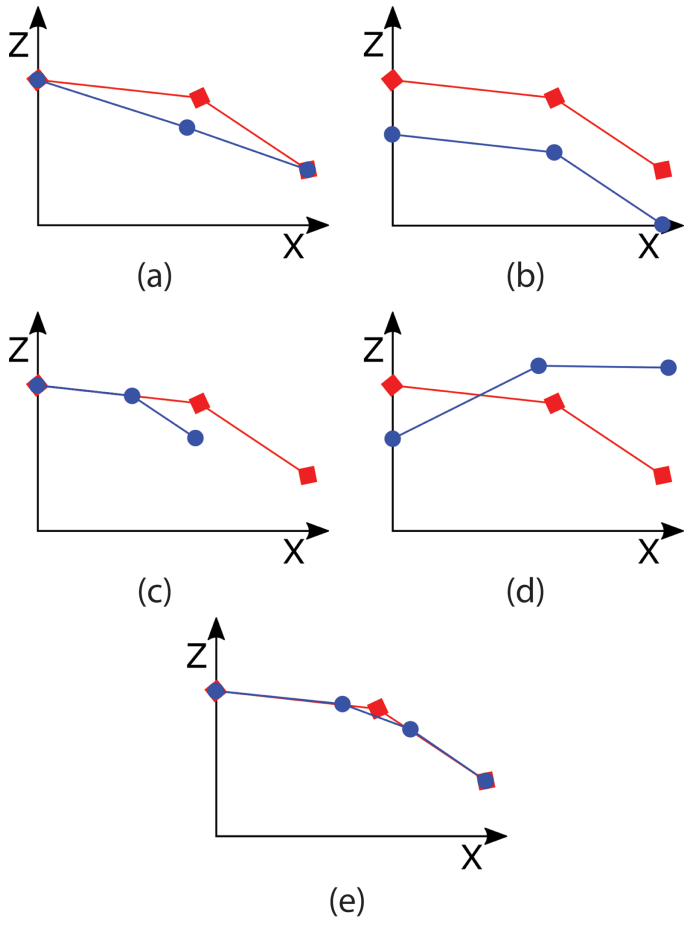

Figure 3.1.: The desired shape in red and the actual shape in blue [18]

3.3.1. Conditions

A polygon is needed for the mapping from incremental primary compliance vectors to the shape describing step-functions. For the mapping to be valid, the orientation of the PCV should not change over the deformation. Furthermore, the desired and actual PCV should be aligned. The equality constraint in eq. (3.12), which is valid for a twist PCV, introduces this condition.

$$c_1 = \boldsymbol{\rho}(\mathbf{x})_i \cdot \boldsymbol{\rho}^* - 1 = 0 \tag{3.12}$$

where c_1 is the first equality constraint, and $\boldsymbol{\rho}$ is the PCV direction vector. The desired PCV direction ($\boldsymbol{\rho}^*$) should not change over the deformation.

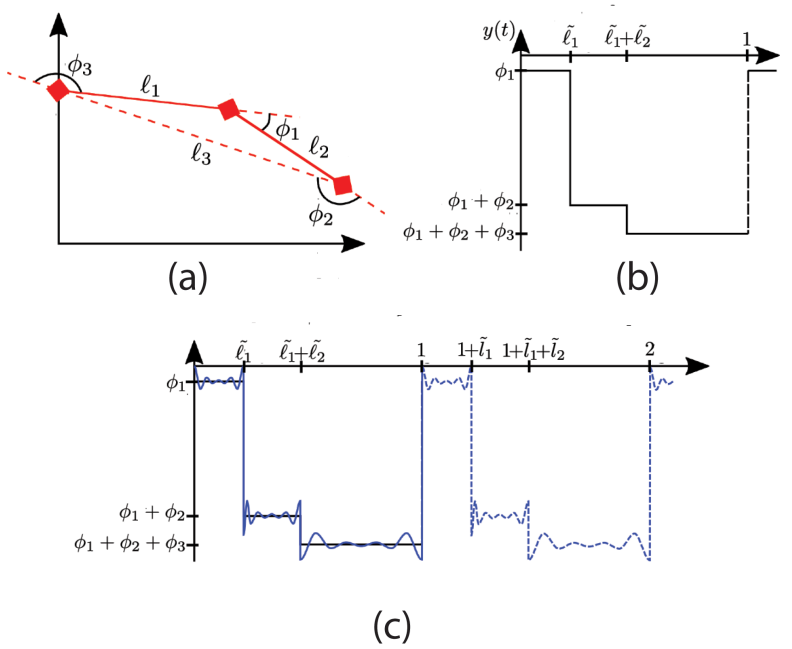

Figure 3.2.: An arbitrary path, the matching step-function, and the Fourier transform of that step-function

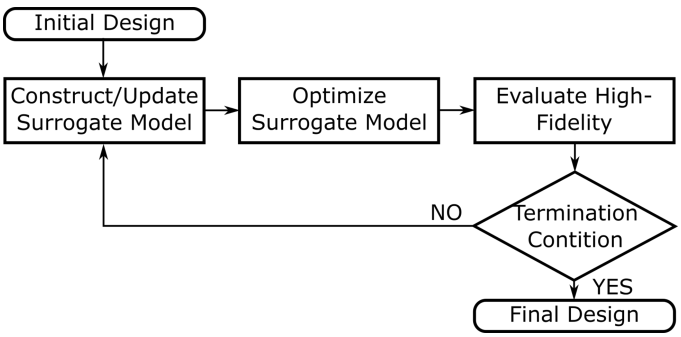

Figure 3.3.: Flowchart of the surrogate-based optimization process

3.3.2. Objective Formulation

The goal of shape optimization in this paper is for the final mechanism to follow a specific trajectory. To that end, we introduce the PCV path. The PCV path connects the PCV locations resulting from incremental application of load along the PCV. As such, the PCV path represents a trajectory wherein the mechanism achieves lowest strain energy. By definition, the PCV is the twist (or wrench) that results in the

lowest potential energy. When applied in a geometrically non-linear analysis, the PCV path is calculated by applying a moment along the PCV at each load step.

The PCV path is illustrated with blue line segments in fig. 3.6 for some flexures with moment applied as shown. In this particular planar case, the PCV is always an eigentwist caused by a moment applied in the direction perpendicular to the illustrated plane.

PCV parameters such as location and direction are determined through manipulation of the stiffness matrix as described in Lipkin and Leemans [8, 9]. The stiffness matrices are extracted from non-linear finite element analysis of the mechanism. For each load step in the analysis, the PCV location can be calculated as the shortest vector ($\mathbf{r}_i$) between the point of applied load (or displacement) and the line of the PCV. That is,

$$\mathbf{r}_i = \frac{(\boldsymbol{\delta}_i - h_i \boldsymbol{\rho}_i) \times \boldsymbol{\rho}_i}{\boldsymbol{\rho}_i \cdot \boldsymbol{\rho}_i} \tag{3.13}$$

where $\boldsymbol{\delta}_i$ is the translation vector of the PCV, $\boldsymbol{\rho}_i$ is the direction vector, and h_i is the pitch. The PCV pitch is calculated as

$$h_i = \frac{\boldsymbol{\rho}_i \cdot \boldsymbol{\delta}_i}{\boldsymbol{\rho}_i \cdot \boldsymbol{\rho}_i}. \tag{3.14}$$

Together all PCV locations form the PCV path. This path is projected on a plane and expressed as vertices of a polygon.

The PCV path can be characterized by its shape, location, orientation, and overall length in terms of the curve representation method described in section 3.2.2. The bend angle ϕ_i and normalized arc-length $\tilde{\ell}_i$ characterize the shape (fig. 3.2a). We choose the location of the undeformed PCV as the path location. Orientation and length are calculated from the vector between the undeformed PCV and the final PCV.

Error formulation

Error is calculated between the PCV path for a mechanism design and the desired PCV path such that

$$\Psi_{tot} = w_s\left(\frac{\Psi_s}{\Psi_{s_1}}\right)^2 + w_d\left(\frac{\Psi_d}{\Psi_{d_1}}\right)^2 + w_\theta\left(\frac{\Psi_\theta}{\Psi_{\theta_1}}\right)^2 + w_\ell\left(\frac{\Psi_\ell}{\Psi_{\ell_1}}\right)^2 \tag{3.15}$$

where Ψ_s is path shape error, Ψ_d is location error, Ψ_θ is orientation error, Ψ_ℓ is length error, w represents the weight-factors, and subscript 1 indicates the initial error value. The error calculations are normalized with respect to an initial design. The errors are scaled such that each error term of the initial design equals unity. The conceptual design approximates the desired characteristics, thus values of unity are reasonable for the initial design. Scaling the individual errors makes them insightful, have a similar magnitude, and makes weight-factors predominantly related to the importance of a characteristic. Further, squaring the individual errors penalizes designs that perform worse than the initial design quadratically, award designs that perform better, and avoids discontinuities due to the sign of each error term.

Path shape error

The path shape error is calculated as the integrated absolute difference between the PCV path and the desired trajectory.

$$\Psi_s = \int_0^1 |y(t) - y^*(t)| dt \tag{3.16}$$

where $y(t)$ is a function that captures the PCV path and $y^*(t)$ is a function that captures the desired PCV path. Both $y(t)$ and $y^*(t)$ should be determined from piecewise linear curves as described in section 3.2.2. The integral limits indicate that the integration is performed over a normalized length scale.

Figure 3.4 is a graphical clarification of the error between the shape of the blue and red path of fig. 3.5a. Figure 3.4a shows both step-functions, while the area of plot in fig. 3.4b represents the error.

Path location error

In most cases, rigid body translations of the mechanism can satisfy the PCV path location objective. Possible design space bounds can limit the range of rigid body translations. Equation (3.17) calculates the distance between the initial primary compliance vectors of the actual and reference PCV path. With this formulation, the framework can satisfy path location while respecting design space limits.

$$\Psi_d = \sqrt{(x_1 - {x_1}^*)^2 + (z_1 - {z_1}^*)^2} \tag{3.17}$$

(x_1, z_1) and (x_1^*, z_1^*) are the initial vertices on the PCV path and the target curve, respectively.

Path orientation error

Analogous to the location, design space bounds can prevent the path orientation objective from being satisfied with rigid body rotations. Equation (3.18) includes the orientation of the PCV path in the total objective. This equation calculates the difference in angle that the closing line segment, the dashed red line in fig. 3.2a, makes with the x-axis.

$$\Psi_\theta = \angle(v_m - v_1) - \angle(v_m^* - v_1^*) \tag{3.18}$$

Path length error.

Error in path length follows from comparing the arc-lengths of the closing line segment between the actual path and reference path.

$$\Psi_\ell = |v_m - v_1| - |v_m^* - v_1^*| \tag{3.19}$$

Path length is strongly related to the displacement of the point of interest and thus the applied boundary conditions and overall compliance. For example, if a load is applied to the POI, the path length could be matched by adapting the overall compliance.

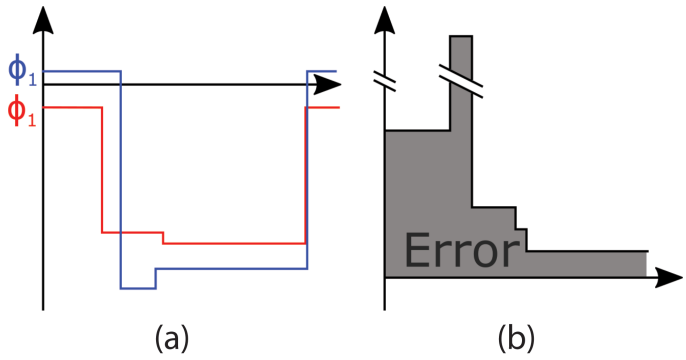

Figure 3.4.: The shape error (in gray) between the red and blue path

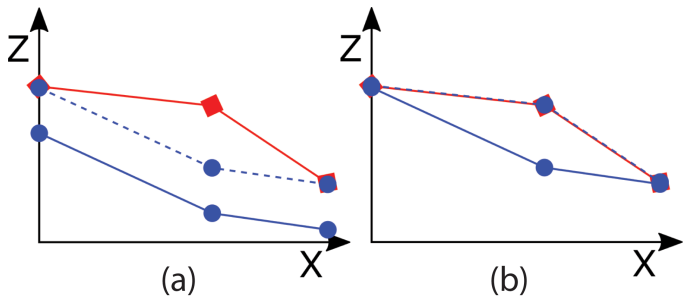

Figure 3.5.: The desired path in red, the actual path in blue, and the design variable effect in dashed blue

Error in path length may be mitigated by placing constraints on the minimum and/or maximum overall compliance, expressing the desired path length as a ratio of the POI displacement, or applying a displacement boundary condition.

3.3.3. Design Variables

Effective design variables are those that when changed impact desired behavior. Consider the three planar geometries shown in fig. 3.6. In this exercise, the PCV path for each is shown in blue. All geometries in fig. 3.6 share the same base and the same point of interest. When a moment is applied at the point of interest in the direction indicated in the figure, this point will rotate about the PCV.

Figure 3.6a shows a straight flexure with a constant cross-section. In fig. 3.6b the top of the flexure is thickened to a thickness t_2, the lower part still has a thickness of t_1. This change in geometry moves the location of the PCV path towards the base of the mechanism. This is logical since most deformation will occur there. The shape of the path is not severely affected.

In fig. 3.6c the curvature along flexure length alters the initial geometry. The flexure shape is produced by a spline that connects the base, the point (m,d) and

the point of interest (POI). These variables change the PCV path shape compared to fig. 3.6a , without appearing to have a significant impact on overall magnitude of compliance. These two examples highlight types of variables that change the behavior of the PCV.

In this paper, we consider mechanisms comprised of single isotropic materials, so the design variables are limited to the geometry of the mechanism. We consider both planar compliant mechanisms and spatial compliant shell mechanisms. As alluded above, the PCV path shape of planar mechanisms is driven largely by mechanism shape (e.g. curvature) and less so by thickness changes. Variables that may affect the PCV path in compliant shell mechanisms pertain more to the overall mechanism shape, rather than the local thicknesses. Thickness changes can be used to change the location of the PCV path (assuming that slender beams or thin shells remain so).

3.3.4. Solution Method

The selected solution method is the surrogate-based optimization algorithm in the Matlab Global Optimization Toolbox [22]. It is selected because of the earlier mentioned advantages. An additional advantage is the requirement of lower and upper bounds on the design variables. These bounds help to enforce a search-space for which the finite element model converges.

A penalty objective function implements constraints, because the surrogate-based optimization algorithm does not accept constraint equations, and because the number of FEM evaluations should be kept to a minimum. If statements enforce constraint violations. If a constraint is violated, the objective is set to a large value.

3.4. Design Examples

The design examples in this section give an indication of the use, outcome, and generality of the presented framework. We apply the framework to a straightforward flexure mechanism and a more complicated shell mechanism. First, we introduce a design case and a conceptual design. Second, we formulate the objective, followed by the parametrization and modelling of the mechanism. Finally, we present the outcome.

3.4.1. Curved Flexure Mechanism

Case

A rod needs support while maintaining a rotational degree of freedom, and during rotation, its center must displace horizontally, like a rod rolling on a table. Figure 3.7 illustrates the problem together with a conceptual solution. Dashed lines illustrate the deformed configuration.

The conceptual design connects a curved flexure mechanism (in gray) to the rod with a rigid element (in black). When the twist compliance vector of the flexure and the rotational axis are aligned properly, the flexure allows for the rotational degree of freedom. However, the PCV path (in red) requires design refinement to meet the horizontal displacement requirement.

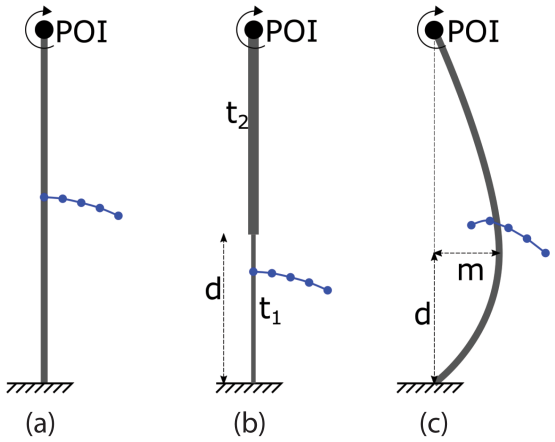

Figure 3.6.: Three flexure geometries with their PCV path in blue

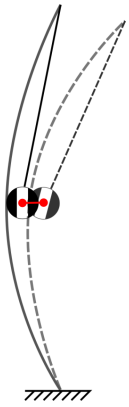

Figure 3.7.: Desired rod behavior supported by a curved flexure and a rigid element

Objective

The objective is a straight line PCV path such that $v_i^* = (0.001(i-1), 0)$ for $i = 1..11$. Location and orientation are not in the objective, because the design space allows for rigid-body transformations. These transformations can satisfy orientation and location objectives. Thus, a linear relation between the desired x and z components describes the desired PCV path. Furthermore, we will select design variables that have little effect on path length, making the initial and final location of the PCV arbitrary. Equation (3.15) presents the objective function. w_s is equal to unity, all other weight-factors are equal to zero, because the only objective to be met is related to path shape.

Parameterization.

Design variables as suggested in fig. 3.6c, curvature amplitude (m) and location of the maximum amplitude (d), are used to obtain a straight line PCV path. These variables are able to affect the shape of the PCV path, and they do not influence path length in a significant way. They affect path location and orientation, so rigid body transformations can overcome misalignment of location and orientation after optimizing mechanism shape.

Other parameters like dimensions, thickness, and material properties are presented in table 3.1 and kept constant.

Finite element modeling

Finite element modelling was performed in the ANSYS APDL environment. The geometry is defined by key-point locations, which are related to the design variables and calculated by Matlab. The key-points form an area, and shell (SHELL181) elements are used to mesh this area. Shell element were used with the assumption that the in-plane thickness remain small compared to the other dimensions and also so that the three dimensional stiffness matrix could captured.

Connecting all nodes that form the attachment edges with rigid (RIGID184) elements achieves rigidity of these respective edges. A pilot point is added to the middle of both edges, representing the fixed point and the POI. Loads and displacement constraints are applied to these points. The twist PCV over a large range of motion follows from applying a 0.25m torque on the top pilot point.

Auto-stepping in the ANSYS non-linear solver was used to solve the model. The global stiffness matrix was extracted from ANSYS at given loading intervals and then exported to Matlab. The optimization algorithm then calculates the PCV path and determine new values for the design variables. One of the benefits calculating the shape error (rather than the structural error) is that it is much more amenable to auto-stepping.

Results

Running a surrogate-based optimization as described in section 3.3.4, with 200 iterations and a search space as indicated by table 3.2, produces the optimized design in fig. 3.8a. The final curvature amplitude (m) equals: -0.019m; the final location of the maximum amplitude (d) is equal to 0.240m. This figure also gives insight into the performance of the optimized geometry. The PCV path (in blue) closely approaches the desired straight-line path shape. Figure 3.8b presents the perpendicular distance between the desired horizontal path and the actual PCV path. It shows that the maximum deviation is 0.1mm over a PCV path length of 12mm, and a POI rotation of 19.5° .

3.4.2. Scoliosis Brace Mechanism

Case

A passive scoliosis brace that provides corrective loads while retaining patient mobility could significantly increase scoliosis bracing treatment success [23]. The

Table 3.1.: Constant curved flexure parameters

Height	0.2	[m]
Width	0.1	[m]
Thickness	2	[mm]
Modulus	2	[GPa]
Poisson ratio	0.4	[1]

Table 3.2.: Search-space bounds

	Amplitude (m)	location (d)
lower-bound	-0.2	0.1 $height$
upper-bound	0.2	0.9 $height$

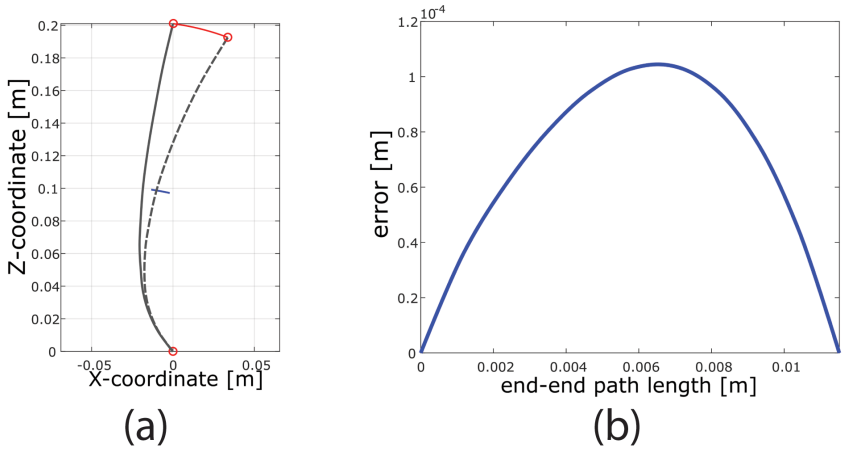

Figure 3.8.: Resulting PCV trajectory of the optimized curved flexure design

brace should permit sagittal bending while applying corrective load.

Figure 3.9a presents a conceptual design that has a single relative degree of freedom - the blue twist PCV in the sagittal bending direction. A torque actuation on the top of the mechanism (black arrow in fig. 3.9a) and fixation of the bottom (red area) introduces sagittal bending to the design. The extent to which sagittal bending is allowed and brace comfort depend on the alignment of mechanism PCV and the sagittal bending axis of the spine. Proper alignment during the entire motion prevents over-constraint and uncomfortable loads on the torso.

Objective

The optimization should refine the conceptual design into a detailed design that matches the location and trajectory of the desired sagittal bending axis. Dries measured the spinal movement of scoliosis patients and calculated twist axes for

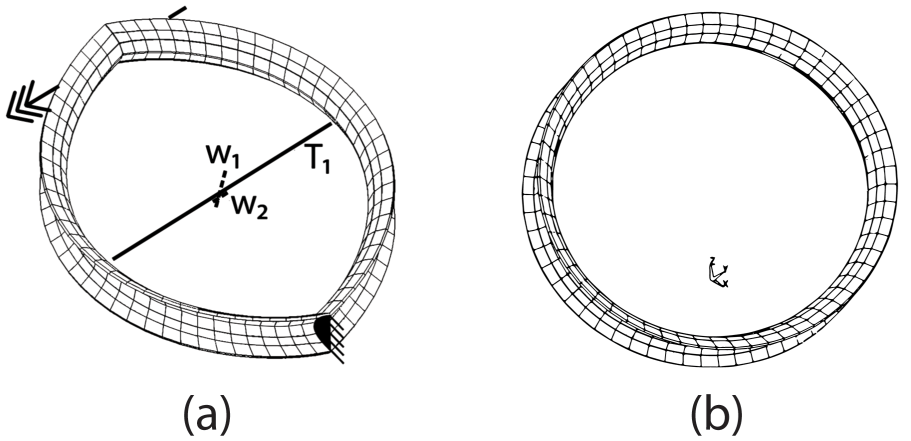

Figure 3.9.: (a) Conceptual design with the twist PCV (T_1) and secondary (w_1) and tertiary (w_2) compliance directions (b) Optimized design

sagittal bending between the pelvis and upper torso [24]. Table 3.3 presents the points on the target polygon curve. The axis is initially located at $x = 0.01$m and $z = 0.075$m in mechanism coordinates.

The path length is arbitrary because the design is parameterized in such a way that path length can be changed after optimization and the trajectory is close to a linear relation. Therefore, the path length error weight-factor is set to zero.

The extent to which rigid body transformations can be performed is limited because the mechanism has to circumscribe the torso. Therefore, the objective includes path orientation and location. The human spine can overcome deviations in path shape by engaging vertebrae to a different extent. Thus, path shape is rated less important than path orientation and path location. Weight-factors related to these characteristics are set to three. The path shape weight-factor is set to unity. Equation (3.15) presents the objective formulation.

Parameterization

The initial concept design to address this scoliosis brace problem is to combine two half-period sinusoidal helices as shown in fig. 3.9a. The geometry is captured with the following parameterization

$$x(u,v) = \left(0.088 + 0.055\left(1 - \cos\frac{5\pi}{3}v\right)\right)\cos u \tag{3.20}$$

$$y(u,v) = \left(0.11 + 0.055\left(1 - \cos\frac{5pi}{3}v\right)\right)\sin u \tag{3.21}$$

$$z(u,v) = p\ |u| - v \tag{3.22}$$

Where: x, y, and z are the respective coordinates. $-\pi \leq u \leq \pi$ represents the

Table 3.3.: Polygon data belonging to the sagittal bending axis

load-step	1	2	3	4	5	...
x^* $[m]$	0.010	0.013	0.016	0.019	0.022	...
z^* $[m]$	0.075	0.077	0.079	0.081	0.084	...
load-step	6	7	8	9	10	11
x^* $[m]$	0.025	0.028	0.031	0.034	0.037	0.040
z^* $[m]$	0.086	0.088	0.090	0.092	0.094	0.096

rotation in radians, $-0.015 \leq \ v \leq \ 0.015$ represents shell width in meters, and p is the pitch in meters per radian.

Table 3.4 presents material properties and thickness of the mechanism. t is a thickness variation that will be discussed later on.

To be able to satisfy the total objective function, design variables should affect path location, orientation, and shape. They should influence individual characteristics without worsening other characteristics, or be able to compensate secondary effects such as pitch.

Mechanism pitch strongly relates to mechanism shape. Pitch describes the inclination per rotation between the fixed point and the POI (see fig. 3.10). This makes it a good parameter for optimizing path shape. Pitch does not rotate the mechanism but it has an effect on the relative orientation of the red dots in fig. 3.10. It also affects path orientation and location.

To compensate secondary effects of pitch and meet the orientation objective, rotation around the Y-axis is the second design variable (β in fig. 3.10). It is formulated in such a way that the relative orientation of the pilot points is bounded by the combination of pitch and rotation. For example, a small pitch value allows for a large rotation value because these values leave enough room for a human torso between the red dots in fig. 3.10. To guarantee enough room for the patient's torso, the geometric equations include rotation in such a way that the horizontal distances remain constant. This parameterization does affect mechanism length, so path length could be affected. This design variable also affects path location.

A difference in thickness between the front and back half of the mechanism (t_1 and t_2 in fig. 3.10) shifts path location along the line connecting the attachment points. A final design variable that shifts the entire mechanism in the vertical direction (d in fig. 3.10) allows moving the path in 2 dimensions, in combination with the difference in thickness. Thus, it is possible to meet the path location objective.

The finite element model was directly meshed in the ANSYS APDL environment using SHELL181 elements. The elements were generated using the parametric equations of the shell in eq. (3.20) -eq. (3.22) using 6 elements across the sinusoidal cross section and 30 elements along the helical arc-length for each half of the mechanism. The model was discretized to use a small number of elements while also achieving sufficient accuracy.

The twist PCV over a large range of motion follows from applying a 0.75N m torque on the top pilot point.

Table 3.4.: Brace mechanism parameters

thickness	2±t	[mm]
E-modulus	2	[GPa]
Poisson's ratio	0.4	[1]

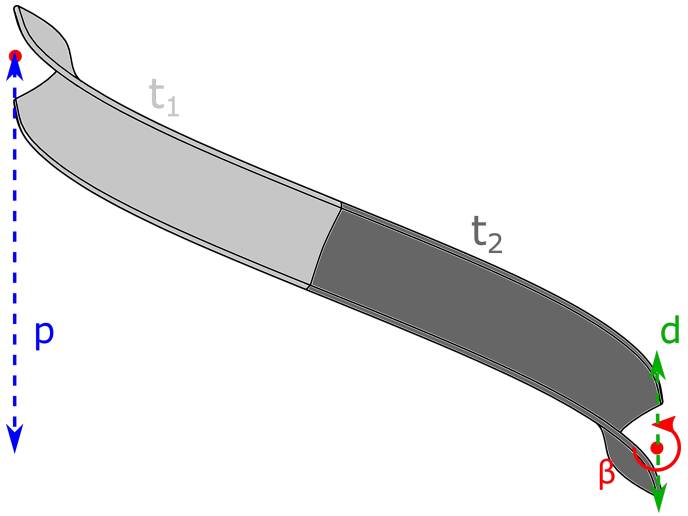

Figure 3.10.: Visualization of brace-mechanism design variables

Result

Running a surrogate-based optimization as described in section 3.3.4, with 398 iterations and a search space as indicated by table 3.5, produces the optimized design in fig. 3.9b. The purple half of the design has a thickness of 2.3mm, the cyan half has a thickness of 1.8m, mechanism pitch is 0.0076m rad^{-1}, rotation is 41°, and vertical shift is 0.0095m.

Table 3.5.: Search-space bounds

	Amplitude (m)	location (d)
lower-bound	-0.2	0.1 $height$
upper-bound	0.2	0.9 $height$

Figure 3.11 gives insight into the performance of the optimized geometry. The optimized PCV path (in red) closely approaches the desired PCV path, the blue arrow indicates the desired orientation and location. The black line indicates the initial PCV path. Figure 3.12 presents the perpendicular distance between the desired path and the actual PCV path. It shows that the maximum path deviation is 0.44mm with a POI rotation of 40.5°. The initial PCV location is off by 0.30mm, and the difference in orientation is 0.76°. The black line represents the PCV path of the conceptual

design. Furthermore, fig. 3.13 presents the unified compliance ratios. The relative compliance of w_1/T_1 reaches a maximum value near 0.2, this indicates that the mechanism is at least 5 times stiffer in all other directions compared to the PCV path.

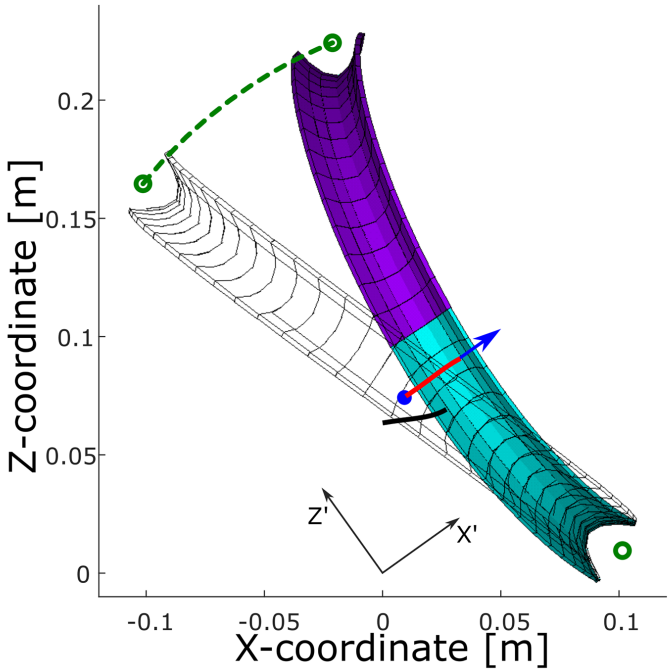

Figure 3.11.: Resulting PCV path in red under large deformation, desired orientation and location in blue, initial PCV path in black

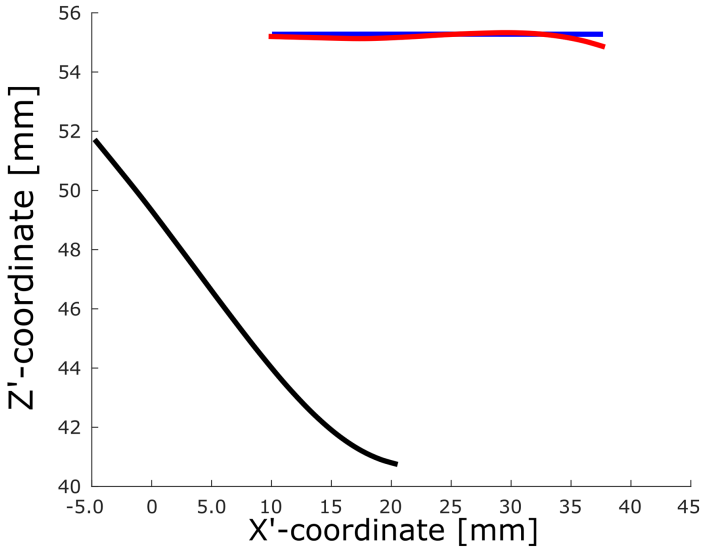

Figure 3.12.: Rotated close up of the desired (blue), actual PCV path (red), and PCV path of the initial design (black)

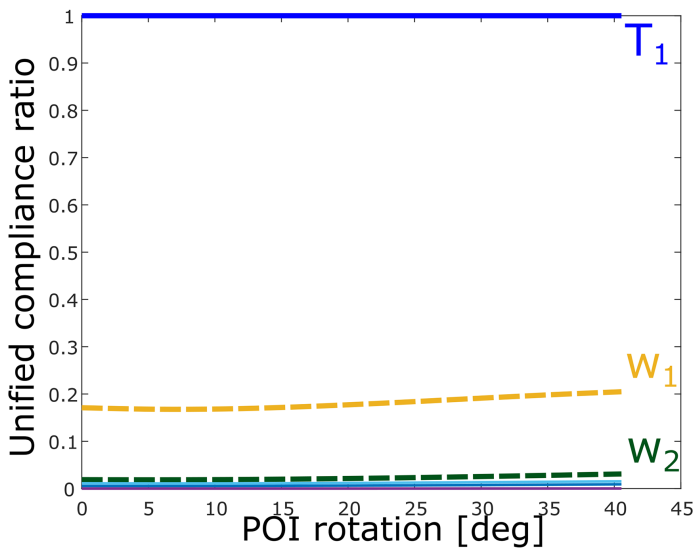

Figure 3.13.: Unified compliance ratios indicating the degrees of freedom

3.5. Discussion

3.5.1. Optimization Framework

In this paper, we have presented a framework for the design optimization of compliant mechanisms with respect to PCV path. Through the two examples in section 3.4, we demonstrated that the framework is capable of generating optimized geometries while separately accounting for PCV path shape, length, orientation, and position. In the examples, there is only marginal error between desired and actual PCV path as shown in fig. 3.8b and fig. 3.12. That the optimization resulted in good matching of the PCV path with very simple geometries is evidence that the formulation is well posed. Also, because of the use of the Fourier Descriptors, the optimization is not sensitive to the size of load steps taken by the non-linear FEA solver. This is significant, because this would not be possible with an objective based on structural error.

In this paper we only considered PCVs that remain aligned during deformation. If we relax this condition, the piece-wise linear curve might not be in a single plane. The objective formulations then need to capture the 3D nature of this curve. Furthermore, the piece-wise linear curves are no longer fully described by the step-function representation. A 3D rotation formalism needs to be used to capture the changing alignment of the PCV.

The PCV is determined from the tangent compliance (or stiffness) matrix. This tangent compliance matrix can be split into two matrices, the physical stiffness matrix and the geometric stiffness matrix [25].

$$\mathrm{C}_t^{-1} = \mathrm{K}_t = \int_V (\mathrm{B}^{\mathrm{T}}\mathrm{DB} + \mathrm{G})\, dV = \mathrm{K_p} + \mathrm{K_g} \tag{3.23}$$

where B is the differentiation matrix, D is the elasticity matrix which includes material properties, G is the geometric stiffness matrix, which when integrated over the volume is equal to K_g. Lastly, K_p is the physical stiffness matrix. The physical stiffness matrix, K_p, describes the initial un-deformed behavior, whereas the geometric matrix, K_g, is based on changing geometry and captures the geometrically non-linear behavior. Because the tangent compliance matrix contains all instantaneous kinematic characteristics of a compliant mechanism, design variables that influence the physical stiffness matrix have an effect on the location of the undeformed PCV. Affecting the path of the PCV (fig. 3.5b) is more challenging. Design variables must have an impact on K_g to influence the path of the PCV. Leemans suggests that changes in overall second moment of area and overall mechanism length in compliant shell mechanisms also impact the path of the PCV [9].

The primary contribution of this paper is the optimization for the PCV path in compliant mechanisms. Whereas in previous work [9, 10] only analyzed the behavior of the PCV path, this paper presents a systematic framework to optimize a design for an arbitrary desired PCV path. In research pertaining to topology optimization of path generating compliant mechanisms, output paths of resulting mechanisms are often sensitive to perturbation of loads at the output. This is because the optimization problem is posed with respect to the path of the mechanism under

prescribed loading. The PCV path, however, represents a trajectory with the lowest stored strain energy for a given displacement. By optimizing for the path of lowest strain energy, it is possible to design mechanisms that are preferentially compliant only in the desired motion directions.

In this paper the topologies of the mechanisms were pre-selected such that they were both single degree of freedom, while the optimization guided the selection of parameters to achieve the specified path. While topology synthesis is outside the scope of this paper, it is notable that the quality of the optimization results depends largely on the appropriate selection of the mechanism topology.

One of the principle challenges in the design of compliant mechanisms is to effectively exploit complex elasto-kinematic relationships to attain desired kinematic behavior. The presented framework deals directly with these elasto-kinematic relationships by relating kinematic behavior to the path of the PCV. The PCV is an intrinsic characteristic of a mechanism [9], so there is no ambiguity in the selection of loading (or boundary) conditions by following the PCV path. With the goal of a PCV path, designs that are susceptible to significant parasitic errors due perturbations of the end-load are more easily avoided.

3.5.2. Objective Formulation

The objective formulation presented in section 3.3.2 is distinct from the original Fourier Series Descriptors described by Zahn [15] and later implemented by Ullah [17] and Mankame [18] in that the shape of the target and designed curve is represented by step functions of angle changes parameterized by a normalized arc length, i.e. bend function. The key distinction in the presented work is that the error between the step functions is directly integrated to calculate error. Zahn suggests to represent the step functions as Fourier Series and subsequently to calculate the error of harmonic amplitudes and phase shifts. The fourier series serves to smooth target and actual slope function, although the best representation of the non-continuous step functions requires utilization of higher harmonics and ideally result in a nearly discontinuous function. Like the harmonic amplitude of the fourier descriptors, the bend function is independent of the size, orientation, and position of the curve. Utilizing the discrete bend functions in the objective formulation directly measures shape and was effective in optimizing for the PCV path as demonstrated in fig. 3.8 and fig. 3.11.

3.6. Conclusion

This paper introduced a framework to optimize the large deformation kinematic behavior of a compliant shell mechanism. We presented the PCV path to represent the lowest energy path of a mechanism trajectory. This is in contrast to formulations that prescribe loading without considering the PCV and may suffer from path deviation due to load perturbation. The bend function representation presented in this paper enabled comparison of open piecewise linear curves independent of location, scale, and orientation. Together the PCV path and bend function were

effectively implemented in an optimization framework that resulted in mechanism designs that with minimal path deviation.

3.7. Author Contributions

H.K. and C.J.K. proposed the research. H.K. designed the research and did the analyses and wrote the paper. C.J.K., W.W.P.J.S. and J.L.H. supervised the project and reviewed the paper.

Bibliography

[1] H. Kooistra, C. J. Kim, W. W. P. J. van de Sande, and J. L. Herder. “Shape optimization framework for the path of the primary compliance vector in compliant mechanisms”. In: *Journal of Mechanisms and Robotics* 12.6 (2020).

[2] L.L. Howell. *Compliant Mechanisms*. New York: Wiley, 2001.

[3] B. P. Trease, Y.-M. Moon, and S. Kota. “Design of Large-Displacement Compliant Joints”. In: *Journal of Mechanical Design* 127.4 (Nov. 2004), pp. 788–798.

[4] A. K. Rai, A. Saxena, and N. D. Mankame. “Unified synthesis of compact planar path-generating linkages with rigid and deformable members”. In: *Structural and Multidisciplinary Optimization* 41 (2010), pp. 863–879.

[5] B. Zhu, X. Zhang, H. Zhang, J. Liang, H. Zang, H. Li, and R. Wang. “Design of compliant mechanisms using continuum topology optimization: A review”. In: *Mechanism and Machine Theory* 143 (2020), p. 103622.

[6] N. Wang and K. Tai. “Design of grip-and-move manipulators using symmetric path generating compliant mechanisms”. In: *Journal of Mechanical Design* 139.11 (Sept. 2008), p. 112305.

[7] C. B. Pedersen, T. Buhl, and O. Sigmund. “Topology synthesis of large-displacement compliant mechanisms”. In: *International Journal for numerical methods in engineering* 50.12 (2001), pp. 2683–2705.

[8] H. Lipkin and T. Patterson. “Geometrical properties of modelled robot elasticity: part I - Decomposition”. In: *ASME Design Tech. Conf. and Computers in Engineering Conf.* Vol. 45. 1992, pp. 179–185.

[9] J. R. Leemans, C. J. Kim, W. W. P. J. van de Sande, and J. L. Herder. “Unified Stiffness Characterization of Nonlinear Compliant Shell Mechanisms”. In: *Journal of Mechanisms and Robotics* 11.1 (2019).

[10] W. W. P. J. van de Sande and J. L. Herder. “Analysis of parasitic motion in compliant mechanisms using eigenwrenches and eigentwists”. In: *International Design Engineering Technical Conferences and Computers and Information in Engineering Conference*. Quebec City, Canada, Aug. 2018.

[11] M. Farshad. *Design and analysis of shell structures*. Vol. 16. New York: Springer Science & Business Media., 2013.

[12] K. A. Seffen. “Compliant shell mechanisms”. In: *Philosophical Transactions of the Royal Society A: Mathematical, Physical and Engineering Sciences* 370.1965 (2012). 2010, pp. 2010–2026.

[13] G. Radaelli and J. Herder. “Gravity balanced compliant shell mechanisms”. In: *International Journal of Solids and Structures* 118-119 (2017), pp. 78–88.

[14] L. L. Howell, S. P. Magleby, and B. M. Olsen, eds. *Handbook of Compliant Mechanisms*. New Delhi, India: John Wiley & Sons Ltd., 2013, p. 342.

[15] C. T. Zahn and R. Z. Roskies. “Fourier Descriptors for Plane Closed Curves”. In: *IEEE Transactions on Computers* C-21.3 (1972), pp. 269–281.

[16] J. M. Selig. *Geometric Fundamentals of Robotics (Monographs in Computer Science)*. SpringerVerlag, 2004.

[17] I. Ullah and S. Kota. “Optimal Synthesis of Mechanisms for Path Generation Using Fourier Descriptors and Global Search Methods”. In: *Journal of Mechanical Design* 119.4 (Dec. 1997), pp. 504–510.

[18] N. D. Mankame and G. K. Ananthasuresh. “Synthesis of contact-aided compliant mechanisms for non-smooth path generation”. In: *International Journal for Numerical Methods in Engineering* 69.12 (2007), pp. 2564–2605.

[19] A. I. Forrester and A. J. Keane. “Recent advances in surrogate-based optimization”. In: *Progress in Aerospace Sciences* 45.1 (2009), pp. 50–79.

[20] S. Koziel, D. E. Ciaurri, and L. Leifsson. “Surrogate-Based Methods”. In: *Computational Optimization, Methods and Algorithms*. Ed. by S. Koziel and X.-S. Yang. Berlin, Heidelberg: Springer Berlin Heidelberg, 2011, pp. 33–59.

[21] H.-M. Gutmann. “A radial basis function method for global optimization”. In: *Journal of global optimization* 19.3 (2001), pp. 201–227.

[22] MathWorks. *Global Optimization Toolbox User’s Guide*. English. MathWorks. 2018.

[23] D. Rolton, C. Nnadi, and J. Fairbank. “Scoliosis: a review”. In: *Paediatrics and child health* 24.5 (2014), pp. 197–203.

[24] T. Dries. “A biomechanical characterization of spinal motion data for the design of a compliant scoliosis brace”. English. MA thesis. 2018.

[25] J. Nijssen. “A Type Synthesis Approach to Compliant Shell Mechanisms”. English. MA thesis. 2017.

4

Kinetic analysis of spatial compliant mechanisms using eigenscrew decomposition

Werner W.P.J. van de Sande, Just L.Herder

Parasitic motions and loads are unwanted behaviour accompanying the desired behaviour in compliant mechanisms. These parasitic motions often cannot be avoided in compliant mechanisms, but usually are to be kept at a minimum. The instantaneous kinematic characteristics of a compliant mechanism are encoded in the stiffness matrix. An eigenscrew decomposition will help visualize these kinematics as principal screws. These lines are called eigenwrenches and eigentwists. Any wrench or twist that is not an eigenwrench or -twist will lead to parasitic motion. This article introduces two parasitic motion metrics using eigenscrew decomposition: axis misalignment and axis drift. Axis drift is the amount of translation or moment accompanying the desired rotation or force respectively. Axis misalignment expresses the misalignment between a desired degree of freedom with the actual freedom space. These metrics are applied to two spatial compliant mechanisms to showcase their usefulness, namely a tip-tilt-piston platform and a tape spring.

This chapter is submitted to *Precision Engineering* as: W.W.P.J. van de Sande and J.L. Herder.,"Kinetic analysis of spatial compliant mechanisms using eigenscrew decomposition".

Introduction

Compliant mechanisms obtain their motion from the elastic deformation of their material. The benefits of compliant mechanisms are numerous. Their lack of play and hysteresis ensures deterministic system behaviour [1]. This makes them useful in applications where precision and repeatability are important. They also have some drawbacks, such as limited range of motion and inherent parasitic motion [2].

Parasitic motions and loads are the unwanted behaviour accompanying the desired behaviour. Part of this is due to the elastic deformation of the flexures; another part is due to the topology of the mechanisms. An example of this parasitic motion is the so-called shortening effect in a parallel leaf spring guidance [3]. As the coupler link translates in the desired direction it also moves laterally. This parasitic motion arises from the topology of the mechanism, which is based on a parallelogram type four-bar linkage. Additionally, as the leaf spring guidance moves, the coupler link also rotates [4, 5]. This parasitic motion is due to the elastic deformation of the flexures and is therefore not present in pseudo rigid body models [6]. The parasitic rotation can be eliminated when the force is applied at the proper location, i.e. the centre of compliance halfway along the length of the flexures [3]. Both the parasitic translation and rotation are considered undesired responses to a specific load and are characteristic of the parallel leaf spring guidance.

Another example is the axis drift or centre shift in cross-flexure joints. These types of mechanisms are intended to act as revolute joints. However, during rotation the axis of rotation moves, limiting their use as high precision joints. This centre shift has been already analysed in depth in literature [7, 8]. In these works it is used as a metric for the change in location of the rotational axis of the flexural pivot. Lobontiu et al. [9] have done similar work on notch hinges which also are intended to act as revolute joints. Lai et al. [10] have introduced a method using screw theory to model the rotational precision of compliant revolute/spherical joints in 3D.

Most methods of classifying parasitic motion are only valid for a single type of mechanism and are often only valid in the planar case. Some examples exist that introduce a more comprehensive method for all types of mechanisms. Patil et al.[11] introduce a method that treats flexure joints as screw vectors with scalar compliance parameters connected to these vectors to represent their compliance. They use this simplified model of the compliance of a mechanism to investigate the effects of geometric errors. Li et al.[12] introduce a method to minimize parasitic motion by decomposing the mechanism in its rigid and compliant parts. The mechanism is then reconfigured, given some constraints, to minimize the parasitic motion. In both cases simplifications of the mechanism are made in order to analyse them or apply the proposed method.

We observe that end-effectors of compliant mechanisms without any parasitic motion have decoupled motion; meaning that a load (force or moment, respectively) in one direction leads to motion (translation or rotation, respectively) in the direction of the load only, in other words, parasitic motion is not present. This behaviour is easily represented by a diagonal compliance matrix. Generally, the compliance matrix of a compliant mechanism may have non-zero off-diagonal terms, in which case a force or moment in one direction leads to motion in multiple directions.

For non-diagonal compliance matrices, the compliance (or stiffness) matrix can be decomposed in its principle screws of potential [13]. These eigenscrews come in two variants: eigenwrenches and eigentwists. Eigenwrenches describe a combination of a force and a moment and induce a parallel translation; eigentwists describe a combination of a translation and a rotation and induce a parallel moment. In addition, the decomposition yields eigenstiffnesses, which are the stiffnesses of these eigenscrews.

As such, we can use the full rank 6-by-6 compliance or stiffness matrix of any mechanism or structure in a given pose to analyse parasitic motions and loads in three dimensions. Any load or motion can be described as a screw. When an applied load is an eigenwrench, the response will be a translation parallel to the eigenwrench and there will be no parasitic motion. Similarly, if an applied motion is an eigentwist, the response will be a moment parallel to the eigentwist and there will be no parasitic loads. Conversely, when a screw is not a eigenscrew, there will be parasitic motions or loads.

In this article we demonstrate how the eigenscrew-decomposition can be used to analyse the behaviour of a compliant mechanism under specific loads or motions. As the decomposition is based on the 6 by 6 compliance matrix, behaviour can be analysed in three dimensions. Another benefit is that all compliant mechanisms can be analysed by the same method. We introduce two metrics than can be used to analyse any compliant mechanism at any relevant pose. The metrics are all based on the property that any screw (load or motion) can be expressed as a linear combination of eigenscrews. This linear combination is unique for each screw. By extension, this also allows the use of the metrics on any kind of elastic structure, such as compliant shell mechanisms. Compliant shell mechanisms are spatially curved thin-walled structures that are capable of transferring motion and loads through elastic deformation [14]. As these mechanisms often have complex spatial and non-intuitive behaviour, the eigen-decomposition and the associated metrics could be crucial to understand those mechanisms.

The article first presents the relevant fundamentals of screw theory and state-of-the-art of the eigenscrew-decomposition. These fundamentals are then used to develop metrics to evaluate the parasitic behaviour present in compliant mechanisms. The metrics are illustrated with the help of two examples: a tip-tilt-piston platform and a folded tape spring, which is a type of shell mechanism. The article ends with an discussion and conclusion on the usability and limitations the metrics and of the benefit of using eigenscrews for parasitic motion analysis.

Fundamentals

In this section we discuss the fundamentals and state-of-the-art of the eigenscrew-decomposition. Since the decomposition yields screws, wrenches and twists are introduced first. Afterwards we look at the decomposition and related concepts.

A compliance matrix maps loads to displacements; the stiffness matrix does the reverse. The loads or wrenches are expressed in Plücker coordinates [15].

$$W = \{f \quad | \quad m\}^T = \{f \quad | \quad r_W \times f + h_W f\}^T \tag{4.1}$$

The force f makes up the upper half and the moment m the lower half of the wrench W in eq. (4.1). The moment has a term that is perpendicular to the direction of the force f and is equal to the cross product of the force and the location vector r_W. The other term is parallel to the force and influenced by the scalar pitch h_W.

Displacement or twists T are screws where the translation δ makes up the upper half and the rotation ρ the lower half.

$$T = \{\delta \quad | \quad \rho\}^T = \{r_T \times \rho + h_T \rho \quad | \quad \rho\}^T \tag{4.2}$$

Like the moment in a wrench, the translation δ also has two terms. One term is perpendicular to the direction of the rotation ρ and is the product of the rotation and the location vector r_T. The second term is parallel to the rotation and influenced by the scalar pitch h_T. Note that the location dependent part of the twist is in the upper half, whereas it is in the lower half for the wrench.

The pitch of a screw can be determined by the dot product of the upper half and bottom half. So for a wrench and twist the pitch (h_W and h_T respectively) can be determined as follows [15].

$$h_W = \frac{f \cdot m}{f \cdot f} \; ; \; h_T = \frac{\rho \cdot \delta}{\rho \cdot \rho} \tag{4.3}$$

The location of a screw can be determined by using the cross product. The location vectors (r_W and r_T respectively) for a wrench and a twist are determined as follows:

$$r_W = \frac{f \times m}{f \cdot f} \; ; \; r_T = \frac{\rho \times \delta}{\rho \cdot \rho} \tag{4.4}$$

In general, the magnitude of a wrench is defined as the magnitude of the force component and the magnitude of a twist is defined as the magnitude of the rotational component. In the cases where only a pure moment or translation exists, i.e. when the force and rotational components are zero, the magnitude of the moment and the translation are used for the magnitude of the wrench and twists respectively [13].

The centre of compliance is the point P in a compliant mechanism where a load applied at that location yields a motion in the same direction [3]. In a coordinate system that has that point P as the origin, this will yield a diagonal compliance matrix for the compliant mechanism.

More generally, Lipkin and Patterson developed the eigenscrew-decomposition of a stiffness or compliance matrix to describe the stiffness properties of a robot [13]. It is a decomposition of a single stiffness matrix, so the resulting eigenscrews and eigenstiffnesses only describe the behaviour of the end-effector at single pose of the mechanism. The decomposition shows that a full rank compliance or stiffness matrix always has six uncoupled load-displacement relations. The result is two 3-systems: a system of forces and parallel translations and a system of rotations and parallel

moments. The centre of compliance exists in the unique case when the 3-systems are co-located and aligned. Ciblak and Lipkin have defined several other unique cases where one or more eigenscrews align or intersect [16].

A 6×6 stiffness matrix, $\mathbf{K}$, and its inverse, $\mathbf{C}$, can be decomposed by solving two eigenvalue problems [13], which are defined as:

$$\mathbf{k}_{\hat{\mathbf{W}}}\hat{\mathbf{W}} = \mathbf{K}\Gamma\hat{\mathbf{W}} \tag{4.5}$$

$$\mathbf{c}_{\hat{\mathbf{T}}}\hat{\mathbf{T}} = \mathbf{C}\Delta\hat{\mathbf{T}} \tag{4.6}$$

where

$$\Gamma = \begin{bmatrix} I & 0 \\ 0 & 0 \end{bmatrix}, \Delta = \begin{bmatrix} 0 & 0 \\ 0 & I \end{bmatrix} \tag{4.7}$$

and $\hat{\mathbf{W}}$ are eigenwrenches, $\mathbf{k}_{\hat{\mathbf{W}}}$ are the corresponding eigenstiffnesses, $\hat{\mathbf{T}}$ are eigentwists and $\mathbf{c}_{\hat{\mathbf{T}}}$ are the corresponding eigencompliances.

Since the matrices $\mathbf{K}\Gamma$ and $\mathbf{C}\Delta$ are of rank 3, the stiffness matrix yields 3 eigenwrenches and 3 eigenstiffnesses and the compliance matrix yields 3 eigentwists and 3 eigencompliances. These eigenwrenches $\hat{W}_i$ induce pure and parallel translations $\check{T}_i$ and the eigentwists $\hat{T}_i$ induce pure and parallel moments $\check{W}_i$.

The eigenbasis of wrenches ($\bar{\mathbf{W}}$ in eq. (4.8)) is defined as the combination of eigenwrenches $\hat{\mathbf{W}}$ and induced moments/wrenches $\check{\mathbf{W}}$. Similarly the eigenbasis of twists ($\bar{\mathbf{T}}$) is defined as the combination of induced translations/twists $\check{\mathbf{T}}$ and eigentwists $\hat{\mathbf{T}}$, as follows:

$$\bar{\mathbf{W}} = \begin{bmatrix} \hat{\mathbf{W}} & \check{\mathbf{W}} \end{bmatrix}, \bar{\mathbf{T}} = \begin{bmatrix} \hat{\mathbf{T}} & \check{\mathbf{T}} \end{bmatrix} \tag{4.8}$$

The complete system of stiffness multipliers is defined as a diagonal matrix composed of the translational eigenstiffnesses ($\mathbf{k}_{\hat{\mathbf{W}}}$) and the inverse of the rotational eigencompliances $\mathbf{c}_{\hat{\mathbf{T}}}$. The complete system of compliance multipliers is the inverse of this.

$$\mathbf{k} = \begin{bmatrix} \mathbf{k}_{\hat{\mathbf{W}}} & \mathbf{0} \\ \mathbf{0} & \mathbf{c}_{\hat{\mathbf{T}}}{}^{-1} \end{bmatrix}, \mathbf{c} = \begin{bmatrix} \mathbf{k}_{\hat{\mathbf{W}}}{}^{-1} & \mathbf{0} \\ \mathbf{0} & \mathbf{c}_{\hat{\mathbf{T}}} \end{bmatrix} \tag{4.9}$$

The elements of the decomposition compose the stiffness and compliance matrices as follows.

$$\mathbf{K} = \bar{\mathbf{W}}\mathbf{k}\bar{\mathbf{W}}^T, \mathbf{C} = \bar{\mathbf{T}}\mathbf{c}\bar{\mathbf{T}}^T \tag{4.10}$$

The eigenbasis of wrenches can be divided into four sub-matrices.

$$\bar{\mathbf{W}} = \begin{bmatrix} \hat{\mathbf{W}} & \check{\mathbf{W}} \end{bmatrix} = \begin{bmatrix} \mathbf{W_A} & \mathbf{0} \\ \mathbf{W_B} & \mathbf{W_D} \end{bmatrix} \tag{4.11}$$

The eigenwrenches $\hat{\mathbf{W}}$ consists of force part $\mathbf{W_A}$ and a moment part $\mathbf{W_B}$. The induced wrenches $\check{\mathbf{W}}$ consists of pure moments, $\mathbf{W_D}$, only ; therefore the force part is zero.

Simarly, the eigentwists $\hat{\mathbf{T}}$ consists of a rotation part $\mathbf{T_D}$ and a translation part $\mathbf{T_B}$. The induced twists $\check{\mathbf{T}}$ consists of translations, $\mathbf{T_A}$, only.

$$\bar{\mathbf{T}} = \begin{bmatrix} \hat{\mathbf{T}} & \check{\mathbf{T}} \end{bmatrix} = \begin{bmatrix} \mathbf{T_A} & \mathbf{T_B} \\ \mathbf{0} & \mathbf{T_D} \end{bmatrix} \tag{4.12}$$

The matrices $\mathbf{T_D}$ and $\mathbf{T_A}$ are the directions of eigentwists and induced twists respectively. These matrices are orthonormal and form a rotation matrix. Since the eigentwists and induced twists are parallel to the induced wrenches and eigenwrenches respectively, the following equalities hold:

$$\mathbf{T_A} = \mathbf{W_A}, \mathbf{T_D} = \mathbf{W_D} \tag{4.13}$$

The matrix $\mathbf{W_B}$ contains the pitches and locations of the eigenwrenches. After the decomposition, this matrix is expressed in the global coordinate frame. When it is expressed in the orientation frame of the eigenwrenches, i.e. transformed by the matrix ${\mathbf{W_A}}^T$, the matrix looks as follows.

$${}^{\mathbf{W_A}}\mathbf{W_B} = {\mathbf{W_A}}^T\mathbf{W_B} = \begin{bmatrix} h_{\hat{W}_1} & -r_{\hat{W}_{2z}} & r_{\hat{W}_{3y}} \\ r_{\hat{W}_{1z}} & h_{\hat{W}_2} & -r_{\hat{W}_{3x}} \\ -r_{\hat{W}_{1y}} & r_{\hat{W}_{2x}} & h_{\hat{W}_3} \end{bmatrix} \tag{4.14}$$

In this matrix $h_{\hat{W}_1}$, $h_{\hat{W}_2}$ and $h_{\hat{W}_3}$ are the pitches of the eigenwrenches. The off-diagonal terms are the components of the location vectors. These terms are in the orientation frame of the eigenwrenches, $\mathbf{W}_A$, and therefore they have no component parallel to the eigenwrenches or

$$r_{\hat{W}_{1x}} = r_{\hat{W}_{2y}} = r_{\hat{W}_{3z}} = 0. \tag{4.15}$$

The same holds for the eigentwists and the matrix $\mathbf{T_B}$. Here, the structure of eq. (4.14) emerges after the matrix is expressed in the orientation frame of the eigentwists, i.e. transformed by the matrix ${\mathbf{T_D}}^T$.

The system of eigentwists and induced twists and the system of eigenwrenches and induced wrenches form a basis. As such, any twist or wrench respectively is a linear combination of these bases. The linear combination can be obtained using Gaussian elimination.

$$\begin{bmatrix} \hat{\mathbf{W}} & \check{\mathbf{W}} & | & W \end{bmatrix} \rightarrow \begin{bmatrix} \mathbf{I} & | & \begin{matrix} \lambda \\ \mu \end{matrix} \end{bmatrix} \tag{4.16}$$

$$\begin{bmatrix} \check{\mathbf{T}} & \hat{\mathbf{T}} & | & T \end{bmatrix} \rightarrow \begin{bmatrix} \mathbf{I} & | & \begin{matrix} \mu \\ \lambda \end{matrix} \end{bmatrix} \tag{4.17}$$

The linear combination can be interpreted as a screw in the eigenbasis coordinate system. The linear combination of the eigenscrews, λ, can be seen as the direction of the screw. The linear combination has a location; the parameter μ shifts the screw to the desired location and pitch; it does nothing to the direction of the screw.

Any twist can be expressed by the linear combination of elements of the eigenbasis of twists.

$$T = \begin{bmatrix} \check{\mathbf{T}} & \hat{\mathbf{T}} \end{bmatrix} \begin{bmatrix} \mu \\ \lambda \end{bmatrix} \tag{4.18}$$

The stiffness matrix maps the twist to the resulting wrench as follows

$$\begin{bmatrix} \check{\mathbf{T}} & \hat{\mathbf{T}} \end{bmatrix} \begin{bmatrix} \mu \\ \lambda \end{bmatrix} \xrightarrow{\mathbf{K}} \begin{bmatrix} \hat{\mathbf{W}} & \check{\mathbf{W}} \end{bmatrix} \mathbf{k} \begin{bmatrix} \mu \\ \lambda \end{bmatrix} \tag{4.19}$$

Likewise a wrench can be expressed by the eigenbasis of wrenches and the linear combination.

$$W = \begin{bmatrix} \hat{\mathbf{W}} & \check{\mathbf{W}} \end{bmatrix} \begin{bmatrix} \lambda \\ \mu \end{bmatrix} \tag{4.20}$$

The compliance matrix maps the twist to the resulting wrench as follows.

$$\begin{bmatrix} \hat{\mathbf{W}} & \check{\mathbf{W}} \end{bmatrix} \begin{bmatrix} \lambda \\ \mu \end{bmatrix} \xrightarrow{\mathbf{C}} \begin{bmatrix} \check{\mathbf{T}} & \hat{\mathbf{T}} \end{bmatrix} \mathbf{c} \begin{bmatrix} \lambda \\ \mu \end{bmatrix} \tag{4.21}$$

The induced screws have no location and can be seen as vectors instead of screws. A linear combination λ of eigenscrews will lead to the same linear combination of induced screws scaled by the eigenstiffness or -compliances.

$$\hat{\mathbf{T}}\lambda \xrightarrow{\mathbf{K}} \check{\mathbf{W}}\mathbf{k}_{\hat{\mathbf{T}}}\lambda, \quad \hat{\mathbf{W}}\lambda \xrightarrow{\mathbf{C}} \check{\mathbf{T}}\mathbf{c}_{\hat{\mathbf{W}}}\lambda \tag{4.22}$$

Visually this is represented as a unit sphere that is mapped to an ellipsoid [17]. The linear combination (λ) is a radial vector. This radial vector is then scaled when mapped to the ellipsoid which changes the length and the direction.

As there are two types of induced screws, there are only two ellipsoids. The stiffness ellipsoid (fig. 4.1) maps a linear combination of eigentwists to a moment; the semi-major axes of the ellipsoid are the lengths of the three rotational eigenstiffnesses, $k_{\hat{T}_i}$. The compliance ellipsoid (fig. 4.2) maps a linear combination of eigenwrenches to a translation; here the semi-major axes of the ellipsoid are the lengths of the three translational eigencompliances, $c_{\hat{W}_i}$.

The degrees of freedom and constraints in three dimensions of a mechanism add up to six. A full rank compliance or stiffness matrix of such a mechanism is also of rank 6. Therefore the six eigencompliances, $\mathbf{c}$, or the eigenstiffnesses, $\mathbf{k}$ can be used to ascertain the degrees of freedom and constraints of a mechanism. It can be used similar to modal analysis, where the eigencompliances are akin to the modal frequencies and the eigenscrews are akin to the modal shapes. The eigencompliances (or -stiffnesses) for the eigenwrenches and (or -twists) are sorted separately to ascertain the number of degrees of freedom for each 3-system. This can be done by inspecting the compliances and determine what the order of magnitude of the eigencompliances are.

The eigencompliances of the two 3-systems, $\mathbf{c}_{\hat{\mathbf{T}}}$ and $\mathbf{c}_{\hat{\mathbf{W}}} = \mathbf{k}_{\hat{\mathbf{W}}}{}^{-1}$, cannot be directly compared because they have different units. The unified stiffness characterization introduced by Leemans et al. [18] enables systematic and meaningful ordering of the

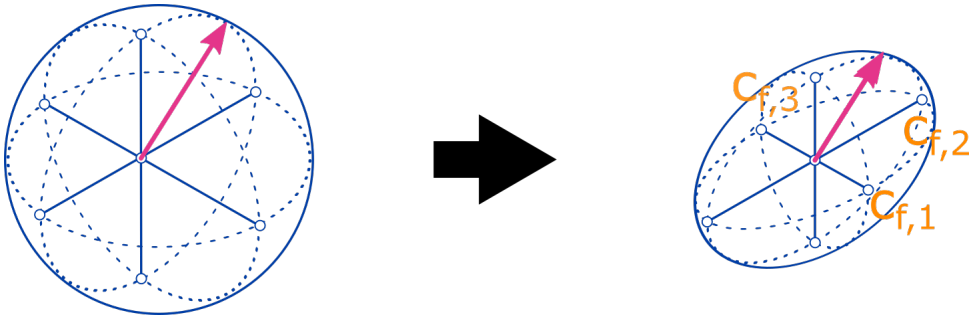

Figure 4.1.: Mapping of a linear combination of eigenwrenches to the corresponding linear combination of the induced twists; this linear combination is scaled by the eigencompliances. Visually a unit sphere is scaled to an ellipsoid.

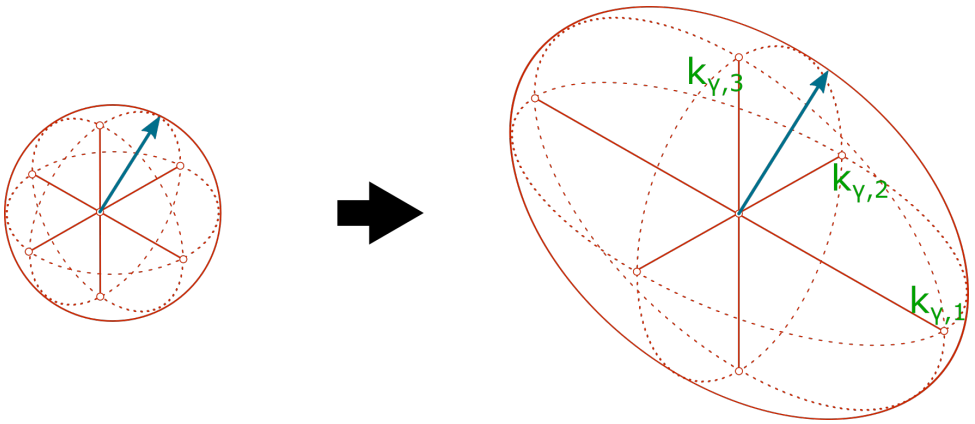

Figure 4.2.: Mapping of a linear combination of eigentwists to the corresponding linear combination of the induced wrenches; this linear combination is scaled by the eigenstiffnesses. Visually a unit circule is scaled to an ellipsoid.

rotational and translational compliances. The unification multiplier χ_i allows the rotational eigencompliances to be expressed as translational eigencompliances,

$$\tilde{c}_{\bar{\mathbf{W}}} = \begin{bmatrix} c_{\hat{W}_1} & c_{\hat{W}_2} & c_{\hat{W}_3} & \chi_1^2 c_{\hat{T}_1} & \chi_2^2 c_{\hat{T}_2} & \chi_3^2 c_{\hat{T}_3} \end{bmatrix} \tag{4.23}$$

where the unification multiplier, χ_i, is defined as follows.

$$\chi_i = \sqrt{h_i^2 + |r_i|^2} \tag{4.24}$$

Here h_i is the pitch of the i^{th} eigentwist, and r_i is the shortest distance from the point of interest of a mechanism to the line of an eigentwist. The pitch and/or

the distance to the end-effector will generally exist and are unique and non-trivial. However, problems arise when eigentwists pass through the end-effector and/or have no pitch. In this situation the compliance of that rotation becomes zero (infinitely stiff). This corresponds with the actual behaviour of the mechanism, but is not helpful in expressing rotational compliances as translational compliances. For those cases, Leemans et al.[18] provide the option to do the reverse: to express the translational compliances as rotational compliances. The reconciliation of units in eq. (4.23) is significant in that the relative compliance of the eigentwists and eigenwrenches can be directly compared. Lipkin showed that the eigentwists and eigenwrenches are invariant under coordinate transformation, and Leemans et al. showed that the unified characterization is also invariant.

Metrics

The eigenstiffness and eigenscrews can be used directly to analyse mechanism behaviour [19]. However, an eigenscrew alone does not show if it is a constraint or a degree of freedom and how it evolves over the range of motion. A screw that describes desired behaviour can be expressed by the linear combination of eigenscrews. This linear combination might change over the range of motion, which in turn changes the behaviour of that screw; e.g. a free screw can become a constrained screw. In this section we introduce two metrics that use the elements of the decomposition to obtain insight in the parasitic behaviour present in a compliant mechanism.

The difference between the actual revolute axis of a hinge mechanism and the desired one is often called axis drift [20]. This is equal to comparing a desired rotation twist with the eigentwist that is an actual degree of freedom of the system. In two dimensions this only involves an offset of the axis. In three dimensions the axes can also differ in orientation. Axis drift is thus made up out of two parts: axis misalignment, i.e. a difference in orientation, and actual axis drift, e.g. a difference in location.

Axis misalignment

A desired orientation of a degree of freedom (or a constraint) can be directly compared with the orientation of a actual degree of freedom (or constraint). The misalignment between the desired orientation and the eigentwist or -wrench can be obtained with their cross product as follows:

$$\varepsilon_T = \|\omega_{desired} \times \omega_{\hat{T}}\| \tag{4.25}$$

$$\varepsilon_W = \|f_{desired} \times f_{\hat{W}}\| \tag{4.26}$$

Here the axis misalignment, ϵ_T for a twist and ϵ_W for a wrench, is obtained from cross product of the direction of the twist, $\omega_{desired}$, and wrench, $f_{desired}$ under review with an eigentwist $\omega_{\hat{T}}$ or eigenwrench, $f_{\hat{W}}$, respectively.

The λ and μ vectors can also be used to compare two screws in three dimensions. When there is a clear delineation in the eigenstiffnesses, the λ vector can be subdivided between the freedom space and the constraint space.

$$\lambda = \lambda_{DoF} + \lambda_{constr} \tag{4.27}$$

Ideally, constraints have infinite stiffness and degrees of freedom have infinite compliance. In reality, this is never the case and the stiffness of constraints and degrees of freedoms are typically separated by several orders of magnitude at most. The eigenstiffness values help split the λ vector into a constraint part and a freedom part.

$$\lambda_{DoF} = \frac{\mathbf{c}\lambda}{c_{max}} \tag{4.28}$$

$$\lambda_{constraint} = \frac{\mathbf{k}\lambda}{k_{max}} \tag{4.29}$$

As constraints will have significantly higher stiffness, pre-multiplying the λ-vector with the eigenstiffnesses, $\mathbf{k}$, and dividing it by the highest eigenstiffness, k_{max}, will emphasise the part of the vector that is in the constraint space (see eq. (4.29)). The same holds for the degrees of freedom; however the λ-vector is scaled by the eigencompliances. When constraints have infinite stiffness and degrees of freedom have infinite compliance, eq. (7.4) and eq. (4.29) will add up to the λ vector. If there is a clear delineation between constraints and degrees of freedom, the summation will be close to the λ vector. When this is not so, λ_{DoF} and $\lambda_{constraint}$ will be almost equal and will not add up to λ.

Depending on the desired nature of the twist or wrench, either λ_{DOF} or λ_{constr} is of interest and can be compared to the entire λ-vector. The misalignment of two vectors is derived with the cross product. In the case of a desired DOF, the axis misalignment is defined as,

$$\varepsilon_{DOF} = \frac{\|\lambda_{DoF} \times \lambda\|}{\|\lambda_{DoF}\|} \tag{4.30}$$

whereas in the case of a desired constraint it is defined as follows:

$$\varepsilon_{constr} = \frac{\|\lambda_{constr} \times \lambda\|}{\|\lambda_{constr}\|} \tag{4.31}$$

The concept of axis misalignment can be illustrated by the example of a parallel leaf spring guidance; this mechanism is designed to provide a straight-line motion, see fig. 4.3. However, after some motion the end-effector starts to move in the z-direction as well as move in the desired x-direction. The intended straight line motion is described by the λ vector, whereas the λ_{DOF} vector describes the combined motion in the x- and z-directions. The misalignment of the desired λ vector with its sub-vector denotes how much the λ vector is in the desired space. Explicitly, increasing axis misalignment indicates increasing stiffness or compliance of the λ vector for a desired DoF or constraint, respectively. Conversely, increasing

axis misalignment can also indicate parasitic motions or loads with respect to the desired DoFs or constraints respectively. For instance, a motion will follow the path of least resistance and will not move into a constraint direction unless forced; since additional forces are required to force that motion. This will cause increased stiffness. When the motion is not forced, the mechanism moves within the DoF space only. The difference between the desired motion and the actual motion is the parasitic motion. For a constraint, the stiffness in the desired direction is reduced or the true constraint direction has changed.

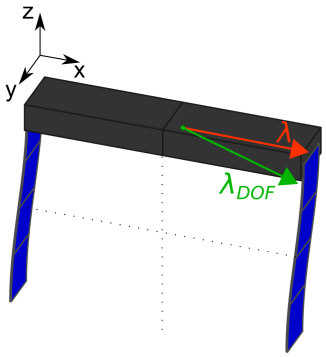

Figure 4.3.: A straight-line guidance: as the leaf springs deflect, the end-effector moves in positive x-direction (desired), but also in negative z-direction (parasitic).

Axis drift

Concurrently, the vector μ expresses how much a line of a twist or wrench is shifted from the linear combination of eigenscrews. When two screws are parallel, the difference in μ is the distance between the two screws. This is the same as axis drift of a compliant hinge in the planar case. Here the amount of axis drift denotes the amount of parasitic translation of an end-effector. When comparing two parallel screws, their μ vectors can be used to express their location with respect to each other.

When two screws are not parallel, the difference between two μ vectors is only an indication of the distance between the two screws. Mathematically, the vector μ defines the amount of induced screws in the linear combination. In other words, in that situation the screw is not a linear combination of eigenscrews, but a linear combination of eigenscrews and induced screws. For a twist this means that the resulting wrench will not be a pure moment; there will also be a parasitic force. For a applied wrench, the resulting twist will not be a pure translation and there will be a parasitic rotation. Therefore the vector μ is also a measure for parasitic motions or load.

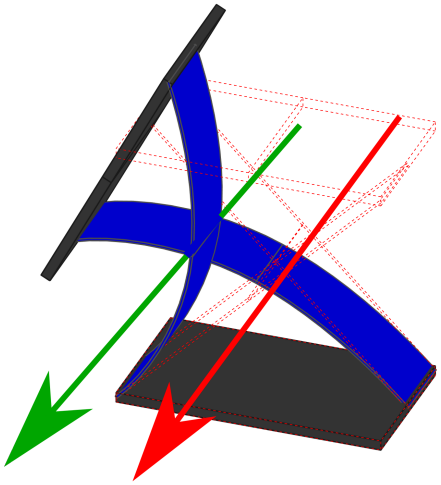

Figure 4.4.: A cross-flexure hinge: as the leaf springs deflect, the end-effector rotates, but also translates laterally.

Using the axis drift of a compliant cross-flexure hinge as an example, the vector μ denotes the amount of induced twists, i.e. translations, in the linear combination of the desired motion. The rotational degree of freedom is the the most compliant eigentwist. Axis drift can be analysed by comparing the most compliant eigentwist in the neutral position and the most compliant eigentwist in a deflected pose (red and green line in fig. 4.4 respectively). These poses have their own eigenbasis. However, when one eigentwist is expressed in the eigenbasis of the other, induced twists are needed. The presence of these induced twists in the linear combination indicates parasitic motion which in this case is a translation.

In this work axis drift is defined as the length of the μ vector.

$$\beta = \|\mu\| \tag{4.32}$$

Like with axis misalignment, axis drift can be explained in several ways. Any twist can be applied by a linear combination of eigentwists and induced twists. Forcing the twist adds additional stiffness terms. Leaving the location of the twist free, i.e. only the combination of eigentwists, but enforcing the direction, does not add stiffness terms; however, there will be parasitic translation with respect to the desired twist.

Induced wrenches are needed to be able to create any random wrench. When induced wrenches are present in the linear combination they add compliant terms which results in parasitic rotations. If no parasitic motion is wanted, μ has to be kept zero; this results in a pure translation. However, since no additional compliance terms are allowed, the stiffness is higher than when parasitic motion would be there. An overview of the effects of the μ vector for twists and wrenches is shown table 4.1.

Table 4.1.: Effects on twist and wrenches when a parasitic component is present

	parasitic component	no parasitic component
twist	parasitic translation	increased stiffness (forced twist location)
wrench	parasitic moment decreased stiffness (forced wrench location)	-

From the stiffness (eq. (4.19)) and compliance mapping (eq. (4.21)), it can be seen that a non-zero μ vector will always add stiffness or compliance terms to the response for a twist or wrench respectively. This is irrespective of whether the linear combination of eigenscrews is a DoF or a constraint. Simultaneously, the set of added induced screws can be mostly in the DoF or constraint space. As such, the effect of the added induced screws on the mechanism behaviour will differ. Therefore axis drift does not provide the same insight as axis misalignment when it comes to stiffness behaviour.

Example Tip-Tilt-Piston platform

The metrics are illustrated using a tip-tilt-piston platform. It is constructed by three wire flexures placed in the same plane, but their axial lines are not intersecting at the same point; this a plane of lines in FACT terminology [21] (see fig. 4.5). It allows for two in-plane rotations and an out-of-plane (z) translation.

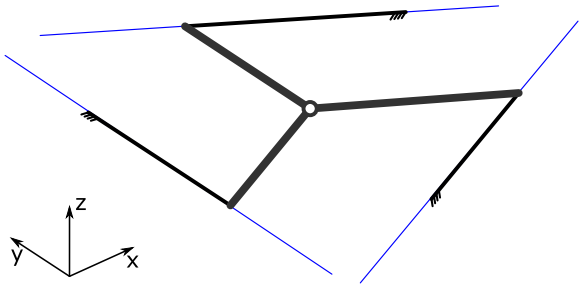

Figure 4.5.: A tip-tilt-piston platform with the FACT constraint lines highlighted in blue and the end-effector denoted by the white dot. The platform consists of three rigid links (thick black lines); the platform is connected to the ground through three wire flexures (thin black lines).

The specifications of the platform are listed in table 4.2. The mechanism is modelled in the SPACAR program [22]. The wire flexures are modelled with four beam elements each and the centre platform is modelled with three rigid beams. A moment of 5N m is applied in the y-direction in 100 steps; this causes the plaform to rotate about 20°.

As the platform moves, the wire flexures deflect, changing the behaviour of the mechanism. This change of behaviour is investigated by evaluating specific screws.

Table 4.2.: Specifications of the platform

	value	unit
length wire flexures	100	mm
width wire flexures	2	mm
height wire flexures	2	mm
radius platform	100	mm
Poisson's ratio wire flexures	0.3	-
Young's Modulus wire flexures	210	GPa

Four screws are evaluated; two wrenches of which one is a DoF and one is a constraint and two twists, again one DoF and one constraint. All screws under review pass through the centre of the platform; this location is defined as the end-effector. Its location changes when the platform moves and as a result the screws are updated. However, the orientation of the screws is maintained. In the neutral position the screws are as follows.

$$W_{DoF} = \{0 \quad 0 \quad 1 \quad 0 \quad 0 \quad 0\}^T \tag{4.33}$$

$$W_{constr} = \{1 \quad 0 \quad 0 \quad 0 \quad 0 \quad 0\}^T \tag{4.34}$$

These are a vertical out-of-plane force and an in-plane force respectively. The twists in Plücker co-screw coordinates are as follows.

$$T_{DoF} = \{0 \quad 0 \quad 0 \quad 0 \quad 1 \quad 0\}^T \tag{4.35}$$

$$T_{constr} = \{0 \quad 0 \quad 0 \quad 0 \quad 0 \quad 1\}^T \tag{4.36}$$

These are an in-plane rotation and a vertical rotation respectively. For all screws the eigenstiffnesses, the axis misalignment and the axis drift are evaluated to show the behaviour of that screw. The platform can rotate about the y-axis of the system (see fig. 4.7); this rotation is caused by a moment. In Plücker screw coordinates this moment is defined as follows.

$$W_2 = \{0 \quad 0 \quad 0 \quad 0 \quad 1 \quad 0\}^T \tag{4.37}$$

The platform is rotated 20° in total due to a moment applied in the x-direction. As the platform rotates the eigenwrenches and -twists also change. They start out coincident at the end-effector, see fig. 4.6. As the rotation increases, the two three-systems rotate, but not in the same manner as the platform itself. They are also no longer coincident, see fig. 4.7.
At an angle 20°, one eigenstiffness of the eigenwrench is only about 4% of the original stiffness in the neutral position (red line in upper graph of fig. 4.8).

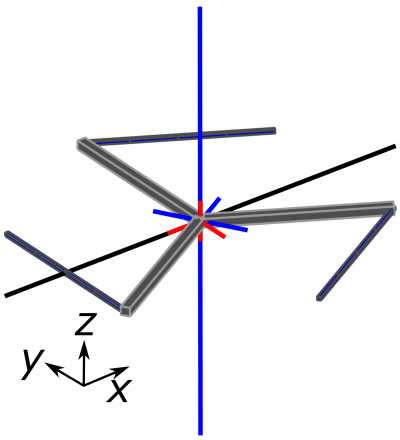

Figure 4.6.: System of eigenscrews in the neutral pose with the eigentwists in red and the eigenwrenches in blue

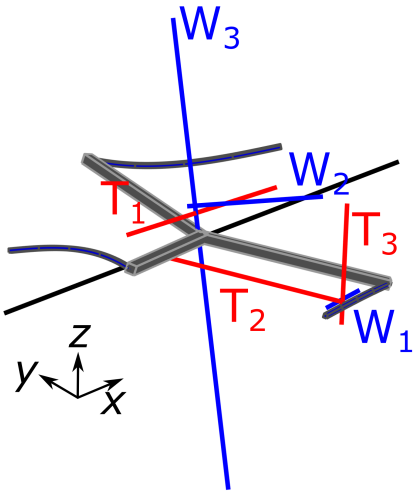

Figure 4.7.: System of eigenscrews in the deformed pose with the eigentwists in red and the eigenwrenches in blue, the eigenscrews are labeled for reference.

However, constraints and degrees of freedoms are still strongly separated. The eigenstiffness of the eigenwrench DoF (yellow line in upper graph of fig. 4.8) remains roughly constant. These eigenstiffness were obtained by decomposing the 6×6 stiffness matrix at every incremental step; the eigenvalues of those matrices are the eigenstiffnesses.

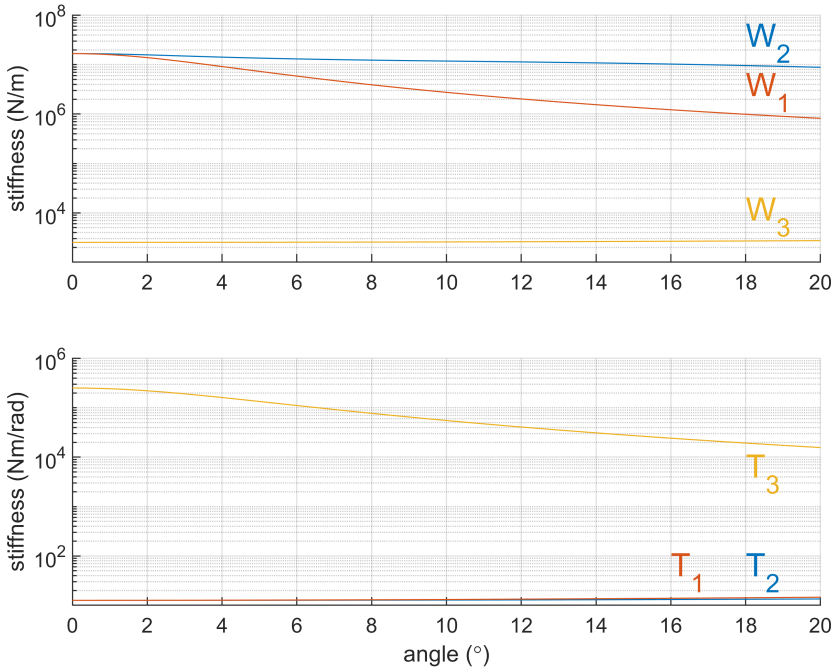

Figure 4.8.: Stiffness of all eigenwrenches and eigentwists during motion plotted on a semi-log scale. Colours denote direction of original/undeformed eigenscrews: red and blue are in the plane of the platform, yellow is in the vertical direction, the labels refer to the labels in fig. 4.7.

For the eigentwists, the eigenstiffnesses of the two DoFs (red and blue lines in lower graph of fig. 4.8) stays roughly similar in stiffness; the constraint (yellow line in lower graph of fig. 4.8) is only about 7% of the original stiffness. Again, the constraints and degree of freedom stay clearly separated.

The misalignment of the wrenches and twists can be seen in fig. 4.9 and fig. 4.10 respectively. The original screws become slightly less aligned with their corresponding eigenscrews; i.e. the desired DoF becomes less aligned with the free eigenscrews and the desired constraints become less aligned with the constrained eigenscrews. This result indicates increased stiffness for the original DoFs and decreased stiffness of the original constraints.

Checking both direct misalignment and the misalignment with the free-

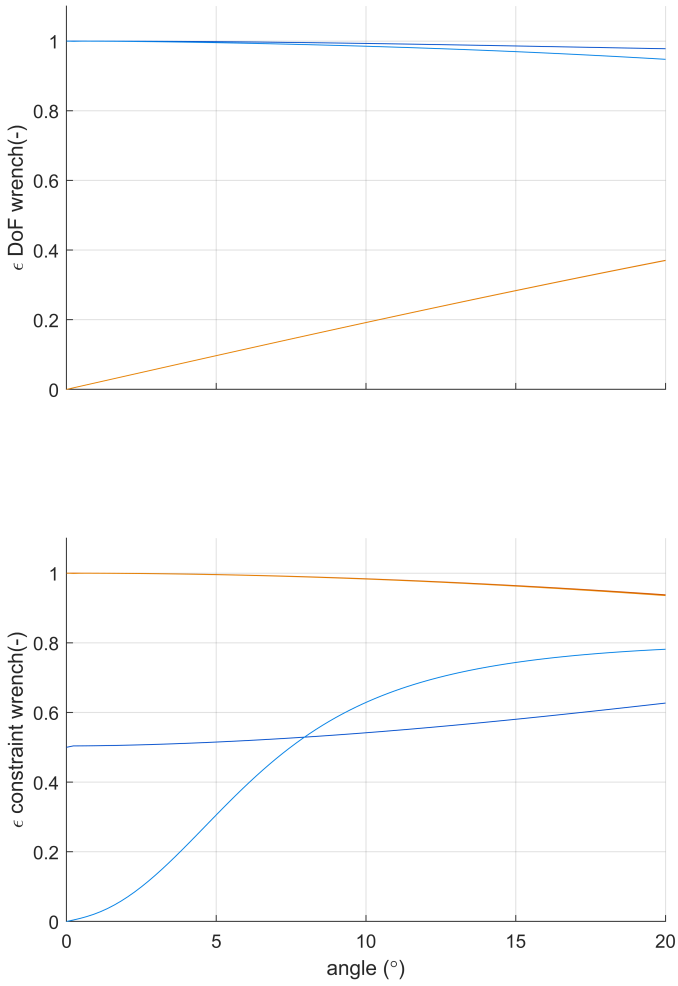

Figure 4.9.: The misalignment of the two wrenches under review between the freedom space (orange), between the constraint space (light blue) and the direct misalignment between an originally horizontal eigenwrench (dark blue) and the vertical eigenwrench (red); the misalignment with the freedom space and the free wrench completely overlap.

dom/constraint space works well for the free wrench and twist and for the constraint twist. However, the constraint misalignments of the constraint wrench appear different. This has two causes. First, the wrench under review is only in-plane

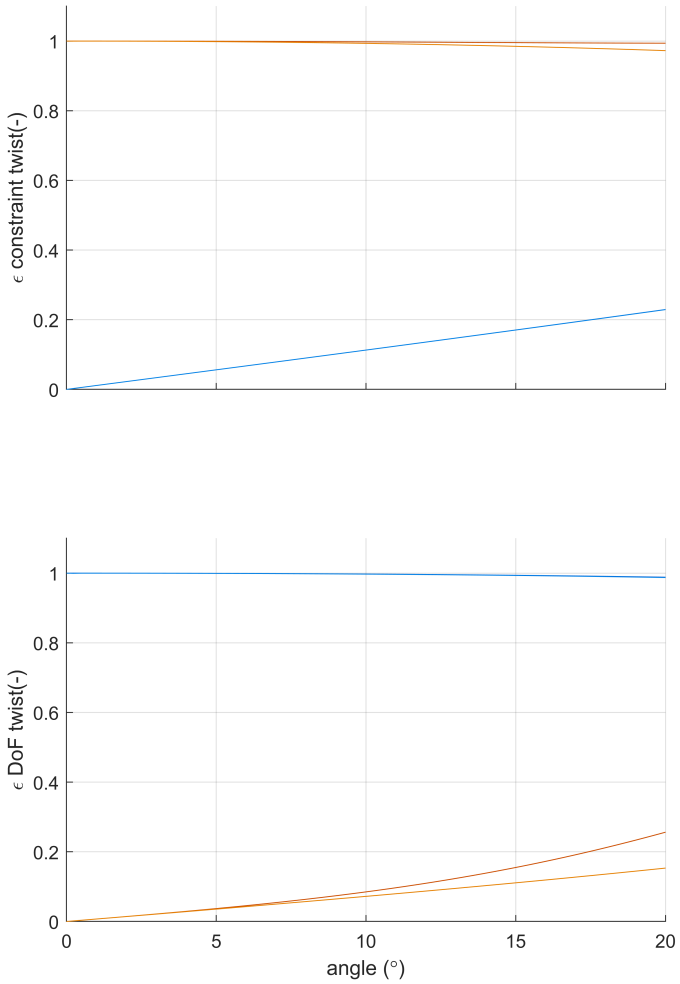

Figure 4.10.: The misalignment of the two twists under review between the freedom space (orange), between the constraint space (light blue) and the direct misalignment between an originally horizontal eigentwist (red) and the vertical eigentwist (dark blue); the misalignment with the constraint space and the constraint wrench completely overlap.

with the constraint eigenwrenches; it is not perfectly aligned with either of them. This results in a higher direct misalignment from the start (dark blue in bottom graph fig. 4.9). Second, as the wrench under investigation is a linear combination

of the two constraint eigenwrenches it also has a component of the eigenwrench that loses stiffness during the range of motion. Due to the scaling of the constraint misalignment metric this shows as a increased misalignment.

For both wrenches under review the misalignment with the freedom space and the free wrench completely overlap. This should be the case, as the freedom space of the wrenches only contains the free (vertical) wrench. Similarly, the misalignment with the constraint space and the vertical eigentwist overlap for the twists under review; again, this corresponds with the fact that the constraint space of the twists only contains the vertical twist.

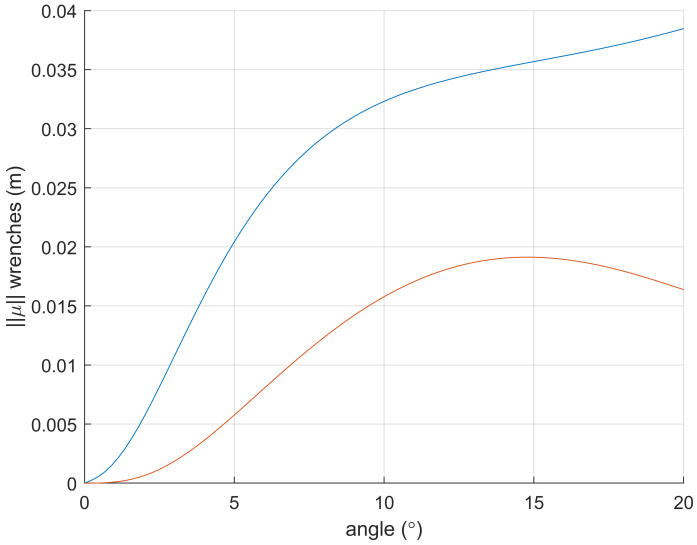

Figure 4.11.: Axis drift of the two wrenches under review, with the free wrench in red and the constraint wrench in blue

The axis drift of the wrenches and twists can be seen in fig. 4.11 and fig. 4.12 respectively. Most screws show a quick rise in axis drift but start to level off at 10°. This can be seen in fig. 4.7, where most of the eigenscrews have moved away from the center of the platform. In addition, the location of the flexures causes the platform to also rotate as it moves upward; this motion is like a screw motion, i.e. a screw with a pitch. The motion away from the centre and the pitches in the eigenscrew all cause parasitic motions and loads. The difference in axis drift is most apparent in the twists; the free twists have the lowest axis drift, whereas the constraint twist has the greatest axis drift of all screws. Again, this can be seen in fig. 4.7 where the vertical (constraint) eigentwist has moved away from the centre quite severely. The horizontal (free) eigentwists only have moved a little. The constraint wrench under investigation has quite some axis drift, since one of the constraint horizontal eigenwrenches has also moved away from the centre. The free wrench has lower axis drift, but still more than the location of the free eigenwrench

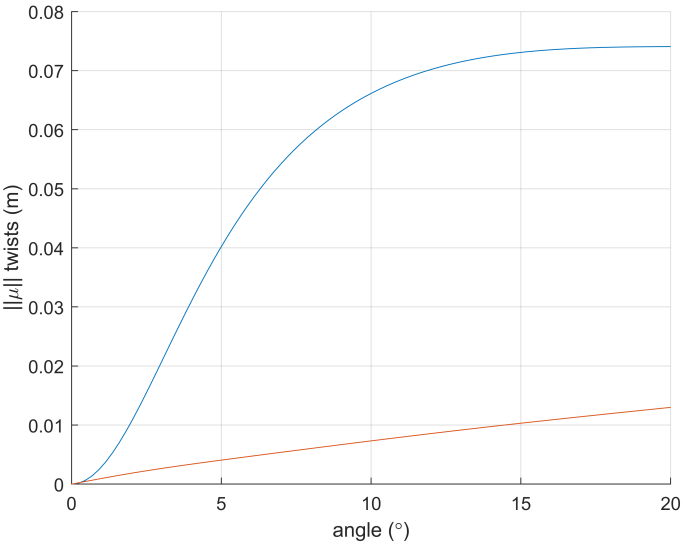

Figure 4.12.: Axis drift of the two twists under review, with the free twist in red and the constraint twist in blue

in fig. 4.7 would indicate. This is due to the pitch of that eigenwrench.

For the twists, the axis drift indicates parasitic translation, which can be understood as the platform moving up or down as the platform is actuated along the twists under review. The parasitic motion accompanying the wrenches is rotation. When the wrenches under review are applied, they induce a parasitic moment causing the platform to rotate about one of the eigentwists. However, when the stiffness of these eigentwist is high, the parasitic rotation will be minimal. This is the case for the vertical eigentwist, but not the two horizontal eigentwists.

Example Folded Tape Spring

The metrics will also be used on a folded tape spring. This is a shell structure; these type of structures often have less intuitive behaviour. A tape spring has one constant radius of curvature. The behaviour of tape springs has been studied in literature before. Specifically, the buckling of tape springs has been investigated [23–27]. At first the tape spring is completely undeformed (left in fig. 4.13). When a moment in the x-direction or a force in the z direction is applied, the tape spring bends. At a certain load the tape spring will buckle and a localised fold will start to form (middle in fig. 4.13). This fold has a constant radius when fully formed (right in fig. 4.13). As the tape spring buckles, it displays negative stiffness as the required moment for bending rapidly decreases. Further rotation does not require additional loads; i.e. post buckling the tape spring displays zero stiffness behaviour.

There are two ways to fold a tape spring, so called opposite and equal sense

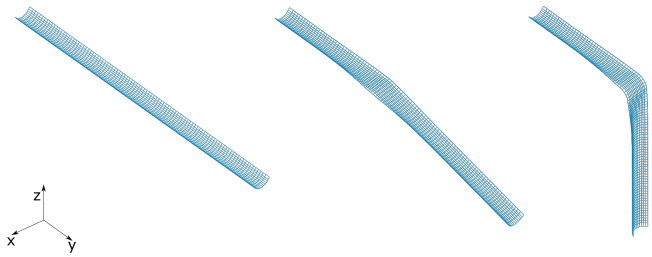

Figure 4.13.: Development of a tape spring fold subjected to opposite sense bending

bending [27]. In equal sense bending the tape spring is bent such that the concave sides face each other after buckling. Opposite bending is bending in the opposite direction, i.e. the convex sides face each other after buckling. With opposite sense bending there is snap-through after which the range of zero stiffness is reached (B in fig. 4.14). When the fold is formed and the rotation is reversed there is snap-back, but at a smaller angle than the snap-through (D in fig. 4.14). The moment required to achieve buckling in opposite sense bending is higher (A in fig. 4.14) than in equal sense bending (F in fig. 4.14). Equal sense bending does not display hysteretic behaviour when reversing the rotation.

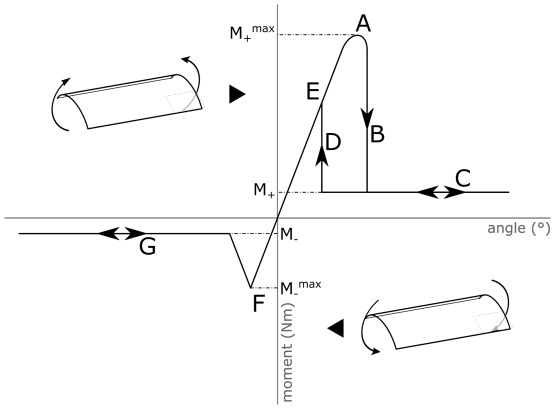

Figure 4.14.: Moment-angle graph of tape spring folding, with opposite sense bending as positive, figure adapted from [27].

Vehar et al. [28] describe a tape spring fold as a dyad with a moveable revolute joint and two coupled prismatic joints (see fig. 4.15). The two prismatic joints are coupled as the tape spring length is fixed; therefore the prismatic joints have equal but opposite displacements. As such a tape spring fold has two degrees of freedom: the rotation due to the revolute joint and a translation due to the coupled motion of the two prismatic joints. Both these degrees of freedom have zero stiffness.

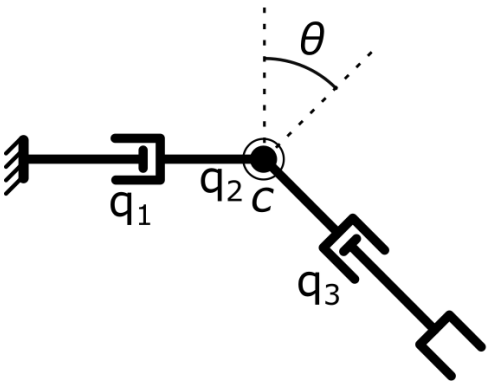

Figure 4.15.: Rigid body kinematics of a tape spring fold

The goal is to validate the use of the eigenscrew decomposition to obtain kinematic traits of a shell. In this example we will analyse the degrees of freedom and possible parasitic motion of a folded tape spring. We consider an initially straight clamped tape spring. Its end-effector is located at the free end. The kinematics can be modeled by an open-loop PSP chain as shown in fig. 4.15. In order to conserve length, the prismatic joints in fig. 4.15 have equal but opposite displacements: $q_3 = -q_1$. Any planar rigid body transformation of this point can be expressed as follows.

$$P(t) = \mathbf{A}(t)p = \begin{bmatrix} \mathbf{R}(\theta+\mathbf{q_2}) & \mathbf{t} \\ \mathbf{0} & 1 \end{bmatrix} p \tag{4.38}$$

in which the homogeneous transformation matrix $\mathbf{A}$ transforms the original point p at $\theta = 0$ to a new point P at a new location. The transformation matrix $\mathbf{A}$ consists of a 2-D rotation matrix $\mathbf{R}(\theta + \mathbf{q_2})$ and translation $\mathbf{t}$. For brevity the rotation matrix is denoted as $\mathbf{R}$, unless otherwise specified.

The movement of the end-effector of a tape spring can be described as three consecutive transformations. First we apply a transformation along the along prismatic joint q_3 of the tape spring. Then we apply a rotation along the fold centre and finally we apply a translation along prismatic joint q_1, which is equal in magnitude as the translation along q_3 but in the opposite direction. The total transformation is equal to the product of these transformation matrices,

$$\mathbf{A}_{tot} = \mathbf{A}_1\mathbf{A}_2\mathbf{A}_3 \tag{4.39}$$

in which first the translation of $-q_1$ along the second link is described: $-\mathbf{q_1} = -\{q_1, 0\}^T$,

$$\mathbf{A}_3 = \begin{bmatrix} \mathbf{I_2} & -\mathbf{q_1} \\ \mathbf{0} & 1 \end{bmatrix} \tag{4.40}$$

followed by a rotation along the fold centre; which is a pure rotation around a specific point $\mathbf{c}$. This transformation is expressed as follows [15],

$$\mathbf{A}_2 = \begin{bmatrix} \mathbf{I_2} & \mathbf{c} \\ \mathbf{0} & 1 \end{bmatrix} \begin{bmatrix} \mathbf{R} & \mathbf{0} \\ \mathbf{0} & 1 \end{bmatrix} \begin{bmatrix} \mathbf{I_2} & -\mathbf{c} \\ \mathbf{0} & 1 \end{bmatrix} = \begin{bmatrix} \mathbf{R} & \mathbf{(I_2 - R)c} \\ \mathbf{0} & 1 \end{bmatrix} \tag{4.41}$$

ending with a translation of q_1 along the first link.

$$\mathbf{A}_1 = \begin{bmatrix} \mathbf{I_2} & \mathbf{q_1} \\ \mathbf{0} & 1 \end{bmatrix} \tag{4.42}$$

The resulting transformation matrix is as follows.

$$\mathbf{A}_{tot} = \begin{bmatrix} \mathbf{I_2} & \mathbf{q_1} \\ \mathbf{0} & 1 \end{bmatrix} \begin{bmatrix} \mathbf{R} & \mathbf{(I_2 - R)c} \\ \mathbf{0} & 1 \end{bmatrix} \begin{bmatrix} \mathbf{I_2} & -\mathbf{q_1} \\ \mathbf{0} & 1 \end{bmatrix} = \begin{bmatrix} \mathbf{R} & \mathbf{(I_2 - R)(c - q_1)} \\ \mathbf{0} & 1 \end{bmatrix} \tag{4.43}$$

From eq. (4.43) it can be seen that if the variable q_1 is zero, i.e. no translation of the fold, the end-effector rotates about the fold centre. However, this rigid body equivalent does not completely describe the movement of a tape spring; as the angle of the fold changes so does the length of the fold itself. This causes a parasitic translation of the end-effector. The fold has a radius and the arc length of the tape spring fold is equal to $l_f = r\theta$. This effect causes the links to shorten by the same amount; this can be described as a translation of the second link along its length by $-\mathbf{l_f} = -\{r\theta, 0\}^T$ (see fig. 4.16).

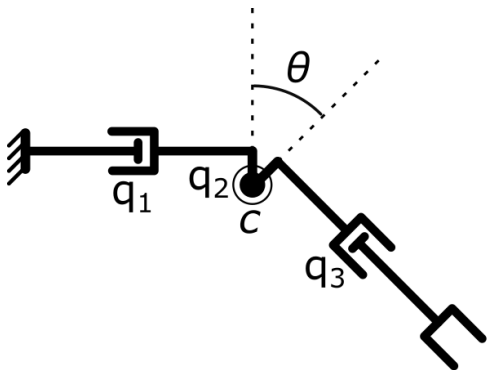

Figure 4.16.: Rigid body kinematics of a tape spring fold that takes fold length into account

This effect can be expressed by adding an additional transformation matrix.

$$\mathbf{A}_{tot} = \begin{bmatrix} \mathbf{I_2} & \mathbf{q_1} \\ \mathbf{0} & 1 \end{bmatrix} \begin{bmatrix} \mathbf{R} & \mathbf{(I_2 - R)c} \\ \mathbf{0} & 1 \end{bmatrix} \begin{bmatrix} \mathbf{I_2} & -\mathbf{l_f} \\ \mathbf{0} & 1 \end{bmatrix} \begin{bmatrix} \mathbf{I_2} & -\mathbf{q_1} \\ \mathbf{0} & 1 \end{bmatrix} \tag{4.44}$$

The effect on the centre of rotation of this extra translation in the rotational degree of freedom can be obtained by setting $\mathbf{q_1}$ in eq. (4.44) to zero which then reduces to the following.

$$\mathbf{A}_{\mathbf{q}_2} = \begin{bmatrix} \mathbf{R} & (\mathbf{I_2}-\mathbf{R})\mathbf{c} \\ \mathbf{0} & 1 \end{bmatrix} \begin{bmatrix} \mathbf{I_2} & -\mathbf{l_f} \\ \mathbf{0} & 1 \end{bmatrix} = \begin{bmatrix} \mathbf{R} & -\mathbf{R}\mathbf{l}_f + (\mathbf{I_2}-\mathbf{R})\mathbf{c} \\ \mathbf{0} & 1 \end{bmatrix} \tag{4.45}$$

The updated centre of rotation can be determined from the upper right part of the transformation matrix [15].

$$\mathbf{c}' = \frac{1}{2-2cos(\theta)}(\mathbf{I_2}-\mathbf{R}^T)((\mathbf{I_2}-\mathbf{R})\mathbf{c}-\mathbf{R}\mathbf{l}_f) \tag{4.46}$$

After some manipulations, this works out to be as follows:

$$\mathbf{c}' = \mathbf{c} + \frac{1}{2-2cos(\theta+q_2)}(\mathbf{I_2}-\mathbf{R})\mathbf{l}_f = \mathbf{c} + \frac{1}{2}\begin{bmatrix} 1 & cot\frac{\theta+q_2}{2} \\ -cot\frac{\theta+q_2}{2} & 1 \end{bmatrix}\mathbf{l}_f \tag{4.47}$$

or rewritten as an orthonormal matrix.

$$\mathbf{c}' = \mathbf{c} + \frac{1}{2sin\frac{\theta+q_2}{2}}\begin{bmatrix} sin\frac{\theta+q_2}{2} & cos\frac{\theta+q_2}{2} \\ -cos\frac{\theta+q_2}{2} & sin\frac{\theta+q_2}{2} \end{bmatrix}\mathbf{l}_f \tag{4.48}$$

This shows that the centre of rotation is off-set from the fold centre, which indicates a parasitic translation in addition to the intended hinge-like behaviour of a folded tape spring.

Equation (4.48) gives a centre of rotation if the rotation from θ to $\theta + q_2$ is applied in a single step. However, this motion is often done in steps. These steps have different instantaneous centres of rotation. These incremental instantaneous centres can be obtained from the incremental transformation matrix. This matrix can be obtained by first transforming back to the original position from the $i-1^{th}$ position after which we transform forward to the i^{th} position.

$$\mathbf{A}_{\mathbf{q}_2,i,i-1} = \mathbf{A}_{\mathbf{q}_2,i}\mathbf{A}^{-1}_{\mathbf{q}_2,i-1} \tag{4.49}$$

Again, the centre of rotation of this matrix can be obtained from the upper right part akin to eq. (4.46).

The direction of the translational degree of freedom, $\mathbf{q}_1$, can be obtained by fixing the revolute joint; i.e. $q_2 = 0$. The corresponding transformation matrix of the second link can be written as translation rotated by an angle θ. The rotation is determined by the angle of the fold:

$$\mathbf{A}_2 = \begin{bmatrix} \mathbf{R}(\theta) & \mathbf{0} \\ \mathbf{0} & 1 \end{bmatrix}\begin{bmatrix} \mathbf{I_2} & -\mathbf{q_1} \\ \mathbf{0} & 1 \end{bmatrix}\begin{bmatrix} \mathbf{R}(\theta)^T & \mathbf{0} \\ \mathbf{0} & 1 \end{bmatrix} = \begin{bmatrix} \mathbf{I_2} & -\mathbf{R}(\theta)\mathbf{q_1} \\ \mathbf{0} & 1 \end{bmatrix} \tag{4.50}$$

the total transformation matrix is then as follows:

$$\mathbf{A_{q_1}} = \mathbf{A_1 A_2} = \begin{bmatrix} \mathbf{I_2} & \mathbf{q_1} \\ \mathbf{0} & 1 \end{bmatrix} \begin{bmatrix} \mathbf{I_2} & -\mathbf{R}(\theta)\mathbf{q_1} \\ \mathbf{0} & 1 \end{bmatrix} = \begin{bmatrix} \mathbf{I_2} & \mathbf{q_1} - \mathbf{R}(\theta)\mathbf{q_1} \\ \mathbf{0} & 1 \end{bmatrix} = \begin{bmatrix} \mathbf{I_2} & (\mathbf{I_2} - \mathbf{R}(\theta))\mathbf{q_1} \\ \mathbf{0} & 1 \end{bmatrix} \tag{4.51}$$

This describes a translation of the prismatic joint q_3 followed by a equal but opposite translation of the prismatic joint q_1. The shape of the upper right part of the matrix A_{q1} in eq. (4.51) is similar to that of eq. (4.47); as such the direction of the degree of freedom is as follows:

$$(\mathbf{I_2} - \mathbf{R}(\theta))\mathbf{q_1} = 2sin\frac{\theta}{2}\begin{bmatrix} sin\frac{\theta}{2} & cos\frac{\theta}{2} \\ -cos\frac{\theta}{2} & sin\frac{\theta}{2} \end{bmatrix}\mathbf{q}_1 \tag{4.52}$$

From this it can be seen that the direction of the degree of freedom is in the direction of half the angle of the fold. Both links change in length. As one gets shorter, the other gets longer by the same amount. However, the second link can be at an angle which influences the overall direction of movement of the end-effector.

The tape spring was modelled in our IGA software operating within MATLAB [29]; the mechanical properties of the studied tape spring are listed in table 4.3. The tape spring was modeled with 15 elements in the transverse direction and 100 elements in the longitudinal direction. One end of the tape spring was fixed; at the other end a rotation is applied perpendicular to the mid-plane of the tape spring. The in-plane translation of the free end was unconstrained, allowing the end-effector to rotate about any axis parallel to the applied rotation. However, the other directions were constrained; i.e. translation in x-direction and rotation around the y and z-directions. This applies a perfect moment and the rotation will be around an eigentwist. The rotation is applied up to 90°; at this angle to fold is fully formed after which the angle is reduced to zero again to observe the snap-back behaviour and get a complete loop. The simulation converged with incremental 97 steps for the total motion, i.e. to 90° and back. This rotation was diplacement controlled.

Table 4.3.: Geometrical and material properties of the simulated tape spring

property	value	unit
subtended angle	0.75π	rad
radius	5	mm
thickness	50	µm
length	0.15	m
Young's modulus	210	GPa
Poisson's ratio	0.3	

First, we look at the moment plot in fig. 4.17. We see that it is similar to the plot of fig. 4.14, which indicates that the tape spring was indeed subjected to opposite sense bending.

Next we will analyse the eigenstiffnesses to validate the amount of degrees of freedom. Additionally, we are interested in the rotational degree of freedom. Two

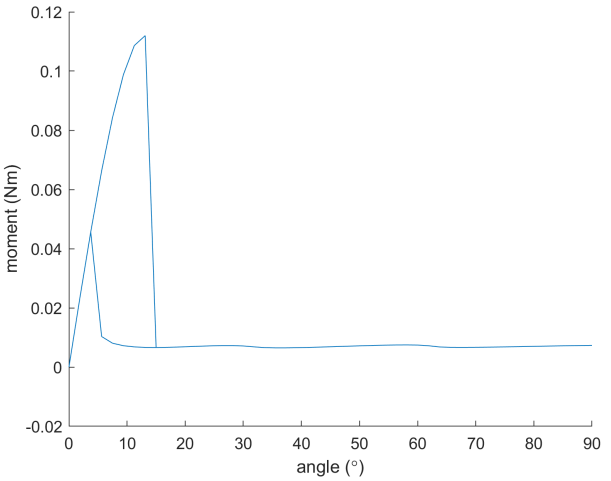

Figure 4.17.: Moment-angle graph of the simulated folded tape spring

things are of particular interest: the location of the centre of rotation and the stiffness of that rotation. The position and orientation of the end-effector can be retrieved at every step. Akin to eq. (4.38) the position of the end-effector at a arbitrary step can be described as follows:

$$P_i = \mathbf{R}_i p_0 + t_i \tag{4.53}$$

in which P_i is the location of the end-effector at an arbitrary step i. The matrix $\mathbf{R}_i$ is the rotation matrix corresponding to that step, retrieved from the orientation of the end-effector. The point p_0 is the location of the end-effector in the undeformed state. The vector t_i describes the translation needed to get to P_i given the rotation of the point p_0 and is the only unknown in this equation. This vector, t_i, is needed to obtain the centre of rotation akin to eq. (4.46).

For the incremental centre of rotation the equation changes. Here the point P_i is obtained from the rotation matrix $\mathbf{R}_i\mathbf{R}_{i-1}^T$, which rotates from the orientation of the end-effector at location P_{i-1} and at step $i-1$ back the undeformed state and then rotates to the orientation at step i. Again, the translation $t_{i,i-1}$ is the only unknown and is needed obtain the incremental centre of rotation using the following equation:

$$P_i = \mathbf{R}_i\mathbf{R}_{i-1}^T P_{i-1} + t_{i,i-1} \tag{4.54}$$

The translation $t_{i,i-1}$ can be written in the shape of eq. (4.45); i.e. the translation split into a rotation around a point plus a pure translation as follows:

$$t_{i,i-1} = (\mathbf{I_2} - \mathbf{R}_i\mathbf{R}_{i-1}^T)c_{fold} + t_{incr} \tag{4.55}$$

Specifically, the additional translation, t_{incr}, of the end-effector is of interest when the centre of rotation is set at the fold centre c_{fold}. This translation can be directly

compared to axis drift as they are both expressions of parasitic translations.

Lastly, we are interested in the translational degree of freedom. Eq. 4.52 and $\mathbf{q_1} = \{q_1, 0\}^T$ gives us the y- and z- components of the direction of the degree of freedom. The x-component should be zero as the mechanism is modelled (and displaced) as a planar mechanism. The axis misalignment metric shows if this direction in the freedom space and allows this direction to be compared to the direction of the lowest stiffness eigenwrench. Next to the direction, the stiffness of that eigenwrench is also investigated.

Figure 4.18 shows how the tape spring bends and buckles; it displays the cross-section of the tape spring in the yz-plane at $x = 0$. The fold centre and radius were obtained by fitting a circle to the cross-section with a linear regression scheme. The fold is not immediately formed: the radius shrinks as the fold angle increases. After 45° of rotation the radius does not change much as the fold seems fully formed. The fold centre shifts during the rotation; this influences the instant centres and the location of the eigentwist; the incremental centres and eigentwist locations match.

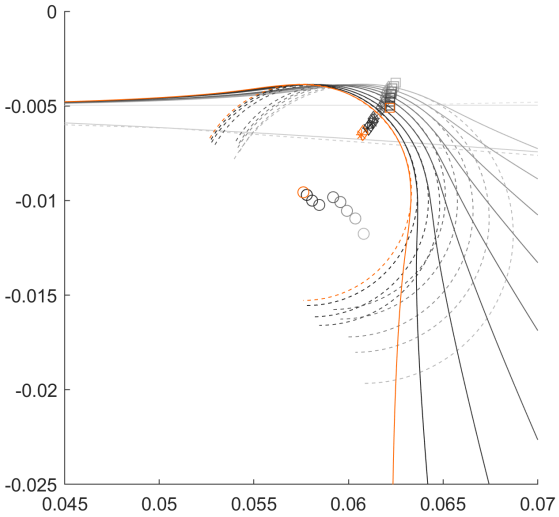

Figure 4.18.: Shape of tape spring during bending, seen at the plane $x = 0$, the shape with the largest angle is shown in orange, the fitted folds are denoted by the dashed lines, the fitted fold centres are circles, the instant centres of rotation by squares, the incremental instant centres of rotation by diamonds and the location of the degree of freedom eigentwist by stars.

The semi-log scale is not suited to show negative stiffnesses as these show up as gaps in the graphs in fig. 4.19. In addition the data was smoothed with a moving average filter to remove high frequency noise. Nonetheless, they do provide some insight. Prior to buckling there is one eigenwrench that is very stiff; this eigenwrench

is in the axial/longitudinal or y-direction of the tape spring as define in fig. 4.13. A tape spring is similar to a leaf spring prior to buckling, so this is clearly a constraint. The next stiffest is the translational stiffness in the x-direction. The stiffness is at least two orders more compliant that the axial direction and remains relatively constant over the full range of motion. The most compliant eigenwrench is the translational degree of freedom covered in the planar analysis. It becomes more compliant when the angles is increased; it roughly reduces stiffness by a factor 5 over the full range. It does not show zero stiffness behaviour. When the fold is fully formed at roughly 45° all eigenwrenches have a stiffness that are within a factor 40 of each other.

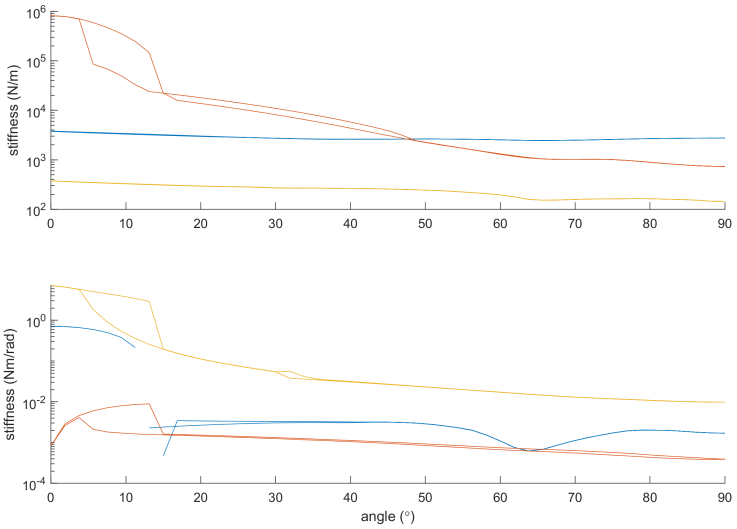

Figure 4.19.: Stiffness of all eigenwrenches and eigentwists plotted on a semi-log scale, note that gaps in the lines denote negative stiffness as they cannot be plotted on a log scale. Colours denote direction or original/undeformed eigenscrews: x-direction (blue), y-direction (red),z-direction (yellow)

Prior to buckling, the distinction between freedoms and constraints of the eigentwists is a lot more clear. The rotation that resembles torsion is at least two orders of magnitude more compliant than the other two directions. This is a degree of freedom of a tape spring not visible in the planar analysis. This degree of freedom slowly becomes slightly more compliant as the angle is increased. The rotation about an axis in the x-direction is at first a constraint but displays negative stiffness during buckling, after which it shows stiffness similar to the torsional stiffness. This is the rotational degree of freedom covered in the planar analysis. The remaining stiffness, that about an axis in the z-direction, also shows a dip in stiffness during buckling but remains always an order of magnitude higher than the other two.

Figure 4.20 shows the eigenstiffness of the planar degree of freedom eigentwist.

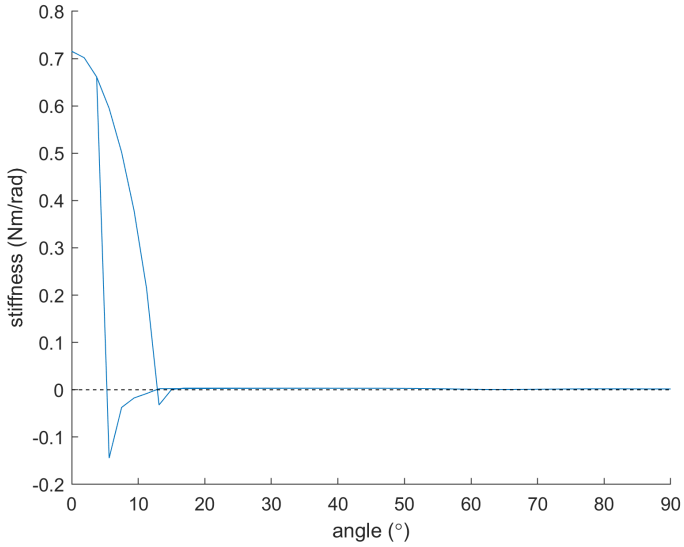

Figure 4.20.: Stiffness of planar degree of freedom eigentwist plotted on a linear scale to show negative stiffness

The occurrence of snap-though and snap-back are clearly visible. Figure 4.21 shows several metrics to obtain parasitic motion. The data starts at an angle of approximately 10°, since the folds only start to appear at that angle. Axis drift and the translation obtained though the incremental rigid body kinematics (see t_{incr} in eq. (4.55)) match. Both express the parasitic translation of the end-effector contrasted with the pure rotation of the tape spring around the fold centre. This shows that axis drift can be used as a metric for parasitic motion. The radius is also plotted in fig. 4.21 as it is related to the incremental translation of the second link, which is $rd\theta$.

Figure 4.22 shows the misalignment of the translational degree of freedom deduced in eq. (4.52). In total three misalignments are shown, these are: the misalignment between the freedom space and the DoF (red in fig. 4.22), the misalignment between the constraint space and the rigid body DoF (blue in fig. 4.22) and the direct misalignment between the highest compliant eigenwrench and the rigid body DoF (yellow in fig. 4.22). The DoF is almost mostly aligned with both the freedom space and the highest compliance eigenwrench, indicating that this rigid body DoF is indeed free. The misalignments appear quite ragged, which is likely due to some numerical errors in the simulation.

Figure 4.23 shows the misalignment of the planar force constraint (perpendicular to the translational DoF). The misalignments between the rigid body constraint and the freedom space, the constraint space and the most corresponding planar eigenwrench (in the yz-plane but perpendicular to the highest compliance eigenwrench) are shown in red, blue and yellow respectively. The rigid body constraint remains

relatively aligned with the corresponding eigenwrench; this makes sense as it this was also the case for the perpendicular DoF; similar results are obtained for the misalignment with the constraint space. The misalignment with the freedom space decreases after 50°, (red in fig. 4.23). This indicates that as the fold is established and grows the compliance in all directions also grows.

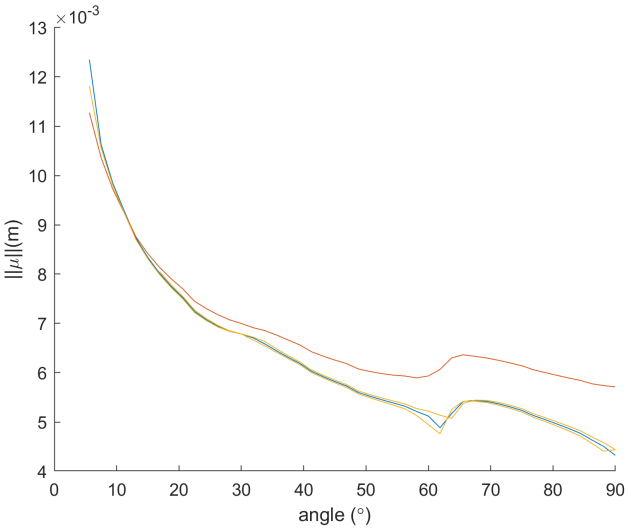

Figure 4.21.: The radius of the fold (red), the axis drift metric for a twist located at the fold centre (blue) and the translation of the end-effector resolved through rigid body kinematics (yellow)

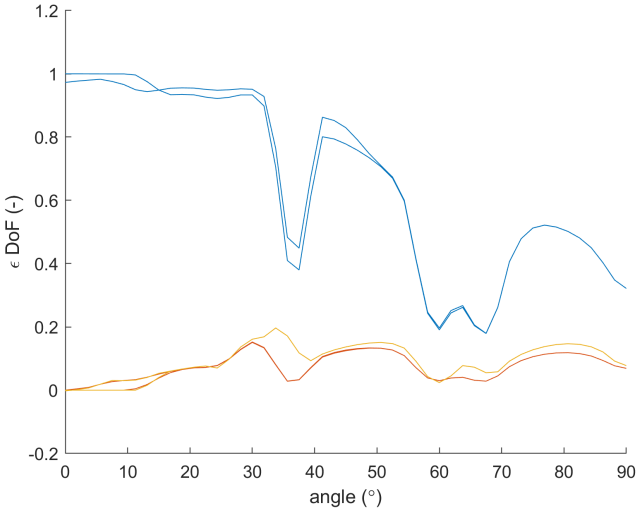

Figure 4.22.: The misalignment between the freedom space and the planar rigid body DoF (red), the misalignment between the constraint space and the planar rigid body DoF (blue) and the direct misalignment between the highest compliant eigenwrench and the planar rigid body DoF (yellow).

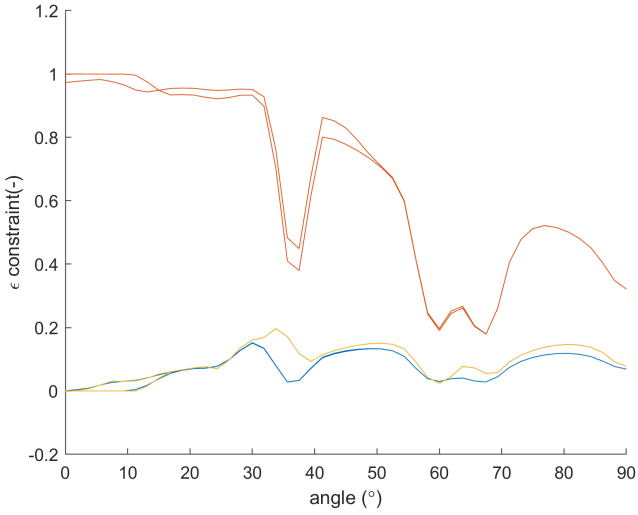

Figure 4.23.: The misalignment between the freedom space and the planar rigid body constraint(red), the misalignment between the constraint space and the planar rigid body constraint (blue) and the direct misalignment between the other eigenwrench in the yz-plane (perpendicular to the highest compliance eigenwrench) and the planar rigid body constraint (yellow)

Discussion

If a mechanism has a full rank stiffness matrix with an arbitrary end-effector at an arbitrary pose, then eigenscrew decomposition is possible; this property makes eigenscrew decomposition uniquely suited for use as an analysis tool for any type of compliant mechanism; this allows side-by-side comparison of a varying array of mechanisms. The examples used in this article have different degrees of freedoms. This showcases that the metrics can be used for any mechanism with an end-effector, having degrees of freedom between 1 and 6. The usefulness of eigenscrew decomposition can be further enhanced by applying the unified stiffness method proposed by Leemans et al. [18], which allows for comparison between rotational and translational stiffnesses.

A downside of using the eigenscrew decomposition is that it is derived from the stiffness matrix. This matrix is often only valid at a single pose and thus decomposition over the full range of motion can be computationally expensive. Irrespective of whether the behaviour of a mechanism can be analysed intuitively or through other metrics, the eigenscrew decomposition and the derived metrics will always provide an insight to the behaviour.

Although the metrics can be applied to any compliant mechanism, some metrics are more useful than others depending on the situation. Axis misalignment is mostly useful for situations where the direction of the DOFs or constraints is expected to change significantly during motion. For instance, this is the case in a parallel leaf spring guidance. Behaviour like the shortening effect, i.e. lateral motion accompanying the desired motion, can be easily studied with the axis misalignment metric. This makes axis misalignment also useful to analyse the evolution of support stiffness during motion, for instance.

The axis drift metric is a relatively straightforward metric: more axis drift means more parasitic motion or load. Axis drift intrinsically has a distance component. This distance has an absolute value; however, the relevance of this value is dependent on the size of the mechanism. A certain value of axis drift is more severe in a small mechanism than a larger mechanism; the size of the mechanism has be kept in mind when assessing the axis drift. Additionally, axis drift also adds either compliance or stiffness that could be, but is not necessarily, detrimental. Axis drift of a parallel leaf spring guidance, for instance, adds compliance in the intended direction, which on its own is not a drawback. The added parasitic rotation could be. If parasitic motion is detrimental, axis drift has to be kept at a minimum. As such, the axis drift metric is very powerful.

Axis misalignment and drift are excellent for expressing parasitic motion, other than that they give only an indication of the behaviour of the mechanism. If the actual behaviour is needed, the actual stiffness or compliance composition is required. It does describe the precise response, but also requires more computation and can be less insightful.

Depending on the situation it can be more beneficial to compare the misalignment between an intended freedom or constraint and its closest eigentwist or -wrench, since it shows precisely whether the intended DoF or constraint is still aligned with one of the principal screws of the compliant mechanism. It is important to ensure

that this principal eigenscrew is still in the freedom or constraint space. This can be done by checking the corresponding eigenstiffness.

The tip-tilt-piston platform has full rank stiffness matrix at every evaluated pose. However, there are many mechanisms that have a rank deficient stiffness matrix at some poses; for instance, mechanisms that have a zero-stiffness degree of freedom. The folded tape spring showed such behaviour; however, due to numerical errors, the stiffness matrix was not rank deficient. Lipkin et al. have touched upon enabling eigenscrew decomposition for rank deficient matrices [13]. This would allow the use of the metric on zero-stiffness mechanisms and not rely on numerical errors to condition the stiffness matrix.

The interpretation of the stiffnesses of the folded tape spring is not straightforward. Intuitively, a tape spring is constrained in all translational directions prior to buckling. However, after buckling the eigenstiffnesses of the eigenwrenches are still quite high; this would indicate that the translational directions are still constrained. It definitely does not show the zero stiffness of one eigenwrench that we would expect from literature. Why this is, is not clear; it could be related to the fact that the stiffness matrix is already near singular due to the zero stiffness eigentwist. Another explanation is that the fold of the tape spring is being compressed, which influences the results. However, in the simulations, in-plane translations are left free and an rotation is applied. This results in a pure moment being applied, which should not compress the fold. Additionally, compressing the fold would influence both the rotational and translational zero stiffness modes, which is not observed. As such, this requires further study.

The results of the eigentwists are more clear. After buckling, it appears that all three eigentwists are degrees of freedom.

The locations of one of the eigentwists line up with the incremental centres of rotation. These eigentwists were derived from stiffness matrices that were obtained incrementally, i.e. tangent stiffness matrices. If we were to obtain the secant stiffness matrices from the neutral position of the tape spring to each of the evaluated poses of the tape spring, they would likely align with the instant centres of rotation. Due to the complexity of the simulation, this was not validated.

Conclusion

We have shown that parasitic motions and loads in compliant mechanisms can be analysed using eigenscrew decomposition. Eigenscrew decomposition is a useful tool to visualize the kinematics of compliant mechanisms. We introduced two metrics that can be used on any compliant mechanism; they are not specific to any type of compliant mechanism. The metrics are suitable to analyse points of interests of mechanisms with any number of degrees of freedom.

The metrics are based on the fact that any screw can be expressed as a linear combination of the eigenscrews and induced screws; this puts the screw in question in eigenbasis coordinates. These coordinates can then be used in the metrics.

In three dimensions two screws can differ in two ways: they can be separated in distance, often described in literature as axis drift. Secondly they can differ

in orientation, which is analysed by the axis misalignment metric. Both axis misalignment and axis drift are indications of parasitic motion/load. Increased axis misalignment is also an indication of changed stiffness behaviour as the intended freedom or constraint space is no longer aligned with the actual freedom or constraint space.

The axis misalignment metric captures the freedom and constraint spaces by scaling the original direction of the screw with the eigencompliances and eigenstiffnesses respectively. Although this metric can exaggerate changed stiffness behaviour, it does allow for directly checking changed stiffness behaviour. In some instances it is better to directly compare the misalignment between a desired screw and a specific eigenscrew of the mechanism. This is the case in a cross-flexure hinge, where the free eigentwist is the only eigenscrew of interest when analysing the degrees of freedom.

The most powerful attribute is that these metrics can be used on any compliant mechanism. To illustrate this, the metrics were used on two very different compliant mechanisms. First, a tip-tilt-piston platform was studied, which has three degrees of freedoms. We explored the parasitic motion when the platform was rotated. Second, we investigated the behaviour of a folded tape spring and analysed the parasitic motion that accompanies the intended hinge-like behaviour. Especially this last example showcases how the metrics and eigenscrew decomposition in general can help gain insight into the behaviour of compliant mechanisms where their motion cannot always be intuitively deduced. These mechanisms often use large deflections or complex geometries and it can be very hard to understand their behaviour through conventional means.

4.1. Author Contributions

W.W.P.J.S. proposed and designed the research, performed the numerical calculations and wrote the paper. J.L.H. supervised the project and reviewed the paper.

Bibliography

[1] L.L. Howell. *Compliant Mechanisms*. New York: Wiley, 2001.

[2] N. Lobontiu. *Compliant Mechanisms: Design of Flexure Hinges*. CRC Press, 2002.

[3] H.J.M.R. Soemers. *Design Principles for Precision Mechanisms*. Enschede: T-Pointprint, 2010.

[4] Z. Ni, D. Zhang, Y. Wu, Y. Tian, and M. Hu. "Analysis of parasitic motion in parallelogram compliant mechanism". In: *Precision Engineering* 34.1 (2010). CIRP-CAT 2007, pp. 133–138.

[5] Y. Luo, W. Liu, and L. Wu. "Analysis of the displacement of lumped compliant parallel-guiding mechanism considering parasitic rotation and deflection on the guiding plate and rigid beams". In: *Mechanism and Machine Theory* 91 (2015), pp. 50–68.

[6] L. L. Howell and A. Midha. "A Method for the Design of Compliant Mechanisms With Small-Length Flexural Pivots". In: *Journal of Mechanical Design* 116.1 (Mar. 1994), pp. 280–290. eprint: https://asmedigitalcollection.asme.org/mechanicaldesign/article-pdf/116/1/280/5608378/280_1.pdf.

[7] S. Zelenika and F. D. Bona. "Analytical and experimental characterisation of high-precision flexural pivots subjected to lateral loads". In: *Precision Engineering* 26.4 (2002), pp. 381–388.

[8] J. A. Haringx. "The cross-spring pivot as a constructional element". In: *Flow, Turbulence and Combustion* 1.1 (Dec. 1949), p. 313.

[9] N. Lobontiu, J. S. Paine, E. O'Malley, and M. Samuelson. "Parabolic and hyperbolic flexure hinges: flexibility, motion precision and stress characterization based on compliance closed-form equations". In: *Precision Engineering* 26.2 (2002), pp. 183–192.

[10] L.-J. Lai and Z.-N. Zhu. "Modeling and Analysis of a Compliance Model and Rotational Precision for a Class of Remote Center Compliance Mechanisms". In: *Applied Sciences* 6.12 (2016).

[11] C. B. Patil, S. V. Sreenivasan, and R. G. Longoria. "Analytical and Experimental Characterization of Parasitic Motion in Flexure-Based Selectively Compliant Precision Mechanisms". In: *Volume 2: 32nd Mechanisms and Robotics Conference, Parts A and B*. ASME, 2008, pp. 393–404.

[12] H. Li, G. Hao, and R. C. Kavanagh. "Position-Space-Based Compliant Mechanism Reconfiguration Approach and Its Application in the Reduction of Parasitic Motion". In: *Journal of Mechanical Design* 138.9 (July 2016), p. 092301.

[13] H. Lipkin and T. Patterson. “Geometrical properties of modelled robot elasticity: part I - Decomposition”. In: *ASME Design Tech. Conf. and Computers in Engineering Conf.* Vol. 45. 1992, pp. 179–185.

[14] G. Radaelli and J. Herder. “Gravity balanced compliant shell mechanisms”. In: *International Journal of Solids and Structures* 118-119 (2017), pp. 78–88.

[15] J. M. Selig. *Geometric Fundamentals of Robotics (Monographs in Computer Science)*. SpringerVerlag, 2004.

[16] N. Ciblak and H. Lipkin. “Centers of Stiffness, Compliance, and Elasticity in the Modelling of Robotic Systems”. In: vol. 23rd Biennial Mechanisms Conference: Robotics — Kinematics, Dynamics and Controls. International Design Engineering Technical Conferences and Computers and Information in Engineering Conference. Sept. 1994, pp. 185–195. eprint: https://asmedigitalcollection.asme.org/IDETC-CIE/proceedings-pdf/DETC94/12860/185/6663589/185_1_detc1994-0322.pdf.

[17] H. Lipkin and T. Patterson. “Geometrical Properties of Modelled Robot Elasticity: part II - Center of Elasticity”. In: *ASME Design Tech. Conf. and Computers in Engineering Conf.* Vol. 45. 1992, pp. 187–193.

[18] J. Leemans, C. Kim, W. van de Sande, and J. Herder. “Unified stiffness characterization of nonlinear compliant shell mechanisms”. English. In: *Journal of Mechanisms and Robotics* 11.1 (2019).

[19] H. Kooistra, C. Kim, W. van de Sande, and J. Herder. “Shape Optimization Framework for the Path of the Primary Compliance Vector in Compliant Mechanisms”. In: *Journal of Mechanisms and Robotics* 12 (July 2020), pp. 1–24.

[20] D. Farhadi Machekposhti, N. Tolou, and J. Herder. “A Review on Compliant Joints and Rigid-Body Constant Velocity Universal Joints Toward the Design of Compliant Homokinetic Couplings”. In: *Journal of Mechanical Design* 137 (Mar. 2015), p. 032301.

[21] J.B. Hopkins and M.L. Culpepper. “Synthesis of Multi-Degree of Freedom, Parallel Flexure System Concepts Via Freedom and Constraint Topology (FACT)—Part I: Principles”. In: *Precision Engineering* 34.4 (2010), pp. 259–270.

[22] J. B. Jonker and J. P. Meijaard. “SPACAR — Computer Program for Dynamic Analysis of Flexible Spatial Mechanisms and Manipulators”. In: *Multibody Systems Handbook*. Ed. by W. Schiehlen. Berlin, Heidelberg: Springer Berlin Heidelberg, 1990, pp. 123–143.

[23] K. Seffen. “On the Behavior of Folded Tape-Springs”. In: *Journal of Applied Mechanics* 68 (May 2001).

[24] K. Seffen and S. Pellegrino. “Deployment dynamics of tape springs”. In: *Proceedings of The Royal Society A: Mathematical, Physical and Engineering Sciences* 455 (Mar. 1999), pp. 1003–1048.

[25] J. Yee, O. Soykasap, and S. Pellegrino. “Carbon Fibre Reinforced Plastic Tape Springs”. In: *45th AIAA/ASME/ASCE/AHS/ASC Structures, Structural Dynamics & Materials Conference*. 2004. eprint: https://arc.aiaa.org/doi/pdf/10.2514/6.2004-1819.

[26] J. C. Yee and S. Pellegrino. “Composite Tube Hinges”. In: *Journal of Aerospace Engineering* 18.4 (2005), pp. 224–231.

[27] K. Seffen, Z. You, and S. Pellegrino. “Folding and deployment of curved tape springs”. In: *International Journal of Mechanical Sciences* 42.10 (2000), pp. 2055–2073.

[28] C. Vehar, S. Kota, and R. Dennis. “Closed-Loop Tape Springs as Fully Compliant Mechanisms: Preliminary Investigations”. In: vol. Volume 2: 28th Biennial Mechanisms and Robotics Conference, Parts A and B. International Design Engineering Technical Conferences and Computers and Information in Engineering Conference. Sept. 2004, pp. 1023–1032. eprint: https://asmedigitalcollection.asme.org/IDETC-CIE/proceedings-pdf/IDETC-CIE2004/46954/1023/2617091/1023_1.pdf.

[29] A.P. Nagy. “Isogeometric design optimisation”. PhD thesis. Delft, the Netherlands: Delft University of Technology, 2011.

II

Analysis and Synthesis of Two-Fold Tape Loops

5

Properties of Two-fold Tape Loops: The Influence of the Subtended Angle

Marinus G. de Jong, Werner W.P.J. van de Sande, Just L.Herder

Tape springs are thin-walled structures with zero longitudinal and constant transverse curvature. Folding them twice and connecting both ends create a tape loop which acts as a linear guide. At this time, there is insufficient understanding of the influence of the tape spring's cross section on its behaviour. This study investigates the influence of the subtended angle on the tape spring's behaviour, especially the energy distribution and the fold radius. First, some key aspects in the design of a twofold tape loop are discussed. By performing a curvature analysis of this folded geometry, the different regions within a tape spring are identified. This information is used to identify the influence of the subtended angle on the geometry and energy state of the tape loop. The fold radius and fold angle are determined by analysing the geometry of the fold region. The analysis showed that the energy within the transition regions cannot be neglected. The energy within these regions and the length of the transition regions both increase with the subtended angle. It is also shown that the fold radius is not constant when the subtended angle is small. The subtended angle should be above 100 deg to ensure a constant radius.

This chapter originally appeared as M. G. De Jong, W. W. P. J. van de Sande, and J. L. Herder. "Properties of Twofold Tape Loops: The Influence of the Subtended Angle". In: *Journal of Mechanisms and Robotics* 11.2 (2019)[1]

5.1. Introduction

Compliant mechanisms are mechanisms that move due to elastic deformation of slender segments. These mechanisms have advantages compared to traditional mechanisms such as reduced wear, reduced or eliminated backlash, no need for lubrication and possibilities for monolithic designs [2].

Most compliant mechanisms consist of beam flexures that move in a plane, such as compliant grippers [3] and MEMS devices [4]. A relatively new area in the field of compliant mechanisms is that of shell mechanisms. These mechanisms have curved flexures and have complex shapes and kinetics [5].

As shells are defined as curved thin-walled structures, one of the most basic shell elements is a tape spring: a thin-walled open cylindrical structure with zero longitudinal and constant transverse curvature. A carpenters tape is an example of such geometry. Despite its simple geometry, a tape spring has some remarkable properties, such as being stiff before buckling while being compliant after buckling, having a constant fold radius [6] and constant moment after buckling [7]. Because of these properties, tape springs are used as hinges [8] or as deployable structures in space [9–14].

A special configuration of a folded tape spring is a tape loop, which is a tape spring with multiple folds and its ends connected to each other. Vehar [15] examined different setups with a different number of folds and determined the degrees of freedom. The simplest configuration of a tape loop is with two folds, which acts as a zero force and zero stiffness linear guide.

A two-fold tape loop is the monolithical equivalent of a rolamite, which has the same working principle [16]. A rolamite can act as force generator by changing the geometry of the band [17, 18]. In further analogy to the rolamite, a tape loop can be turned into a force generator by changing the cross section of the tape spring. Radaelli [19] suggested a constant force mechanism using a two-fold tape loop with a tapered tape spring. However, to make a more generic force generator out of a tape loop, more insight into the influence of the tape spring's cross section on its geometry and energy state is desired.

Quite some theoretical research has been performed on tape spring buckling [20], deployment dynamics [7] and the fold curvature [21]. Seffen derived an analytical formula of the strain energy within the fold region of a tape spring [22]. The fold region however is not the only region where strain energy is stored. There is also a transition region between the undeformed region and the bent region, which contains an amount of strain energy. However, it is not known how much energy is stored in that region.

This paper first presents several key aspects in the design of a two-fold tape loop: such as the range of motion, limits on the thickness of the shell and existing expressions for the energy state. Together these aspects comprise the mechanical behavior of the tape loop. The influence of the subtended angle on this behavior is investigated. The subtended angle is the angle in transverse direction of the tape spring. This analysis is divided into two categories: the influence on the geometry and the influence on the energy state of the tape loop. The description of the energy state of the tape loop is desired in the synthesis of a force generator using

tape loops. Another important factor that is determined is whether the fold radius remains constant while varying the cross-section, since otherwise the tape loop will not act as a straight-line guide.

This paper starts with presenting aspects of mechanical behavior of a tape loop. Then the methods used in analysis are explained. Subsequently, the results of the FEM analysis are shown. In the discussion, the reprecussions of the results and the limitations of the method are discussed. Finally the paper concludes with some remarks.

5.2. Tape spring basics

5.2.1. Parameters of a Folded Tape Spring.

A tape spring fold is created by applying a moment to both ends of a tape spring. A tape spring can be folded into two directions: equal sense or opposite sense. The fold is defined as equal sense when the concave sides of the tape spring are facing towards each other, opposite sense when they are facing away [22]. Figure 5.1 shows an equal sense folded tape spring together with its undeformed geometry. The length direction is designated the longitudinal direction and the curved direction the transverse direction. The original geometry has a constant transverse radius R and zero longitudinal radius with a so-called subtended angle α, thickness t and length L. The fold can be created by buckling the tape spring; this creates an area of equally deformed geometry. There is some discussion whether the fold radius is equal to the tape spring radius [6, 10]. The transverse radius is also called the tape spring radius; the folded geometry has a fold radius R^* with a fold angle θ.

5.2.2. Tape Spring Regions.

Three different regions can be identified within a folded tape spring. Figure 5.2 shows a folded tape spring with the different regions numbered.

The first region is the undeformed region. This is where the tape spring has its original underformed shape. In this region, the transverse curvature is $\frac{1}{R}$ and the longitudinal curvature is zero. The second region is the transition region. In this region the tape spring goes from the original to fully deformed shape. The transverse and longitudinal curvatures are between the curvatures in the undeformed and deformed regions. The third region is called the fold region. Here the tape spring is fully deformed, having a transverse curvature of zero and a longitudinal curvature of $\frac{1}{R^*}$.

Tape Loop.

By folding a tape spring twice and connecting both sides, a two-fold tape loop is created. The motion is applied to the upper side of the loop while the lower side is clamped, as shown in fig. 5.3. This creates a compliant straight-line mechanism.

Using a tape spring in the two-fold tape loop configuration has two implications for the parameters: 1) the folding angle θ of the two folds is constant and around

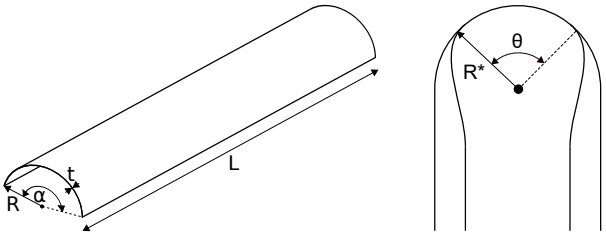

Figure 5.1.: Parameters of an undeformed tape spring (left) and a equal-sense folded tape spring (right)

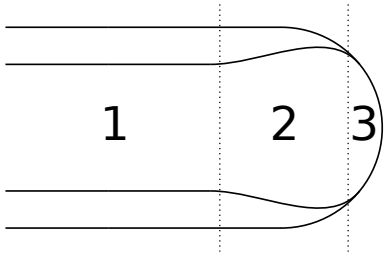

Figure 5.2.: Different regions within a folded tape spring: 1) undeformed region, 2) transition region, 3) fold region

π radians, 2) the subtended angle α can have a maximum value of π radians, otherwise the top and bottom sides of the tape loop would collide.

The first implication pertains to the fact that the orientation between the upper and lower segments is always π radians; most of this orientation change is attributed to the fold. Part of it will be due to the transition region; together they effect a π radians orientation change. The second implication comes from the fact that the longitudinal radius R^* is almost equal to the transverse radius R. The angle of the fold is near π radians. When the subtended angle is also π radians, the edges of the tape spring of the upper and the lower segments are close together. The distance between the upper and lower segments seen in fig. 5.3 goes to zero. Any subtended angle higher than this value might cause collisions between the upper and lower segments.

Range of Motion.

As the tape loop moves left or right, at some point one of the folds will near the clamping, see fig. 5.3. When the transition region hits the clamping, the part of the tape spring at the edge of the clamping wants to flatten in transverse direction. This flattening is restricted by the clamping. This results in a high stiffness in the direction of the motion, which limits the range of motion (ROM).

The range of motion without this stiffening effect is determined by the length of the undeformed regions at the the bottom. If we assume that the tape spring is clamped along a line, the clamping has no length. We choose the tape loop to have

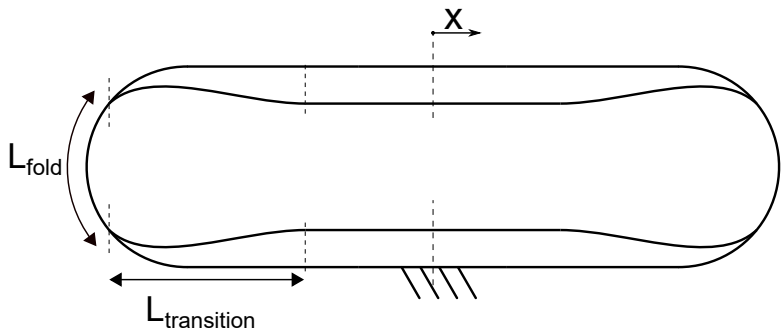

Figure 5.3.: A two-fold tape loop, some characteristic lengths are highlighted, the end-effector is denoted by x

a length of $2L$. The position of x is maximum when the length of the left bottom undeformed region is zero. The transition zone then hits the clamping as can be seen in fig. 5.3.

$$\begin{aligned} x_{max} &= -L_{transition} + (L - L_{fold} - L_{transition}) \\ &= L - L_{fold} - 2L_{transition} \end{aligned} \tag{5.1}$$

The start and the end of the fold have the same x-coordinate; therefore the length of the fold does not directly contribute to the x-position. The remainder of the tape loop half forms the upper region; the length of this remainder can be expressed as a function of the tape spring length, the length of the fold and the lower region. The position of x is at a minimum when the length of the bottom right underformed region is zero.

$$\begin{aligned} x_{min} &= L_{transition} - (L - L_{fold} - L_{transition}) \\ &= -L + L_{fold} + 2L_{transition} \end{aligned} \tag{5.2}$$

The range of motion is the difference between these outermost positions.

$$\begin{aligned} ROM &= x_{max} - x_{min} \\ &= 2L - 2L_{fold} - 4L_{transition} \end{aligned} \tag{5.3}$$

Relation Between Radius and Thickness.

The von Mises principal plane stress is

$$\sigma_v = \sqrt{\sigma_1^2 - \sigma_1\sigma_2 + \sigma_2^2}. \tag{5.4}$$

Kirchhoff-Love plate theory for an isotropic and homogeneous plate without shear strain gives an expression for the stress, $\vec{\sigma}$:

$$\vec{\sigma} = \begin{bmatrix} \sigma_1 \\ \sigma_2 \end{bmatrix} = \frac{E}{1-\nu^2} \begin{bmatrix} 1 & \nu \\ \nu & 1 \end{bmatrix} \vec{\epsilon}_{\max} \tag{5.5}$$

where $\vec{\epsilon}_{\max}$ is the maximum strain, E the Young's modulus and ν the Poisson's Ratio. In case of an equal sense folded tape spring, the maximum strain is in the fold; the strain in the longitudinal direction is $\epsilon_1 = t/2R^*$ and in the transverse direction $\epsilon_2 = -t/2R$. Equation (5.4) can put into eq. (5.5) to obtain an expression for the von Mises stress. In the case of $R^* = R*$, this equation simplifies to the following expression.

$$\sigma_v = \frac{Et\sqrt{3}}{2R(1+\nu)}. \tag{5.6}$$

This expression shows that the von Mises stress increases with the thickness and decreases with the radius. According to the von Mises yield criterion, a material starts to yield when the von Mises stress reaches the yield strength of a material, so $\sigma_v \leq \sigma_y$ to prevent plastic deformation. Using this criterion, eq. (5.6) can be rearranged to obtain the required relation between t and R

$$t < \frac{2\sigma_y(1+\nu)}{E\sqrt{3}}R. \tag{5.7}$$

Equation of Energy.

The potential strain energy, U, for a fold in a tape spring without twist, using the definitions as shown in fig. 5.1 and fig. 5.4, is given by

$$U = \frac{\alpha D}{2}\int_{-\theta/2}^{\theta/2}\left[\frac{R}{r(\beta)} + \frac{r(\beta)}{R} \pm 2\nu\right]d\beta \tag{5.8}$$

with the flexural rigidity $D = Et^3/12(1-\nu^2)$, [22]. The plus-minus sign is for respectively opposite or equal sense bending. This equation does not take the transition regions into account.

With the use of several other assumptions, eq. (5.8) can be simplified. It has been suggested that the fold radius is constant ($r(\beta) = R^*$) and that the fold radius R^* is equal to R [6]. Furthermore, since in this paper a single fold of a two-fold tape loop is considered, the fold angle θ can be set to π. With these assumptions, eq. (5.8) can be reduced to

$$U = D(1 \pm \nu)\alpha\pi \tag{5.9}$$

where the plus-minus sign represents respectively opposite and equal sense bending [7].

Investigation

The goal for our investigation is twofold. What is the influence of the subtended angle on the geometry of the tape loop and what is the influence on its energy state? A tape spring is modeled in a FEM model. One of the endpoints is clamped while the other endpoint is rotated π radians to create a single fold. The tape spring is

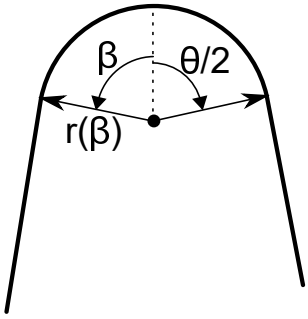

Figure 5.4.: Definition of parameters associated with deformation of a tape spring [22].

bent such that a equal sense fold is obtained. The subtended angle will be varied between 80 and 170 degrees in steps of 5 degrees. All other parameters as shown in fig. 5.1 are constant as given in table 5.1.

The output of the model is the deformed geometry and the strain energy per surface area within the tape spring. The deformed geometry is used to find the different regions within the tape spring by analyzing the curvature. The curvature in the undeformed region is zero in the longitudinal direction and $1/R$ in the transverse direction. In the fold region, this is the reversed; the longitudinal curvature is $1/R^*$. The different regions can be identified by analyzing the curvature in transverse direction. The transverse curvature will decrease in the transition zone. In the fold region, it will be zero. The curvature is obtained by curve fitting circles on transverse lines along the longitudinal direction of the tape spring.

Some definitions are required to obtain the regions; the transition region starts when the curvature drops below $1/R$. The transition region ends when the curvature falls below 5% of the original tape spring curvature. This value is chosen to accommodate for errors in the FEM analysis. Below this value, the fold region starts.

As the different regions are defined, the length of the transition region can be determined by measuring the length between the start of the transition region and the start of the fold region.

Once the regions are known, other geometry and energy information can be obtained. The range of motion is known when the lengths of the regions are known. The fold radius is determined by fitting a circle to the data points in the fold region in the longitudinal direction. The fold angle is determined by calculating the angle between the edges of the fold region and the center of the fitted circle. The strain energy is summed per region to get the energy division among regions.

FEM Analysis.

A Matlab based finite element software package of the Delft University of Technology is used for this analysis [23]. The model is based on isogeometric analysis (IGA). Within this framework a geometry is defined using NURBS. For a detailed description of the IGA working principle, the reader is referred to [24].

Table 5.1.: Used values for tape spring parameters

R [mm]	t [mm]	L [mm]	θ [rad]	E [GPa]	ν [-]
21	0.2	1000	π	210	0.3

The cross section of the tape spring geometry is defined by an arc with a subtended angle α that is linearly divided into 21 points in the transverse direction. The geometry in the length direction is then defined by linearly spacing these cross sections in longitudinal direction over length L, divided into 300 points. In addition, two pilot points are defined at the centroid of the cross section at both ends of the geometry which are connected through beams to each point of the corresponding curved edges. The motions are applied to these pilot points.

The folding process, shown in fig. 5.5, is performed in two steps: first a rotation of π is applied to one of the pilot points while the other pilot point is fixed, which forces the tape spring to buckle. Secondly the rotated endpoint is translated to the same height as the fixed pilot point while constraining the rotation.

5.3. Results

Not all subtended angles resulted in a converged simulation. The following angles in degrees did converge and were included in the analysis.

$$\boldsymbol{\alpha} = (85^\circ, 90^\circ, 95^\circ, 100^\circ, 105^\circ, 110^\circ, 115^\circ, 120^\circ, 125^\circ, 140^\circ, 145^\circ, 155^\circ, 160^\circ, 165^\circ 170^\circ). \quad (5.10)$$

In the remainder the subtented angles are expressed in radians. By analyzing the curvature of the cross sections in transverse direction, the undeformed, transition and fold regions were determined.

The transverse curvature starts at its undeformed value, indicated by the dashed line in fig. 5.6. It rises when it nears the transition zone; however this change in curvature amounts to a radial change of at most $0.4mm$: twice the thickness of the tape spring. When the curvature falls below the original curvature its decreases sharply, this marks the start of the transition zone. The other dashed line indicates 5% of the original curvature. This marks the start of the fold region and the end of the transition zone. This value was chosen to filter out some numerical errors in the simulation in the fold region. Allthough this value is somewhat arbitrary, it does not change the lengths of the region significantly since the slope of the curvature is so severe.

This data is used to obtain the geometry of the tape spring. Figure 5.7 shows the length of a single transition region as well as the fold radius and angle as a function of the subtended angle. It shows that the length of the transition regions increases

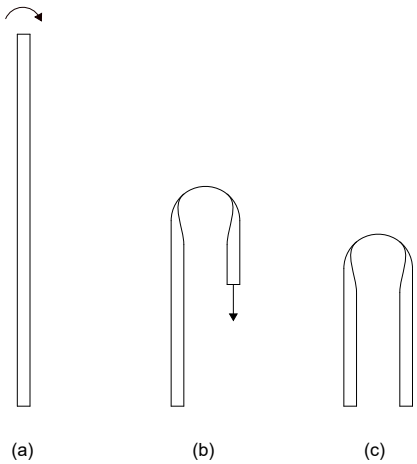

Figure 5.5.: FEM steps: a) end-point rotation of π, b) vertically displace end-points to same height, c) final deformed geometry

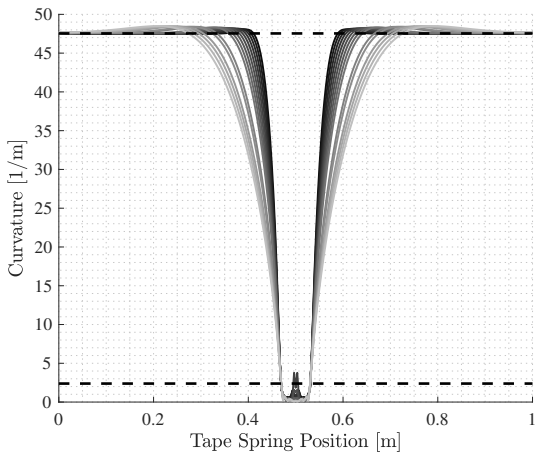

Figure 5.6.: Transverse curvature along the length of the tape springs of the solved simulations, dashed lines indicate bounds of the transition region, darker lines indicate a smaller subtended angle

with the subtended angles. An second order ordinary least square fit is performed on the simulation data and found an expression with a standard error of $1.1 \cdot 10^{-3}$.

$$L_{transition}(m) = 1.7 \cdot 10^{-2} - 1.1 \cdot 10^{-2}\alpha + 2.3 \cdot 10^{-2}\alpha^2 \tag{5.11}$$

The transition zone length L_{trans} is a function of the flexural rigidity D and the subtended angle α in radians.

The figure shows that fold radius is larger than the tape spring radius (indicated

by the dashed line in fig. 5.7), with a mean value 22.1mm. The maximum difference between the tape spring radius and the fold radius is 7%. Above 1.75 radians the radius is fairly constant.

Figure 5.7 also shows that the fold angle θ is not equal to π radians but varies between 2.68 radians and 2.75 radians with a mean value of $\bar{\theta} = 2.73$ radians or 156.2 °.

The range of motion can be determined using eq. (5.3) from the geometry parameters seen in fig. 5.7. The range of motion decreases with increasing subtended angle (fig. 8.5). The transition zone and the fold region is not dependent on the tape loop length. With a smaller tape loop length the ROM might go to zero.

The resulting region decomposition can be seen in an overview in fig. 5.9. The fold circumference, e.g. the product of the fold radius and angle, is constant.

Using the information of the different regions within a tape spring, the energy related to each region could be determined. This energy is summed per region to see the distribution between the different regions, as shown in fig. 5.10. The figure shows that a significant part of the total energy is within the transition regions, starting at roughly 35% of the fold energy at a subtended angle of 1.5rad to about 80% of the fold energy at a subtended angle of 3 °. There is also a small amount of the energy in the undeformed region at smaller subtended angles; this was neglected since it amounted to less than 1% of the total energy content. The energy for both regions was fitted with a first and second order ordinary least square fit for the fold and transition region respectively. The standard errors are $2.5 \cdot 10^{-4}$ and $2.2 \cdot 10^{-3}$ for the fold and transition zone fits respectively; the expressions are as follows.

$$U_{transition} = D(1-\nu)\bar{\theta}(0.967 - 1.12\alpha + 0.543\alpha^2) \tag{5.12}$$

$$U_{fold} = D(1-\nu)\bar{\theta}(-0.163 + 1.06\alpha) \tag{5.13}$$

Figure 5.10 and eq. (5.13) show that the fitted energy profiles in the fold are close to the theoretical values stated in literature (see eq. (5.9)). The energy is the transition zones is epressed in the same manner, but it has a quadratic term.

The total energy contained within a tape spring can be seen in fig. 5.11. This energy is the sum of the energy of the fold and transition zones.

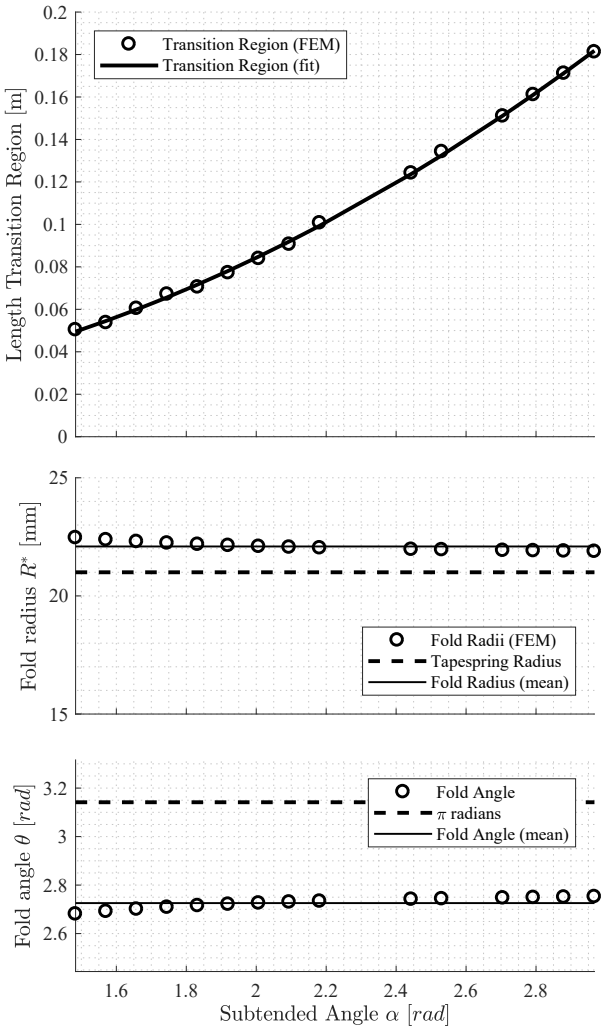

Figure 5.7.: Length of the transition zones, fold radius and fold angle as function of the subtended angle

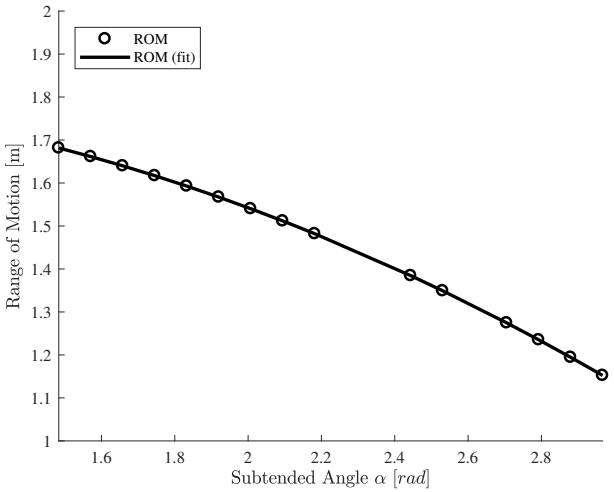

Figure 5.8.: Range of motion for different subtended angles, the length of the total tape loop is 2m

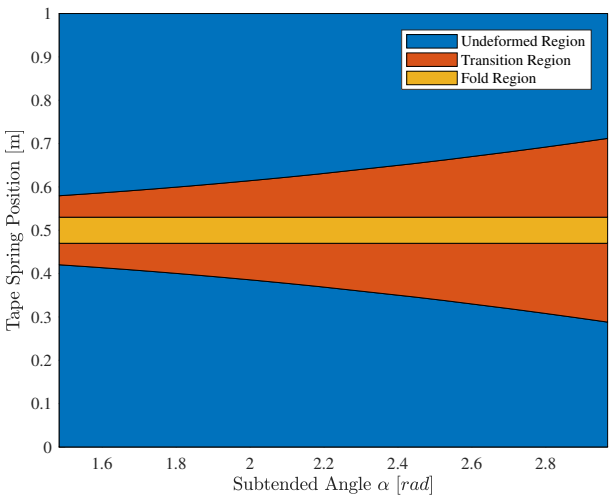

Figure 5.9.: Regions in half of a tape loop for different subtended angles

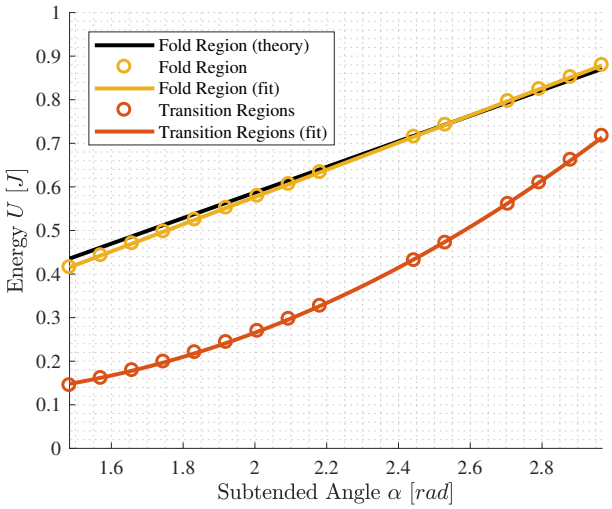

Figure 5.10.: Energy per region for different subtended angles

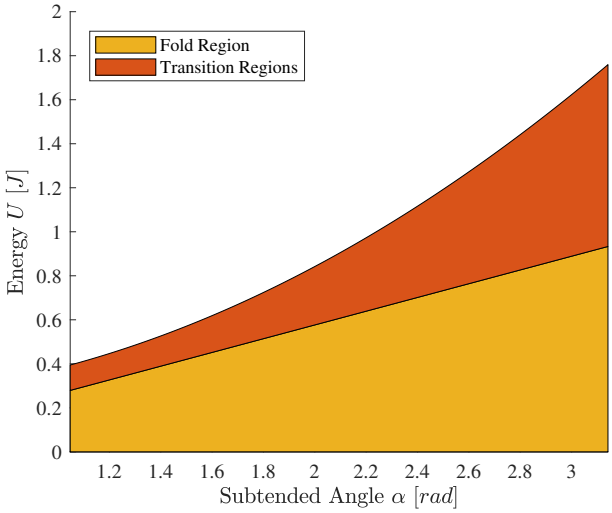

Figure 5.11.: Total energy in a tape loop half for different subtended angles; the energy is divided per region

5.4. Discussion

Figure 5.11 shows that the energy in the transition zone cannot be neglected. The ratio of the transition and the fold region increases with the subtended angle. At small subtended angles, there is also a negligible fraction of the energy within the undeformed region. At even lower subtended angles it can be understood that a tape spring starts to behave like a flat leaf spring. In a leaf spring, the energy is not concentrated at a fold like in a tape spring, but is evenly distributed in the whole structure. The energy of the underformed energy might also be due to an inaccurate definition of the regions. There are small inaccuracies in the simulation themselves. The method also uses certain limits to determine the length of the regions; these limits are chosen and have a margin of error.

There is agreement between the simulation and the simple equation of energy in the fold. As such, this equation can be used for synthesis. The results of the simulation also indicate a limit on the usability of the expression. Below 100 degrees tape loop behavior is no longer assured and the equation becomes inaccurate. In addition, the energy in the transition region cannot be neglected and must be included. As far as the authors are aware no analytical formulation exists that describe the energy content of the transition region; the expression in this paper serves as a first estimation of this formulation.

The results were obtained using FE simulation; it could also be done using the analytical formulations. This would eliminate uncertainties introduced by the FE modelling. In this article all variables of a tape spring were set to a single value except the subtended angle. The qualitative behavior might be different at different values of e.g. the radius, thickness, etc. However, part of the results match with theory which indicates that the chosen parameters are descriptive of a general tape spring.

Three simulations did not converge: 80, 130 and 135 degrees. The initial rotation to create a fold is a buckling problem. Equal sense buckling of a tape spring has a bending and a torsional component. The rotation applies a moment which creates torsional folds near the ends of the tape spring. If the rotation is increased further these folds merge into each other creating a tape spring fold [7]. In some simulations this merger did not happen and caused the simulation to fail. The reason behind this is not entirely clear. The amount of elements is the same in each simulation, therefore the element size is different in each simulation. This likely causes the problem to become ill-conditioned.

The fold radius is clearly not the same as the tape spring radius with a maximum difference of 7%. However, when comparing the energy with the actual fold radii using eq. (5.8) and simplified eq. (5.9) where the radii are assumed to be equal, the maximum difference in calculated energy is only 0.32%. This difference is small enough to be neglected. Furthermore, the fold radius gets larger at small subtended angles. This can be explained by the same phenomena as with the energy distribution. When folding a leaf spring, the smallest energy state of the leaf spring is with the largest radius as possible. Analogously a tape spring with a small subtended angle has a large fold radius. When using a tape spring with varied subtended angle as a force generator, this results in an imperfect straight line linear

guidance. However, when the subtended angle is larger than 100 °, the fold radius is fairly constant. So when keeping the subtended angle above this value, a tape loop could be used as a linear force generator. Figure 5.7 shows that the fold angle is not equal to π radians, but varies from 2.68 radians to 2.75 radians. This is explained by the fact that the curvature of the structure in transverse direction is still not zero, while the structure starts to deform in longitudinal direction. The definition of fold region is that it starts when the curvature in transverse direction is zero, so a small part of the folding already occurs in the transition regions. The product of the fold radius and the fold angle, the fold circumference was independent of the subtended angle. This was unexpected, but the reason is not understood.

The fits show remarkable agreement with the data points. The order of the fits was chosen by hand. The expression for the energy in the fold region has also a term independent of the subtended angle in it; this makes it different from the simplified equation (eq. (5.9)).These values are influenced by the simulation results below 100°, which skew the fit. However, the energy in the fold is linear with respect to the subtended angle and the fit is close to the theoretical expression found in literature.

5.5. Conclusion

We have presented several key aspects that are important for the behavior of a two-fold tape loop.

We have investigated the influence of the subtended angle on these key aspects. FE simulations where the subtended angle was varied between 85 degrees and 170 degrees were used to analyse the geometry and energy state of the tape loop. By using the transverse curvature in a folded tape spring, the lengths of regions of a tape loop were identified. From this all other geometry and energy states were determined.

We have found expressions for the length of the transition zones and the energy in the transition zones and fold regions. The energy in the transition zones is not negligible and has to be taken into account in the design of force generators. At large subtended angles the energy in the transition zone is about 80% of the energy of the fold region. The energy in the fold region increases linearly with the subtended angle and closely agrees with the theoretical expression. The energy in the transition zone increases quadratically with respect to the subtended angle.

The fold radius gets larger with a smaller subtended angle and is always larger than the tape spring radius. The radius dependency can be a problem when a tape loop is used as a linear guide. Nonetheless, this problem can be limited by using subtended angles above 100 degrees.

The fold angle is not a constant of π radians, but varies between 2.68 radians to 2.75 radians with a mean value of 2.73 radians.

These results imply that the transition regions can not be neglected, but should be incorporated into the synthesis method of a force generator using two-fold tape loops. The subtended angle should preferably be larger than 100 degrees to limit the subtended angle dependency of the fold radius.

5.6. Author Contributions

M.G.J. and W.W.P.J.S. proposed the research. M.G.J. designed the research and performed the numerical calculations. M.G.J. wrote the core of the paper, which was accepted as a conference paper. W.W.P.J.S. extended on the theory presented and rewrote the paper for journal publication. W.W.P.J.S. and J.L.H.supervised the project and reviewed the paper.

Bibliography

[1] M. G. De Jong, W. W. P. J. van de Sande, and J. L. Herder. “Properties of Twofold Tape Loops: The Influence of the Subtended Angle”. In: *Journal of Mechanisms and Robotics* 11.2 (2019).

[2] L. L. Howell, S. P. Magleby, and B. M. Olsen, eds. *Handbook of Compliant Mechanisms*. New Delhi, India: John Wiley & Sons Ltd., 2013, p. 342.

[3] A. Lamers, J. A. G. Sánchez, and J. L. Herder. “Design of a statically balanced fully compliant grasper”. In: *Mechanismand Machine Theory* 92 (2015), pp. 230–239.

[4] S. Kota, J. Joo, Z. Li, S. M. Rodgers, and J. Sniegowski. “Design of Compliant Mechanisms: Applications to MEMS”. In: *Analog Integrated Circuits and Signal Processing* 29 (2001), pp. 7–15.

[5] G. Radaelli and J. L. Herder. “Gravity balanced compliant shell mechanisms”. In: *International Journal of Solids and Structures* 118-119 (2017), pp. 78–88.

[6] C. R. Calladine. “The theory of thin shell structures 1888-1988”. In: *Institution of Mechanical Engineers* 202.A3 (1988), pp. 141–149.

[7] K. Seffen and S. Pellegrino. “Deployment dynamics of tape springs”. In: *Proceedings of The Royal Society A: Mathematical, Physical and Engineering Sciences* 455 (Mar. 1999), pp. 1003–1048.

[8] Ö. Soykasap. “Analysis of tape spring hinges”. In: *International Journal of Mechanical Sciences* 49 (2007), pp. 853–860.

[9] F. P. J. Rimrott. “Storable tubular extendible members”. In: *Engineering Digest* (1966).

[10] K. Seffen, Z. You, and S. Pellegrino. “Folding and deployment of curved tape springs”. In: *International Journal of Mechanical Sciences* 42.10 (2000), pp. 2055–2073.

[11] K. Seffen, Z. You, and S. Pellegrino. “Folding and deployment of curved tape springs”. In: *International Journal of Mechanical Sciences* 42.10 (2000), pp. 2055–2073.

[12] J. Costantine, Y. Tawk, C. G. Christodoulou, J. Banik, and S. Lane. “CubeSat Deployable Antenna Using Bistable Composite Tape-Springs”. In: *IEEE Antennas and Wireless Propagation Letters* 11 (2012), pp. 285–288.

[13] H. Mallikarachchi and S. Pellegrino. “Quasi-Static Folding and Deployment of Ultrathin Composite Tape-Spring Hinges”. In: *Journal of Spacecraft and Rockets* 48.1 (Jan. 2011), pp. 187–198.

[14] A. Yellowhorse and L. L. Howell. “Deployable lenticular stiffeners for origami-inspired mechanisms”. In: *Mechanics Based Design of Structures and Machines* 46.5 (2018), pp. 634–649.

[15] C. Vehar, S. Kota, and R. Dennis. “Closed-Loop Tape Springs as Fully Compliant Mechanisms: Preliminary Investigations”. In: vol. Volume 2: 28th Biennial Mechanisms and Robotics Conference, Parts A and B. International Design Engineering Technical Conferences and Computers and Information in Engineering Conference. Sept. 2004, pp. 1023–1032. eprint: https://asmedigitalcollection.asme.org/IDETC-CIE/proceedings-pdf/IDETC-CIE2004/46954/1023/2617091/1023_1.pdf.

[16] NASA. *Rolamite: New Mechanical Design Concept*. Tech. rep. 67-10611. Springfield, Virginia: NASA, 1967.

[17] R. V. Cadman. *Rolamite - Geometry and Force Analysis*. Tech. rep. Albuquerque, N. Mex.: Sandia Laboratories, 1970, p. 294.

[18] C. English and D. Russell. “Implementation of variable joint stiffness through antagonistic actuation using rolamite springs”. In: *Mechanism and Machine Theory* 34 (1999), pp. 27–40.

[19] G. Radaelli and J. Herder. “Gravity balanced compliant shell mechanisms”. In: *International Journal of Solids and Structures* 118-119 (2017), pp. 78–88.

[20] S. Bourgeois, B. Cochelin, F. Guinot, and E. Picault. “Buckling analysis of tape springs using a rod model with flexible cross-sections”. In: *European Journal of Computational Mechanics* 21.3-6 (2012), pp. 184–194.

[21] S. Walker and G. Aglietti. “A study of tape spring fold curvature for space deployable structures”. In: *Proceedings of the Institution of Mechanical Engineers, Part G: Journal of Aerospace Engineering* 221.3 (June 2007), pp. 313–325.

[22] K. A. Seffen. “On the Behavior of Folded Tape-Springs”. In: *Journal of Applied Mechanics* 68 (2001), pp. 369–375.

[23] G. Radaelli and J. L. Herder. “Shape optimization and sensitivity of compliant beams for prescribed load-displacement response”. In: *Mechanical Sciences* 7 (2016), pp. 219–232.

[24] J. A. Cottrell, T. J. R. Hughes, and Y. Bazilevs. *Isogeometric analysis : toward integration of CAD and FEA*. Wiley, New York, USA, 2009, p. 335.

6

Design and evaluation of a passive constant force mechanism for a cardiac ablation catheter

Werner W.P.J. van de Sande, Awaz Ali, Giuseppe Radaelli

Contact force management has been proven to have a positive effect on the outcome of cardiac ablation procedures. However, no method exists that allows maintaining a constant contact force within a required and effective range. This work aims to develop and evaluate such a constant force mechanism for use in an ablation catheter. A passive constant force mechanism was designed based on a tape-loop. The tape-loop consists of two tapered springs that work in parallel. A finite element analysis was carried out to verify the behavior and performance of the design. A design based on requirements for a constant force ablation tip showed an average force of about $7.8 \times 10^{-2}\,\mathrm{N} \pm 8 \times 10^{-3}\,\mathrm{N}$ *over* $20\,\mathrm{mm}$ *in simulation. A scaled prototype was built and evaluated to prove the validity of the concept; this prototype provides an average force of* $1.3 \times 10^{-1}\,\mathrm{N} \pm 1.6 \times 10^{-2}\,\mathrm{N}$ *over* $35\,\mathrm{mm}$. *The mechanism allows for controlled delivery of contact force within a desired and effective range. Based on these findings it can be concluded that the approach is successful but needs to be optimized for future applications. Being able to control the delivery of contact force in a constant range may increase the effectivity of cardiac ablation procedures and improve clinical outcomes.*

This chapter originally appeared as W. W. P. J. van de Sande, A. Ali, and G. Radaelli. "Design and evaluation of a passive constant force mechanism for a cardiac ablation catheter". In: *Journal of Medical Devices* 15.2 (2021)[1]

6.1. Introduction

RADIO Frequency (RF) ablation catheters are commonly used for the treatment of atrial fibrillation (AF). For an effective treatment that isolates the rhythm disturbances, the contact between ablation tip and heart tissue must be constant and lead to transmural lesions. More specifically, the amount of applied contact force plays a significant role in the treatment when creating transmural lesions [2]. The amount of contact force that is applied to the tissue is dependent on the controllability and stability of the catheter tip. Generally, the electrophysiologist experiences a variable contact force that increases and decreases along with the cardiac cycle, ranging between 0 and 0.39 N. In addition to the cyclic cardiac movements and blood flow, the complex atrial anatomy as well as the clinical requirements for circumferential or linear ablations make it a challenging task to deliver the appropriate amount of contact force and generate transmural lesion. A contact force below the required value goes at the expense of the effectivity of the treatment. A contact force higher than the required value can result in tissue perforations and steam pops. Earlier studies showed a recurrence rate of 100% one year post treatment when the mean catheter contact force was below0.10 N [3]. When the mean contact force was above 0.20 N, the success rate of the procedure increased to 80% [3]. Moreover, as the lesions are created by ablating a subsequent number of transmural points, the risk of incomplete isolation remains with variable stability and therefore with variable contact force. A constant contact force range could prevent the decreased effectivity or negative side-effects related to the fluctuating contact force. It would additionally allow the possibility of dragging the ablation catheter tip along the pathway, hereby decreasing the risk of incomplete isolation. However, no such ablation catheter exists yet.

Even though there are no known catheters that allow for a constant contact force, some efforts have been made in the past decade to simplify or solve the issue using different methods or surrogates [4]. First, contact force sensors are widely applied in ablation catheters and allow a visualization of the amount of applied force. Commercially available examples of this type of ablation catheter include the TactiCath® catheter (St. Jude, MN, USA) showing real-time visualizations of the contact force, and the ThermoCool® SmartTouch™ catheter (Biosense Webster, USA) which displays graphical and numerical visualizations of the contact force. The IntelliSense® (Hansen Medical Inc., Mount View CA, USA) provides besides contact force visualization, also feedback in the form of vibration. Multiple studies have proven the positive effect of the systems on the effectivity of the procedure [5, 6]; however, these systems do not provide a feedback loop in adjusting the contact force. Second, various efforts have been made to compensate for the beating heart motion and thereby simplify the manipulation of the catheter during ablation. Examples include robotic systems and steerable catheters that have shown significant improvements in the control of the amount of delivered contact force [7–9] such as the Agilis steerable sheath and the Stereotaxis magnetic system. Third, various balloon- and basket- configurations have been developed to aid the placement and stabilization of the catheter tools inside the heart while the ablation is carried out [10, 11]. However, none of the developed and studied systems allows for

controlled delivery of a contact force within a desired and effective range.

In terms of efficiency and effectivity, the ablation procedure can potentially benefit from a mechanism that provides a constant force at the catheter tip. Actively controlled mechanisms, in which the applied force is measured and controlled by a feedback loop and an actuator, e.g. an electromotor, present multiple challenges and drawbacks for the present case. This includes for example the reliability, feedback time delay, miniaturization, complexity and costs. A passive mechanism that applies a constant force without active control could lead to a more elegant, collocated solution. There are numerous examples of passive constant force mechanisms for various applications and sizes [12–17]. However, most systems found in literature occupy a large volume with respect to the range of motion where the force is constant. The large volume-to-range ratio makes these systems unsuitable for the current application because the mechanism must be fed through the narrow catheter sheath. The known systems where the range of motion is large, e.g. [15] and [18], present other drawbacks in terms of lateral stiffness and drift with respect to the desired rectilinear motion in the direction of the applied force. In the current case this can lead to uncontrolled positioning of the catheter tip.

A tape loop [19, 20] is a compliant mechanism that has a better volume-to-range ratio. A tape loop is created when the two ends of a tape spring are connected. This determines the kinematics of the resulting mechanism, namely a rectilinear motion. A basic tape loop has a constant cross section which creates a zero force and zero stiffness straight-line guidance. The force output of a tape loop can be tailored by varying the geometry or material properties. A linearly decreasing profile of the cross-section creates a near constant force profile. Because such a mechanism can be scaled down, it can be used as a constant force catheter tip. The objective of this paper is to present the novel concept of a tapered tape loop used to generate a constant force, applicable to the tip of an ablation catheter. To do so, a finite element analysis will be performed to validate the design and a scaled prototype will be constructed and evaluated. The paper is structured as follows. The method section presents the design context and the requirements derived from it, an elaboration on the conceptual design and the dimensioning of the design based on a simplified mechanical model. Subsequently, the finite element analysis and its results are shown. Then the physical realization of the scaled prototype is dicussed and next the experimental setup and the results is described. The paper ends with the discussion and the conclusion.

6.2. Method

There are several requirements on the tape loop for it to be used as a constant force catheter tip.

Passive constant force mechanism The passive mechanism must apply a constant force for the desired range of motion at high speed beating heart movements. The amount of constant contact force is set to 0.20 N with a tolerance of 10%. Studies have shown major improvements in the outcomes of ablation

of atrial fibrillation procedures when a mean contact force of 0.20 N could be maintained [4].

Biocompatible materials The mechanism must consist of biocompatible materials, typically used in catheter systems, to ensure a safe biological response of the cardiovascular environment. Typical materials included in the catheter tip comprise metals and metallic alloys such as stainless steel and nitinol, as well as polymeric materials such as polyurethanes and polyethylene.

Dimensions To make it suitable for use in an ablation catheter, the constant force mechanism must be designed with a diameter that can ultimately be downsized to 2 mm to 3 mm. The length of the constant force mechanism is preferably short enough to allow additional tip length for other functions such as steerable joints. Additionally, the mechanism must fit inside or atop of a catheter. To generate a first experimental prototype and evaluating the working principle, the dimensions of the manufactured prototype are set larger but must be down-sizable.

Relative movement The mechanism must allow the possibility for relative movement within the catheter to function along with an ablation catheter. This requires that the mechanism must be integrated inside or on top of a catheter, while leaving space for ablation electrodes, irrigation channels, and other typical components.

Simplicity To not complicate regular catheters and their control, the added constant force mechanism must be as simple as possible. The simplicity is expressed in the number of parts and by keeping those low, it is expected that the manufacturability as well as control of the mechanism are simpler.

There are two types of constant force devices: devices in which the elastic potential energy remains constant and devices in which the elastic potential energy increases linearly. In the first case the force is zero, in the second the force is non-zero. In both cases the second derivative of the potential energy function will be zero; the result is a mechanism with zero stiffness.

The principle of constant potential energy is seen in tape loops with a constant cross-section. A specific length of tape spring is folded twice, and the two ends are connected, see fig. 7.1. Tape springs are defined by a length L, a radius R, a thickness t and a subtended angle α, see fig. 7.3.

A basic two-fold tape loop has constant geometric and material properties along its length. This tape loop consists of four parts: two folds and two mostly undeformed tape spring segments. The two segments contain so-called transition-zones. In these zones a tape spring transitions from solely transverse curvature to the solely longitudinal curvature of the fold. The length of these zones is dependent on the properties of the tape spring [21].

Potential energy in a tape loop is stored in the folds and in the transition zones. The energy in a fold is linear with the angle of the fold. As the fold has a constant radius R^*, the strain state is the same everywhere in the fold. Therefore, the strain

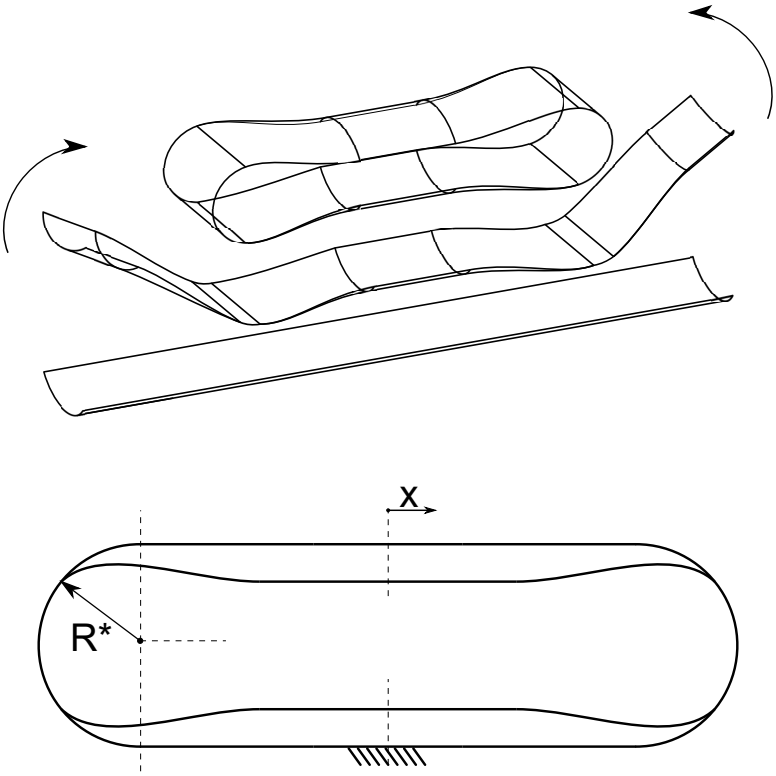

Figure 6.1.: A tape-loop is obtained by connecting two ends of a tape spring. In the obtained closed loop the distance between the straight segments is constant and rolling can be done without changing the potential energy of the system thus requiring zero elastic force. Pictures are modified from [20, 21].

energy density is the same at any part of the fold. Material moves in and out of the fold during motion of the tape loop.

Motion is created by rolling the tape loop; it has one degree of freedom. In this rolling movement, segments of the tape spring move from the un-deformed sections into the fold and vice versa. The shape of the tape loop remains unchanged. The tape loop acts as a linear guidance. As the same amount of material moves into the fold as out of the fold, the obtained loop is in a state of neutral equilibrium, since the position of the folds has no influence on the total potential energy of the system. As a result, a rolling movement can be performed without elastic resistance, even though the material is continuously deforming elastically.

When the cross-section of the tape spring is not constant along its length, a non-zero force is generated. After connecting the two ends the system is not in a state of neutral equilibrium anymore, but rather moves the folds towards the most narrow part of the tape spring. The amount and gradient of the force can

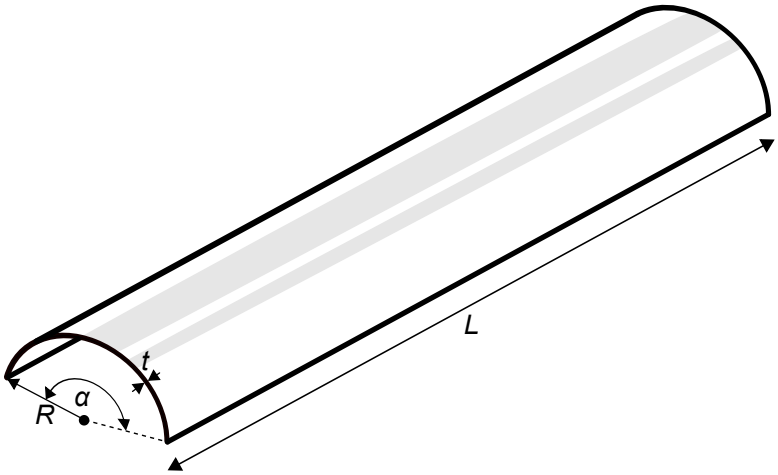

Figure 6.2.: Geometry of a piece of tape spring with a length L, a radius R, a thickness t and a subtended angle α. Pictures are used from [21].

be regulated by the cross-section of the tape spring. This gives the possibility to design different force-displacement characteristics, of which a constant force is a particularly interesting one. The result is a minimalistic, monolithic, scalable design of a rectilinear, self-constrained, constant force mechanism. How the tapered tape loop can be integrated in a catheter tip design is shown in fig. 6.3.

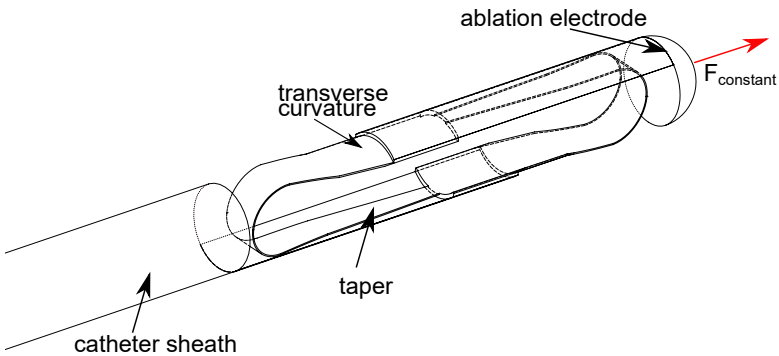

Figure 6.3.: The proposed solution consists of a two-fold tapered tape-loop. The tapering of subtended angle of the spring is responsible for the constant force. The transverse curvature of the tape makes it possible to maintain the radius of curvature, thus the overall diameter, constant without additional constraints [22].

The proposed tape loop is constructed from two tapered tape springs that work in parallel. The requirements of the tape loop can be seen in table 6.1.

The range of motion is defined by the length of the tape spring segment. The

Table 6.1.: Requirements on the design of the tape loop

Property	Symbol	Value	Unit
Range of motion	Δ x	$20.0 \cdot 10^{-3}$	m
Required force	F_{req}	$1.00 \cdot 10^{-1}$	N
Radius of tape loop	R	$1.75 \cdot 10^{-1}$	m

length of the tape spring consists of one piece in the fold of the tape loop, l_{fold} in fig. 8.5, and two relatively undeformed lengths of the tape spring, l_{top} and l_{bottom} in fig. 8.5. The location of the end-effector is shown as x.

The right end of the bottom segment is considered ground and at $x = 0$. The location of the end-effector is as follows.

$$x = -l_{bottom} + l_{top} \tag{6.1}$$

The length of the fold remains constant during motion and does not contribute directly to the x-location of the end-effector. The total length of the tape spring is the sum of all segments [21].

$$L = l_{top} + l_{bottom} + l_{fold} = l_{top} + l_{bottom} + \pi R \tag{6.2}$$

The point on the tape spring where the folds starts is defined as l; as such, l is equal to l_{bottom}. The relation between l and the position of the end-effector, x, is obtained by rewriting eq. (6.2) into eq. (6.1) and substituting l for l_{bottom}.

$$x(l) = L - \pi R - 2l \tag{6.3}$$

The range of motion is determined by the difference between the smallest and largest possible values of l. The smallest possible length of the bottom segment is the length of the transition zone, l_{trans}. At this point, the deformation in the transition zone is hindered by the clamps, which increases stiffness. The same is also true for the largest possible value, which is when the top segment is at is smallest. This gives the following minimum and maximum values.

$$l_{min} = l_{trans}; l_{max} = L - \pi R - l_{trans} \tag{6.4}$$

The range of motion is the determined by the minimum and maximum locations of the end-effector.

$$\Delta x = x(l_{min}) - x(l_{max}) = 2l_{max} - 2l_{min} = 2L - 2\pi R - 4l_{trans} \tag{6.5}$$

This is rewritten to obtain the needed length of the tape spring segment. Considering the radius of the tape loop, it is chosen that the total length of the transition zones is about 1.5 times the length of the fold. This value was estimated after several FE simulations.

$$L = \frac{\Delta x}{2} + \pi R + 2l_{trans} = \frac{\Delta x}{2} + 3.5\pi R = 2.92 \cdot 10^{-2} m \tag{6.6}$$

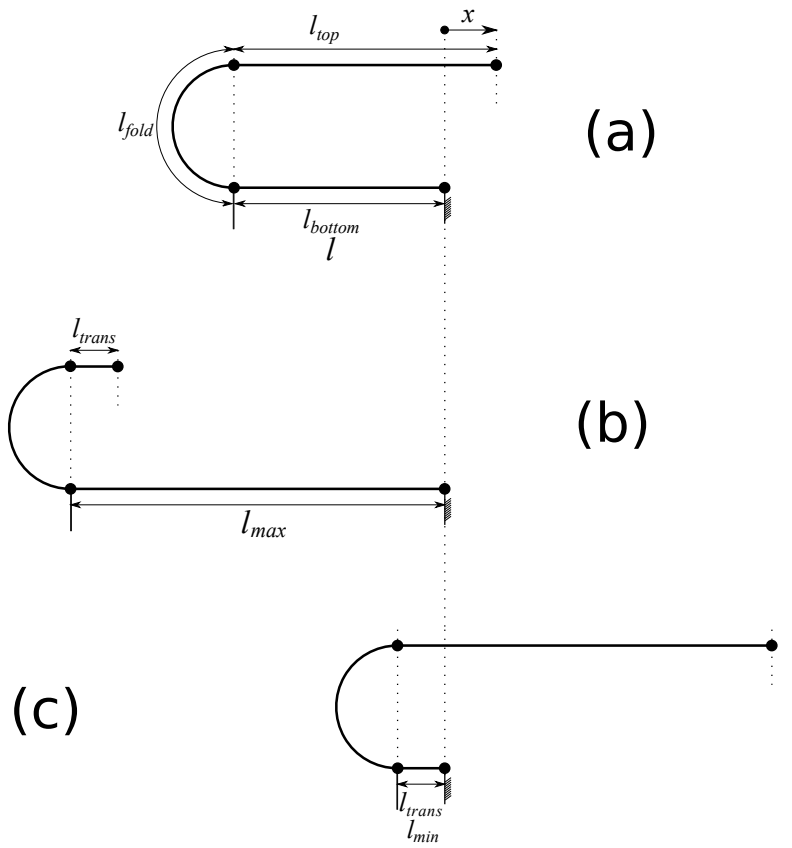

Figure 6.4.: Schematic overview of one half of the tape loop. (a) It consists of 3 parts: 2 relatively un-deformed segments l_{top} and l_{bottom} and the fold, here denoted by l_{fold} which has a radius R^*. The tape spring is connected to ground at the bottom segment and the end-effector is chosen to be the right end of the top segment.(b) The largest value of l, where the top segment is the length of the transition zone, l_{trans}. (c) The smallest value of l, where the bottom segment is the length of the transition, l_{trans}.

The energy of a tape spring fold is as

$$U = D(1-\nu)\theta\alpha \tag{6.7}$$

where $D = Et^3/12(1-\nu^2)$, E is the Young's modulus, t is the thickness and ν the Poisson's ratio. The fold angle is θ, and the subtended angle is α. This formula is derived from the work of Seffen [23]; this work uses a description of energy for a tape spring based on plate theory. In this derivation it is assumed that the longitudinal radius of the tape spring does not change. For simplicity, it is assumed that nearly all energy is stored in the fold and almost no energy in the transition

zones. In this instance we fold the tape spring to πrad and we vary the subtended angle. The energy stored in the fold will vary as the tape loop moves. The required force can be obtained by determining the change in this energy over the required range of motion. Quasi-static behaviour is assumed in this derivation.

$$F_{req} = \frac{\Delta U}{\Delta x} \rightarrow \Delta U = F_{req}\Delta x = D(1-\nu)\pi\Delta\alpha \tag{6.8}$$

We can solve this equation for $\Delta\alpha$. This difference between the start subtended angle and the end subtended angle must be 0.51πrad, which is 92°. The maximum value of the subtended angle is in theory limited to πrad or 180°; any value higher could cause the tape loop to self-intersect. The maximum value is set to 3rad to be safe. Table 6.2 lists all material and geometric properties of the tape spring.

Table 6.2.: Material and geometric properties of the design

Property	Symbol	Value	Unit
Young's Modulus	E	210	GPa
Poisson's Ratio	ν	0.3	-
thickness	t	$35\cdot10^{-6}$	m
length	L	$2.92\cdot10^{-2}$	m
radius	R	$1.75\cdot10^{-3}$	m
maximum subtended angle	α_{max}	0.95π	rad
minimum subtended angle	α_{min}	0.44π	rad

6.3. Numerical Validation

A finite element analysis was carried out to verify the behavior and performance of the design with higher fidelity. The requirements of table 6.1 were used to obtain the variables of table 6.2. These variables were used in the simulation. An isogeometric analysis formulation [24] was used for this purpose. The tape loop was modelled with Kirchhoff-Love shell elements with an isotropic, linear elastic material. In the transverse direction 15 elements are used; lengthwise 130 elements are used. An initially straight portion of a tapered tape loop was bent into a single fold by applying a 180° rotation on one end and fixing the other end. Subsequently, a displacement in the longitudinal direction was applied while maintaining the applied rotation as a constraint, thereby avoiding the need to simulate the other half of the system with the other fold, see fig. 6.5. The curved edges at the two extremes of the tape are stiff and have a stiff connection to a point at which the rotation and displacement boundary conditions were applied. This was done to avoid very local deformation of the shell near the edges to simulate clamping conditions. In the physical implementation this would approach the effect of a rigid clamping of the ends. The force-displacement characteristic resulting from the finite element analysis is shown in fig. 6.6. The force-displacement diagram shows an initial ramp up of the force followed by a smooth transition to a fairly constant force region, and followed by a smooth transition to a steep force increase again. This region

of fairly constant force has an average value of 0.078 N. This value is obtained by determining the average force of segments of the force-displacement graph that are as long as the desired range of motion (20 mm). The segment that has the best least squares fit to that average is selected as the constant force region. The outermost points of the range of motion in the simulation data differ about 10% from the average. The average is 0.078 N, which is below the required 0.1 N for a tape loop half. Figure 6.7 shows the von Mises strains on the tape loop at the last load-step. This is the situation wherein the portion with the largest subtended angle enters the fold region, thus with the highest potential energy state.

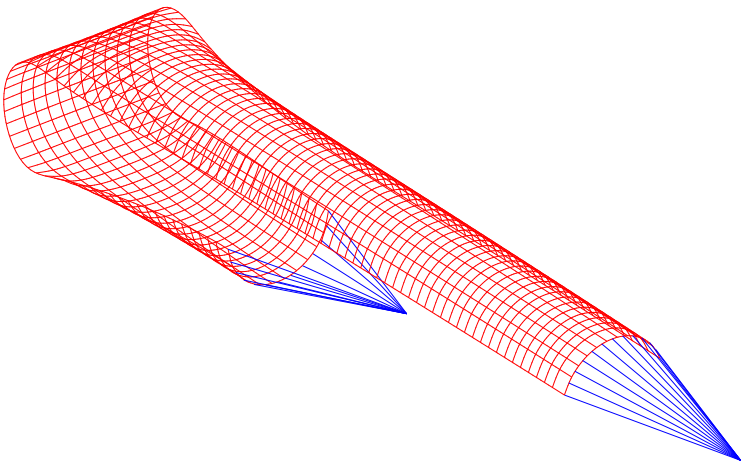

Figure 6.5.: A numerical model of a single fold of the tapered tape loop is simulated using an isogeometric analysis method. The bend is introduced by applying a 180° rotation to one end of the tape while constraining the other end. Subsequently, the rotated point is displaced in longitudinal direction, causing the rolling motion. The edges at the extremes of the loop have a stiff connection to the points of application of the boundary conditions. These connections are represented by the blue lines.

Prototype

A prototype was manufactured to validate the concept. While the intended design could not be manufactured due to limitations, the behavior of this type of mechanism could be validated. The dimensions used for the prototype were based on the current manufacturing possibilities; the dimensions are within one order of magnitude of the intended design. First the flat geometry was cut out of a 100 mm wide and 50 µm thick sheet of stainless steel (1.4310). The flat geometry, see fig. 6.8,

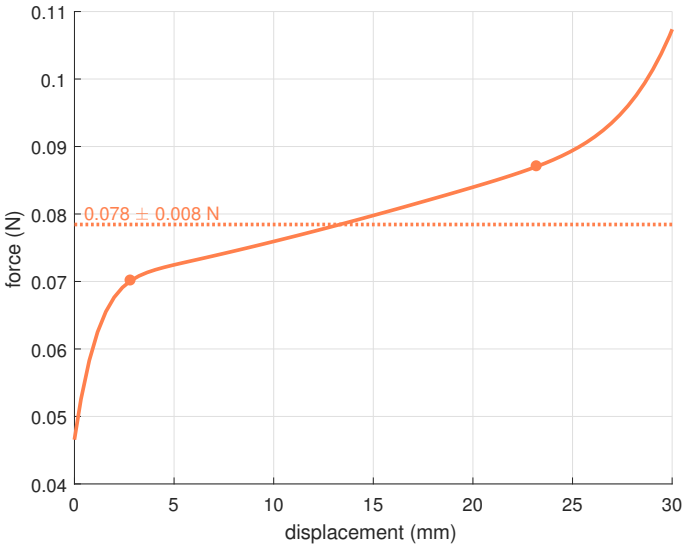

Figure 6.6.: The result of the displacement-controlled simulation of the single fold of the tape. The average value of the fairly constant force region is denoted by the dotted line. The markers denote the outermost positions of the range of motion. The number describes the average value and the deviation of the outermost points from that average. The output force of the entire design, i.e. with a double fold, yields the same force-displacement diagram with double magnitude.

was cut with a manual plate cutting machine and then rolled to a constant radius across its surface. The steel that is used is known for springback. The final radius of the tape spring is therefore not equal to the radius to which it is rolled. The ratio between the rolled radius and the radius after springback was obtained after rolling several tape springs. The steel was rolled to a radius of 2 mm; the actual radius after springback was measured to be 5 mm.

Given this ratio, the flat geometry was determined to have at least a subtended angle of 100° (1.75 rad). This is done to ensure a constant radius of the tape loop fold in motion [21].

The largest subtended angle should be as close to 180° (πrad) as possible, but not exceed it. The width was therefore chosen to not exceed a subtended angle of 170° (2.97 rad). Given the intended radius of the tape springs, the subtended angles were converted to circumferences to create the flat geometry. The tape spring was measured after rolling to obtain the actual radius and subtended angle. After rolling, two equal tape springs were clamped into 3D-printed blocks, which closed the loop, see fig. 6.9. The material is the polymer PLA (Polylactic acid) and it assumed to be rigid enough as to not influence the behavior of the tape loop. The tape spring was clamped along a length of 5 mm at each end. This length was subtracted from the

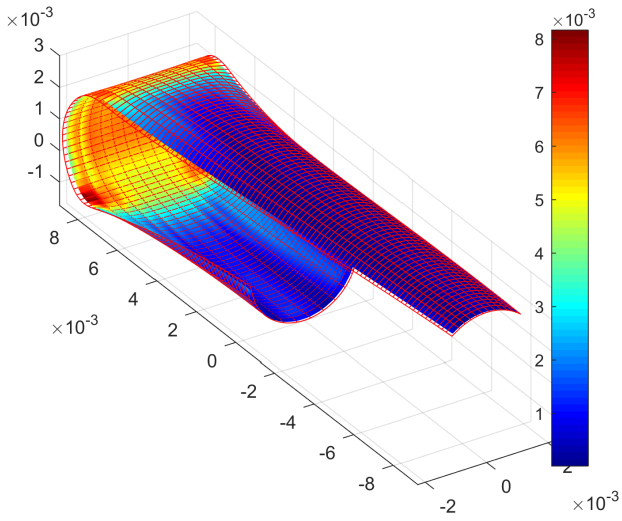

Figure 6.7.: This figure shows the distribution of the von Mises strains on the simulated tape loop in its end position. At the edges of the transition zones the strain concentrations are the highest.

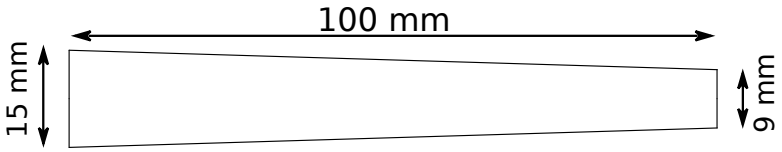

Figure 6.8.: The geometry of the strips that are cut from a sheet of spring steel.

initial length. This also influenced the start and end subtended angles. Table 6.3 contains the values that were obtained for the tape springs.

Table 6.3.: Material and geometric properties of the prototype

Property	Symbol	Value	Unit
Young's Modulus	E	210	GPa
Poisson's Ratio	ν	0.3	-
thickness	t	$50 \cdot 10^{-6}$	m
length	L	$9 \cdot 10^{-2}$	m
radius	R	$5 \cdot 10^{-3}$	m
maximum subtended angle	α_{max}	0.93π	rad
minimum subtended angle	α_{min}	0.59π	rad

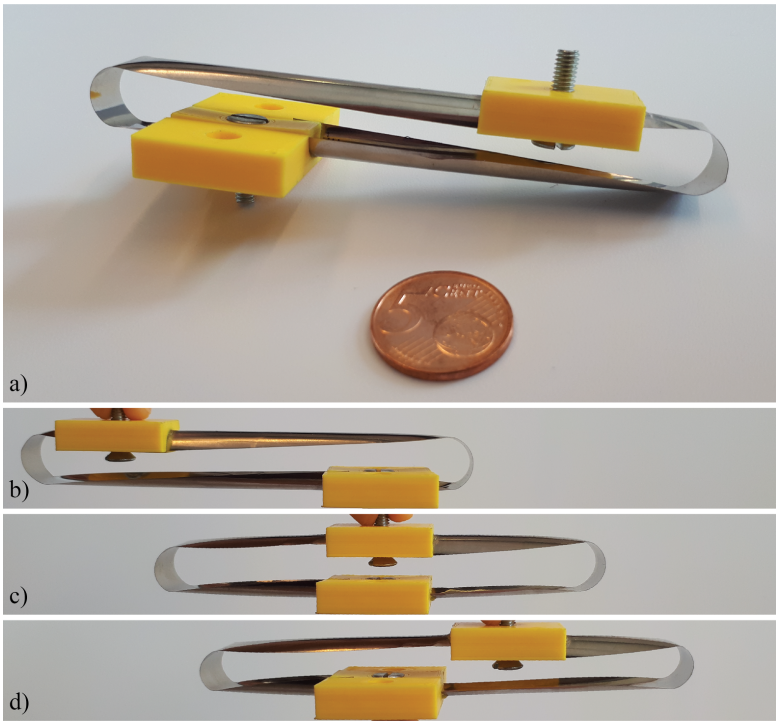

Figure 6.9.: A prototype of the concept was fabricated from a 50 µm. thick stainless-steel sheet, with a diameter of 10 mm. Figures b, c and d show the prototype in three stances within the range of motion.

Experimental Validation

The prototype was validated through an experiment in which the force-displacement was measured. The measurement setup is shown in fig. 6.10. The tape springs and clamps are denoted as D and E in fig. 6.10.

One clamp was rigidly connected to ground. The other was connected to a 1 degree of freedom (DOF) force sensor (C in fig. 6.10) (Futek LSB200, 10 lb) and via a rigid rod (B in fig. 6.10) to a 1 DOF platform (A in fig. 6.10). This platform actuated the tape loop in its degree of freedom.

The rod was aligned as much as possible with the motion direction of the tape loop. The platform pulled the tape loop via the rod. This was done at a speed so that quasi-static behaviour was ensured. The measurement was ended when the force started to increase rapidly. The measurement was additionally conducted backwards, relaxing the tape loop. The force and displacement data was logged in Labview; after which post-processing was carried out in Matlab.

The result of the measurement can be seen in fig. 6.11. The displacement is 70 mm and was divided in 1000 steps. The force measurement was measured at every step with a resolution of 0.024 N. The data was smoothed with a moving

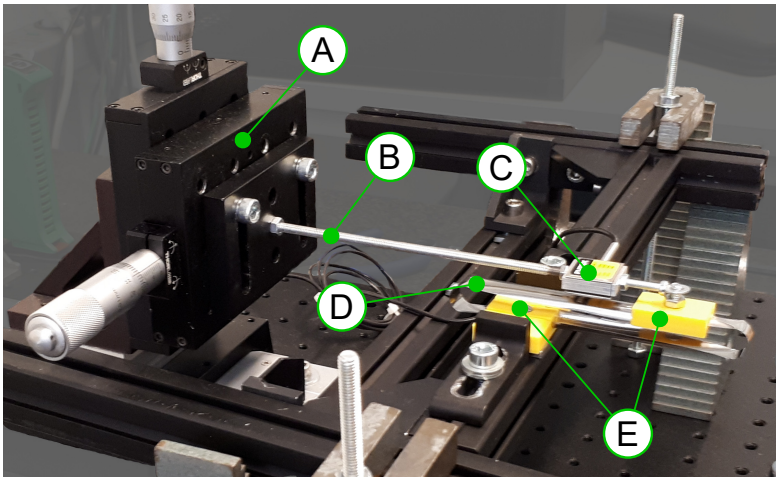

Figure 6.10.: The experimental setup consists of linear motion stage and a force sensor. The motion is transferred to the prototype through a rigid rod.

average filter of 50 samples. The graph shows the measured force for the forward and backward motion, shown in blue in fig. 6.11 respectively. The experimental data was compared to a simulation (orange in fig. 6.11) which used the geometric and material properties outlined in the prototype section. As the simulation only provided the force output of half the tape loop, the amount was doubled.

Again, the averages are obtained by determining the average force of segments of the force-displacement graph that are as long as the range of motion. The segment that has the best least squares fit to that average is selected as the constant force region. The range of motion is obtained using the values in table 6.3 and eq. (6.5); here, the range of motion is 35mm. The thicker tape spring influences the length of the transition zones, which influences the range of motion. In the simulation, the length of the transition zones was chosen to be 1.8 times the length of the bend zone. This value results in a constant force region that is similar in shape as the one obtained in section 6.3. The same range of motion was used for the values obtained in the experiment.

The outermost points of the range of motion in the simulation data differ about 12% from the average. For the experimental data this is 25% and 28% for the forward and backward motion respectively. Furthermore, due to hysteresis the averages of the experimental data exceed the deviations in the simulation data; the area enclosed in the hysteresis loop is wider than the 12% band.

6.4. Discussion

A concept for a constant force catheter tip for use in cardiac ablation tools has been proposed and its working principle has been presented and validated through numerical simulations and experiments. This concept of a constant force mechanism

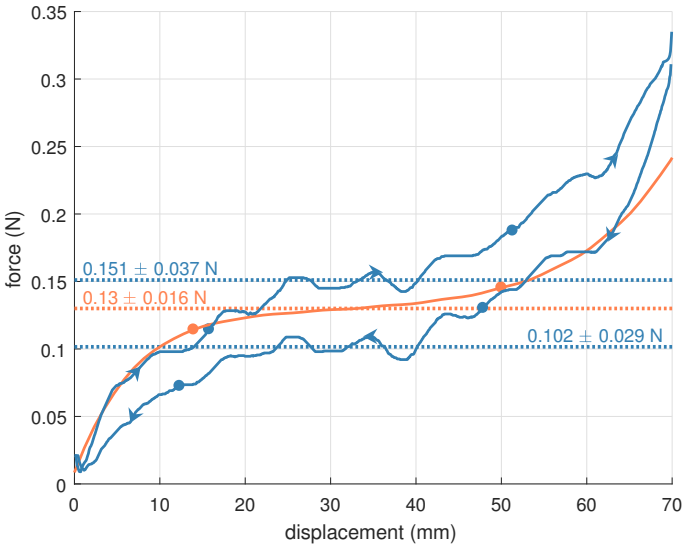

Figure 6.11.: The force-displacement graph shows the measured force in the forward and backward motion (blue) together with the numerical simulation results (orange) of a geometry with matching dimensions. The average values of the fairly constant force regions are denoted by the dotted lines. The markers denote the outermost positions of the range of motion. The deviation of these points to average is listed. This is done for the simulation, the forward and backward motions seperately.

is promising, because of its simplicity and the integrated mechanical functions, i.e. motion guiding and force generation. However, the development is at its initial stage and a number of questions and challenges, both technical as well as clinical, still remain.

Technically, one of the main challenges remaining is the fabrication of the mechanism at real scale. Although the produced prototypes are already unique achievements in terms of the thickness to curvature ratio at the current small scale, the scale required for the application has not yet been achieved. The stresses in the folds of the tape loop are also too high for steel. At the desired scale, these stresses will be even higher. Material choice must be taken into account in future designs. In addition, the design is currently focusing on the mechanical behavior only, while an ablation catheter requires multiple other design features including the electronics and an irrigation system.

Regarding the clinical application, it is unclear whether a constant force mechanism with rectilinear guidance as presented in this study is preferable with respect to a more compliant guidance. In such an alternative concept the constant force could be produced in a given range of motion, allowing sideways deviations from the rectilinear motion. The trade off is the controllability of the surgeon's actions versus

self-adaptivity of the tip with respect to its moving environment.

Finally, even though the developed mechanism has been proposed for an ablation catheter tip, the mechanism could be beneficial in other application domains too. This mainly accounts for circumstances in which a constant force is required but in which the conditions do not permit the use of a complex mechanism. In the medical domain this could be the case in, e.g., instruments for laparoscopy.

The constant force mechanism was realized based on the analytical model of the potential energy in tape loops, considering the energy in the folds while excluding the energy in the transition zone and in the straight zone. This simplification was justified because of the dominant contribution of the folds to the total energy of the system. In addition, in the simplified model the effect of the boundary conditions of the tape loop, i.e. the clamping at both ends, was not taken into account and this served as a second simplification.

These simplifications also cause a lower average force than set by the requirements; the desired force is 0.10 N, whereas the simulation only showed an average force of 0.08 N. It was also noticed that the finite element simulations did not yield a perfectly constant force. This was presumably caused by the first simplification. The second simplification led to a main effect in which the constant force effect was disturbed when the fold was close to one of the clamping zones. In the force-displacement characteristic this resulted in the gradual transition from a steep to a constant slope, and further on from a constant to a steep slope.

From the perspective of the application, these deviations with respect to the desired constant force are not significant because of the large margins on the tolerance of the admissible force. However, from a scientific perspective it is desirable to gain more insight into these phenomena. Once the phenomena are understood and quantified, the design can be adapted to compensate for the observed errors. For example, the subtended angle could be varied non-linearly instead of linearly, in order to get the desired force-displacement.

The measurements and the simulation of the prototype showed good resemblance, both qualitatively as quantitatively. On the one hand this validates the simulation model, while on the other hand it shows that the production of the bended sheet has limited effects that compromise the mechanical functioning. Imperfections originated during or after fabrication, like e.g. small kinks in the sheet, and can be felt when actuating the mechanism by hand, but are not large enough to compromise the mechanism behavior. It is questionable whether these imperfections will still be negligible in the harsh circumstances of a catheter fed through the vessels to reach the heart.

Finally, noteworthy is the amount of hysteresis visible in the measurement result, i.e. the difference in force between forward and backward motion. This indicates the presence of energy losses which are predominantly caused by friction under normal circumstances. Since there are no sliding contacts in this design, it is unclear where the losses originate from. Possible explanations are the internal material hysteresis, i.e. damping, the contribution of which increases at high strains, or (micro)slip in the clamped areas.

6.5. Conclusion

A constant force mechanism for the tip of a cardiac ablation catheter has been presented by showing its working principle numerically and experimentally. This tip, potentially small enough, was designed to provide a more stable contact with the moving heart wall for an improved efficacy of future ablation interventions. The concept consists of a double folded tape loop with a linearly tapered subtended angle. The double folded tape loop provides an inherent rectilinear guidance. The tapered angle realizes a linear variation of the elastic potential energy of the system with respect to the rectilinear motion, thus realizing a constant force mechanism. This design is unique in its simplicity, its range of motion with respect to its occupied volume and the absence of sliding parts and joints. This makes the design a good candidate for the proposed cardiac ablation procedure and potentially other applications with similar requirements.

A design of a tape loop was made based on requirements needed for its use as a constant force catheter tip. In simulation, this design has a constant force region of 20mm with an average force of $7.8 \times 10^{-2}\,\mathrm{N} \pm 8 \times 10^{-3}\,\mathrm{N}$. The concept of a constant force catheter tip was validated with a prototype that was within one order of magnitude of the dimensions of the intended medical device. In simulation this device has a range of motion of 35mm where it provides a force of $1.3 \times 10^{-1}\,\mathrm{N} \pm 1.6 \times 10^{-2}\,\mathrm{N}$. The experiment shows the same trend, but has larger deviations due to hystereris and boundary conditions.

6.6. Author Contributions

W.W.P.J.S., G.R. and A.A proposed and designed the research and wrote the paper. W.W.P.J.S. and G.R. created the prototype, performed the numerical calculations and did the experiment. W.W.P.J.S. edited the paper and acted as corresponding author.

Bibliography

[1] W. W. P. J. van de Sande, A. Ali, and G. Radaelli. “Design and evaluation of a passive constant force mechanism for a cardiac ablation catheter”. In: *Journal of Medical Devices* 15.2 (2021).

[2] R. Fujiwara, K. Imamura, Y. Kijima, T. Masano, R. Nagoshi, A. Kohzuki, H. Shibata, Y. Tsukiyama, R. Takeshige, K. Yanaka, S. Nakano, Y. Fukuyama, and J. Shite. “The importance of catheter stability evaluated by VisitagTM during pulmonary vein isolation”. In: *Journal of Interventional Cardiac Electrophysiology* 46.2 (2016), pp. 161–166.

[3] V. Y. Reddy, D. Shah, J. Kautzner, B. Schmidt, N. Saoudi, C. Herrera, P. Jaïs, G. Hindricks, P. Peichl, A. Yulzari, H. Lambert, P. Neuzil, A. Natale, and K.-H. Kuck. “The relationship between contact force and clinical outcome during radiofrequency catheter ablation of atrial fibrillation in the TOCCATA study”. In: *Heart Rhythm* 9.11 (2012), pp. 1789–1795.

[4] E. P. Gerstenfeld. “Contact Force–Sensing Catheters”. In: *Circulation: Arrhythmia and Electrophysiology* 7.1 (2014), pp. 5–6.

[5] T. Kimura, S. Takatsuki, A. Oishi, M. Negishi, S. Kashimura, Y. Katsumata, T. Nishiyama, N. Nishiyama, Y. Tanimoto, Y. Aizawa, and K. Fukuda. “Operator-blinded contact force monitoring during pulmonary vein isolation using conventional and steerable sheaths”. In: *International Journal of Cardiology* 177.3 (2014), pp. 970–976.

[6] W. Ullah, R. J. Hunter, A. McLean, M. Dhinoja, M. J. Earley, S. Sporton, and R. J. Schilling. “Impact of Steerable Sheaths on Contact Forces and Reconnection Sites in Ablation for Persistent Atrial Fibrillation”. In: *Journal of Cardiovascular Electrophysiology* 26.3 (2015), pp. 266–273.

[7] S. Matsuo, T. Yamane, M. Tokuda, T. Date, M. Hioki, R. Narui, K. Ito, S. Yamashita, Y. Hama, T. Nakane, K. Inada, K. Shibayama, S. Miyanaga, H. Yoshida, H. Miyazaki, K. Abe, K.-i. Sugimoto, I. Taniguchi, and M. Yoshimura. “Prospective randomized comparison of a steerable versus a non-steerable sheath for typical atrial flutter ablation”. In: *Europace* 12.3 (2010), pp. 402–409.

[8] A. Ali, D. H. Plettenburg, and P. Breedveld. “Steerable Catheters in Cardiology: Classifying Steerability and Assessing Future Challenges”. In: *IEEE Transactions on Biomedical Engineering* 63.4 (2016), pp. 679–693.

[9] C. Piorkowski, C. Eitel, S. Rolf, K. Bode, P. Sommer, T. Gaspar, S. Kircher, U. Wetzel, A. S. Parwani, L.-H. Boldt, M. Mende, A. Bollmann, D. Husser, N. Dagres, M. Esato, A. Arya, W. Haverkamp, and G. Hindricks. "Steerable Versus Nonsteerable Sheath Technology in Atrial Fibrillation Ablation". In: *Circulation: Arrhythmia and Electrophysiology* 4.2 (2011), pp. 157–165.

[10] A. D. Russo, G. Pelargonio, and M. Casella. "New high-density mapping catheter: helpful tool to assess complete pulmonary veins isolation". In: *Europace* 10.1 (2007), pp. 118–119.

[11] T. Arentz, J. von Rosenthal, T. Blum, J. Stockinger, G. Bürkle, R. Weber, N. Jander, F. J. Neumann, and D. Kalusche. "Feasibility and Safety of Pulmonary Vein Isolation Using a New Mapping and Navigation System in Patients With Refractory Atrial Fibrillation". In: *Circulation* 108.20 (2003), pp. 2484–2490.

[12] P. Lambert and J. L. Herder. "An Adjustable Constant Force Mechanism Using Pin Joints and Springs". In: *New Trends in Mechanism and Machine Science*. Cham, Switzerland, September 20–23, 2016, pp. 453–461.

[13] R. H. Nathan. "A Constant Force Generation Mechanism". In: *Journal of Mechanisms Transmissions and Automation in Design* 107.4 (1985), pp. 508–512.

[14] M. Li and W. Cheng. "Design and Experimental Validation of a Large-Displacement Constant-Force Mechanism". In: *Journal of Mechanisms and Robotics* 10.5 (2018), p. 051007.

[15] G. Radaelli and J. L. Herder. "Shape optimization and sensitivity of compliant beams for prescribed load-displacement response". In: *Mechanical Sciences* 7 (2016), pp. 219–232.

[16] D. R. Nahar and T. Sugar. "Compliant constant-force mechanism with a variable output for micro/macro applications". In: *2003 IEEE International Conference on Robotics and Automation (Cat. No.03CH37422)*. Tapei, Taiwan, September 14–19, 2003, 318–323 vol.1.

[17] H.-T. Pham and D.-A. Wang. "A constant-force bistable mechanism for force regulation and overload protection". In: *Mechanism and Machine Theory* 46.7 (2011), pp. 899–909.

[18] G. Radaelli and J. Herder. "Gravity balanced compliant shell mechanisms". In: *International Journal of Solids and Structures* 118-119 (2017), pp. 78–88.

[19] C. Vehar, S. Kota, and R. Dennis. "Closed-Loop Tape Springs as Fully Compliant Mechanisms: Preliminary Investigations". In: vol. Volume 2: 28th Biennial Mechanisms and Robotics Conference, Parts A and B. International Design Engineering Technical Conferences and Computers and Information in Engineering Conference. Sept. 2004, pp. 1023–1032. eprint: https://asmedigitalcollection.asme.org/IDETC-CIE/proceedings-pdf/IDETC-CIE2004/46954/1023/2617091/1023_1.pdf.

[20] H. Houwers. "Closed-Loop Two-Fold Tape Spring Transmissions". Master Thesis. Delft University of Technology, 2016, p. 97.

[21] M. G. de Jong, W. W. P. J. van de Sande, and J. L. Herder. “Properties of Twofold Tape Loops: The Influence of the Subtended Angle”. In: *J. Mechanisms Robotics* 11.2 (2019), pp. 020912-020912–7.

[22] G. Radaelli and J. Herder. “Gravity balanced compliant shell mechanisms”. In: *International Journal of Solids and Structures* 118-119 (2017), pp. 78–88.

[23] K. Seffen, Z. You, and S. Pellegrino. “Folding and deployment of curved tape springs”. In: *International Journal of Mechanical Sciences* 42.10 (2000), pp. 2055–2073.

[24] J. A. Cottrell, T. J. R. Hughes, and Y. Bazilevs. *Isogeometric analysis : toward integration of CAD and FEA*. Wiley, New York, USA, 2009, p. 335.

7

Synthesis of force deflection behaviour of tape loops using system identification with a convolution system model

Werner W.P.J. van de Sande, Just L.Herder

A tape spring is a flexure element that has zero curvature in the longitudinal direction and a constant radius in the transverse direction. A two fold tape loops consists of a tape spring folded twice and the ends connected. This creates a zero stiffness straight-line guidance. Other force-deflection behaviour can be achieved by varying the cross-section of the tape spring. Precisely designing this behaviour is difficult due to the strain energy distribution in the tape loop. As the tape loop rolls, material is continuously moving into and out of the folds. This type of deformation has analogies with the system concept of convolution. As such, this deformation can be seen as a system with the strain energy as input and geometry as input.

In this work, we introduce a method to synthesize geometries to achieve specific force-deflection behaviour. We use a system identification approach to obtain a model for the deformation of a tape loop. This estimator is then used to generate geometry in concert with a desired energy profile. A geometry that generates a constant force is synthesized to illustrate the method.

This chapter is submitted to *Mechanism and Machine Theory* as: W.W.P.J. van de Sande and J.L. Herder.,"Synthesis of force deflection behaviour of tape loops using system identification with a convolution system model".

Introduction

Compliant mechanisms have become more prevalent due to their advantages over their rigid link counterparts; these include lack of friction and play, their deterministic behaviour and their simplicity. They are used in multiple fields, such as the precision, aerospace and medical industries [1].

Compliant mechanisms achieve motion by elastic deformation of their constituent parts. As such, it requires force and energy to actuate these mechanisms [1]. Efforts have been made to overcome this inherent stiffness. Reducing the stiffness of a compliant mechanism reduces the energy to operate them or to better transfer the force from the output to the input and vice versa [2, 3]. One solution to lower stiffness is by adding negative stiffness; this strategy has been extensively explored in literature. Designing for a specific stiffness is relatively straightforward with this strategy; both the positive and negative stiffness can be computed using a limited number of formulas [4–7]. The range of motion where this synthesis method is valid is limited.

With these small motions stiffness is considered linear; with larger motions stiffness is often non-linear. Recently, efforts have been made to use this non-linear behaviour to realise other desired force-deflection paths. For instance, constant force mechanisms that have applications in gravity balancers [8, 9]. The synthesis of these mechanisms cannot easily be replicated for other mechanisms of the same type.

A relatively new area in the field of compliant mechanisms with tailored force-displacement behaviour is that of shell mechanisms. These are thin-walled (doubly) curved stuctures that also derive their kinetic behaviour from their deformation [10–14]. Their complex shapes allow for wider options regarding kinematics and force-deflection behaviour compared to their flat counterparts. Their complexity also makes synthesis quite difficult and design strategies often cannot easily be replicated for other mechanisms. In some cases shape optimization is used to obtain geometries that result in the desired behaviour, which is easier to replicate for other mechanisms [15].

The most basic shell element is a tape spring: a thin-walled open cylindrical structure with zero longitudinal and constant transverse curvature. When a tape spring is buckled, the created fold will act as a constant moment hinge with a constant radius [16–18]. This property has been used in many applications, such as extendible booms and strategies to fold out solar panels of satellites [19–27] .

A tape loop is a number of folded tape springs with their ends connected to each other, creating a loop. Vehar et al. [28] examined different setups with a different number of folds. The simplest configuration of a tape loop is a two-fold tape loop, which acts as a zero force and zero stiffness linear guide, see fig. 7.1 [28–30].

A two-fold tape loop is the monolithic equivalent of a rolamite, which has the same working principle [31, 32]. Rolamite consists of two rollers, a frame and a band to constrain the rollers, see fig. 7.2. The rollers can only move in a straight line and are constrained with high stiffness in all other directions. The band is pre-tensioned so that is always in contact with the rollers. The deformation of the band is completely determined by the radius of the rollers. As such, the geometry and deformation are completely decoupled. A rolamite can act as force generator

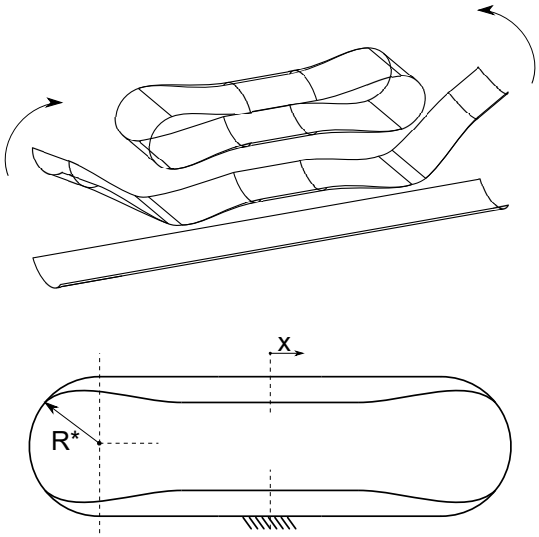

Figure 7.1.: A tape loop is created by folding a tape spring twice and connecting the ends. This creates a straight line mechanism when one undeformed region is connected to the world. The folds have a constant radius R^* [30].

by changing the geometry of the band [33]; in this case, the amount of material deformed by the rollers differs during the range of motion. A whole array of force-deflection behaviours can be synthesised using this strategy.

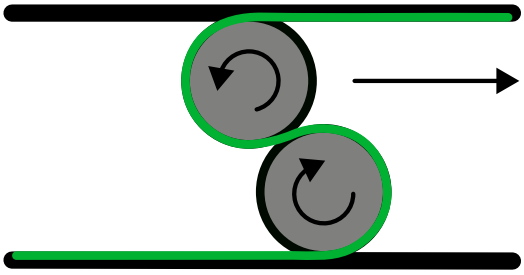

Figure 7.2.: Rolamite consisting of a frame (horizontal lines) and two rollers that rotate in opposite directions; The rollers are constrained by a band (in green) the rollers are pressed against the frame and can only move in a horizontal direction.

A two-fold tape loop can also be turned into a force generator by changing the cross section of the tape spring. A linearly changing subtended angle was suggested to create a constant force mechanism [30]. The strain energy state was simplified to only contain the energy in the fold. This caused an offset from the desired constant

force behaviour in both the magnitude of the force and the stiffness.

In this article we introduce a method to create tape loops with custom force-displacement behaviour. This method uses a more complete representation of the strain energy state to synthesise the desired behaviour. Here we assume that a tape loop acts completely analogous to a rolamite. This implies that the deformation is completely independent of the geometry. This allows us to consider the energy behaviour of a tape loop as a convolution of the geometry and the deformation. This assumption vastly decreases the complexity of generating geometries that match certain force-deflection behaviour. We use discrete convolution as a candidate system model in a system identification scheme. To this end, we perform several simulations that are used as input and outputs in this scheme. The obtained model candidate is then used to generate a constant force profile.

This article first explains the basics of tape springs and tape loops. Next, the analogy with a convolution is discussed and elaborated upon. This analogy is used to propose a synthesis method. This method is then explained and validated by some examples. The manuscript ends with a discussion and a conclusion of the results.

Method

A tape spring is a monoclastically curved structure; its geometry can be defined by its length, radius, thickness and subtended angle, see fig. 7.3.

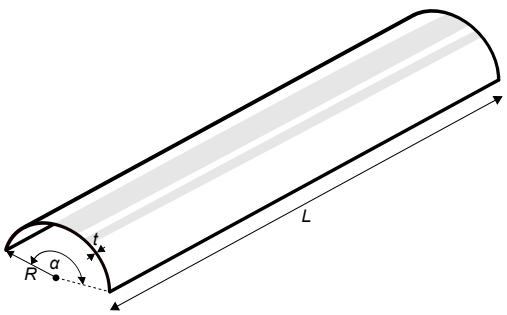

Figure 7.3.: A tape spring and its defining parameters: length L, radius R, thickness t and subtended angle α.

When a moment in the transverse direction is applied to both ends of the tape spring, the tape spring will buckle and a fold will form. There are two distinct buckling moments of a tape spring depending on the polarity of the applied moment, see fig. 7.4.

When folded, a tape spring consists of three separate regions: the fold region, the undeformed region and the transition or ploy region in between, see fig. 7.5 [29, 35, 36]. In the fold region, the tape spring is fully deformed and has a constant radius R^* in the longitudinal direction; there is no curvature in transverse direction. In the undeformed region the opposite is true; the tape spring has its original geometry

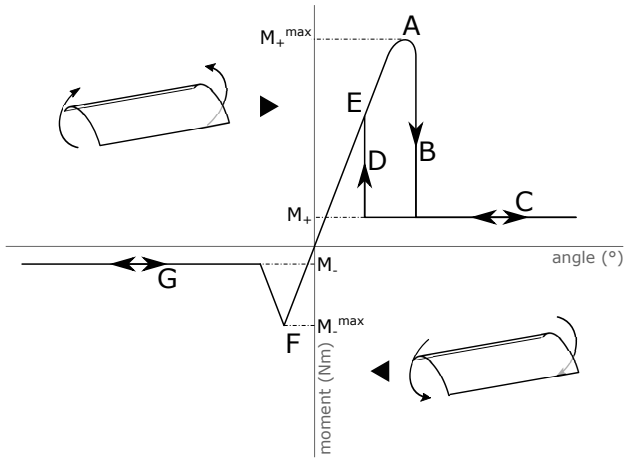

Figure 7.4.: The moment angle curve for tape spring bending. In equal sense bending (bottom left) the moment increases first in relation to the angle, at point (F) the tape spring buckles and the moment decreases to a constant value (G). The reverse displays the same behaviour. In opposite sense bending (top right) the moment also increases linearly with the angle at first (E). It buckles when loaded to a moment (A) and it rapidly snaps (B) to constant moment (C). In the reverse direction the snap back (D) to linear behaviour is at a lower angle than in the forward direction[34].

with a radius R in the transverse direction. These two radii are approximately equal [17]. The transition region is where the curvature changes from completely transverse to completely longitudinal. The shape of the transition region can be approximated analytically [35, 36]; however, this has not been done for varying subtended angles.

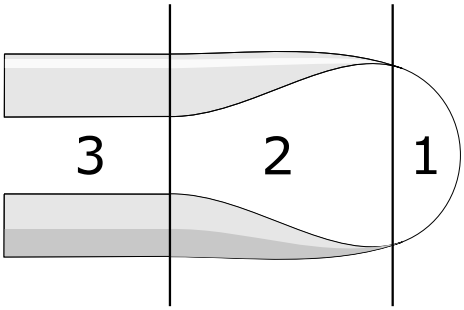

Figure 7.5.: A folded tape spring consists of three distinct deformation zones:, the fold with a constant radius R^* (1), the transition zone (2) and the undeformed regions of the tape spring (3).

When the two ends of a tape loop are connected they create a tape loop. The

simplest tape loop is a two-fold tape loop; it consists of two folds, two undeformed regions and four transition regions (see fig. 7.1). When the bottom undeformed region is clamped and the top is moved, it creates a compliant straight-line guidance [28]. In a tape loop with a constant cross section the energy state of the tape loop does not change. This creates a zero stiffness zero force mechanism [29].

The energy state of a two-fold tape loop can be varied by varying the cross-section. In this article we change the subtended angle, α. The aim of this is to create tape loops with specific force-displacement behaviour. As such the force-displacement behaviour is then related to the change in subtended angle; this creates a connection between the energy state of the tape loop and its geometry.

As a tape loop rolls, material is deformed and undeformed depending on where that material is. This can also be seen as geometry moving in and out of the deformed regions when the tape loop moves (fig. 7.6). This type of behaviour is analogous to a moving weighting function. Mathematically this can be expressed by the convolution of geometry and deformation.

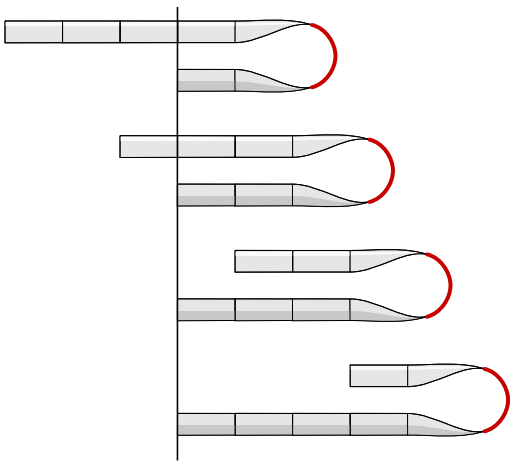

Figure 7.6.: When a tape spring with a single fold is rolled, the deformation moves along the geometry. This is analogous to a moving weighting function or a convolution of the geometry and the deformation.

The energy contained within the fold has already been studied extensively [16, 17, 34]. The energy in a fold of a tape spring with constant cross section can be simplified as follows [29]:

$$U = D(1-\nu)\theta\alpha \tag{7.1}$$

in which U is the energy in the fold and D is the flexural constant given by $D = Et^3/(1-\nu^2)$. The Young's modulus is given by E and the Poisson's ratio of the material is given by ν. Finally, θ is the angle of the fold and the subtended angle is given by α. This energy equation only works for the energy in tape loop folds and assumes a constant subtended angle. Equation (7.1) can be used to derive

a simplified equation for the force produced by a linear tapered tape loop [30] as follows:

$$F = D(1-\nu)\pi\frac{\Delta\alpha}{\Delta x} \tag{7.2}$$

in which the fold angle is set to π. All variables in this equation remain constant, except the subtended angle. As such, the force produced by the tape loop is determined by how the subtended angle varies over the range of motion, here denoted by x. This equation already accommodates for a changing subtended angle. However, it still assumes all the energy is in the fold, not in the transition zone. As such this equation is not sufficient to capture the complete energy distribution in a tape loop.

The energy is contained in all deformed regions, not only in the fold. There have been studies into the strain energy content of the transition zones [35, 36]. However, this has not been done for varying subtended angles and the method is relatively complex.

Geometry moves in and out of these deformed regions when the tape loop moves (fig. 7.3). This is analogous to convolution, with geometry as the input, the deformed regions as the system and the energy state as the output.

First we will prove that the energy state is the convolution of the geometry of the tape spring and the deformed shape of the resulting tape loop. More specifically we express the energy state as the convolution of the geometry of the tape spring and a single fold of a tape loop. Here we assume that we can express the energy in the fold and transition zones by a linear operation on the deformation and the geometry.

A function for the potential strain energy of bending per unit surface area of a tape spring is as follows [34]:

$$U_s = \frac{D}{2}[\kappa_l^2 + \kappa_t^2 + 2\nu\kappa_l\kappa_t] \tag{7.3}$$

in which U is the strain energy, D the flexural rigidity and κ_l and κ_t are the longitudinal and transverse curvature respectively. Integrated over a tape spring of infinite length and a perimeter of $R\alpha$ the total strain energy becomes

$$U = \int_{-R\alpha/2}^{R\alpha/2}\int_{-\infty}^{\infty}\frac{D}{2}[\kappa_l^2 + \kappa_t^2 + 2\nu\kappa_l\kappa_t]dxdy \tag{7.4}$$

the equation can be simplified by solving the integral over y and placing the constants outside of the remaining integral,

$$U = \frac{DR}{2}\int_{-\infty}^{\infty}[\kappa_l^2 + \kappa_t^2 + 2\nu\kappa_l\kappa_t]\alpha dx \tag{7.5}$$

The equation can be shortened by defining the curvature terms as a deformation function:

$$g(x) = [\kappa_l^2 + \kappa_t^2 + 2\nu\kappa_l\kappa_t] \tag{7.6}$$

This function describes the deformation of the tape spring with a single fold. This function is centred around $g(0)$. This fold can move along the length of the tape spring. In order to express this mathematically, the subtended angle, α, also needs to be a function of x. The integral is then as follows:

$$U = \frac{DR}{2} \int_{-\infty}^{\infty} g(x)\alpha(x)dx \tag{7.7}$$

The above equation expresses a stationary situation where the fold stays at a certain location of the tape spring. We introduce the variable l to be able to shift the subtended profile a distance l with respect to the deformation function as follows:

$$U(l) = \frac{DR}{2} \int_{\infty}^{\infty} g(x)\alpha(x+l)dx \tag{7.8}$$

This is the definition of the cross-correlation [37]. As $g(x)$ is a real-valued function, the integral can be rewritten as

$$U(l) = \frac{DR}{2} \int_{\infty}^{\infty} g(x-l)\alpha(x)dx \tag{7.9}$$

The deformation function is considered an even function as the deformation of the tape spring is mirrored around the middle of the fold. As such the integral can be written as

$$U(l) = \frac{DR}{2} \int_{-\infty}^{\infty} g(l-x)\alpha(x)dx \tag{7.10}$$

This is the definition of convolution [37]:

$$U(l) = g(l) * \alpha(l) \tag{7.11}$$

The function $g(x)$ is based on the strain energy formulation [34]. It is dependent on the curvature of the tape spring. This curvature is not independent from the subtended angle, which would make the convolution non-linear. However, in this article we will assume that this is linear to ease computation. We also assume we do not know the exact shape of the curvature and the deformation profile. We will obtain this through system identification [38].

The convolution is used here analogously to how it is used in control engineering: we have an input and an output. The input, subtended angle, is transformed by the system, the deformation function, to the output, energy. System identification is used to obtain information about the system with given inputs and outputs.

In order to identify a system, three things are needed [38]:

1. A data set.
2. A candidate model
3. A rule by which candidate models can be assessed using the data

A data set can be obtained through simulations or experiments. In this specific case we can take the subtended angle profile as input and the resulting energy profile as output.

Any candidate model has to conform to the convolution structure in order to match the mechanics.

In the case of the input and output as a sequence of points, the convolution can be written as a discrete convolution:

$$U(n) = \sum_{j=-\infty}^{\infty} g[n-m]\alpha[m] \tag{7.12}$$

This can also be written in matrix form as follows.

$$U_i = \sum_{j=1}^{m} G_{i,j}\alpha_j \tag{7.13}$$

or

$$U = \mathbf{G}\alpha \tag{7.14}$$

The matrix $\mathbf{G}$ is a model candidate and U the output energy and α the input subtended angle profile written as a column vector.

Multiple column vectors of subtended angle profiles can be described as a matrix, $\mathbf{A}$. The corresponding output energy can be put into a similar shape, $\mathbf{U}$.

In the case of an invertible subtended angle matrix the estimated deformation matrix $\hat{\mathbf{G}}$ is obtained as follows:

$$\hat{\mathbf{G}} = \mathbf{U}\mathbf{A}^{-1} \tag{7.15}$$

However, when $\mathbf{A}$ is not invertible, the pseudo-inverse, $\mathbf{A}^{\dagger}$, can be used [38].

$$\hat{\mathbf{G}} = \mathbf{U}\mathbf{A}^{\dagger} \tag{7.16}$$

The estimator, $\hat{\mathbf{G}}$, and a desired energy profile, $U_{desired}$, can be used to generate the corresponding subtended angle profile, $\alpha_{desired}$. When the estimator is not invertible, the pseudo-inverse should be used as follows:

$$\alpha_{desired} = \hat{\mathbf{G}}^{\dagger} U_{desired} \tag{7.17}$$

The last step in identifying a system is to assess the validity of the estimator. First the usefulness and validity of the inputs should be assesed. When the inputs are not a good representation of expected inputs, a good estimator cannot be determined using eq. (7.15). An insufficiently conditioned problem is represented by a subtended angle matrix, $\mathbf{A}$, with a low column rank. A singular value decomposition of this matrix can be used to ascertain if this is the case [38].

The singular value decomposition of the subtended angle values, $\mathbf{A}$, can be written as

$$\mathbf{A} = U_{\mathbf{A}}\Sigma_{\mathbf{A}}V_{\mathbf{A}}^{T} \tag{7.18}$$

in which $\Sigma_{\mathbf{A}}$ is the sparse matrix with the same size as $\mathbf{A}$ with the singular values on the diagonal. These singular values are usually sorted; when these singular values contain zero entries, the matrix $\mathbf{A}$ is rank deficient and singular. Near-singularity corresponds to near-zero entries in the singular value matrix. An expression for the singularity of these matrices is the condition number where the largest singular value, σ_1, is divided by the smallest singular value, σ_d:

$$c(\mathbf{A}) = \frac{\sigma_1}{\sigma_d} \tag{7.19}$$

This number is a metric for the validity of the inputs; a large condition number points to a badly conditioned input matrix.

In addition, the actual output can be compared to a result obtained via the estimator. The residuals S, from a least square estimate will be used to asses to validity of the estimator.

$$S = \sum_{n=1}^{N} \frac{1}{N} \|\mathbf{U} - \mathbf{A}\hat{\mathbf{G}}\|_2^2 \tag{7.20}$$

This function is already minimised by obtaining the estimation system matrix $\hat{\mathbf{G}}$, see eq. (7.16) [38]. The actual value serves as a metric of how well the actual system is estimated.

7

Results

Simulations are done to generate inputs and outputs. An isogeometric analysis software was used for this purpose [39]. The tape loop was modelled with Kirchhoff-Love shell elements with an isotropic, linear elastic material. In the longitudinal direction 100 elements were used and in the transverse direction 15 elements were used. The undeformed and straight tape spring was bent into a single fold by applying a 180° rotation on one end and fixing the other end. This creates one half of a tape loop, see fig. 7.7. Subsequently, a translation of 1.1 m in the longitudinal direction over 99 steps is applied while maintaining the applied rotation as a constraint. The two ends of the tape spring are modelled to be significantly stiffer than the tape spring itself and also have a very stiff connection to the points where the boundary conditions are applied. This was done to simulate clamping conditions.

The subtended angle profiles are the inputs for the system identification and thus heavily influence the energy profiles. Several subtended angle profiles are selected. The folding of a tape spring is synonymous with buckling the tape spring. This makes the simulation highly susceptible to singularities and as such not every profile will lead to a converged simulation.

The consequence is that only monotonically increasing subtended angle profiles could be used as inputs. All other geometric parameters were kept constant (see table 7.1).

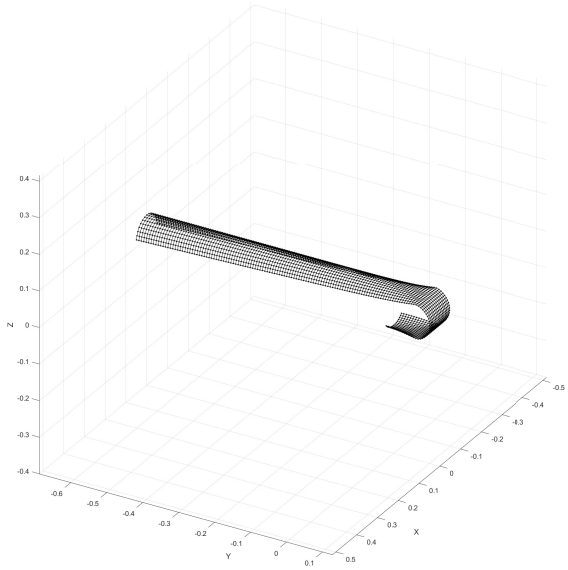

Figure 7.7.: A single fold of a tape spring is modeled using an isogeometric analysis method. The tape spring is folded 180°. Subsequently, the end point is translated in the longitudinal (y) direction.

Table 7.1.: Constant tape spring parameters used in the simulations, with radius R, thickness t, length L, Young's modulus E and Poisson's ratio ν

R	t	L	E	ν
mm	mm	m	GPa	
50	0.5	1	210	0.3

The subtended angle profiles are then generated by three parameters, the minimal subtended angle (α_{min}), the difference between the maximum and minimum subtended angle ($\Delta\alpha$) and the polynomial order of the profile (p) (see table 7.2).

For a tape spring of length L, the subtended angle profile as a function of the longitudinal coordinate l along the tape spring is then expressed as follows.

$$\alpha(l) = \Delta\alpha \left(\frac{l}{L}\right)^p + \alpha_{min} \tag{7.21}$$

All generated subtended profiles that are generated can be seen in fig. 7.8.

A subtended angle profile is evaluated at 99 points, creating a subtended angle

Table 7.2.: The subtended angle profiles used in the simulations, with the difference between the maximum and minimum subtended angle ($\Delta\alpha$), the minimal subtended angle (α_{min}), the polynomial order of the profile (p) and the sum of the squared residuals of the estimated energy profiles when compared to the output of the simulations.

$\Delta\alpha$ rad	α_{min} rad	p	residual J
0.15	0.55	0.5	$5.0 \cdot 10^{-3}$
0.40	0.55	0.5	$7.0 \cdot 10^{-4}$
0.20	0.55	0.7	$5.0 \cdot 10^{-3}$
0.40	0.55	0.7	$1.3 \cdot 10^{-3}$
0.20	0.55	0.8	$1.7 \cdot 10^{-3}$
0.40	0.55	0.8	$4.0 \cdot 10^{-4}$
0.20	0.55	0.9	$5.0 \cdot 10^{-4}$
0.40	0.55	0.9	$1.0 \cdot 10^{-4}$
0.15	0.55	1.0	$4.3 \cdot 10^{-3}$
0.40	0.55	1.0	$2.2 \cdot 10^{-2}$
0.36	0.55	1.0	$2.0 \cdot 10^{-2}$
0.23	0.55	2.0	$9.4 \cdot 10^{-3}$
0.38	0.55	2.0	$3.5 \cdot 10^{-3}$

column vector. The total strain energy from the simulations is evaluated at every step of the translation; this results in energy column vector containing 99 points. The subtended angle is matched in size so that the deformation matrix **G** is square. This is purely a choice, the system can be solved regardless of the size of a subtended angle vector.

All the subtended angle profiles and the energy profiles are concatenated column-wise to create the subtended angle matrix, **A**, and the energy matrix, **U**, respectively. The estimated deformation matrix $\hat{\mathbf{G}}$ is obtained using eq. (7.15). The validity of this estimation was determined by analysing the singular values of this matrix. The matrix has six singular values that are significantly larger than zero, whereas the column size of the matrix is 18. This means that the subtended angle matrix is rank deficient, which would indicate the inputs could be better designed. We will also assess the validity of the estimation by computing the least square error as stated in eq. (7.20). The residuals for all simulations are shown in table 7.2, fig. 7.9 shows a direct comparison between an energy profile of a simulation and the resulting energy obtained with the estimator, $\hat{\mathbf{G}}$, and the original subtended angle profile. This specific estimated profile has the largest residual (10th row in table 7.2), but still matches the actual energy curve in the center of the range of motion. This is the region where the behaviour of the tape loop is not influenced by the clamping.

The goal of this specific synthesis is to generate a subtended angle profile that results in constant force behaviour. In order to generate a subtended angle profile that results in desired mechanical behaviour, we apply the convolution scheme in reverse. In essence we deconvolve the energy with the deformation. For this we

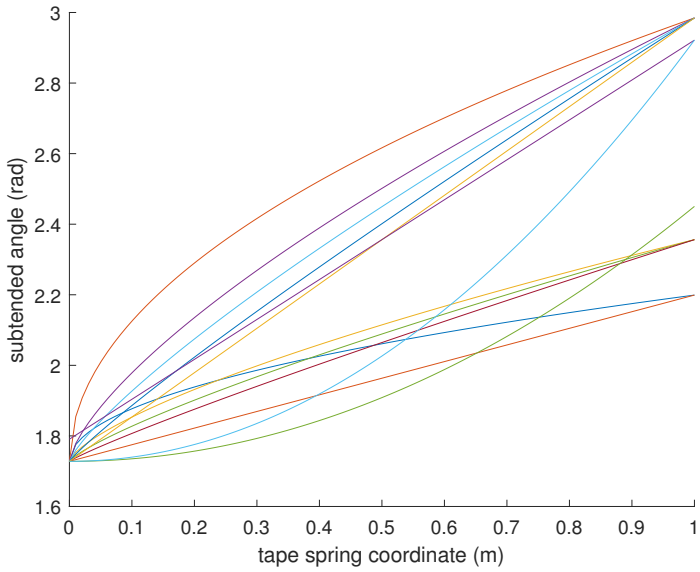

Figure 7.8.: Plot of all subtended angle profile used as inputs in the simulations, the parameters that generated the profiles can be found in table 7.2 and the profiles are generated by eq. (7.21)

first need a desired energy profile from which we can derive the corresponding subtended angle profile.

We take one of the output energy profiles and its subtended angle profile as a base. This subtended angle profile is a linear function with 0.55π rad as α_{min} 0.4π rad as $\Delta\alpha$ and a polynomial order p of 1, see table 7.2. The actual energy profile obtained through simulation is not linearly increasing (black line in fig. 7.10) and is also rapidly increasing and both ends of the range of motion. This is due to the fact that both edges of the tape spring are modelled with high stiffness to approximate clamping conditions.

The estimator, $\hat{\mathbf{G}}$, was conditioned with simulations that had increased strain energy at the edges of the range of motion due to the clamping boundary conditions. We have to consider these effects when constructing a desired energy profile.

A previously simulated energy profile near to linearly increasing strain energy was chosen; this profile was then linearised in the relevant range of motion (blue line in fig. 7.10). This profile was also scaled so that the values and clamping conditions match relatively well with the energy profile resulting from a linearly increasing subtended angle (black line infig. 7.10). An energy profile without clamping effects was also added to show the difference in the behaviour (red line in fig. 7.10). This profile matches the slope of the other linear energy profile in the relevant range of motion. After obtaining the energy profiles, we use eq. (7.17) to generate the subtended angle profiles. We do this for all energy profiles in fig. 7.10.

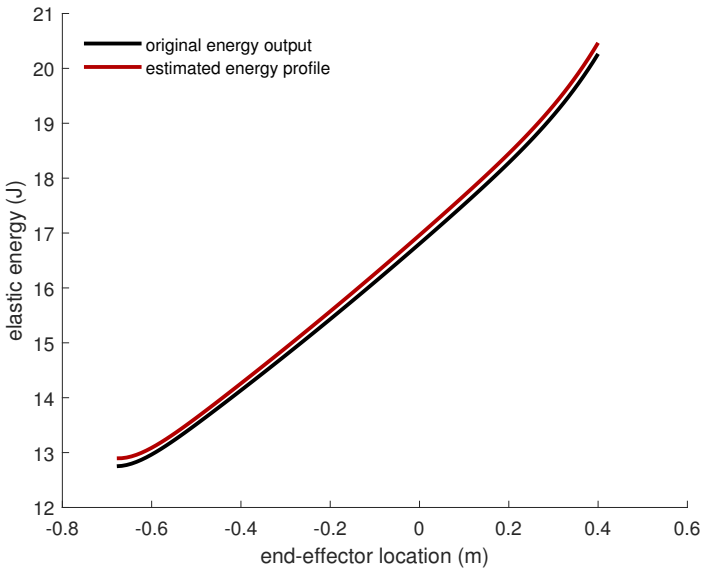

Figure 7.9.: Comparison of the actual energy (black) and estimated force(red) of the estimation with the largest sum of squared residuals

Figure 7.11 shows several subtended angle profiles. There are two sets. The first set contains the actual input of the simulation that was chosen to linearise its energy profile. The other profile in the set is the subtended angle profile derived from the corresponding original energy profile using the estimator. Figure 7.11 shows that the two profiles in the set overlap. The original energy profile was only obtained through simulation. The fact that the generated subtended angle profile matches to the degree it does, indicates that the estimation scheme works well for this type of energy profile. The second set contains the two resulting subtended angle profiles derived from the linear energy profiles. One with clamping effects and one without (fig. 7.11). The estimated subtended angle profile obtained from the purely linear energy profile has values larger than the linear subtended angle profile. In contrast the energy profile with clamping effects is lower than the linear subtended angle profile.

These subtended angle profiles are used in a simulation similar to show the input and output data was obtained. First a polynomial with fitted to the obtained profile; this polynomial has the same parameters as the original subtended angle profiles: the minimal subtended angle (α_{min}), the difference between the maximum and minimum subtended angle ($\Delta\alpha$) and the polynomial order of the profile (p), see table 7.3.

The resulting energy, force and stiffness profiles for these specific subtended angle profiles can be seen fig. 7.12, fig. 7.13 and fig. 7.14 respectively. The energies do not match the desired energy profiles perfectly. Especially the energy profiles

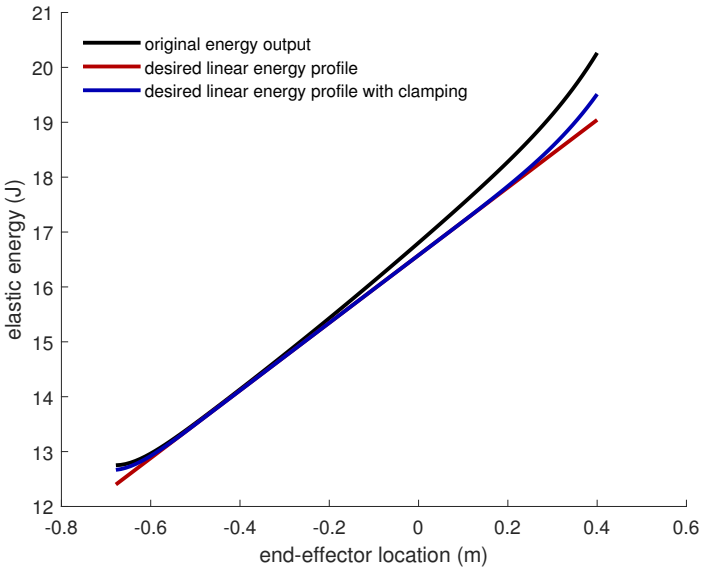

Figure 7.10.: Suggested energy profiles, with original energy profile in black, the linear profile in red and the energy profile with estimated clamping conditions in blue

Table 7.3.: The parameters of the subtended angle profiles; these were fitted to the column vectors of the subtended angle profiles obtained with a desired energy profile and the estimator.

	$\Delta\alpha$ rad	α_{min} rad	p
clamping effects	0.37	0.53	0.77
no clamping effects	0.44	0.54	0.77
interpolation	0.4	0.54	0.78

without clamping effects (red lines in fig. 7.12) differ in magnitude. The energy profiles with clamping effects match quite closely; however, the slope of the energy profile obtained from the estimated subtended angle profile (blue line in fig. 7.12) is visibly flatter than the desired energy profile with clamping effects (blue dashed line infig. 7.12).

The slope in fig. 7.13 determines the actual constant force behaviour and here we see that three force profiles are significantly flatter, but are not quite constant. They are also a significant improvement over the original linear subtended angle profile (black line in fig. 7.13). The force profile obtained considering clamping effects (blue line in fig. 7.13) is lower than the desired force (black dashed line in fig. 7.13). In contrast the force profile obtained without considering clamping effects (red line in

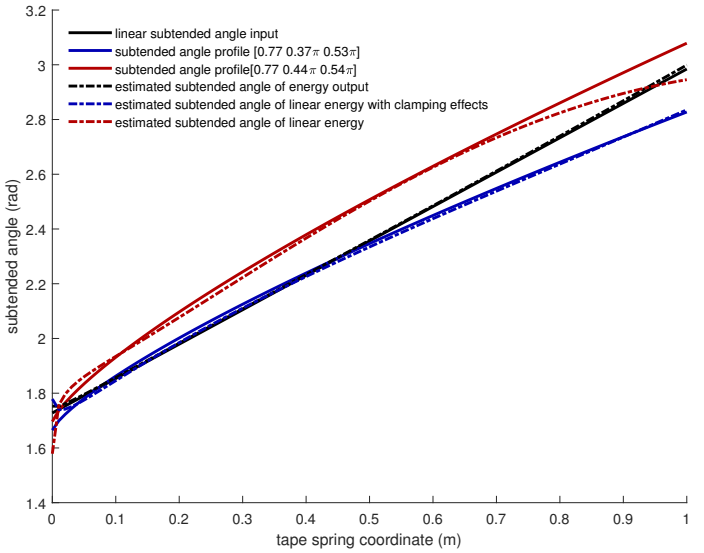

Figure 7.11.: Subtended angle profiles, with the original linear input (black), estimated input base on the original energy profile (black, dashed), the estimated profile of the clamped scenario (blue, dashed) and the estimated profile of the purely linear energy (red, dashed). Simulations were run with two subtended angle profiles that converged and are close to the estimated subtended angle profiles. The parameters are in the same order as table 7.2.

fig. 7.13) overshoots the desired force. To remedy this, a third force profile was introduced and simulated that is an interpolation of the other two profiles. The parameters can be seen in table 7.3. The force profile (purple line in fig. 7.13) matches the desired force quite closely; the energy profile is quite a bit higher.

The stiffness of all profiles is significantly lower than the stiffness of the original profile and remain low over a range of approximately 0.3m, see fig. 7.14. The slope in this range is negative, indicating a softening stiffness. The profile with the largest change in subtended angle (red line in (fig. 7.14) has the lowest stiffness and the smallest plateau of low stiffness. The reverse is true for the profile with the smallest subtended angle profile, which is the profile obtained considering clamping effects.

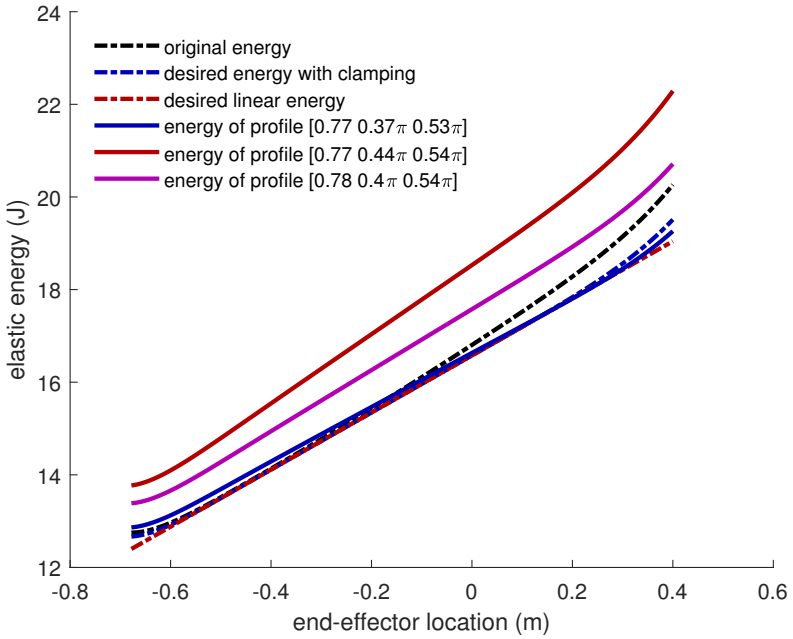

Figure 7.12.: Comparison of energy profiles using the subtended angle profiles shown in fig. 7.11, with the original energy profile (black,dashed), the two desired energy profiles: with clamping (blue, dashed) and purely linear (red, dashed). The red and blue energy profiles results from the subtended angle profiles of the same color in fig. 7.11. The purple profile results from an interpolation of the two subtended angle profiles.

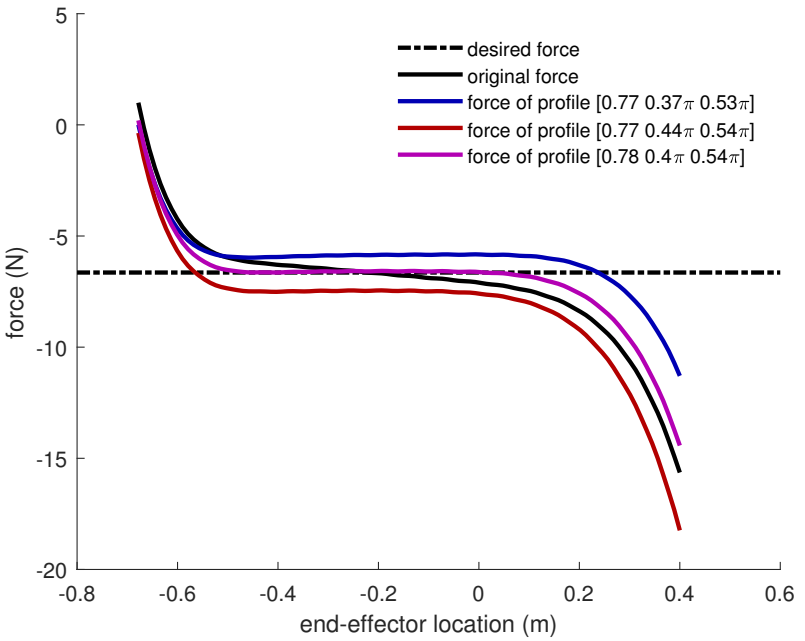

Figure 7.13.: Comparison of force profiles using the subtended angle profiles shown in fig. 7.11, with the original force profile (black) and the desired constant force (black,dashed) . The red and blue force profiles results from the subtended angle profiles of the same color in fig. 7.11. The purple profile results from an interpolation of the two subtended angle profiles.

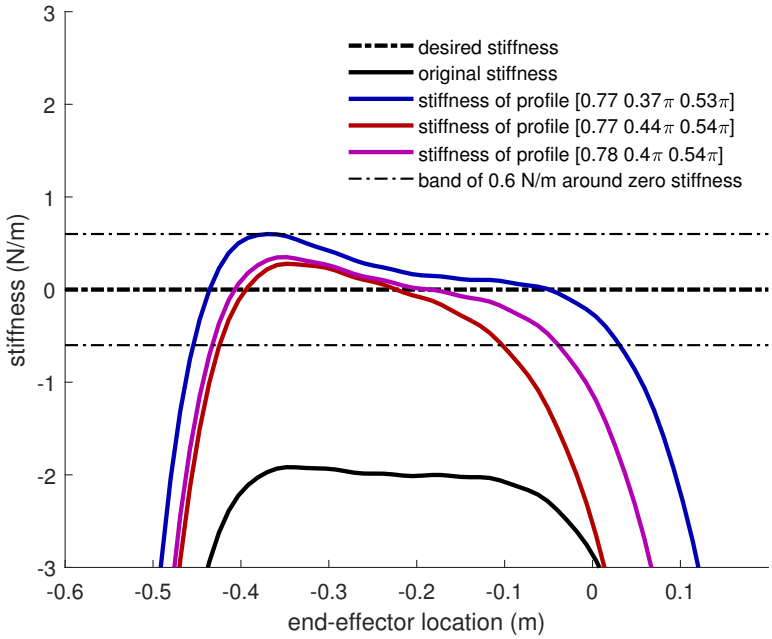

Figure 7.14.: Comparison of stiffness using the subtended angle profiles shown in fig. 7.11, with the desired zero stiffness (black,dashed bold) and the maximum stiffness in the relevant range of motion of the new geometries (black, dashed). The red and blue profiles results from the subtended angle profiles of the same color in fig. 7.11. The purple profile results from an interpolation of the two subtended angle profiles.

Discussion

The deformation of the transition zones is not completely decoupled from the geometry [29]. As such, the convolution model does not accurately describe reality. Nonetheless, the method is able to improve upon previous results [30]. Incorporating these non-linearities in the method will improve the results, but also adds a lot of complexity. It is more feasible that the fidelity of the results can be improved by better conditioning the input geometries. The number of non-zero singular values is significantly below the number of inputs, which indicates that the problem is not conditioned properly. Good results could still be gained from this limited set of inputs. The inputs were all monotonically increasing functions, which also reduces the possible variety of the inputs. This was done in order to get the simulations to converge. Other profiles were attempted, but these simulations did not solve over the entire range of motion. Non-monotonic profiles can result in multi-stable behaviours, which might cause the simulations to fail.

In addition, most profiles had a polynomial order lower than one. The goal was to create a constant force profile; in previous research a order of one resulted in a positive stiffness of the tape loop [30]. As such, the solution was expected to have an order lower than one. The simulations are computationally expensive, so most simulations were done around this polynomial order. This also limited the variety of the inputs.

The minimum angle is 0.5π to ensure tape loop behaviour [29]; the maximum subtended angle is π to avoid self collision. Therefore the difference between the maximum and minimum subtended angle was at most 0.5π. The energy content of the transition zones increases with increasing subtended angles [29]. So a large subtended angle difference between the ends exacerbates the non-linearities in the energy content. The linear assumption works better with small subtended angle differences as the changing energy content of the transition zones can be neglected more easily.

One of the biggest unknowns in this method is how to model the clamping conditions. Not modelling the clamping conditions led to an overestimation of the subtended angle gradient, $\Delta\alpha$, whereas the estimated clamping conditions led to an underestimation of the profile gradient. The actual profile that yielded the proper behaviour had the same order, but had a subtended angle change that was somewhere in the middle. It remains an open question how to properly model these clamping conditions. A better conditioned input matrix can perhaps improve this. Another option is to use only the parts that are not influenced by the clamping in the system identification. In allowing more complex polynomials the effects of the clamps can be negated altogether. The subtended angle can be purposefully reduced near the edges to compensate for the added stiffness of the clamps; this could increase the effective range of motion.

The actual profiles that were used to validate the results differ slightly from predicted subtended angle profiles. The exact matches did not converge for the entire range of motion. This happens for certain inputs. The mesh, geometric and material properties were kept the same, only the subtended angle profile was changed. Usually the simulation would solve the buckling problem, i.e. the folding,

only to fail in the rolling motion. This might be due to the fact that this rolling motion is has a very low stiffness, causing the stiffness matrix to be near singular. This rolling motion was displacement controlled, which should be possible. In the end we chose profiles that converged and were close to the proposed solutions.

The biggest benefit of this method is that it can provide a probable solution within seconds based on an existing database of simulation results. As this database grows, this method will become the more powerful.

The convolution system model is a useful model to describe the behaviour when the geometry and deformation are sufficiently decoupled. There might be other classes of mechanisms where synthesis can be achieved in this manner; certainly rolamite is one of these mechanisms. Further exploration to find other suitable classes of mechanisms is could be a promising research avenue.

Conclusion

In this work we introduce a method to synthesize force displacement behaviour of tape loops. This is done by treating the rolling motion of a tape loop as a convolution of its geometry and deformation; this is possible since the geometry and deformation are largely uncoupled.

A discrete convolution model is a valid system model of tape loop kinetics. The geometry, specifically the subtended angle profile, is treated as input and the resulting strain energy is seen as the output. The input and outputs are then used to perform system identification to obtain an estimator for the convolution system model. With the estimator and a desired energy profile, candidate subtended angle profiles are then synthesized.

We obtained several geometries that result in constant force profiles using this method. These profiles can be generated using a simple matrix multiplication and do not require any computationally intensive simulations. The profiles were validated using a simulation. The geometry and deformation are not completely decoupled; however, the linear convolution model is still able to generate adequate candidate geometries. Clamping conditions influenced the results significantly and these could not be modelled reliably. Even so, the resulting constant force profiles had a stiffness of $0.6\mathrm{N\,m^{-1}}$ at most over a range of 0.3metre minimum, which is 27% of the actuated distance. The original stiffness (black in fig. 7.14 of the linear subtended angle profile has a similar range of low stiffness; however the stiffness of the estimated profiles are lower by at least a factor 3.

The method can be used for any continuous energy profile, given that the system identification problem is sufficiently conditioned.

7.1. Author Contributions

W.W.P.J.S. proposed and designed the research, performed the numerical calculations and wrote the paper. J.L.H. supervised the project and reviewed the paper.

Bibliography

[1] L.L. Howell. *Compliant Mechanisms*. New York: Wiley, 2001.

[2] P. Lambert and J. L. Herder. “An Adjustable Constant Force Mechanism Using Pin Joints and Springs”. In: *New Trends in Mechanism and Machine Science*. Ed. by P. Wenger and P. Flores. Vol. 43. Springer International Publishing, 2017, pp. 453–461.

[3] A. Lamers, J. A. G. Sánchez, and J. L. Herder. “Design of a statically balanced fully compliant grasper”. In: *Mechanismand Machine Theory* 92 (2015), pp. 230–239.

[4] P. R. Kuppens, J. L. Herder, and N. Tolou. “Permanent Stiffness Reduction by Thermal Oxidation of Silicon”. In: *Journal of Microelectromechanical Systems* 28.5 (2019), pp. 900–909.

[5] J. van Eijk and J. Dijksman. “Plate spring mechanism with constant negative stiffness”. In: *Mechanism and Machine Theory* 14.1 (1979), pp. 1–9.

[6] P. Kuppens, M. Bessa, J. Herder, and J. Hopkins. “Monolithic binary stiffness building blocks for mechanical digital machines”. In: *Extreme Mechanics Letters* 42 (2021), p. 101120.

[7] K. Hoetmer, G. Woo, C. Kim, and J. Herder. “Negative Stiffness Building Blocks for Statically Balanced Compliant Mechanisms: Design and Testing”. In: *Journal of Mechanisms and Robotics* 2 (Nov. 2010), p. 041007.

[8] G. Radaelli and J. L. Herder. “Shape optimization and sensitivity of compliant beams for prescribed load-displacement response”. In: *Mechanical Sciences* 7 (2016), pp. 219–232.

[9] G. Radaelli and J. Herder. “Gravity balanced compliant shell mechanisms”. In: *International Journal of Solids and Structures* 118-119 (2017), pp. 78–88.

[10] S. Kok, A. Amoozandeh, and G. Radaelli. “Neutrally stable double-curved shells by inflection point propagation”. In: *Journal of the Mechanics and Physics of Solids* 171 (Nov. 2022), p. 105133.

[11] R. Mak, A. Amoozandeh, G. Radaelli, and J. Herder. “A Curved Compliant Differential Mechanism With Neutral Stability”. In: Nov. 2022.

[12] A. Yellowhorse and L. L. Howell. “Deployable lenticular stiffeners for origami-inspired mechanisms”. In: *Mechanics Based Design of Structures and Machines* 46.5 (2018), pp. 634–649.

[13] G. Radaelli. “Reverse-twisting of helicoidal shells to obtain neutrally stable linkage mechanisms”. In: *International Journal of Mechanical Sciences* 202-203 (May 2021), p. 106532.

[14] M. Schenk and S. D. Guest. “On zero stiffness”. In: *Proceedings of the Institution of Mechanical Engineers, Part C: Journal of Mechanical Engineering Science* 228.10 (2014), pp. 1701–1714.

[15] G. Radaelli and J. L. Herder. “Shape optimization and sensitivity of compliant beams for prescribed load-displacement response”. In: *Mechanical Sciences* 7 (2016), pp. 219–232.

[16] K. Seffen, Z. You, and S. Pellegrino. “Folding and deployment of curved tape springs”. In: *International Journal of Mechanical Sciences* 42.10 (2000), pp. 2055–2073.

[17] K. Seffen and S. Pellegrino. “Deployment dynamics of tape springs”. In: *Proceedings of The Royal Society A: Mathematical, Physical and Engineering Sciences* 455 (Mar. 1999), pp. 1003–1048.

[18] K. Seffen, Z. You, and S. Pellegrino. “Folding and deployment of curved tape springs”. In: *International Journal of Mechanical Sciences* 42.10 (2000), pp. 2055–2073.

[19] F. P. J. Rimrott. “Storable tubular extendible members”. In: *Engineering Digest* (1966).

[20] H. Mallikarachchi and S. Pellegrino. “Quasi-Static Folding and Deployment of Ultrathin Composite Tape-Spring Hinges”. In: *Journal of Spacecraft and Rockets* 48.1 (Jan. 2011), pp. 187–198.

[21] J. Costantine, Y. Tawk, C. G. Christodoulou, J. Banik, and S. Lane. “CubeSat Deployable Antenna Using Bistable Composite Tape-Springs”. In: *IEEE Antennas and Wireless Propagation Letters* 11 (2012), pp. 285–288.

[22] Ö. Soykasap. “Analysis of tape spring hinges”. In: *International Journal of Mechanical Sciences* 49 (2007), pp. 853–860.

[23] S. Walker and G. Aglietti. “A study of tape spring fold curvature for space deployable structures”. In: *Proceedings of the Institution of Mechanical Engineers, Part G: Journal of Aerospace Engineering* 221.3 (June 2007), pp. 313–325.

[24] C. R. Calladine. “The theory of thin shell structures 1888-1988”. In: *Institution of Mechanical Engineers* 202.A3 (1988), pp. 141–149.

[25] S. Bourgeois, B. Cochelin, F. Guinot, and E. Picault. “Buckling analysis of tape springs using a rod model with flexible cross-sections”. In: *European Journal of Computational Mechanics* 21.3-6 (2012), pp. 184–194.

[26] J. Yee, O. Soykasap, and S. Pellegrino. “Carbon Fibre Reinforced Plastic Tape Springs”. In: *45th AIAA/ASME/ASCE/AHS/ASC Structures, Structural Dynamics & Materials Conference*. 2004. eprint: https://arc.aiaa.org/doi/pdf/10.2514/6.2004-1819.

[27] J. C. Yee and S. Pellegrino. “Composite Tube Hinges”. In: *Journal of Aerospace Engineering* 18.4 (2005), pp. 224–231.

[28] C. Vehar, S. Kota, and R. Dennis. “Closed-Loop Tape Springs as Fully Compliant Mechanisms: Preliminary Investigations”. In: vol. Volume 2: 28th Biennial Mechanisms and Robotics Conference, Parts A and B. International Design Engineering Technical Conferences and Computers and Information in Engineering Conference. Sept. 2004, pp. 1023–1032. eprint: https://asmedigitalcollection.asme.org/IDETC-CIE/proceedings-pdf/IDETC-CIE2004/46954/1023/2617091/1023_1.pdf.

[29] M. G. de Jong, W. W. P. J. van de Sande, and J. L. Herder. “Properties of Twofold Tape Loops: The Influence of the Subtended Angle”. In: *J. Mechanisms Robotics* 11.2 (2019), pp. 020912-020912–7.

[30] W. W. P. J. van de Sande, A. Ali, and G. Radaelli. “Design and Evaluation of a Passive Constant Force Mechanism for a Cardiac Ablation Catheter”. In: *Journal of Medical Devices* 15.2 (Dec. 2020). 021003. eprint: https://asmedigitalcollection.asme.org/medicaldevices/article-pdf/15/2/021003/6605619/med_015_02_021003.pdf.

[31] R. V. Cadman. *Rolamite - Geometry and Force Analysis*. Tech. rep. Albuquerque, N. Mex.: Sandia Laboratories, 1970, p. 294.

[32] NASA. *Rolamite: New Mechanical Design Concept*. Tech. rep. 67-10611. Springfield, Virginia: NASA, 1967.

[33] C. English and D. Russell. “Implementation of variable joint stiffness through antagonistic actuation using rolamite springs”. In: *Mechanism and Machine Theory* 34 (1999), pp. 27–40.

[34] K. A. Seffen. “On the Behavior of Folded Tape-Springs”. In: *Journal of Applied Mechanics* 68 (2001), pp. 369–375.

[35] V. Jain and F. Rimrott. “The ploy region of a slit tube(Slit tube flat-to-circular transition during extension, considering mathematical model for curvature change, modulus of elasticity and Poisson ratio effects)”. In: *CASI TRANSACTIONS* 4 (1971), pp. 140–144.

[36] K. Seffen, B. Wang, and S. Guest. “Folded orthotropic tape-springs”. In: *Journal of the Mechanics and Physics of Solids* 123 (2019). The N.A. Fleck 60th Anniversary Volume, pp. 138–148.

[37] A. Papoulis. *The Fourier Integral and its Applications*. New York: McGraw-Hill, 1962.

[38] L. Ljung. *System Identification: Theory for the User*. Pearson Education, 1998.

[39] J. A. Cottrell, T. J. R. Hughes, and Y. Bazilevs. *Isogeometric analysis : toward integration of CAD and FEA*. Wiley, New York, USA, 2009, p. 335.

III

Curved Metamaterials

8

A general method for the creation of dilational surfaces

Freek G.J. Broeren, Werner W.P.J. van de Sande, Volkert van der Wijk, Just L.Herder

Dilational structures can change in size without changing their shape. Current dilational designs are only suitable for specific shapes or curvatures and often require parts of the structure to move perpendicular to the dilational surface, thereby occupying part of the enclosed volume. We present a general method for creating dilational structures with arbitrary shape, where all motions are tangent to the described surface. This method consists of triangulating the target curved surface and replacing each of the triangular faces by pantograph mechanisms according to a tiling algorithm that avoids collisions between neighboring pantographs. Following this algorithm, any curved surface can be made to mechanically dilate and could, theoretically, scale from the fully expanded configuration down to a single point. We illustrate the method with three examples of increasing complexity and varying Gaussian curvature.

This chapter originally appeared as F. G. J. Broeren, W. W. P. J. van de Sande, V. van der Wijk, and J. L. Herder. "A general method for the creation of dilational surfaces". In: *Nature Communications* 10.1 (2019)[1]

8.1. Introduction

Expandable structures are of significant relevance in nature and engineering and come in a variety of forms. Natural examples include the stowing of the precious wings of beetles[2] or the fitting of young leaves into buds[3]. Numerous engineering examples can be found as well, including satellite antennas and solar panels that need to be compact for launch and expand for operation[4–7], and medical stents that need to be moved through arteries[8] or the esophagus[9] in compacted form and deploy at the target position.

Most expandable structures rely on an underlying mechanism to allow them to be reversibly compacted. One well-known example of an expandable structure in which the mechanism is clearly visible is the Hoberman Sphere[10, 11]. This mechanism dilates, i.e. its envelope changes in size without changing its shape[12, 13]. We define dilational structures as structures composed of mechanisms whose only degree of freedom corresponds to dilation. Other examples of dilational structures are dilational polyhedral linkages [14, 15].

Dilational structures have also been studied in the field of mechanical metamaterials[16, 17], particularly for auxetic behavior where the Poisson's ratio is negative[18–20]. A Poisson's ratio of exactly -1 corresponds to dilation.

Currently, several limitations in dilational structures exist. Firstly, most dilational structures have been designed for a specific shape or curvature, making these mechanisms applicable to a very limited set of shapes; for example, the buckliball[21], which is based on a polyhedral linkage that resembles a sphere. Secondly, linkages such as the Hoberman Sphere use mechanisms that move perpendicular to the described surface, making them protrude into the enclosed volume, which, for instance, could be a problem in stent design. Thirdly, to the authors knowledge, no examples of spatial mechanical metamaterials exist that can be sculpted to thin, curved surfaces. The unit cell that governs the behavior of such structures inherently has a finite volume, making the construction of thin dilational surfaces with only motion tangent to the plane impossible. Also, the current planar auxetic metamaterials can not, in general, be used, since the underlying kinematics are not valid for arbitrarily curved surfaces.

In this paper, we present a general method to create mechanism-based dilational structures fitting to any spatially curved surface, by which we mean 2-manifolds with or without boundary. Our method improves on existing work on two key points. Firstly, the resulting mechanism structure is placed on the surface, with no parts of the mechanism moving into the enclosed volume and normal to the surface, unlike for instance the Hoberman mechanism. Secondly, the method is applicable to surfaces with any curvature and can even be applied to non-closed surfaces, i.e. surfaces containing holes or cuts. Enabling these properties in dilational structures makes them of use in, for instance, structures that grow with a person such as medical braces for children and expandable furniture, medical devices that require stowability or compression but need to be stiff otherwise, or implants that need to accommodate some motion but maintain their shape, such as aortic stents.

In the following, we will describe the method, where we first triangulate the surface and then place pantograph mechanisms on each of the faces of the triangulation.

We will prove that this method can be used for any spatially curved surface and comment on the maximum scaling factor possible for these structures. Then, we apply our method to three surfaces of increasing complexity, illustrating its versatility.

8.2. Design Strategy

8.2.1. Dilation

Dilation is a homothetic transformation that relates two similar shapes with respect to a homothetic center[22]. Any two figures related by a dilation are similar and have the same orientation (see fig. 8.1). This transformation preserves the shape and orientation of the figure, but changes the size of each of the elements of the structure by the same factor. In a dilational structure the distances between a representative set of points on the structure, typically corner joints, all scale by the same factor during actuation.

8.2.2. Triangulation

The first step of the presented design method is to triangulate the curved surface from which we want to create a dilational structure. Triangulation is a common strategy to approximate curved surfaces by a mesh of triangular faces and lies at the basis of the STL file format used in 3D printing[23, 24]. Triangulation is illustrated in fig. 8.2 for a sphere. It is observed that the accuracy of the approximation increases

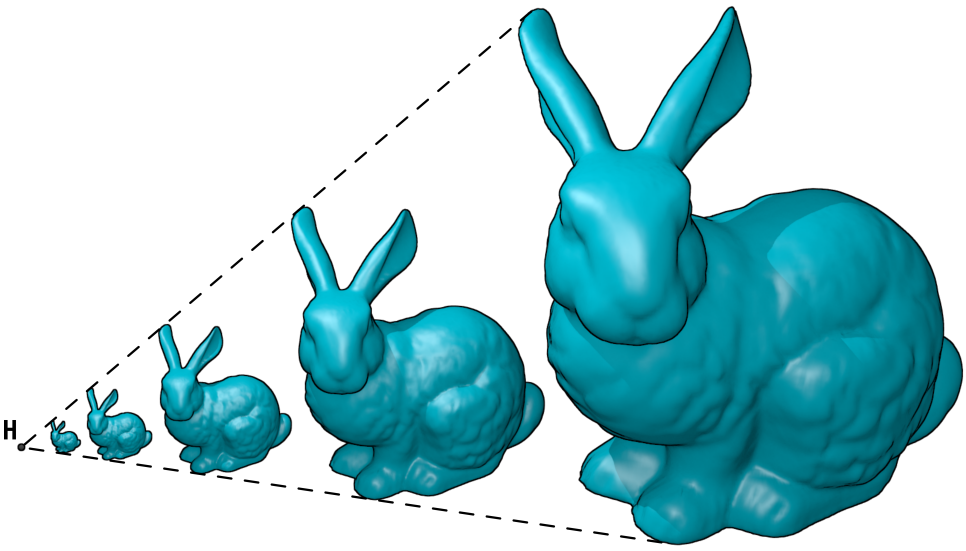

Figure 8.1.: Under dilation, a structure scales with respect to a homothetic center (point H in this figure), preserving its size and orientation.

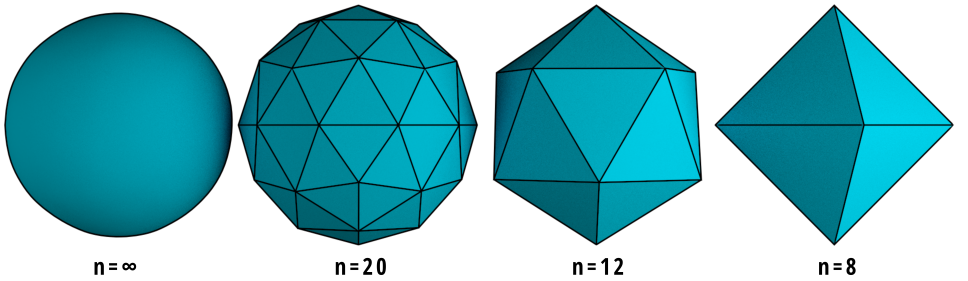

Figure 8.2.: Any curved surface, in this case a sphere, can be approximated by a mesh of triangles in a process called triangulation. A larger mesh of triangular faces gives a better approximation of the original surface. Shown are polyhedral triangulations of a sphere with n triangular faces.

with the number of triangular faces in the resulting mesh.

The triangulation results in a polyhedral surface with only triangular faces. It can be shown that every surface (by which we mean a 2-manifold with or without boundary) can be triangulated such that at most two triangular faces share an edge [25]. If the resulting polyhedron undergoes dilation, the number of triangles, their shapes and their respective relations must stay constant. Only the size of the triangles is allowed to change, their aspect ratio and orientation are preserved.

8.2.3. Pantograph linkage

To transform the polyhedral surface into a movable linkage with dilational motion, we employ the skew, or Sylvester's, pantograph mechanism [26–28].

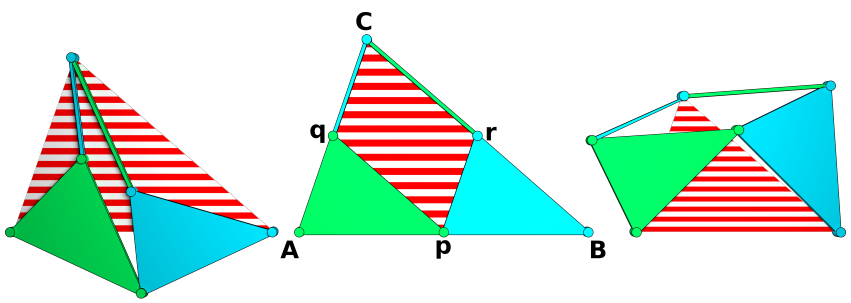

Figure 8.3.: The skew pantograph is a one-degree-of-freedom mechanism that scales the spanned triangle (i.e. the red-striped area) determined by three of its joints; the similarity points, indicated A, B and C. The pantographs has revolute joints at p, q, C and r. For the neutral position, shown in the middle, the spanned triangle equals the triangular shape of the pantograph, this is a useful pose for constructing dilational surfaces.

The skew pantograph is a four-bar mechanism of which two adjacent links are extended into triangles. The mechanism has revolute joints at p, q, C and r, as illustrated in fig. 8.3. The link Cq is equal in length to side rp, as are Cr and qp, which makes $pqCr$ a parallelogram. Also, the triangles Apq and pBr are similar. A resulting feature from these properties is that in any pose of the mechanism the triangle ABC is similar to triangles Apq and pBr. The proof can be found in Hall (1961)[29]. When the mechanism moves, the distances AC, AB and BC become smaller as the parallelogram decreases in area. As a result, the mechanism has a single degree of freedom and during motion the striped red triangle described by its three similarity points (indicated A, B and C) changes in size but remains similar of shape, as is illustrated for three poses. These three joints will be referred to as the similarity points of the pantograph linkage.

The maximum scaling that can be achieved with a skew pantograph depends on the placement of the joints on the edges of the spanned triangle in the neutral position. We place the joint in the middle of the sides of the spanned triangle in the neutral position, such that $Aq = qC$. In this way, the rigid triangles are sized down by a factor 2 relative to the spanned triangle, which allows the spanned triangle to scale down to a single point.

8.2.4. Coupling the pantographs

Each of the faces obtained by triangulating the curved surface is replaced by a skew pantograph mechanism. In this way, we ensure that each individual face can only deform by scaling, keeping its original shape.

The pantograph mechanisms ensures the proper scaling of each individual face. However, in order for the whole structure to dilate, it is also required that each face simultaneously scales by the same factor and that the faces do not rotate with respect to each other. We achieve this by connecting neighboring pantograph mechanisms by means of compound universal joints, whose description follows.

Two adjacent faces of the triangulated surface share a single edge and two vertices. In order to maintain the mobility of the neighboring pantograph mechanisms, they can only be connected at the vertices. At these points, we connect the pantograph mechanisms with universal joints (two consecutive revolute pairs), of which the axes are parallel to the normals of the respective faces, as is illustrated in fig. 8.4. This configuration constrains the rotation about the shared edge of the faces and therefore preserves the relative orientation of the two faces.

Because the two neighboring pantograph mechanisms are now connected along the shared edge, their degrees of freedom are also coupled. When one of the pantograph mechanisms moves, the length of the shared edge will change, causing a movement in the other pantograph. In this way, it is ensured that both pantographs are scaled simultaneously by the same factor and maintain their relative orientation.

Each set of neighboring pantograph mechanisms is connected in this way, creating compound universal joints at the corners of the faces. This preserves the relative angles of all faces and ensures the same scale factor for each of the faces. Therefore, the total resulting motion will be dilation.

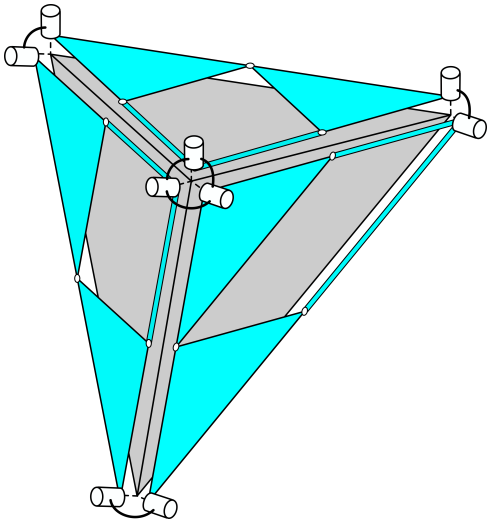

Figure 8.4.: The relative orientation of adjacent pantograph mechanisms is maintained by compound universal joints. This figure shows part of a dilational surface, the triangular faces are shown in grey, and the rigid parts of the pantograph mechanisms are shown in blue. At each of the corners of the pantographs, they are coupled to their neighbors by universal joints, indicated in the figure by a chain of two revolute joints (white cylinders in the figure).A compound universal joint is created at an intersection when three (or more) triangular faces meet.

8.3. Implementation

Kinematically, a structure constructed from the proposed pantograph mechanisms can scale down to a point. In reality, the range of motion of the planar pantographs is limited because of collisions among the rigid bodies that make up the pantographs. In this section, we highlight the factors limiting the range of motion of the dilational mechanisms constructed from pantographs and discuss how to minimize their effects.

8.3.1. Range of Motion of the pantograph

We have described the pantograph mechanism used to make the triangular faces of the polygons dilational. The motion of the mechanism can be described by a single parameter θ and the sides of the spanned triangle are scaled by a factor $\lambda = \cos\theta$ when the mechanism is actuated [30]. The area of the spanned triangle is then scaled by a factor of $\lambda^2 = \cos^2\theta$, see fig. 8.5.

Starting at the neutral position, where $\theta = 0$, the mechanism can move in two directions: θ can increase or decrease, corresponding to a counter-clockwise or clockwise rotation of the lower left rigid triangle. In both cases, the effect on the scaling of the spanned triangle will be the same, since $\cos\theta$ is symmetric around

$\theta = 0$.

In the case where θ increases, the mechanism will protrude out of the spanned triangle at two edges, while it will open up free space at the third edge. Conversely, when θ decreases, the mechanism protrudes out of the spanned triangle at one edge, and opens up space at the other two edges.

When the rigid bodies of the pantograph mechanism are allowed to overlap and cross each other, the minimum area of the spanned triangle is obtained at $\theta = \pm\frac{\pi}{2}$ for the two different cases, both resulting in a scaling factor $\lambda = 0$. When collisions are considered, these values of θ can no longer be reached and often, the scaling factor λ differs between the two motion directions.

Internal Collisions

If the pantographs are designed to be planar and therefore move within a single plane, the range of motion is limited by internal collisions of the links. All pantograph mechanisms in the dilational surface are linked to have a single degree of freedom. Therefore, when one pantograph is actuated such that, for that mechanism, we obtain a rotation θ in its triangular faces, all other pantograph mechanisms in the dilational surface will have a rotation of $\pm\theta$. This causes the complete mechanism to reach the end of its motion as soon as self-collision occurs in any pantograph of the structure. Therefore, this is the main limiting factor on the maximum scaling factor of the assembled dilational mechanism.

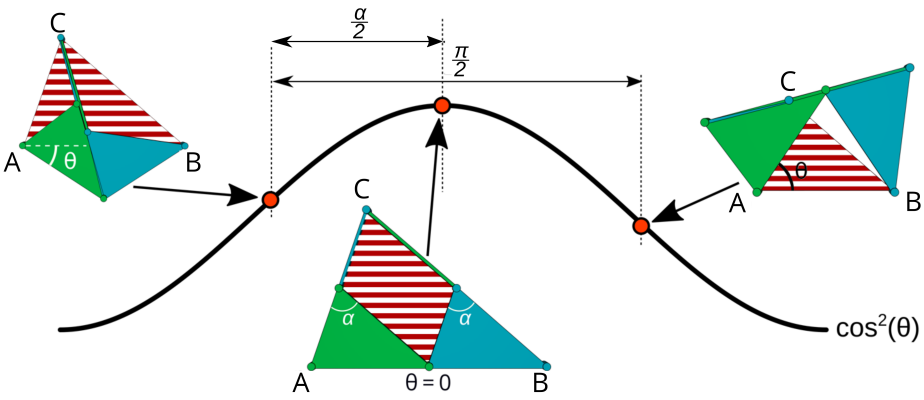

Figure 8.5.: The limits of scaling of a skew pantograph. The area of the spanned triangle (the red-striped area) scales with $\cos^2\theta$. The red dots illustrate the value of θ in each of the drawings. The end of motion is reached when the bars of the linkage become collinear (left and right drawings). Between these states, the rotation angle of θ is always $\frac{\pi}{2}$. The distribution of this range over the left and right motion directions depends on the top angle α.

Looking at fig. 8.5, we can see that the pantograph mechanism reaches the end of its range of motion when $\theta = -\frac{\alpha}{2}$ for one direction of motion, or when $\theta = \frac{\pi-\alpha}{2}$ for the other direction, where α is the top angle of the spanned triangle. At these points, the binary links of the pantograph mechanism become collinear. In this calculation, we have considered the links as lines of zero width. In reality, the links and joints from which the pantograph mechanisms are constructed will have finite width. This will cause collisions to happen earlier and limits the range of motion further.

The total range of θ is $\frac{\pi}{2}$ radians, because the internal angles between the links at two adjacent corners of a parallelogram four-bar linkage always add up to π. For the case where the links have zero width, the optimal scaling factor would be found when $\alpha = 0$ or when $\alpha = \pi$, allowing only for motion in one direction.

However, in both of these cases, the pantograph degenerates to a line, in which case no feasible mechanism would be possible. For simplicity and ease of tiling, it is beneficial when both motions directions have the same range from the neutral position. This is the case for $\alpha = \frac{\pi}{2}$; i.e. when the pantograph mechanisms are right-angled. In this case, the maximal scaling factor is $\lambda = \cos\left(\frac{\pi}{4}\right) = \frac{\sqrt{2}}{2} \approx 0.71$. So, when self-collisions are considered, the distances between points on the dilational surface can be scaled down by at most 29% relative to the neutral position.

8.3.2. Placement of the pantographs

When the pantograph mechanism moves, some parts of the mechanism protrude out of the spanned triangle, while other parts move into the spanned triangle. When all the faces of a triangulated surface are replaced by pantograph mechanisms, two neighboring pantographs could have parts moving out of the respective spanned triangles at their shared edge. This will cause neighboring pantographs to collide, locking the motion of the structure and thereby no longer allowing the scaling of the structure. To remedy this, we have created an algorithm that places the pantographs on a triangulated surface such that neighboring pantographs move along with each other, i.e. when one side of a pantograph has parts that move out of the spanned triangle, the corresponding side of the neighboring pantographs will have parts moving inwards. The algorithm consists of the following procedure.

We first construct the dual graph to the triangulated surface. In this graph, there is one node for each triangular face and two nodes are connected if the two corresponding faces share an edge. Note that, as was mentioned in section 8.2.2, at most two faces share an edge since the original surface is a 2-manifold. The dual graph to an octahedron is shown in fig. 8.6a. For closed surfaces, this creates a simple, connected, 3-regular graph. We assign a direction to each of the edges in the graph to represent the motions of the pantograph mechanisms placed on the triangulated surface. A directed dual graph for an octahedron is shown in fig. 8.6b. Since each edge in the dual graph can only have a single direction, the sides of the triangles are enforced to move along with each other.

The movement of the pantograph mechanisms is such that either the links on two sides move out of the spanned triangle and the links on the other into it or vice-versa, as shown in fig. 8.3. Therefore, we require for each vertex of the graph

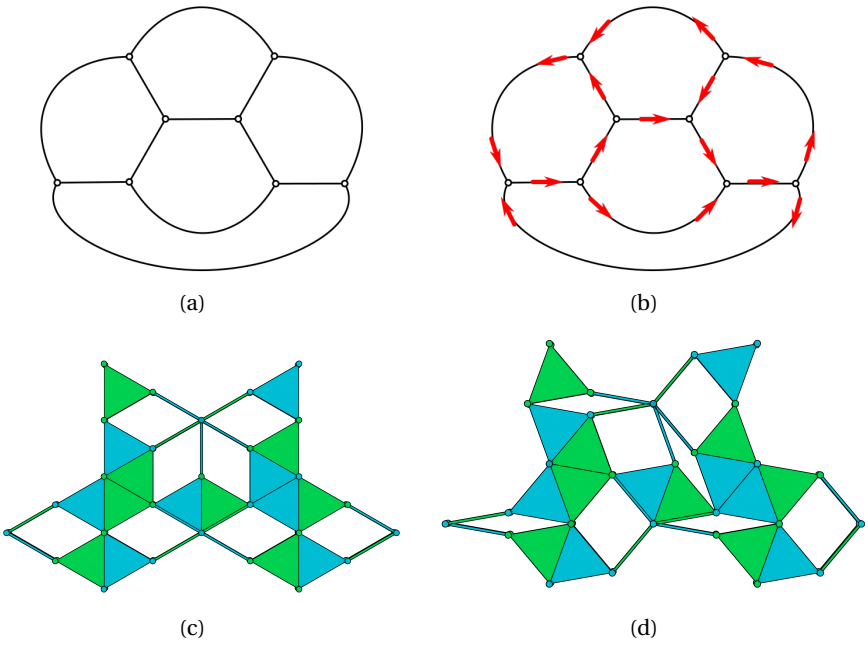

Figure 8.6.: Steps in obtaining a correct tiling pattern of pantographs: (a) dual graph of the net where the vertices are the faces of the triangulated surface, (b) directed dual graph with correct orientation, (c) correct tiling pattern, (d) correct tiling pattern with $\theta = 20°$

that its indegree and outdegree are larger than zero. In Supplementary Note 1[†] of the full paper [1], we show that for each simple connected graph where every node has a degree of at least 2, it is always possible to find an orientation of the graph such that both the indegree and outdegree of every node are larger than zero. The dual graph to every feasible triangulated surface always has nodes of degree at least 3; nodes with degree larger than three correspond to holes in the surface. Therefore, there must exist an orientation of the pantographs on each surface such that movement without collisions between the pantograph mechanisms is possible.

To find a suitable orientation, we use an algorithm that searches for flows through the representing graphs. A flow through a vertex ensures that the difference between the indegree and outdegree is one. This algorithm is further discussed in Supplementary Note 2[†] of the full paper [1]. Once this orientation is found, the pantographs can be placed accordingly, see fig. 8.6c for an example.

[†]The supplementary materials can be found at https://www.nature.com/articles/s41467-019-13134-0.

8.4. Examples

In this section, we will show the application of our method to three surfaces: an octahedron as a simple example[30], a cardioid with both positive and negative Gaussian curvature, and the Stanford Bunny as an advanced example. For all three examples, the reported maximum scaling is based on the pantographs in the resulting structure with the largest and smallest top angle, as described in section 8.3.1.

8.4.1. Octahedron

The octahedron can be viewed as a very rough triangulation of a sphere, comprised of only 8 triangular faces. The eight faces of the octahedron are replaced by pantograph mechanisms, see fig. 8.7. In this way, a dilational surface with only equilateral faces is obtained ($\alpha = 60°$);hlthis gives them a range of $[-30°, 60°]$. Any placement of the pantograph linkages will include pantographs with opposite motion directions, the maximum scaling can therefore be calculated to be $\lambda = \cos(30°) = 0.866$.

8.4.2. Cardioid

The cardioid is a planar curve obtained by tracing a point on a circle, which is rolled around a second circle with equal radius. This curve can be parameterized as follows:

$$x(t) = a(2\cos(t) - \cos(2t)) \tag{8.1}$$

$$y(t) = a(2\sin(t) - \sin(2t)). \tag{8.2}$$

By revolving this curve around the x-axis, we obtain a spatial surface, as is shown in fig. 8.8.

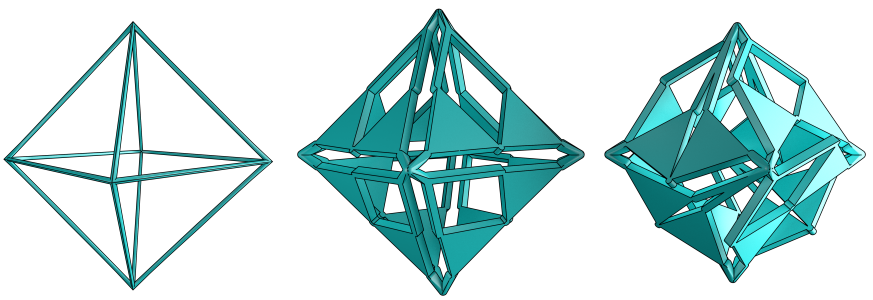

(a) (b) (c)

Figure 8.7.: Eight pantograph linkages are placed on the octahedron. (a) shows the wireframe of an octahedron. (b) shows the dilational structure in the neutral position, ($\theta = 0$) and (c) shows a compacted position ($\theta = 25°$).

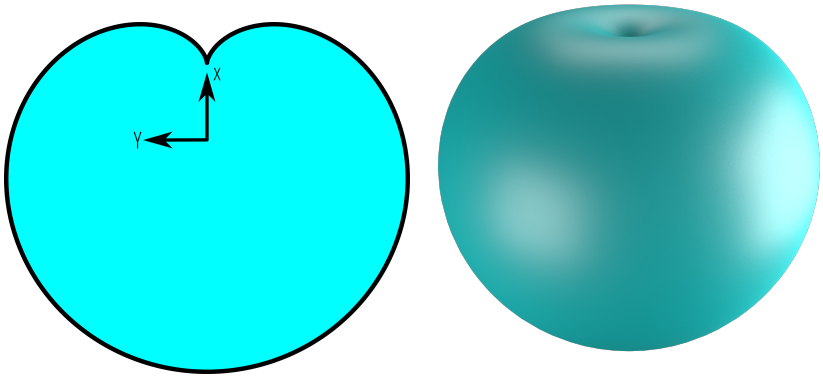

(a) (b)

Figure 8.8.: The cardioid surface is constructed by revolving the planar cardoid curve. (a) shows the curve, (b) shows the complete revolved cardioid.

We have triangulated this shape by taking a planar map of the surface and performing a Delaunay triangulation [31, 32] on this map. The points of the triangulation have been chosen to minimize the number of sharp angles in the triangulation. This triangulation is shown in fig. 8.9a .

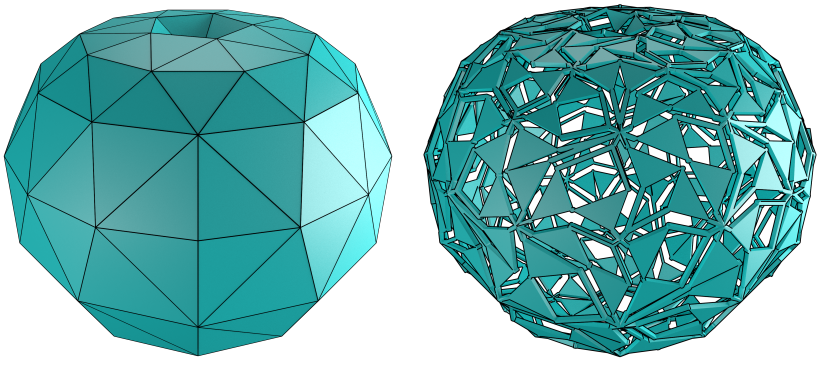

(a) (b)

Figure 8.9.: The surface of the cardioid is first triangulated (a), after which each triangular face is replaced by a skew pantograph (b) to obtain a dilational surface. A movie of the final mechanism is included in the supplementary material [†].

[†]The supplementary materials can be found at https://www.nature.com/articles/s41467-019-13134-0.

On this triangulated surface, we apply our method. First, the dual graph of this surface is determined and we apply the placement algorihm on that graph to determine a suitable placement of the pantograph mechanisms. When the mechanisms are placed on the surface according to this placement, we obtain the shape shown in fig. 8.9b.

For the cardoid we have constructed here, the rotation angle θ can lie in the range $[-20.5°, 20.3°]$, resulting in a maximum scaling factor of $\lambda = 0.937$. A movie of the resulting dilational surface moving between its extremal points is included in the supplementary materials [†].

8.4.3. Stanford Bunny

As a final example, we have taken the Stanford Bunny[33], shown in fig. 8.10a.

For the bunny, we took an available triangulation[34], and edited the triangulation manually to remove the triangles with the sharpest angles in order to increase the maximum scaling factor. The resulting model is shown in fig. 8.10b. This mesh was then fed into our algorithm, which computed a suitable placement of the pantograph mechanisms. The resulting dilational mechanism is shown in fig. 8.10c.

For this mechanism, the rotation angle θ can lie in the range $[-15.0°, 13.1°]$, resulting in a maximum scaling factor $\lambda = 0.966$. This scaling factor is not limited by the shape of the Stanford Bunny, but rather by the specific triangulation used to approximate it and the placement of the pantographs on the triangulation. The maximum scaling factor could be increased further by triangulating the Stanford bunny such that the triangles are close to equilateral, thereby removing even more sharp angles from the polyhedron. Even so, the linear scaling of 3.4% obtained here

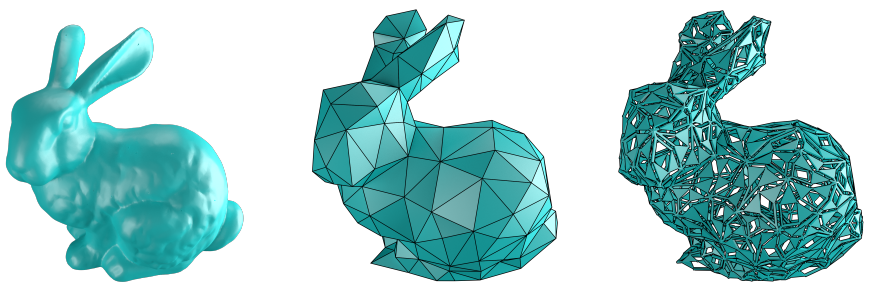

(a) (b) (c)

Figure 8.10.: (a) shows the original Stanford bunny[33]. (b) shows our adaptation of the triangulated version by Thingiverse user johnny6[34], which was used to create the dilational surface shown in (c) by replacing each triangular face with skew pantograph mechanisms. The resulting surface has a scaling factor of $\lambda = 0.966$. A movie of the final mechanism is included in the supplementary material [†].

[†]The supplementary materials can be found at https://www.nature.com/articles/s41467-019-13134-0.

is already similar to the diametric expansion of human arteries during the cardiac cycle [35].

8.5. Discussion and Conclusion

In this work we introduce a comprehensive strategy to achieve dilation of any surface. We do this by triangulating the surface and replacing the triangular faces with Sylvester's pantographs. The similarity points of this pantograph always span a similar triangle. We constrain these triangles in such a way that their orientation is preserved, this preserves the shape of the triangulated surface while allowing it to scale.

Kinematically, a structure constructed using this strategy can be scaled to a single point from its original size. In practice, however, the range of motion of the pantographs is limited by both collisions between links within a pantograph, and collisions between neighboring pantograph mechanisms.

Collisions within the pantograph linkage cause the pantograph with the smallest range of motion to limit the motion of the whole structure, since all pantographs share a single degree of freedom. This could be improved by changing the triangulation strategy and optimizing the placement of the pantographs such that the top-angle of the triangles comes out more favorable (possibly favoring one motion direction over the other). Better pantograph placements might be found, since our pantograph placement algorithm yields non-unique solutions to the pantograph placement problem.

We avoid collisons between neighboring pantograph mechanisms by tiling them in a specific manner. We used a graph-based approach to generate suitable placemements of mechanisms and showed that this approach works for any triangulated surface.

We have illustrated our method with three examples: an octahedron, a cardioid and the Stanford bunny. These surfaces increase in complexity and have varying Gaussian curvature. For the octahedron, the maximal scaling and suitable tiling can be determined by hand. For the cardioid and the Stanford bunny, there are many more triangular faces and the faces are more irregular, for which we present computational methods to generate dilational structures for these surfaces.

The planar kinematics of the pantographs ensure that the resulting dilational mechanism stays close to the described surface throughout the range of motion. This leaves the encompassed interior entirely empty.

A interesting side-effect is that our implementation of the method is directly compatible with the often used STL file format for 3D objects. As such, our strategy could be implemented as a one-click solution to create dilational models.

8.6. Author Contributions

F.G.J.B. and W.W.P.J.S. proposed and designed the research, performed the numerical calculations and wrote the paper. F.G.J.B. wrote the algorithm. J.L.H. proposed the cardioid example. V.W. and J.L.H. supervised the project and reviewed the paper.

Bibliography

[1] F. G. J. Broeren, W. W. P. J. van de Sande, V. van der Wijk, and J. L. Herder. “A general method for the creation of dilational surfaces”. In: *Nature Communications* 10.1 (2019).

[2] J. H. Brackenbury. “Wing Folding in Beetles”. In: *IUTAM-IASS Symp. Deployable Struct. Theory Appl.* Springer, Dordrecht, 2000, pp. 37–44.

[3] D. De Focatiis and S. Guest. “Deployable membranes designed from folding tree leaves”. In: *Philos. Trans. R. Soc. London A Math. Phys. Eng. Sci.* 360.1791 (2002).

[4] J. M. Fernandez, M. Schenk, G. Prassinos, V. J. Lappas, and S. O. Erb. “Deployment Mechanisms of a Gossamer Satellite Deorbiter”. In: *15th Eur. Sp. Mech. Tribol. Symp.* Noordwijk, The Netherlands, 2013.

[5] M. Schenk, S. G. Kerr, A. M. Smyth, and S. D. Guest. “Inflatable Cylinders for Deployable Space Structures”. In: *Proc. First Conf. Transform.* Ed. by F. Escrig and J. Sanchez. Seville, 2013.

[6] H. Petroski. “Engineering: Deployable Structures”. In: *Am. Sci.* 92.2 (2004), pp. 122–126.

[7] Z. You and S. Pellegrino. “Foldable bar structures”. In: *Int. J. Solids Struct.* 34.15 (May 1997), pp. 1825–1847.

[8] K. Kuribayashi, K. Tsuchiya, Z. You, D. Tomus, M. Umemoto, T. Ito, and M. Sasaki. “Self-deployable origami stent grafts as a biomedical application of Ni-rich TiNi shape memory alloy foil”. In: *Mater. Sci. Eng. A* 419.1-2 (Mar. 2006), pp. 131–137.

[9] M. N. Ali, J. J. C. Busfield, and I. U. Rehman. “Auxetic oesophageal stents: structure and mechanical properties”. In: *J. Mater. Sci. Mater. Med.* 25.2 (Feb. 2014), pp. 527–553.

[10] C. Hoberman. *Reversibly Expandable Doubly-curved Truss Structure*. New York, NY, 1990.

[11] C. Hoberman. *Retractable structures comprised of interlinked panels*. Aug. 2002.

[12] G. W. Milton. “Composite materials with poisson’s ratios close to — 1”. In: *J. Mech. Phys. Solids* 40.5 (July 1992), pp. 1105–1137.

[13] G. W. Milton. “New examples of three-dimensional dilational materials”. en. In: *Phys. status solidi* 252.7 (July 2015), pp. 1426–1430.

[14] G. Kiper and E. Söylemez. “Polyhedral linkages obtained as assemblies of planar link groups”. In: *Front. Mech. Eng.* 8.1 (Mar. 2013), pp. 3–9.

[15] C. M. Gosselin and D. Gagnon-Lachance. “Expandable Polyhedral Mechanisms Based on Polygonal One-Degree-of-Freedom Faces”. In: *Proc. Inst. Mech. Eng. Part C J. Mech. Eng. Sci.* 220.7 (2006), pp. 1011–1018.

[16] K. Bertoldi. “Harnessing Instabilities to Design Tunable Architected Cellular Materials”. In: *Annu. Rev. Mater. Res.* 47.1 (July 2017), pp. 51–61.

[17] A. A. Zadpoor. “Mechanical meta-materials”. en. In: *Mater. Horizons* 3.5 (Apr. 2016), pp. 371–381.

[18] K. E. Evans. “Auxetic polymers: a new range of materials”. In: *Endeavour* 15.4 (Jan. 1991), pp. 170–174.

[19] K. E. Evans and A. Alderson. “Auxetic Materials: Functional Materials and Structures from Lateral Thinking!” en. In: *Adv. Mater.* 12.9 (May 2000), pp. 617–628.

[20] G. N. Greaves, A. L. Greer, R. S. Lakes, and T. Rouxel. “Poisson’s ratio and modern materials”. en. In: *Nat. Mater.* 10.11 (Nov. 2011), pp. 823–837.

[21] Shim, C. Perdigou, E. R. Chen, K. Bertoldi, and P. M. Reis. “Buckling-induced encapsulation of structured elastic shells under pressure”. In: *Proc. Natl. Acad. Sci. United States Am.* 109 (2012).

[22] B. Meserve. *Fundamental concepts of geometry*. Cambridge (Mass.): Addison-Wesley, 1955.

[23] N. J. Lennes. “Theorems on the Simple Finite Polygon and Polyhedron”. In: *Am. J. Math.* 33.1/4 (Jan. 1911), p. 37.

[24] T. Grimm. “The Rapid Prototyping Process”. In: *User’s Guid. to Rapid Prototyping*. Society of Manufacturing Engineers (SME), 2004. Chap. 3, pp. 49–84.

[25] E. E. Moise. “Geometric topology in dimensions 2 and 3”. In: vol. 47. Graduate Texts in Mathematics. Lemma 4. New York: Springer-Verlag, 1977. Chap. 4, p. 38.

[26] J. J. Sylvester. “On the Plagiograph aliter the Skew Pantigraph”. In: *Nature* 12 (July 1875), p. 168.

[27] J. J. Sylvester. “History of the Plagiograph”. In: *Nature* 12 (July 1875), pp. 214–216.

[28] E. Dijksman. *Motion geometry of mechanisms*. English. Cambridge, UK : Cambridge University Press, 1976.

[29] A. S. Hall. Prentice-Hall Engineering Science Series. Prentice-Hall, 1961, p. 162.

[30] F. G. J. Broeren, W. W. P. J. van de Sandel, V. van der Wijk, and J. L. Herder. “Dilational Triangulated Shells Using Pantographs”. In: *2018 International Conference on Reconfigurable Mechanisms and Robots (ReMAR)*. June 2018, pp. 1–6.

[31] B. Delaunay. “Sur la Sphère Vide”. In: *Bull. Acad. Sci. USSR* 12.6 (1934), pp. 793–800.

[32] D. T. Lee and B. J. Schachter. “Two algorithms for constructing a Delaunay triangulation”. In: *Int. J. Comput. Inf. Sci.* 9.3 (June 1980), pp. 219–242.

[33] S. U. C. G. Laboratory. *Stanford Bunny*. http://graphics.stanford.edu/data/3Dscanrep/. 1994.

[34] johnny6. *Low Poly Stanford Bunny*. https://www.thingiverse.com/thing:151081. licensed under CC Attribution - Non-Commercial. September 13, 2013.

[35] N. J. Weissman, I. F. Palacios, and A. E. Weyman. “Dynamic expansion of the coronary arteries: Implications for intravascular ultrasound measurements”. In: *Am. Heart J.* 130.1 (July 1995), pp. 46–51.

IV

Conclusion and back matter

9

Conclusion

This chapter provides a discussion of the chapters present in this thesis, states their main contributions and provide some recommendations for further exploration.

Overview

As stated in the introduction of this thesis, shells are structures that can have many shapes and geometries. An in-depth exploration of all shells is too extensive for a single thesis. Rather than exploring the full range of topics concerning shell mechanisms, this thesis aims to a lay a foundation for the analysis of all shell mechanisms. It does this by first introducing the eigenscrew decomposition as the basis of analysis for shell mechanisms. Secondly, the thesis explores the behaviour and capabilities of a buckled tape spring. The tape spring is the simplest shell and is therefore the most logical candidate for an extensive analysis. The third part of the thesis discusses curved metamaterials. This part discusses a completely different type of shell mechanism; it illustrates how varied shell mechanisms can be. The third part also lays a foundation of sorts by providing a method to apply a lattice on a curved surface.

As the thesis itself, this discussion is split into several parts, starting with a discussion on the eigenscrew decomposition, followed by commentary of the tape spring flexure. Subsequently, curved metamaterials are discussed after which a conclusion reiterates the contributions of this thesis.

Part I, Eigenscrew decomposition and its uses in compliant mechanism design

The power of the eigenscrew decomposition lies in the fact that geometric kinetic insight can be gained from the numerical values of the stiffness matrix. The stiffness matrix is usually only valid at a single pose of a elastic structure or mechanism. In order to evaluate the kinetics of a structure, the stiffness matrix needs to be obtained at several poses in a path. This can be computationally expensive; existing metrics need to do this as well or only evaluate the kinetics for small deflections.

Eigenscrew decomposition can also be done for large deformations and does not have this limitation.

The eigenscrew decomposition is useful for shells, as it gives insight into the kinetics of complex non-intuitive structures. The decomposition can also be immensely useful for other compliant mechanisms. The examples given in chapter 4 show that behaviour such as parasitic motions can be adequately expressed by the eigenscrew decomposition. In addition, attributes such as support stiffness can also be analysed more thoroughly. A load bearing stiffness is highly dependent on the location of the load. This load can be seen as a wrench, which can be expressed as a linear combination of eigenwrenches. The presence of induced wrenches represents increased compliance of the wrench, reducing support stiffness. This can be helpful in analysing and designing compliant mechanisms in high precision applications.

Degrees of freedom are not obtained from reciprocal relations as it is done normally in screw theory. After the decomposition, all six eigenstiffnesses are immediately known. It does not require extra steps. At the same time the eigenstiffnesses are only numbers. Without prior knowledge or insight it is not immediately clear whether an eigenstiffness constitutes a degree of freedom or a constraint. Even a significant difference in the magnitude of the stiffnesses does not necessarily indicate the split between DoFs and constraints. For instance, in a leaf spring both the axial stiffness and the lateral bending stiffness are high enough to consider them constraints. However, the axial stiffness is often still orders of magnitude higher than the lateral stiffness. Only when a degree of freedom and a constraint are known, the complete spectrum of stiffnesses becomes clear and the character of the other eigenstiffnesses can be interpolated.

A similar problem arises with comparing rotational stiffnesses with translational stiffnesses. Here the unified stiffness model can be used to cast all stiffnesses in the same unit. This cannot be done without some insight. If a free eigentwist is located at the point of interest it will not show up as a DoF. As the unified length is equal to zero, the stiffness will be infinite. Similarly when a free eigenwrench is located at the point of interest, the unified length is also zero. This leads to unified rotational compliance of zero. As such the unified stiffness method can be of use, but must be used with care. Often times, prior knowledge of degrees of freedom and constraints works best. This can be seen in the example of the buckled tape spring in chapter 4. From intuition is clear that a straight tape spring is stiff in the axial direction, while it is compliant is torsion. The rotational stiffness in the transverse direction is also high at first. When the tape spring buckles it will reach zero stiffness, which constitutes a second degree of freedom. As a result we have a constraint and a degree of freedom in the rotational domain and as such the entire range of behaviour is known. With this spectrum the character of the other rotational stiffness can be interpolated. The nature of the translations is less certain, leading to ambiguity in the number of degrees of freedom. Further investigation to resolve this ambiguity is needed to use the eigenscrew decomposition to full effect.

The eigenscrew decomposition is also able to show zero and negative stiffness behaviour. The usage of the decomposition with singular stiffness matrices was already discussed in the founding articles by Lipkin et al. [1, 2]. However, the

implications were not investigated thoroughly in these papers nor in this thesis. As such, more research is required to rigorously explore the effects of zero stiffness on the decomposition.

The design aspect of the eigenscrew decomposition was highlighted in chapter 3. In this work the attributes of eigenscrews were used in two distinct ways. The desired path of the degree of freedom was obtained through optimisation. The objective function of this optimization was the location of a free eigentwist. This has some similarity to Burmester's approach for linkage synthesis [3, 4]. More interestingly perhaps is how the scoliosis brace was created. It used the eigenscrew decomposition of a helical shell [5] and core principles of serial and parallel mechanisms. A serial chain only has constraints that are shared by all its constituent parts; similarly a parallel mechanism only has degrees of freedom that are shared by all its constituent chains. This was used to cut the helix into smaller segments until a desired number of degrees of freedom was obtained. Two of these helix segments were then connected such that the helices shared a free eigentwist. As a result, the parallel structure also had this free eigentwist, whereas all other degrees of freedom of a single helix were constrained by the other helix. This approach is discussed in detail in the work of Kim [6]. This showcases a powerful method of synthesizing compliant parallel mechanisms consisting of (shell) flexures using the eigenscrew decomposition. Further research on both the mathematics and application of this synthesis tool is required to fully leverage its power.

Part II, Analysis and Synthesis of Two-Fold Tape Loops

Chapter 4 in part I serves as a bridge to part II. Chapter 4 discusses the behaviour of a buckled tape spring from an eigenscrew perspective and gives insight into its degrees of freedom and kinetic behaviour. Table 9.1 shows all six eigenstiffnesses for a straight and buckled tape spring (at 90 degrees) and a straight leaf spring of the same dimensions. The length of the cross-sectional arc of the tape spring is taken as the width of the leaf spring. The degrees of freedom are underlined in table 9.1. The fact that a leaf spring flexure has three degrees of freedom is well-known. The stiffnesses of the pre-buckled tape spring indicate it has only one degree of freedom: the torsional rotation. This can be empirically validated by taking a piece of tape spring and testing the possible motions. A straight tape spring can create a compliant revolute joint with a single flexure.

When we take the degrees of freedom of a straight tape spring as a benchmark, the buckled tape spring appears to have three degrees of freedom: the rotations, see table 9.1.

These results do not line up with what we know of buckled tape springs. The zero stiffness of the rotation is observed, but the zero stiffness of the rolling motion is absent. The reason for this result in chapter 4 is not entirely clear; it might be an error that is introduced due to the fact that the stiffness matrix is near singular. From literature we know that there should be two planar degrees of freedom: the rolling translation and the rotation [7]. This discrepancy should be investigated further. Regardless of the exact configuration of freedoms of the buckled tape spring,

Table 9.1.: The eigenstiffnesses of eigenwrenches (k_{W_i}) and eigentwists (k_{T_i}) of a straight tape spring, buckled tape spring and a leaf spring flexure. The degrees of freedom are underlined

eigenstiffness	straight tape spring	buckled tape spring	straight leaf spring flexure
k_{W_1}	$3.7\times10^{3}\,\mathrm{N\,m^{-1}}$	$7.2\times10^{2}\,\mathrm{N\,m^{-1}}$	$5.1\times10^{3}\,\mathrm{N\,m^{-1}}$
k_{W_2}	$8.2\times10^{5}\,\mathrm{N\,m^{-1}}$	$2.8\times10^{3}\,\mathrm{N\,m^{-1}}$	$8.3\times10^{5}\,\mathrm{N\,m^{-1}}$
k_{W_3}	$3.8\times10^{2}\,\mathrm{N\,m^{-1}}$	$1.2\times10^{2}\,\mathrm{N\,m^{-1}}$	$\underline{9.2\times10^{-2}\,\mathrm{N\,m^{-1}}}$
k_{T_1}	$7.2\times10^{-1}\,\mathrm{N\,m\,rad^{-1}}$	$\underline{1.5\times10^{-3}\,\mathrm{N\,m\,rad^{-1}}}$	$\underline{1.7\times10^{-4}\,\mathrm{N\,m\,rad^{-1}}}$
k_{T_2}	$\underline{8.3\times10^{-4}\,\mathrm{N\,m\,rad^{-1}}}$	$\underline{3.9\times10^{-4}\,\mathrm{N\,m\,rad^{-1}}}$	$\underline{2.6\times10^{-4}\,\mathrm{N\,m\,rad^{-1}}}$
k_{T_3}	$7.1\,\mathrm{N\,m\,rad^{-1}}$	$\underline{9.7\times10^{-3}\,\mathrm{N\,m\,rad^{-1}}}$	$9.5\,\mathrm{N\,m\,rad^{-1}}$

it will be a unique set of degrees of freedom that is not seen in another single flexure. This also makes it a interesting addition the collection of flexures.

The zero stiffness behaviour is one of the defining features of a buckled tape spring. Part II investigates this feature in depth and analyses and synthesizes tape loop behaviour. It considers the two-fold tape loop, but the methods discussed in part II also work for tape loop with three or more folds.

Part II moves from analysis of tape loops to the synthesis of tape loop behaviour. The knowledge gained from chapter 5 and chapter 6 is used in chapter 7 to synthesize specific tape loop behaviour. Each chapter highlights some limitations and interesting avenues for research.

In chapter 5 only the effect of the subtended angle is investigated; other geometric parameters could also be changed. However, by changing the radius the flexure would not longer be a tape spring. Varying the thickness is certainly a possibility, but shells with varying thickness is a whole new category on its own.

In chapter 6 the aim was to create a constant force device for use in minimally invasive surgery. This research highlights the continuing struggle to pack as much energy into a shell while the stresses should not reach the fatigue or yield limit. As the shape of a tape spring is set, the material is dominant in this consideration. One question that remains open is how to increase the energy density of these shells through the usage of new materials. Another aspect of tape loop mechanism that was highlighted in chapter 6 was the fabrication of tape springs. In literature only tape springs with a constant transverse radius are discussed. Off-the-shelf tape springs usually do not have this constant radius. External parties were also not able to create such a tape spring without defects. Consequently, we had to make our own. Perhaps befittingly of research into tape loops, the rolamite mechanism proved inspirational. In the original rolamite mechanism the two rollers are of the same radius. This radius is such that the band only deforms elastically as it is bent around the rollers. In our version, one roller was intentionally made so small so that it deforms a piece of spring steel plastically, see fig. 9.1. The deformation is constant across the spring steel; a tape spring with a constant transverse radius is then made

from this spring steel sheet. There is springback in the steel, but this appears also to be constant. This mechanism for fabrication proved helpful to create the tapered tape loops that can be seen in chapter 6 .

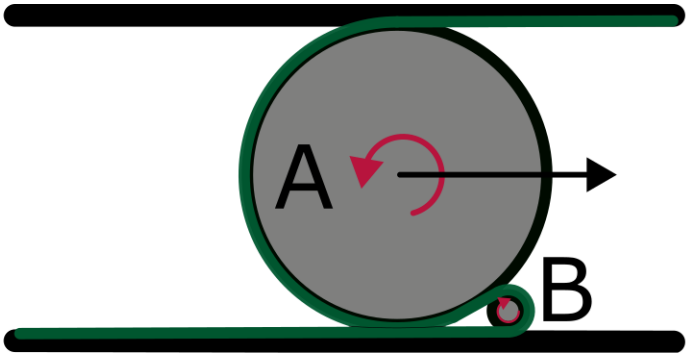

Figure 9.1.: A rolamite mechanism to fabricate tape springs; the smaller roller B deforms spring steel plastically and uniformly. This creates a tape spring with a constant radius.

The approach introduced in chapter 7 is novel in many ways. The use of system identification in mechanism synthesis is a new way to approach mechanism design. Especially with the advent of machine learning this could be a powerful tool to analyse mechanisms and use that data to design new ones. For tape loops this an adequate candidate model of the mechanism is needed. For tape loops this was the convolution model. This link was rather straightforward as the tape loop actually rolls. There are other mechanism classes where relevant design parameters are decoupled enough so that synthesis becomes easier; rolamite is the perfect example of this. It does not have to be convolution, however. Another example is the design of zero-stiffness stages; here negative stiffness element is added to a compliant mechanism with a positive stiffness. Here the deformation of the negative stiffness element is relatively independent of the geometry. The geometry is responsible for the amount of negative stiffness, whereas the deformation controls the range of motion [8, 9]. These two relatively uncoupled effects simplifies the synthesis of compliant mechanism with a specific stiffness. These examples could be only a few of many; further research might lead to finding new classes where this is possible.

Tape springs and tape loops are extensively covered in literature. Part II deepened some of that knowledge and provided design strategies for tape loops.

In the introduction of this thesis tape springs were introduced as the simplest shell. The amount of possible shapes extends much further. A next step would be to do this for the other classes of shells, such as double or hyperbolic parabolic shapes. The body of literature for these shapes is not as extensive as it is for tape springs, but some work has been done [5, 10]. Further research could continue and fill in the gaps in the collection of shell flexure.

Part III, Curved Metamaterials

Chapter 8 is different from the other chapters. The dilational surfaces discussed in this chapter are not smooth shells and the dilational behaviour cannot be captured by the eigenscrew decomposition. It is not a continuous shell either as it has holes in it. However, it is able to transfer loads and displacements and the surface does have a curvature. As such, it meets the criteria of a shell, which were posited by Calladine and were discussed in chapter 1. It is a structurally continuous shell that can derive its motions from elastic deformation; as such, it does fit within the category of compliant shell mechanisms.

The novelty of this type of shell is that it has kinematics within the surface of the membrane of the shell as opposed to other shell mechanisms that work primarily through the bending of the membrane. These deformations within the membrane lead to more complex deformation patterns and provides new design freedom and a new avenue of research.

An unexplored effect in this thesis is the connection between the Poisson ratio of the lattice and the type of bending behaviour. Dilational materials, i.e. materials with a Poisson ratio of -1, display synclastic behaviour when bended. In other words, the direction perpendicular to the line of bending displays the same type of curvature as the applied curvature through bending. Materials with a positive Poisson ratio display anticlastic behaviour or curvature in the opposite direction than the applied curvature [11]. This effect could lead to interesting new designs of shells. An examle of this is the work by La Magna et al. [12] which creates a toroidal shape with an initially flat lattice. The toroidal shape emerges when the lattice is bent properly. This work and chapter 8 are but the first steps into this new research area and illustrates what can be done with lattices and shells.

Although it was not the main contribution of chapter 8, quite a bit of time was spent trying to get dilational shells fabricated. The aim was to exactly get the one degree of freedom that is typical of dilational materials. Through different fabrication techniques such as 3D-printing or rigid link models, the structures were either heavily underconstrained or heavily overconstrained, respectively. With 3D-printing, the structure can be monolithic but printing perfect revolute joints proved too difficult, as the geometry and the material caused the joint to have multiple degrees of freedom. This resulted in the structure having more deformation modes than only the dilational mode. Creating revolute joints was possible with a rigid link model; however, using only revolute joints creates many overconstraints in the structure. Since the structure is a lattice of connected joints, small misalignments in one of the overconstrained joints causes a complete loss of mobility of the entire structure. These effects are also seen in literature, where metamaterials are kept in place with specific boundary conditions to ensure proper kinematics [13–15] or have limited range of motions due to the overconstraints present in the lattices. This is something that needs to be addressed before these latticed structures can be implemented in practise.

Conclusion

In this dissertation we have shown the usefulness of the eigenscrew decomposition in the analysis and design of compliant and compliant shell mechanisms. Although this decomposition is not new, the application to compliant and compliant shell mechanisms is. The resulting eigenscrews informs us about the kinematics and kinetics of any compliant mechanism. This is especially useful for shell mechanisms where the kinetics typically cannot be intuitively understood because of the complex shapes. The strength of this approach is that it can be applied to the end-effector of any mechanism that has a stiffness matrix, which makes it more widely applicable that other metrics. It can also be used for compliant mechanisms with near-zero stiffness behaviour. Moreover, this method can be used in design; this thesis provided an example of this in chapter 3. A parallel shell mechanism was synthesized using a free eigentwist. This eigentwist was then used as a objective function in an optimisation scheme.

In addition, this thesis presents an in-depth investigation into the properties of buckled tape springs in three dimensions. Their geometry provides benefits over regular flat flexures, such as: compact shape with respect to their range of motion, inherent pre-stress, and wide range of designable behaviour. The analysis of chapter 5 and the design of chapter 6 lead to the introduction of a synthesis method in chapter 7, which can be used to design tape loops with an extensive range of force-deflection behaviour.

Chapter 8 presents a curved lattice structure that is able to dilate; the innovation in this type of structures is that the kinematics are within the surface of a shell, while other shell mechanisms derive their motion from the bending of the shell membrane. The key contribution of this method is that any surface can be made to dilate.

In this thesis progress has been made towards better analysis and design strategies for compliant shell mechanisms. The field of compliant shell mechanisms is relatively new and the contributions of this thesis will help further study and development of these mechanisms.

Bibliography

[1] H. Lipkin and T. Patterson. “Geometrical properties of modelled robot elasticity: part I - Decomposition”. In: *ASME Design Tech. Conf. and Computers in Engineering Conf.* Vol. 45. 1992, pp. 179–185.

[2] H. Lipkin and T. Patterson. “Geometrical Properties of Modelled Robot Elasticity: part II - Center of Elasticity”. In: *ASME Design Tech. Conf. and Computers in Engineering Conf.* Vol. 45. 1992, pp. 187–193.

[3] R. Hartenberg and J. Denavit. *Kinematic Synthesis of Linkages*. McGraw-Hill series in mechanical engineering. McGraw-Hill, 1964.

[4] M. Ceccarelli and T. Koetsier. “Burmester and Allievi: A Theory and Its Application for Mechanism Design at the End of 19th Century”. In: *Journal of Mechanical Design* 130.7 (May 2008), p. 072301.

[5] J. Nijssen. “A Type Synthesis Approach to Compliant Shell Mechanisms”. English. MA thesis. 2017.

[6] C. J. Kim. “On the Geometry of Stiffness and Compliance Under Concatenation”. In: *Journal of Mechanisms and Robotics* 12.2 (Feb. 2020), p. 021113.

[7] C. Vehar, S. Kota, and R. Dennis. “Closed-Loop Tape Springs as Fully Compliant Mechanisms: Preliminary Investigations”. In: vol. Volume 2: 28th Biennial Mechanisms and Robotics Conference, Parts A and B. International Design Engineering Technical Conferences and Computers and Information in Engineering Conference. Sept. 2004, pp. 1023–1032. eprint: https://asmedigitalcollection.asme.org/IDETC-CIE/proceedings-pdf/IDETC-CIE2004/46954/1023/2617091/1023_1.pdf.

[8] J. van Eijk and J. Dijksman. “Plate spring mechanism with constant negative stiffness”. In: *Mechanism and Machine Theory* 14.1 (1979), pp. 1–9.

[9] K. Hoetmer, G. Woo, C. Kim, and J. Herder. “Negative Stiffness Building Blocks for Statically Balanced Compliant Mechanisms: Design and Testing”. In: *Journal of Mechanisms and Robotics* 2 (Nov. 2010), p. 041007.

[10] A. Broshuis. “Negative Stiffness in Compliant Shell Mechanisms: To develop a passive stroke rehabilitation device”. English. MA thesis. 2019.

[11] M. J. Mirzaali, A. Ghorbani, K. Nakatani, M. Nouri-Goushki, N. Tümer, S. J. P. Callens, S. Janbaz, A. Accardo, J. Bico, M. Habibi, and A. A. Zadpoor. “Curvature Induced by Deflection in Thick Meta-Plates”. In: *Advanced Materials* 33.30 (2021), p. 2008082. eprint: https://onlinelibrary.wiley.com/doi/pdf/10.1002/adma.202008082.

[12] R. La Magna and J. Knippers. “Tailoring the Bending Behaviour of Material Patterns for the Induction of Double Curvature”. In: Sept. 2018, pp. 441–452.

[13] A. A. Zadpoor. “Mechanical meta-materials”. In: *Mater. Horiz.* 3 (5 2016), pp. 371–381.

[14] X. Ren, R. Das, P. Tran, T. D. Ngo, and Y. M. Xie. “Auxetic metamaterials and structures: a review”. In: *Smart Mater. Struct.* 27.2 (Feb. 2018), p. 023001.

[15] F. Broeren, V. van der Wijk, and J. Herder. “Spatial pseudo-rigid body model for the analysis of a tubular mechanical metamaterial”. In: *Mathematics and Mechanics of Solids* 25 (Sept. 2019), p. 108128651987550.

Acknowledgements

Saint Augustine ponders in his Confessions: “Is any man skilful enough to have fashioned himself?” Although I suspect his answer leaned towards the divine, I think it is applicable to the human experience in general. We do not operate in a vacuum; we are not the sole actors in our lives and plans. This is especially true while pursuing a PhD. Personally, I have woven such a complex web of people that helped in some way me over the years, that it is impossible to thank them all and not forget anyone.

Still, there are some people that I would like to thank for their help and support over the years.

First, I would like to thank my promotor, Just Herder, whose trust and supervision have made this PhD-dissertation a reality. The inspiring discussions and positive support provided me with enthusiasm and joy.

More generally I would like to thank the entire MSD group for creating a pleasant and welcoming work environment. Particularly, I would like to thank all the PhD-candidates and Post-Docs in the MSD-lab for the wonderful time I had there. We had inspiring discussions, fun times and adventures over the years. Thank you all, you know who you are! Specifically, I express my gratitude towards Freek and Giuseppe, who were not only co-authors of my papers, but also valued colleagues and friends. It is always a joy talking to you. First as fellow PhD-candidates and now as teachers.

On the topic of co-authors, I would also like to thank, Joost, Hylke, Charles, Martijn, Awaz, Ali and Volkert for the fruitful collaborations we had over the years.

Also, I thank all the master students I have supervised for the interesting collaborations, exciting discussions and helping me realise how fun and rewarding education is.

I am also thankful toward the lab staff and support staff of PME without whose support nobody would be able to achieve anything academically related.

Lastly and most importantly I would like my family and friends. Early in my PhD-track, I did not understand why parents were congratulated whenever a student graduated. It was, after all, the students’ achievements and not that of the parents. Now, being a parent myself, I realise that raising your children to be able to graduate requires a lot of effort. So, thank you, mom and dad, for helping me to get here. And, related to that, I would like to thank my two daughters, Annabel and Leonie, for reigniting my curiosity, your words of encouragement and helping me put things into perspective. The hugs also helped a lot.

Finally, I am very grateful for the support of my wife Lieke. Without her love, help and support I would have probably gone mad. Thank you for your listening to my ramblings and being the voice of reason and love I needed.

Werner van de Sande
Helvoirt, February 2024

Curriculum Vitæ

Werner Wilhelmus Petrus Johannes van de Sande

19-10-1985 Born in 's-Hertogenbosch, the Netherlands.

Education

1998–2003 **VWO** Natuur en Techniek en Natuur en Gezondheid
Gymnasium, Maurick College
Vught, the Netherlands

2005-2011 **B.Sc.** in Industrial Design Engineering (Industrieel Ontwerpen)
University of Twente
Enschede, the Netherlands

2012-2015 **M.Sc.** in Mechanical Engineering (Werktuigbouwkunde)
University of Twente
Enschede, the Netherlands

2015-2023 **Ph.D** in Precision and Microsystems Engineering
Delft University of Technology
Delft, the Netherlands
Thesis: Theory and synthesis of shell flexures
Promotor: Prof. dr. ir. J. L. Helder

Research output

Patents

1. G. Radaelli, A. Ali, and **W. W. P. J. van de Sande**. *Instrument for minimal invasive surgical operations, comprising a rod or catheter and a tip mounted on the rod or catheter with an elastically deformable element.* Dutch Patent 2019454, March 27, 2017

Journal publications

9. **W.W.P.J. van de Sande** and J.L. Herder. *"Synthesis of force deflection behaviour of tape loops using system identification with a convolution system model". Submitted to Mechanism and Machine Theory* †

8. **W.W.P.J. van de Sande** and J.L. Herder. *"Kinetic analysis of spatial compliant mechanisms using eigenscrew decomposition".Submitted to Precision Engineering* †

7. A. A. Nobaveh, G. Radaelli, **W. W. P. J. van de Sande**, R. A. van Ostayen, and J. L. Herder. "Characterization of spatially curved beams with anisotropically adaptive stiffness using sliding torsional stiffeners". In: *International Journal of Mechanical Sciences* 234 (2022)

6. **W. W. P. J. van de Sande**, A. Ali, and G. Radaelli. "Design and evaluation of a passive constant force mechanism for a cardiac ablation catheter". In: *Journal of Medical Devices* 15.2 (2021) †

5. H. Kooistra, C. J. Kim, **W. W. P. J. van de Sande**, and J. L. Herder. "Shape optimization framework for the path of the primary compliance vector in compliant mechanisms". In: *Journal of Mechanisms and Robotics* 12.6 (2020) †

4. F. G. J. Broeren *, **W. W. P. J. van de Sande** *, V. van der Wijk, and J. L. Herder. "A general method for the creation of dilational surfaces". In: *Nature Communications* 10.1 (2019) †

3. **W. W. P. J. van de Sande**, R. G. Aarts, and D. M. Brouwer. "Effects of misalignments on the static and dynamic behaviour of a multiple overconstrained compliant 4-bar mechanism". In: *Precision engineering* 60 (2019)

*authors contributed equally to this work
†included in this thesis

2. M. G. De Jong, **W. W. P. J. van de Sande**, and J. L. Herder. "Properties of Twofold Tape Loops: The Influence of the Subtended Angle". In: *Journal of Mechanisms and Robotics* 11.2 (2019) †

1. J. R. Leemans, C. J. Kim, **W. W. P. J. van de Sande**, and J. L. Herder. "Unified Stiffness Characterization of Nonlinear Compliant Shell Mechanisms". In: *Journal of Mechanisms and Robotics* 11.1 (2019) †

Peer-reviewed conference publications

6. H. Kooistra, C. J. Kim, **W. W. P. J. van de Sande**, and J. L. Herder. "Shape Optimization Framework for the Path of the Primary Compliance Vector in Compliant Mechanisms". In: *International Design Engineering Technical Conferences and Computers and Information in Engineering Conference*. Anaheim, California, USA, Aug. 2019

5. F. G. J. Broeren, **W. W. P. J. van de Sande**, V. Van Der Wijk, and J. Herder. "Dilational triangulated shells using pantographs". In: *2018 International Conference on Reconfigurable Mechanisms and Robots (ReMAR)*. Delft, the Netherlands, June 2018

4. **W. W. P. J. van de Sande** and J. L. Herder. "Analysis of parasitic motion in compliant mechanisms using eigenwrenches and eigentwists". In: *International Design Engineering Technical Conferences and Computers and Information in Engineering Conference*. Quebec City, Canada, Aug. 2018

3. J. R. Leemans, C. J. Kim, **W. W. P. J. van de Sande**, and J. L. Herder. "Unified Rotational and Translational Stiffness Characterization of Compliant Shell Mechanisms". In: *International Design Engineering Technical Conferences and Computers and Information in Engineering Conference*. American Society of Mechanical Engineers. Quebec City, Canada, Aug. 2018

2. M. G. de Jong, **W. W. P. J. van de Sande**, and J. L. Herder. "Influence of the Subtended Angle on the Behavior of Folded Tape Springs". In: *International Design Engineering Technical Conferences and Computers and Information in Engineering Conference*. Quebec City, Canada, Aug. 2018

1. **W. W. P. J. van de Sande**, R. G. Aarts, and D. M. Brouwer. "System behaviour of a multiple overconstrained compliant four-bar mechanism". In: *Proceedings of the 30th annual meeting of the American Society for Precision Engineering (ASPE)*. Austin, Texas, USA, Nov. 2015

MSc thesis projects supervised

- Mengying Zang, *Design of a multi-purpose research cabin mounted upon a hexapod motion simulator*, (2016, Sep)
- Joost Leemans, *Characterization of non-linear compliant shell mechanisms*, (2018, May)
- Martijn de Jong, *Synthesis of a Force Generator using Two-Fold Tape Loops*, (2018, May)
- Nick van Dijk, *Ergonomic Exoskeleton Synthesis*, (2018, June)
- Kenny Lam, *A Large Stroke Load-Carrying Member*, (2018, July)
- Elco Heijmink, *The Ring Screw: Modelling, Development and Evaluation of a Novel Screw Transmission*, (2018, Aug)
- Stefhan van der Kemp, *Design of a compact wearable arm support utilizing shape optimized shell mechanisms*, (2018, Oct)
- Hylke Kooistra, *Scoliosis Brace Design: Utilizing Compliant Shell Mechanisms and Primary Compliance Vector Path Optimization*, (2019, April)
- Bas Wagemaker, *A classification and performance comparison of force-generators for application in exoskeletons and robotic manipulators*, (2019, Sept)
- Jan Maarten Verzendaal, *Increasing energy storage in compliant tape-spring mechanisms*, (2020, May)
- Jaap Resink, *The quantification of stability of kinematic couplings using robotic grasping measures*, (2022, Oct)
- Jelle Kortman, *Design optimization for a kinematic coupling for use in vacuum with minimum particle generation*, (2023, Jan)
- Sam van den Oever, *Analysis and design of a sprung rotational energy harvester for wrist-worn wearables subject to a range of low frequency excitations*, (2023, May)
- Anna van Soest, *Analyzing out-of-plane deformations caused by varying Poisson ratio distributions in a metamaterial*, (2023, August)

BSc thesis project supervised

- Daniel Boehmer, Dominique Crouwel, Eline Janse, *Effects of pre-stress on the stiffness of a compliant bearing???*, (2016, June)